Cermet anodes for solid oxide fuel cells (SOFC) systems operating in multiple fuel environments: effects of sulfur and carbon composition as well as microstructure.

Julie Suzanne O'Brien

Thesis submitted to the
Faculty of Graduate & Postdoctoral Studies
University of Ottawa
In partial fulfillment of the requirements for the
Ph.D. degree in the Ottawa-Carleton Chemistry Institute

Department of Chemistry
Faculty of Science
University of Ottawa

Table of Contents

List of Figures

Figure 2.20 Nyquist plot and mathematical parameters for a reaction with double layer capacitance in parallel with a Faradaic charge transfer.

Figure 2.21 Serial equivalent circuit depicting an RC element containing Z_d, and unconventional circuit element.

Figure 2.22 Nyquist plot and mathematical parameters for an irreversible oxidation-dependent reaction with double layer capacitance in parallel with Faradaic charge transfer resistance and a diffusion impedance element, Z_d.

Figure 2.23 Inductor element (L).

Figure 2.24 Constant phase element (Q).

Figure 2.25 Nyquist plot and mathematical parameters for a depressed semi-circle.

Figure 2.26 Example of a typical impedance spectrum collected for a button cell with $Ni_{0.7}Co_{0.3}$-YSZ anode at 850°C and 50 sccm flow of H_2 at OCV.

Figure 2.27 Circuit elements RC and RQ.

Figure 2.28 Serial equivalent circuit models proposed by Mogensen (a), and Fleig (b), (c). Equivalent circuit model proposed for fitting to experimental data for this research work (d).

Figure 2.29 Schematic overview of the entire fuel cell set-up.

Figure 2.30 Sample Nyquist (left) and Bode (right) plots for $Ni_{0.7}Co_{0.3}$-YSZ anode. For the case of the Bode plot, the real component data (■) and the phase angle data (■) are shown on the same graph.

Figure 3.1 Powder X-ray diffraction data for powders "as synthesized" before sintering.

Figure 3.2 Powder X-ray diffraction data for the series of $Ni_xCo_{(1-x)}O$-YSZ cermet powders after sintering to 1380°C for 4 h; (■) YSZ (a major phase), (*) NiO (a major phase), (▼) Ni (a very minor phase).

Figure 3.3 Unit cell parameters of the NiO phase in the $Ni_xCo_{(1-x)}O$-YSZ samples synthesized over the Co concentration shown.

Figure 3.4 SEM micrographs of the $Ni_{0.85}Co_{0.15}O$-YSZ cermet powder after sintering. (a) shows two particle size ranges, mag 200 x, bar 100 μm; (b) shows high crystallinity, mag 10 000 x, bar 1 μm; (c) shows a large particle, mag 2000 x, bar 10 μm; (d) shows small particles, mag 4000 x, bar 1 μm.

Figrue 3.5 EDS of the two particle types observed in the $Ni_{0.85}Co_{0.15}O$-YSZ sample. (a) shows an amorphous particle, (b) shows a crystalline particle. The measurement bar on both SEM images shows 20 µm.

Figure 4.1 Impedance spectra of a $Ni_{0.7}Co_{0.3}O$-YSZ cermet anode in pure hydrogen at 850°C, plotted as a Nyquist plot, at the following overpotentials: (♦) η=0 mV at OCV, (■) η= 50 mV, (♦) η=100 mV, (■) η=150 mV, (♦) η=200 mV, and (■) η=250 mV. The frequency, in Hertz, of each of the low frequency arcs is indicated; the frequency of the high frequency arc is also indicated.

Figure 4.2 Examples of typical mathematical (complex non-linear least squares, CNLS) fits for both Bode plot (left) and Nyquist plot (right). The fit is ideal over the indicated frequency (left) and real impedance (right) values.

Figure 4.3 Resistor element fitting parameters for the indicated equivalent circuit over the overpotential range shown for the $Ni_{0.7}Co_{0.3}O$-YSZ cermet anode at 850°C. Resistors (♦) R_1, (▲) R_2, and (■) R_3 as indicated. Error bars are included for all three data series, although only those for R_2 are large enough to be visible.

Figure 4.4 Direct current data plotted as overpotential and ln(current) for a $Ni_{0.7}Co_{0.3}O$-YSZ cermet anode in pure hydrogen fuel at 850°C for the purpose of extracting exchange current density values. The peak at high overpotential is due to an instrument crossover, and thus is unrelated to any electrochemical process on the anode.

Figure 4.5 Data from many $Ni_{0.7}Co_{0.3}O$-YSZ cermet anodes in pure hydrogen fuel at 850°C. (A) Data derived from potentiostatic measurements at various overpotentials for the purpose of constructing (B) performance plots.

Figure 4.6 Performance data for the $Ni_{0.7}Co_{0.3}O$-YSZ cermet anodes in pure hydrogen fuel at 850°C over the first 14 hours of data collection, demonstrating the stability of the anode for many button cells in hydrogen gas.

Figure 5.1 Calculated phase diagram using DFT for nickel in the partial pressure gas mixture range shown. The regions are as follows: pure nickel (white), increasing surface coverage in the downward vertical direction (dark grey), and Ni_3S_2 (light grey). The black points indicate experimental results (refer to paper for details). The boundary lines are as follows: the phase boundary between nickel and nickel with adsorbed sulfur (black line bounding white and dark grey regions), calculated phase boundary of adsorbed sulfur and bulk (grey line bounding two grey regions), and experimental bulk Ni_3S_2 phase diagram boundary (black line bounding two grey regions).

Figure 5.2 Primary reaction pathways followed during the pyrolysis of hydrogen sulfide between 800°C and 1100°C.

Figure 7.2 Exchange current densities (i_o) values for cells 1 and 2 (open and closed shapes, respectively) collected at various CO/H_2 fuel ratios. The data is calculated from impedance spectra measurements (AC). For cell 2, the initial H_2 value is indicated at 2.1 mA/cm^2, followed by the next point with pure CO at 1.1 mA/cm^2. Decreasing amounts of CO in the fuel ratio then follow towards pure H_2. The value of n, corresponds to the ratio of CO in the fuel inlet with a balance of H_2, where *n* is given by the formula: $n_{CO}/(100-n)_{H2}$.

Figure 7.3 Raw impedance data for Cell 1 (panels A, C) and Cell 2 (panels B, D). Data from pure H_2 (black squares), and low CO concentration, in the range 20/80 (grey triangles) to 30/70 (open squares) CO/H_2 is shown (panels A, B). Data from pure H_2 (closed squares) and high CO concentration, in the range 60/40 (closed triangles) to 80/20 (open squares) CO/H_2 is shown (panels C, D). Note the different vertical and horizontal axes between panels.

Figrure 7.4 Exchange current density (i_o) values for cells 1 and 2 (open and closed shapes, respectively) collected at various CO/H_2 fuel ratios. For cell 2, the initial H_2 value at 4.1 mA/cm^2 is followed by the point at 1.1 mA/cm^2 for pure CO. Decreasing amounts of CO in the fuel ratio then follow towards pure H_2. The value of n, corresponds to the ratio of CO in the fuel inlet with a balance of H_2, where *n* is given by the formula: $n_{CO}/(100-n)_{H2}$.

Figure 7.5 Fuel cell run continuously for 9 days. Following H_2 measurements for 2 days (Day 0, triangle), a fuel ratio of 25/75 CO/H_2 was run for 7 days (Days 1-7, diamonds). (A) OCV values (B) i_o values derived from electrochemical impedance data.

Figure 7.6 Scanning electron micrograph of the $Ni_{0.7}Co_{0.3}$-YSZ anode material post-run following the 7 day run with a fuel mixture of 25/75 CO/H_2. Panel A shows a magnification of 100x with a measurement bar of 100 μm, and panel B shows 5000x with a measurement bar of 1 μm. The powder sample was mounted on carbon tape.

Figure A1. A Nyquist plot of a button cell with a $Ni_{0.7}Co_{0.3}$-YSZ anode at 800°C in H_2 at 50 sccm. The data between the arrows will be used for the fitting shown in figure A2.

Figure A2. CNLS fit of the raw data using the *ZView* software.

Figure A3. Numerical values obtained from fitting the equivalent circuit shown to the data in figure A2 using the *ZView* software.

Figure A4. Nyquist plot indicating the data ranges utilized for data fitting of R_{CT} for Figure A5. The increasing data range used corresponded to P_0 to P_1, increasing to P_0 to P_{15}.

Figure A5. R_{CT} values obtained from fitting the data in the ranges shown in figure A4.

List of Tables

List of Abbreviations

AC – Alternating Current

AFC – Alkaline Fuel Cell

BD – Biodiesel

BDDT – Brunawer, Deming, Deming, Teller

BET – Brunawer, Emmett, Teller

C – Capacitor Circuit Element

CA – Chronoamperometry

CDB – Carbon Deposition Boundary

CNLS – Complex Non-Linear Lease Squares

CPE – Constant Phase Element

CV – Cyclic Voltammetry

DC – Direct Current

DCV – Direct Cyclic Voltammetry

DFT – Density Functional Theory

EA – Elemental Analysis

EIS – Electrochemical Impedance Spectroscopy

EDS – Energy Dispersive Spectroscopy

GDC – Gadolinium Doped Ceria

i_o – Exchange Current Density

ICS – Ion Chromatography Scan

LSM – Lanthanum Strontium Manganite

MCFC – Molten Carbonate Fuel Cell

MIEC – Mixed Ionic-Electronic Conductors

ML - Monolayer

MO – Metal Oxide

NMR – Nuclear Magnetic Resonance

OCV – Open Circuit Voltage

PAFC – Phosphoric Acid Fuel Cell

PEFC – Polymer Electrolyte Fuel Cell

PDF – Powder Diffraction File

Q – Constant Phase Element Circuit Element

R – Resistor Circuit Element

R_{CT} – Charge Transfer Resistance

R_S – Serial Resistance

SEM – Scanning Electron Microscopy

SSZ – Scandia Stabilized Zirconia

SOFC – Solid Oxide Fuel Cell

TPB – Three Phase Boundary

XRD – X-ray Diffraction

YSZ – Yttria Stabilized Zirconia

Z_i – Imaginary Impedance

Z_r – Real Impedance

Publications

Peer reviewed articles have been published as a result of my work during the past four years. Chapter 7 of this document has been submitted for publication at the time of publication of this thesis to the Journal of Power Sources.

Grgicak, C. M.; Pukulska, M. M.; O'Brien J. S.; Giorgi, J. B. *Synergistic effects of* $Ni_{(1-x)}Co_{(x)}$*-YSZ and* $Ni_{(1-x)}Cu_{(x)}$*-YSZ alloyed cermet SOFC anodes for oxidation of hydrogen and methane fuels containing* H_2S. J. Power Sources, 183(1), 26-33, (2008).

O'Brien, J. S., Giorgi, J.B., *Carbon and sulfur poisoning in SOFC anodes:* $Ni_{0.7}Co_{0.3}$*-YSZ Performance with Hydrocarbons, Alcohols and Biodiesel Fuels containing* H_2S*,* ECS Transactions, 2010, 28 (23), 221-231, (2010).

O'Brien, J. S.; Giorgi, J. B. *SOFC with NiCo-YSZ cermet anode for oxidation of* CO/H_2 *fuel mixtures*. J. Power Sources, 200, 14-20, (2012).

Summary

A series of cermet powders of composition $Ni_xCo_{(1-x)}O$-YSZ were synthesized for testing as cermet anode materials for SOFCs. The Co is found by powder XRD to become incorporated into the crystal lattice of the NiO, thus forming a true alloyed material. SEM and EDS results show two types of particles upon sintering to 1380°C: small, amorphous particles of YSZ and large, crystalline particles of nickel.

The electrochemical oxidation of hydrogen on a cermet anode composed of $Ni_{0.7}Co_{0.3}O$-YSZ was investigated using a series of many button cells. Through EIS data, cyclic voltammetry data, the exchange current densities for these button cells were determined. Although a relatively large variation was found (expected to be due to microstructural variation) the average values for both methods of measurement is in good agreement in hydrogen.

Following reduction in pure hydrogen, the fuel was changed to a mixture with high concentration of H_2S. It was found that a concentration of 10 % H_2S/H_2 produced a sudden change in anode microstructure and resulted in loss of exchange current density. Lowering the amount of H_2S in the initial fuel feed, which allowed for a more gradual microstructural change, allowed the cell to eventually function at concentrations in excess of 10 % H_2S/H_2. It was determined by OCV values in various concentrations of H_2S/H_2 that hydrogen is the predominant fuel of choice, even if H_2S is available. Following electrochemical testing, slow cooling in a 10 % H_2S/H_2 mixture following produced metal sulfide spheres, as determined by SEM and EDS.

Investigation in hydrocarbon, alcohol and biodiesel fuels was then undertaken to test the fuel variability of the given cermet anode material. Methane containing 10 % H_2S was found to have increased exchange current density relative to poisoned hydrogen. Ethane and biodiesel experienced no increase in exchange current density, but a lengthening of the functional lifetime of the cell was observed, indicating reduced carbon poisoning. Methanol is a promising oxygen-containing SOFC fuel since it produced exchange current density

values larger than hydrogen, and showed no evidence of coke formation by post-mortem SEM.

Since oxygen-containing fuels are known to decompose in the gas phase at typical SOFC operating temperatures, the performance in a mixture of various CO/H_2 fuels was then investigated. The $Ni_{0.7}Co_{0.3}O$-YSZ cermet anode gave higher exchange current density values for low ratio of CO/H_2 fuels in the range 20/80 and 30/70 compared to pure H_2. This is the first example of a Ni-based anode providing higher performance with a CO/H_2 mixed fuel than for a pure H_2 fuel. Finally, continuous running of a cell with fuel ratio 25/75 CO/H_2 for 7 days produced exchange current density values, which were observed to increase significantly above the values for pure H_2 during days 1-4 followed by deterioration below the value for hydrogen on subsequent days.

Acknowledgements

First, I would like to thank Professor Javier B. Giorgi, my research supervisor, for his support with this research project. Both his attention to detail and search for the big picture provided unending guidance.

I would like to thank all of the Giorgi group members who are presently in the group and those who have graduated in the past. In particular, I thank Dr. Richard G. Green and Dr. Catherine M. Grgicak for laying the foundation of this research project and getting me started during my induction period. I also wish to acknowledge Ron Hartree for his assistance in the XRD lab and Dr. Wendy Pell for many insightful electrochemical discussions.

Finally, I would like to thank my mother for her infinite patience and unerring support through my extensive university “career”

1

General Introduction

1.1 Fuel Cells – A General Description

Fuel cells are a means of converting energy from chemical fuels to electrical energy directly with no other conversion steps. The most common electrochemical reaction which takes place in a fuel cell is the oxidation of a fuel, commonly hydrogen, and the reduction of an oxidant, commonly oxygen from the air. The reaction between these two parts produces electrical energy and heat as well as the byproduct of the electrochemistry, water, as shown in equation 1.1.

$$\textit{Hydrogen} + \textit{Oxygen} \rightarrow \textit{Water} + \textit{electrical energy} + \textit{heat} \quad (1.1)$$

A physical description of the fuel cell itself provides a picture of the setup, whereupon the above electrochemistry takes place. An electrolyte constructed of a non-porous material is used to separate two porous electrodes, namely the cathode and anode. These latter two electrodes are in electrical and ionic contact with the electrolyte to allow a circuit to be closed. The anode is exposed to the fuel, whereas the cathode is exposed to the oxidant. The fuel cell will continue to produce usable energy as long as these two electrodes are continuously supplied with their desired chemicals. Fuel cells are a desirable alternative to battery technology, since they can produce usable current continuously for as long as fuel and oxidant are supplied – this makes the fuel cell a thermodynamically open system.

Fuel cells have a high conversion efficiency (as will be discussed in detail below) during conversion of chemical energy into usable electrical energy. In comparison with combustion engines and other energy sources, fuel cell losses due to mechanical energy and conversion of fuel into heat energy are not an issue. As shown in equation 1.1, heat produced by the fuel cell can be utilized for maintaining the desired temperature. Also, production of pollutants such as NO_x and SO_x as well as particulate matter is negligible. Since the efficiency of fuel cells is relatively independent of the size of the cell, it can be tailored for specific uses or applications. The fuel cell itself does not produce any noise; therefore, depending on the support system, the fuel cell is expected to be a very quiet fuel source. Finally, fuel cells are capable of running on many types of fuels, especially high temperature cells.

In the case of a cell with a ceramic electrolyte, shown in figure 1.1, one of the two most common types of fuel cell, it does not experience corrosion of the electrolyte layer nor electrolyte management problems. Flexibility of shape and design make it an attractive technology for usable current production. In this case, the charge carrier in the electrolyte layer is the oxygen dianions, which carries electrons through from the cathode to the anode electrode.

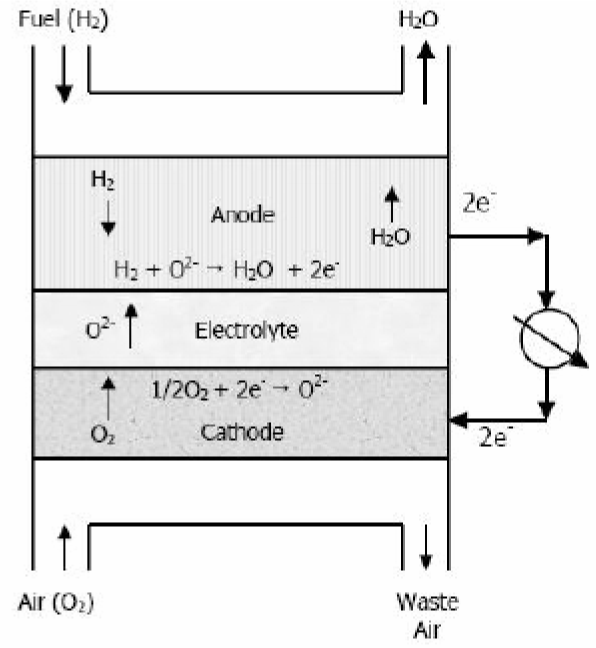

Figure 1.1 General schematic of a solid oxide fuel cell showing the three main components and their relative orientations: anode, electrolyte and cathode. Here, the hydrogen fuel is reduced to produce water and usable current, and oxygen dianions conduct the charge across the solid oxide electrolyte in the direction indicated.[1 2011 #24]

A second common fuel cell has a polymer electrolyte, shown in figure 1.2, where protons act as the charge carrier across the electrolyte layer. Here, the charge carrier possesses the opposite charge to that of solid electrolyte fuel cells, a positively charged proton, and travels in the reverse direction, from the anode to the cathode electrolyte. The choice of fuel for this type of cell is more limited due to the lower operating temperatures, which range from approximately room temperature to almost 200°C, which generates a need for an external reforming catalyst if hydrocarbon fuels are desired.

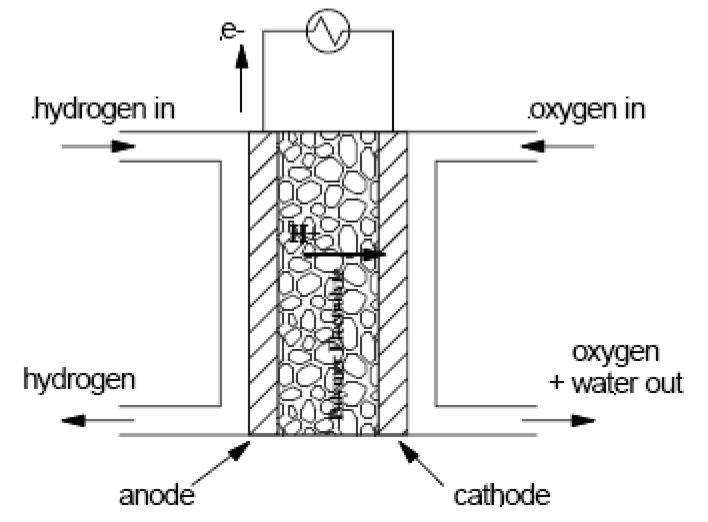

Figure 1.2 General schematic of a polymer electrolyte fuel cell which outlines the three main components and their relative orientations: anode, electrolyte and cathode. Here, the hydrogen fuel is reduced to produce water and usable current, and proton cations conduct the charge across the solid oxide electrolyte in the direction indicated. [2]

1.1.1 Types of fuel cells

Fuel cells can currently be classified into five groupings. The convention is to distinguish the types by the electrolyte used to separate the anode from the cathode. There are many differences between the types of cells, among which those of note are operating temperature and phase of fuel. These main types include solid oxide fuel cells (SOFCs), polymer electrolyte membrane (PEFC), phosphoric acid (PAFC), alkaline (AFC), and molten carbonate (MCFC). Generally, as the temperature increases, so does the range of fuel choices, upon which the cell can be operated. The following table presents the five types of fuel cell classification and their various optimized conditions.

Table 1.1 General conditions for each of the five types of fuel cells. [3]

	Solid Oxide Fuel Cell (SOFC)	Molten Carbonate Fuel Cell (MCFC)	Phosphoric Acid Fuel Cell (PAFC)	Alkaline Fuel Cell (AFC)	Polymer Electrolyte Fuel Cell (PEFC)
Typical Electrolyte	Solid YSZ (Y_2O_3-stabilized ZrO_2)	Molten Li_2CO_3-K_2CO_3	H_3PO_4	KOH solution	PFS* acid membrane
Electrolyte Support	None	$LiAlO_2$	SiC	Asbestos	None
Cathode	LSM (Sr-doped $LaMnO_3$)	Li-doped NiO	PTFE**-bonded Pt on C	Pt-Au	PTFE-bonded Pt on C
Anode	Ni/YSZ	Ni	PTFE-bonded Pt on C	Pt-Pd	PTFE-bonded Pt on C
Interconnect	Doped $LaCrO_3$	Stainless Steel with Ni	Glassy carbon	Ni	Graphite
Operating Temperature	1000^oC	$650\,^oC$	$200\,^oC$	$100\,^oC$	$80\,^oC$
Operating Pressure	1 atm	1-3 atm	1-8 atm	1-10 atm	1-5 atm
Fuel (most common)	H_2, CO	H_2, CO	H_2	H_2	H_2
Oxidant	O_2	O_2 and CO_2	O_2	O_2	O_2
Contaminant Tolerance	< 10-100 ppm S	< ppm range S	< 1-2 % CO < 50 ppm S	No CO_2, CO No S	< 50 ppm CO No S

*PFS = Perfluorosulfonic

**PTFE = Polytetrafluoroethylene

1.1.2 Historical Background

The first principles of fuel cell technology were developed by Sir William Grove in 1839. [4] A cell constructed of dilute sulfuric acid electrolyte operated at room temperature produced a small current when switched off in the opposite direction to expected electron flow for the electrolysis of water. Using platinum as both cathode and anode, with the sulfuric acid electrolyte, he recorded a current flow when hydrogen and oxygen were supplied at each electrode.

Solid oxygen-ion conductors were discovered by Nernst while trying to develop a "glower" for use as a synthetic light source in the late 19th century. [5] Nernst used solid ZrO_2 with 15 % w/w doping of Y_2O_3 (the Nernst mass) in the development of his light source. Nernst's discovery that YSZ became conductive to ions at temperatures above $600^{o}C$, where it is an insulator at room temperature, lead to its later employment in fuel cells. YSZ is still one of the most prominent ceramic electrolytes currently used in SOFC research. He also experimented with doping zirconia with other oxides such as calcia, and magnesia, though they were less successful than yttria.

The first example of ceramic fuel cells is reported by Baur and Preis in 1937. [5] They fabricated cells with electrolytes of 10 % w/w MgO doped ZrO_2 and 10 % w/w Y_2O_3 doped ZrO_2, anodes of iron or carbon, and cathodes of Fe_3O_4. With a tubular design, H_2, CO or natural gas as fuel and operating temperatures between 1000 and $1050^{o}C$, they observed open-circuit voltages (OCVs) of 0.8 to 1.2 V. This early model provided more of a proof of concept than an operational energy source, since current outputs were very low compared to battery technology.

An increase in the research associated with fuel cells did not happen until the 1960s. Space-technology by NASA developed early alkaline fuel cells for use in space exploration. This was followed in the 1970s, by the development of thin-walled cells, which improved overall cell performance. The next development of SOFCs, which employed Ni/YSZ anode, doped In_2O_3 cathode and doped $CoCr_2O_4$ interconnect, was made soon after. In the 1980s, the flat-plate cell and the honeycomb structured cell increased power densities dramatically and the material for the cathode was changed to $LaMnO_3$ and $LaCoO_3$. [5] Currently, many avenues of research are being followed, explored and expanded such as microstructure optimization of cathode and anode electrode materials, optimization of electrolyte conductivity, development of electrode materials which are resistant to common poisons, and fuel cell manufacturing (interconnect, cell support system) materials and technologies.

1.1.3 Solid Oxide Fuel Cells

Solid oxide fuel cells have an electrolyte constructed of dense yttria-stabilized zirconia, commonly doped with 8 % w/w Y_2O_3 in ZrO_2. This material becomes conductive to ions, namely oxygen dianions, O^{2-}, at high temperatures in the range 600-1000°C. Because of this high operating temperature, SOFCs have a high degree of fuel flexibility, and can be used with common fuels, such as H_2, as well as less common ones, such as CO, H_2S, small hydrocarbons (CH_4, C_2H_6) as well as large ones (biodiesel), and alcohols (CH_3OH, CH_3CH_2OH). Due to its abundance, oxygen from the atmosphere is used as the oxidant. The overall reaction which occurs in the fuel cell is shown in equation 1.2, where *a* specifies a species located at the anode electrode, and *c* specifies a species located at the cathode electrode.

$$H_{2,a} + \tfrac{1}{2}\, O_{2,c} \rightleftharpoons H_2O_a \qquad (1.2)$$

This reaction can be broken into two half reactions, one of which occurs at the cathode: the reduction of oxygen with 2 free electrons to produce an oxygen dianion (here the *e* subscript specifies the electrolyte phase).

$$\tfrac{1}{2}\, O_{2,c} + 2\, e^{-} \rightleftharpoons O^{2-}_{e} \qquad (1.3)$$

The second half reaction occurs at the anode: oxidation of the fuel with the required number of electrons (here 2 electrons are liberated by the reduction of hydrogen), to produce water as the byproduct of electrochemical oxidation.

$$H_{2,a} + \tfrac{1}{2}\, O^{2-}_{e} \rightleftharpoons H_2O_a + 2\, e^{-} \qquad (1.4)$$

The circuit can be described as the oxidation of the chosen fuel (pure or mixed) at the anode which liberates electrons. These electrons are conducted through the external electrical circuit, perform work, and return to the fuel cell at the cathode. Here, the oxygen is reduced and conducted across the YSZ electrolyte as oxygen dianions. These species are then available to oxidize the fuel at the anode, thus completing the electrical circuit.

The high power density available from a SOFC stack makes it an appealing power source for stationary applications, such as in residential, or commercial. Furthermore, because the fuel does not undergo multiple phase conversions (such as chemical to mechanical to electrical), the efficiency of the cell is very high.

1.1.4 SOFC Efficiencies

The overall efficiency, ε_{FC}, is a function of the thermodynamic (ε_T), heating (ε_H), current/Faradaic (ε_i) and voltage (ε_V) efficiencies, [6, 7] as given below.

$$\varepsilon_{FC} = \varepsilon_T \varepsilon_H \varepsilon_i \varepsilon_V \qquad (1.5)$$

1.1.4.1 Thermodynamic Efficiency

The thermodynamic efficiency relates, ΔH_T^o**,** the standard enthalpy and, ΔG_T^o, the Gibbs energy of reaction at a specified temperature *T* through the following equation.

$$\varepsilon_T = \frac{\Delta G_T^o}{\Delta H_T^o} \qquad (1.6)$$

For electrochemical cells, it is possible to convert all of the free energy to electrical energy. However, Kirchoff's Law and the Gibbs-Helmholtz equations are required due to variations of enthalpy and Gibbs energy values, which occur at high temperatures needed for SOFC operation.

$$\Delta H^{o}{}_{T2} = \Delta H^{o}{}_{T1} + \int_{T1}^{T2} \Delta C_P dT \qquad (1.7)$$

$$\Delta G^{o}{}_{T2} = \frac{T_2}{T_1} \Delta G^{o}{}_{T1} + \Delta H^{o}{}_{T1} \left(\frac{T_1 - T_2}{T_1} \right) \qquad (1.8)$$

Here, ΔC_P relates to the heat capacity of reactants and products for reaction of hydrogen with oxygen to form water in the gas phase. For fuels such as hydrogen and carbon monoxide, common to SOFCs, the thermodynamic efficiency will be less than one, as is expected, since both ΔH and ΔG are negative (or zero for the case of hydrogen). As an example, for the case of $H_{2(g)} + O_{2(g)} \rightarrow H_2O_{(g)}$, equations 1.6 through 1.8 can be utilized to calculate the thermodynamic efficiency of a cell running on hydrogen fuel. Given the value of heat capacity of -9.9 J/K·mol, [8] and a temperature of 1123 K, the most common fuel cell operating temperature in this thesis, a value of 0.77 is found for the thermodynamic efficiency.

1.1.4.2 Heating Efficiency

The heating efficiency relates, ΔH^{o} **,** the enthalpy of all combustible fuel species available to generate electricity and, ΔH_{com}**,** the amount of enthalpy contained by the combustible chemical by the following equation.

$$\varepsilon_H = \frac{\Delta H^{o}}{\Delta H_{com}} \qquad (1.9)$$

This relationship is especially important when the fuel is diluted by an inert chemical or when it contains impurities such as other combustibles in significant concentrations in addition to the desired electrochemically active species. For SOFCs operating at high temperature with simple fuels such as hydrogen, methane, and hydrogen sulfide, the heating efficiency is expected to be close to one.

1.1.4.3 Current Efficiency

The current efficiency relates to Faraday's Law by the following equation.

$$\varepsilon_i = \frac{i_{measured}}{i_{theoretical}}, \text{ where } i_{theoretical} = nF\frac{\partial f}{\partial t} \qquad (1.10)$$

Here, n is the number of transferred electrons, F is the Faraday constant and $\frac{\partial f}{\partial t}$ is the molar flow rate of the fuel. This efficiency relates the measured current with the theoretical current. This efficiency value can also be expressed as fuel utilization. Fuel cells are purposefully operated at a current efficiency of less than one, since high fuel utilization creates higher diffusion polarization values.

1.1.4.4 Voltage Efficiency

The voltage efficiency depends on, E, the potential under load and, E^o_{FC}, the Nernstian potential, or open circuit potential (OCV), of the cell, through the following equation.

$$\varepsilon_V = \frac{E}{E^o_{FC}} \qquad (1.11)$$

In order to gain a high amount of useful power from the cell, the voltage efficiency must remain high, and the overpotential must be minimized. To minimize overpotential the factors of temperature, pressure, electrolyte composition and electrode material can be optimized. Raising the temperature increases mass transfer and reaction rate, and decreases cell resistance, which lowers polarization thus raising the voltage efficiency.

1.1.5 Polarization

The total cell polarization can be calculated by the sum of the activation polarizations of anode and cathode kinetics, η_a and η_c, respectively, the ohmic polarization, *iR*, and the concentration polarization, η_{cp}, [9] shown below.

$$\eta_{tot} = \eta_a + \eta_c + iR + \eta_{cp} \qquad (1.12)$$

The polarization is related to the current density drawn from the full cell, as shown in the plot below. The general trend is that, as more current is drawn from the cell, the voltage decreases below the theoretical maximum voltage. This relationship shows three regions: activation polarization causes an initial drop in cell potential at low current densities, ohmic losses create a semi-linear region at moderate current densities, and mass transport losses show a sharp decrease at high current densities. These three regions will be described in detail in the following paragraphs.

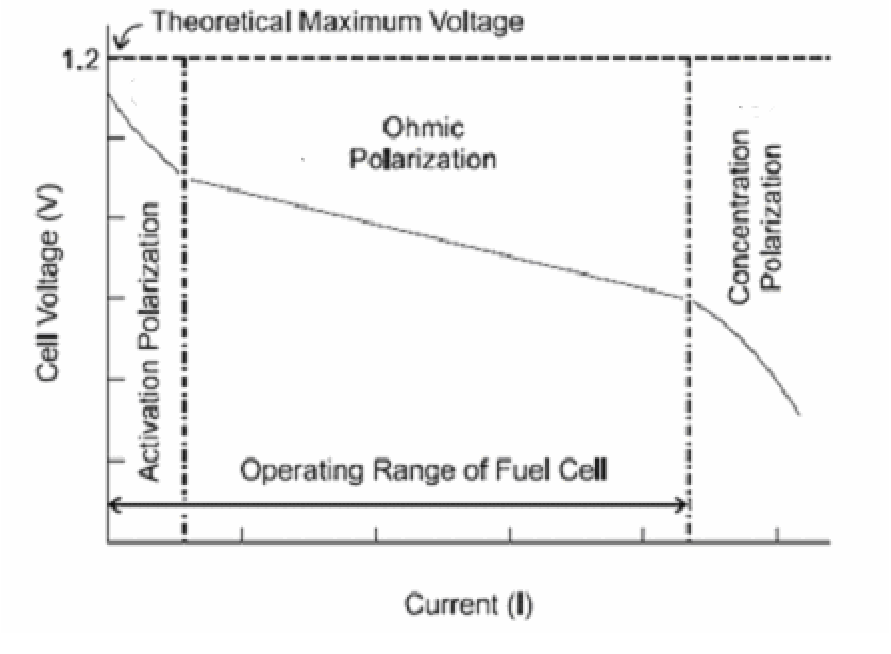

Figure 1.3 Sources of polarization as a function of cell current.

By applying a reference electrode, the individual polarizations for anode and cathode can be determined separately. Their individual contributions to the overall polarization of the cell are shown in the plot below. [10]

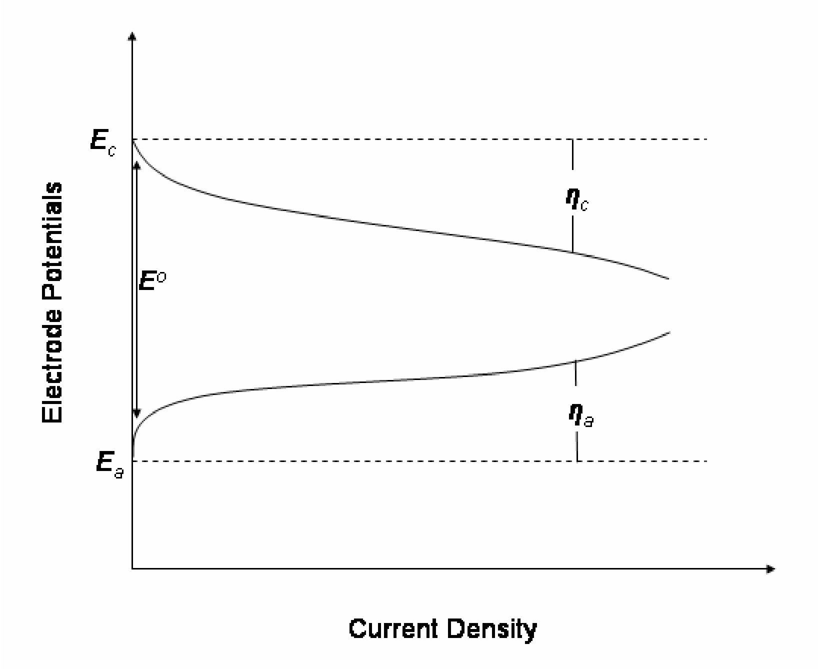

Figure 1.4 Polarization diagram depicting the differences between anodic and cathodic contributions to overpotential. [11]

The overpotentials of both the anode and cathode increase as current density increases, which relates to the capacity to draw power from the cell, namely, at high overpotentials, less power will be available. It is, therefore, desirable to maintain polarizations of the electrodes at a minimum.

1.1.5.1 Activation Polarization

Activation polarization refers to the overpotential needed to change the activation energy of an electrochemical process occurring at an electrode. In order to accomplish this, an additional potential, an overpotential, η, is applied to lower the free energy of activation, $\Delta G^{o\neq}$. This potential provides a driving force such that when applied, the rate of the electrode reaction exceeds the spontaneous rate. This modified electrode reaction rate relates to the exchange current density, i_o, as will be derived below. Here, the free energy of activation, $\Delta G^{o\neq}$, is lowered from its reversible value by $\beta\eta F$, by applying an overpotential, η. The effect of this applied overpotential is that electrons become more abundant at the cathode and less abundant at the anode (the anode becomes an electron 'sink').

$$\Delta G_{\eta}^{\neq} = \Delta G^{o\neq} - \beta\eta F \qquad (1.13)$$

Here, β is a charge-transfer parameter which depends on the symmetry of the energy barrier associated with activation in the reaction process and is assumed to be 0.5 for a one-electron process. The rate constant at equilibrium for standard potential, E^o, is given below.

$$k_o = A\exp\left(-\frac{\Delta G^{\neq}}{RT}\right)\exp\left(-\frac{\beta E^o F}{RT}\right) \qquad (1.14)$$

For a reaction differing from the standard potential, the expression becomes the one shown below.

$$k_E = A\exp\left(-\frac{\Delta G^{\neq}}{RT}\right)\exp\left(-\frac{\beta EF}{RT}\right) \qquad (1.15)$$

This can be re-written as the following expression,

$$k_E = A\exp\left(-\frac{\Delta G^{\neq}}{RT}\right)\exp\left(-\frac{\beta E^o F}{RT}\right)\exp\left(-\frac{\beta\eta F}{RT}\right), \text{ where } E = E^o + \eta \qquad (1.16)$$

which simplifies to the following expression, where k_o is the rate constant for the electrochemical process.

$$k_E = k_o \exp\left(-\frac{\beta \eta F}{RT}\right) \qquad (1.17)$$

Rates for electrochemical processes are measured as currents, thus the activation polarization can finally be expressed by the following equation, where $\vec{i}$ is the net current density for the forward reaction, i_o is the exchange current density, [S] is the concentration of the reacting species, n is the number of electrons, η_c is the cathodic or negative overpotential and β_c ($0<\beta_c<1$) is the symmetry factor associated with the cathodic (forward) branch of the reaction. The anodic (reverse) branch of the reaction can be derived by a similar route.

$$\vec{i} = i_o \exp\left(-\frac{\beta_c \eta_c F}{RT}\right), \text{ where } i_o = nFk_o[S] \qquad (1.18)$$

By applying a 3-electrode geometry and measuring the variation of current density versus overpotential, the performances of the anode and/or cathode can be measured individually. A plot of ln$i$ versus η yields i_o, which relates directly to k_o. This expression will be revisited in further detail in the following chapter.

1.1.5.2 Ohmic Polarization

The ohmic polarization, *iR*, of the cell includes several resistances, among which include the electrolyte resistance, the contact resistances between cell components and the electrical resistances of electrodes. These combined resistances produce the ohmic polarization, also called the *iR* drop, which increases proportionally and linearly with current. When the effect of ohmic polarization (a linear increase) is combined with activation polarization (a natural logarithmic increase) it produces a specific effect; after the initial sharp increase at low current density, the combined relationship becomes relatively linear in the Tafel region, as will be described in the following chapter.

1.1.5.3 Concentration Polarization

The concentration polarization, η_{cp}, of the cell is directly related to the limiting current, i_L by the following expression.

$$\eta_{cp} = \frac{RT}{nF} \ln\left(1 - \frac{i}{i_L}\right) \qquad (1.19)$$

The limiting current dominates when the electrodic process undergoes mass transport effects. This is caused by concentration gradients near the active region of the electrode, which can produce local potential differences. The concentration of necessary electrochemical reagents, which produce current output, are depleted by the progression of the electrode reaction more rapidly than they can be replaced by diffusion. This effect is especially important for electrodes with high porosity, such as the electrodes applied during the manufacture of SOFCs.

1.1.6 Thermodynamics at equilibrium: Nernst's Equation

At equilibrium conditions, thermodynamics can be related to electrochemistry through well known relationships. It is understood that for a given chemical reaction at equilibrium, the concentrations of its products relates to those of its reactants through the Gibbs free energy shown. Here, ΔG^o represents the Gibbs free energy at standard conditions, whereas ΔG is the Gibbs free energy at the equilibrium state under consideration.

$$\Delta G = \Delta G^o + RT \ln\left(\frac{a_{products}}{a_{reac\tan ts}}\right) \qquad (1.20)$$

For an electrochemical reaction where *n* electrons are involved in electrical exchange at an interface, the following general half-reaction can be considered for a metallic species *M* gaining a defined number of electrons e^- at the cathode.

$$M^{n+} + ne^- \rightleftharpoons M \qquad (1.21)$$

This basic equation can be used, which relates standard electrode potential with Gibbs free energy,

$$\Delta G^o = -nFE^o \qquad (1.22)$$

to convert the above relation to reflect the relationship between electrode potentials and electrochemical species concentrations.

$$E = E^o - \frac{RT}{nF} \ln\left(\frac{\Pi a_{reac\tan t}}{\Pi a_{product}}\right) \qquad (1.23)$$

This equation is the famous Nernst equation, first developed in 1904. Here, *F* is Faraday's constant, which has an accepted value of 96485.34 C/mol, *R* is the universal gas constant, and *T* is the absolute temperature of the system at equilibrium. The symbol *E* denotes the electrochemical potential under the specified conditions, and E^o the electrochemical potential under standard state conditions. Since the study of thermodynamics is concerned with initial and final state conditions of a system, the conclusions reached by such a mathematical relationship are not expected to change with time; therefore, this relationship is still an important concept in contemporary research.

1.1.7 Overall Scope of this Research Thesis

Current research into anode materials shows three predominant paths aimed at constructing a SOFC with sulfur and carbon tolerance. [12] The first is the group of cermets composed predominantly of Ni with an ionic conductor such as YSZ, SSZ (scandia stabilized zirconia), and GDC (gadolinium doped ceria). Other metals which have been investigated include silver, copper, iron, cobalt, ruthenium and rhodium. The second group of anode materials includes mixed ionic-electronic conductors (MIECs). This group is composed of $La_{1-x}Sr_xCrO_3$ and its doped sister compounds. Finally, hybrid materials, which are composed of both metal and MIEC such as Cu-CeO_2-YSZ have been investigated.

The anode design must incorporate many basic features such as high electrical conductivity and catalytic activity for the desired oxidation reactions. Here is where the oxide dianions, conducted though the electrolyte layer, are combined with the partially oxidized fuel molecules or atoms. There are many detailed features which are desirable in the design of a robust, desirable anode material such as the ability to withstand thermal and redox cycling; the compatibility, both physical and chemical with the other fuel cell components such as the electrolyte and interconnects; and the electrocatalytic activity towards the desired electrochemical oxidation reactions, but not towards unwanted side reactions.

Nickel-based anodes are the most prevalent anode material in the chemical literature due to their high electrocatalytic activity, low cost, ease of handling and chemical stability. However, nickel does undergo poisoning at low sulfur concentrations, and shows coke formation when exposed to carbon-containing fuels. For the case of fuels with low sulfur concentrations, the sulfur acts as a poison by adsorbing to the surface sites of the nickel, blocking them and effectively reducing the reactive surface area of the metal phase. For the case of carbon-containing fuels, the production of coke as a byproduct of incomplete electrochemical oxidation can have detrimental effects to the physical integrity of the porous anode structure; formation of a volume of coke larger than that of the pore can rupture the porous network of the cermet anode. Because of these features, development of a nickel-based anode that can overcome these flaws is highly desirable.

This thesis explores the performance of solid oxide fuel cells with nickel-based anode cermets in various fuel environments. The anodes of interest are primarily Ni-YSZ and $Ni_{0.7}Co_{0.3}$-YSZ cermets, which will be investigated by comparing their performance in various fuels. The synergy of the NiCo alloy towards the resistance of sulfur and carbon poisoning is evaluated with respect to the same anode run in pure H_2, by employing different fuel mixtures such as, H_2/H_2S, CH_4/H_2S, CH_3OH and H_2/CO. A cermet anode, which shows resistance to both or either sulfur and carbon poisoning relative to pure H_2, is the primary goal of this research thesis.

Since the performance of the anodes, synthesized by a co-precipitation method, is subject to many factors such as anode microstructure, composition, kinetics, and fuel environment, a summary of the current literature relevant to the research and data in each chapter will be presented.

Chapter 2 describes the experimental and analytical considerations important in the synthesis, physical and electrochemical characterization of the anode materials. A detailed description of the fuel cell set-up is also included in this chapter.

Chapter 3 presents the results of the physical (materials) characterization obtained through various methods, as listed and described in the previous chapter.

Chapters 4 and 5 describe and explore the electrochemical performance of the anodes with respect to pure hydrogen and sulfur poisoning in hydrogen containing fuel environments, respectively. Interpretations of the electrochemical data are included herein, as well as subsequent chapters.

Chapter 6 explores the effect of carbon poisoning in the presence of sulfur in the fuel stream, as an example of an alternate fuel environment, whose results relate to the natural gas available in the current city infrastructure. Oxygen containing fuels such as alcohols and biodiesel will also be investigated and presented; in the case of biodiesel, the effects of sulfur in the fuel stream will be shown.

Chapter 7 investigates the possibility of employing a hydrogen/carbon monoxide mixture as a fuel. An optimal fuel ratio will be investigated and presented.

Chapter 8 gives an overall evaluation and summary of the experimental results in the thesis document.

1.2 References

[1] http://www.azom.com/article.aspx?ArticleID=4159, Solid Oxide Fuel Cells - Using Particle Size Analysis to Optimize SOFC Materials, H. Scientific, Date.

[2] http://www.princeton.edu/~benziger/PEMFC.pdf, J.B. Benzinger, Princeton University, Date.

[3] R.M. Omerod, Chem. Soc. Rev. 32 (2003) 17.

[4] W.R. Grove, Phil. Mag. 14 (1839) 127.

[5] S.C. Singhal, K. Kendall, High temperature solid oxide fuel cells, Elsevier Ltd., New York, 2003.

[6] B.D. Boer, SOFC anode: Hydrogen oxidation at porous nickel and nickel/yttria stabilized zirconia cermet electrodes., PhD. Thesie, University of Twente, 1998.

[7] H. Minh, Q., T. Takahashi, Science and Technology of Ceramic Fuel Cells, Elsevier, New York, 1995.

[8] D.R. Lide, CRC Handbook of Chemistry and Physics, 81st Edition, CRC Press, New York, 2000.

[9] B.E. Conway, Notes on thermodynamic, electrochemical and kinetic aspects of battery reactions., Ottawa, 1978, p. 17.

[10] http://www.club-semac.fr/index.php?page=motorisation&lang=en, S.E.M. Club, Date.

[11] C.M. Grgicak, Anodes for solid oxide fuel cell (SOFC) systems operating in multiple fuel environments: Effects of microstructure and composition, University of Ottawa, Ottawa, 2007.

[12] A. Aarva, J. McPhail, A. Moreno, ECS Trans. 25 (2009) 313.

2

Instrumental and Experimental Description and Considerations

2.1 Fuel Cell Set-Up Considerations

The general fuel cell set-up is outlined in Figure 2.1. A customized, stainless steel Ultra-Torr fitting was used to seal the two alumina tubes used for gas inlet and support of the button cell in the furnace as well as provide a small-diameter (0.25 inch) outlet in order to avoid air contamination of the fuel. The button cell was sealed to the top of the alumina tube support using a Pyrex ring. An alumina cap was placed on top of the button cell to provide a small downward force to improve the Pyrex seal. Leads composed of Pt of 0.2 mm diameter (1/4 hard, Fine Pt, Imperial Smelting and Refining Co. of Canada

Ltd) connected the current collector (Pt gauze, 52 mesh woven from 0.1 mm diameter wire, 99.9% metals basis, Alfa Aesar ®) of the anode and cathode, as well as the reference electrode, to the potentiostat (VoltaLab ® 40 PGZ301) used to collect electrochemical measurements. All leads were electrically insulated from each other as well as from the Faraday cage and furnace components. To check that all leads were isolated, a handheld voltmeter was used to verify that the resistance between each of the leads was 'infinitely' high. All electrochemical measurements were collected at 800 or 850 ^{o}C as measured by a K-Type thermocouple placed just above the counter electrode in order to gain temperature information as close to the working electrode as possible. The furnace temperature was ramped in air from room temperature at a rate of 10 ^{o}C/min prior to holding at 900 ^{o}C for 45 to 60 min to soften the Pyrex ring in order to create a good seal between the button cell and alumina tube support, followed by cooling at a rate of 10 ^{o}C/min to the desired operating temperature.

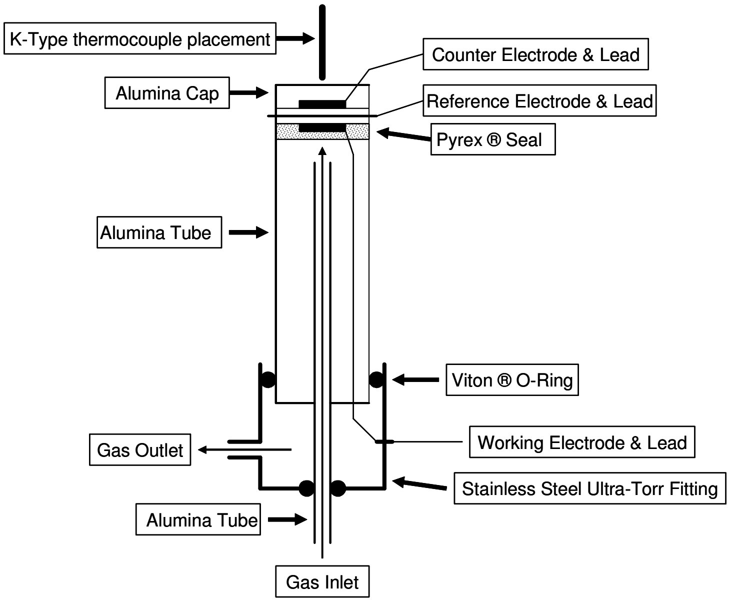

Figure 2.1 Detailed schematic of the fuel cell set up used within the tube furnace.

2.2 Synthesis of Materials

The $Ni_xCo_{(1-x)}O$-YSZ anode precursor materials were synthesized by dissolving appropriate amounts of $NiCl_2*6H_2O$ (Aldrich), $CoCl_2*6H_2O$ (Aldrich), Y_2O_3 (Aldrich) and of $ZrCl_4$ (Strem) into water and acid solutions. The following section outlines in detail the synthesis of the most commonly used of the anode materials. Different appropriate masses were used for the other synthesized powders. The $Ni_{0.7}Co_{0.3}O$-YSZ anode material was prepared by dissolving 15.588 g of $NiCl_2*6H_2O$, 6.662 g of $CoCl_2*6H_2O$, and 4.889 g of $ZrCl_4$ in 100 mL of distilled water. Added to this was 0.4177 g of Y_2O_3 dissolved in 20 mL of 50 % HCl (Fisher). Precipitation of the metals was achieved by concomitant addition of the metal solution and a solution of 2 M NaOH (Aldrich) to a stirred vessel while maintaining a pH of 12 using a pH "Checker" electrode by Hannah. The resulting slurry was stirred for 2 hours and allowed to settle for 18 hours. The precipitate was collected by filtration and washed with 4 x 500 mL of distilled water. The resulting gel was dried at 120°C for 18 hours to yield a dark green powder containing 55 % metal oxide by mass (in the form $Ni_{0.7}Co_{0.3}O$) with a mass balance of 8-YSZ. [1] Anode precursor materials were characterized by powder X-ray diffraction following sintering at 1380°C for 4 hours. The composition of the powders was verified by XRF.

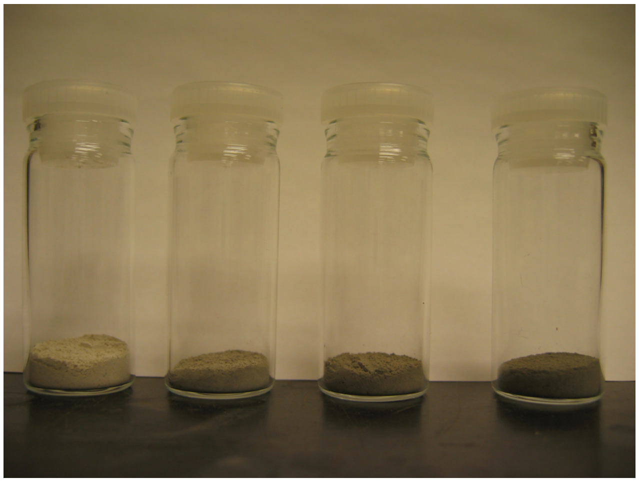

Figure 2.2 Powders, as synthesized, for use in construction of the anode of the button fuel cell. Shown from left to right: NiO-YSZ, $Ni_{0.9}Co_{0.1}O$-YSZ, $Ni_{0.8}Co_{0.2}O$-YSZ, $Ni_{0.7}Co_{0.3}O$-YSZ.

2.3 Fuel considerations

All gaseous fuels (H_2, CH_4, C_2H_6, H_2S) were purchased from BOC Gases at the industrial grade purity, all liquid alcohol fuels (CH_3OH, CH_3CH_2OH) were purchased from Fisher. The gaseous fuels were used 'as is', and all lines running from the gas cylinders to the fuel cell set-up were purged for a minimum time of 10 min at 50 sccm to ensure the purity of the gas in the line was high. The liquid alcohol fuels were used shortly after purchasing fresh bottles, and sealed with Parafilm® as a precaution to avoid water from the atmosphere entering the bottles, especially during the humid summer months. The biodiesel fuel was purchased from Millikan and used 'as is'. Elemental analysis and ion chromatography for biodiesel were performed by Robertson Microlit Laboratories to determine its purity. NMR analysis was performed in-house on a Bruker 500 MHz NMR Spectrometer both before and after the biodiesel fuel was exposed to fuel cell conditions.

For all of the liquid fuels, a heating tape was wrapped around all stainless steel and alumina tubes leading into the fuel cell to provide initial heating of the fuel to a temperature of 200^{o}C, the maximum temperature the o-ring seals could tolerate for long periods of time. This was done to ensure that the liquid fuels evaporate before entering the fuel cell set-up, avoiding standing liquid in the inlet tube. The vapourized fuel would then achieve operating temperature, similar to the other gaseous fuels.

2.3.1 Oxidant

Because of its availability, air is the most common oxidant used. Due to the high operational temperatures used, the difference between the diffusion polarization associated with oxygen from air and pure oxygen is considered to be negligible. Air was the oxidant available to the cathode (and reference) electrode(s) in this study. Also, due to the fact that relative performances were emphasized over absolute performance values, the amount of diffusion polarization associated with the cathode has lower importance.

2.4 Button cell considerations

2.4.1 Current collector

The ability to collect current reliably is paramount to accurate fuel cell operation and data collection. Electrode behaviour cannot be reliably determined if this component of the fuel cell is not optimized. Ideal characteristics of the proper current collector choice are outlined herein. Chemical stability in a reducing and oxidizing environment ensures that the material chosen does not itself undergo chemical reactions before or during electrochemical measurements, thus ensuring that differences in numerical data output are due only to the electrodic processes themselves. For this reason, a Pt current collector was chosen to be the ideal material for this research project. Furthermore, current constriction is a parameter of concern: the current produced by the electrode should be collected in its entirety, and should not be subject to any constriction restrictions. Proper contact between the electrode material and the current collector will ensure this is not a problem.

Two prevalent types of current collector can be found in the literature: paste and mesh. Although paste can both be easily painted onto an electrode and ensure reliable current collector-electrode contact, it has been shown to modify the microstructure of an electrode with time. Guillodo *et al.* [2] have shown that current collectors manufactured from paste can decrease the number of reaction sites over time. Therefore, a mesh current collector was chosen to avoid this degradation. To ensure mesh contact with the electrode material, it was embedded into electrode upon sintering. This choice both ensured that degradation of active sites with time was avoided as well as assuring the mesh was in good contact with the electrode material. Contact resistance was also minimized by employing this method of electrode manufacturing.

There is one further concern with regards to the current collector: possible participation in electrode catalysis. The active thickness of Ni-YSZ cermet anodes has been determined to be approximately 10 μm [3]; therefore, active catalysis only occurs within this region directly adjacent to the non-porous YSZ electrolyte. All anode material associated with thickness beyond this value acts as a current carrier and possible sites for reformation reactions. Due to the use of a mask of defined size and thickness, the current collector was systematically placed between 50 and 60 μm from the electrolyte-electrode interface, as determined by SEM, with a consistent flatness, thus outside the active thickness.

Shown in figure 2.3 is a plot emphasizing the difference between a Ni-YSZ and a blank anode. Here the black data shows the direct current data for the 70% Ni-YSZ cermet anode, whereas the grey data shows the corresponding data for a pure YSZ anode. Both data sets were collected at the same temperature (850^{o}C), flow rate (50 sccm), fuel composition (pure H_2), and approximate anode porosity (identical ratios of powder mass to pore former were employed during synthesis). The small discontinuities in the experimental data are the result of large spikes due to instrument crossover and those data points were removed for clarity. As can be observed, the amount of current collected from the blank YSZ anode is negligible, and constitutes only 3.5 % of the value when compared to the Ni-YSZ anode at the maximum value. Furthermore, all data collected through anodes manufactured by identical methods will experience this same small addition to their current values, thus rendering the errors associated with values relative to each other negligible.

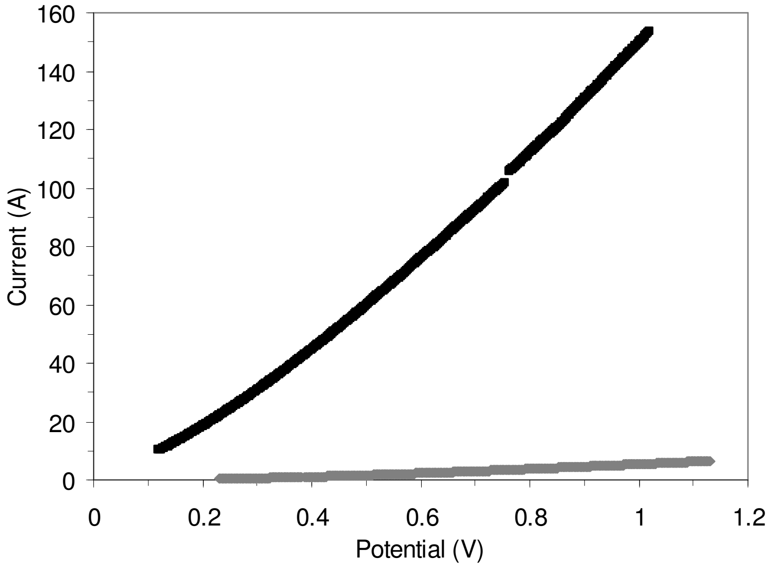

Figure 2.3 Data collected for a Ni-YSZ (■) and a blank (porous YSZ) (■) anode for comparison of the current obtained for each. Both electrodes possessed identical current collectors, apparent areas, porosities, temperatures, fuel environments and flow rates. The current obtained for the blank represents only 3.5 % of the current value collected for the Ni-YSZ anode.

2.4.2 Electrolyte Material

Yttria-stabilized zirconia (8 % w/w Y_2O_3 in ZrO_2) was chosen as the best candidate for the electrolyte material for numerous reasons. Though not the best known ionic conductor at high temperatures, 600-1000°C, (bismuth oxide has the highest measured conductivity), [4] it balances its reasonably high ionic conductivity with several other desirable characteristics, such as low electronic conductivity, physical and chemical stability, low cost and ease of manufacturing. It has a fluorite-type crystal structure, which is a face-centered cubic structure of cations with anions occupying the tetrahedral sites. This structure is considered an “open” structure, which allows for rapid ion migration. [4, 5]

A commercial source was chosen for the YSZ used to form the electrolyte for several reasons. A dense material is desirable after sintering due to its lack of porosity, its increased ionic conductivity and high mechanical strength. Tosoh Corporation, based in Japan, but having a manufacturing plant in the USA, produces a YSZ material with unique properties to fulfill these requirements. The powder grain size of the 8-YSZ is extremely small, in the ultra-fine region, which produces a very high density material when sintered. This resultant high density material then has low grain boundary resistance, thus allowing for a more accurate determination of electrodic processes due to fewer interference factors.

The YSZ electrolyte material will be the mechanical support for the button cells manufactured for use in this work.

2.4.3 Anode Material

The anode material is the primary focus of this thesis, and so will be discussed further throughout the thesis. The general features and requirements of the anode material will, however, be discussed here. The anode provides sites where the fuel is oxidized upon reaction with the oxide dianions provided though the electrolyte. The choice of metal is of crucial importance, since the electrochemical activation of interest is to occur on its surface. The first materials to be investigated were graphite and iron, by Baur and Preis. [6] [4] Graphite has a short life as a component of an anode cermet due to electrochemical oxidative corrosion. Iron is more stable, but eventually succumbs to oxidation at high oxygen partial pressures at high polarizations. Platinum is an attractive choice due to its catalytic activity and chemical stability; however it loses contact easily with the ceramic component of the cermet material. Cobalt is more stable than the metals previously mentioned, but has a higher economic cost, thus making it an attractive secondary metal for the anode. Nickel is the metal of choice to form the majority of the metal component of the cermet anode due to its high electrochemical activity, low economic cost, and chemical stability. However, it does have disadvantages, as will be mentioned below. [4]

Although various anode compositions will be synthesized and tested as SOFC anode materials, they all have many commonalities. All materials are synthesized as 55 % w/w metal oxide with a mass balance of 45 % w/w YSZ, which itself has a composition of 8 mol % Y_2O_3, 92 mol % ZrO_2. The metal oxide will be a solid solution of Ni and Co metals where the composition of Co will range from 0 to 30 % w/w with a balance of Ni. Upon reduction, the metal oxide phase is converted to its corresponding metal alloy, thus changing the overall anode composition to the resulting 70 % w/w metal with a mass balance of 30 % w/w YSZ. Triton X-100 was used as a pore former during sintering. This ensures that there is a porous network of void space throughout the anode material, thus ensuring the gaseous fuel can diffuse to the anode electrolyte interface and products can diffuse away.

The high metal composition ensures electronic conduction occurs easily, and that electrons produced near the anode-electrolyte interface during fuel oxidation reach the current collector. The incorporation of YSZ into the anode to create a cermet material has many primary purposes. [5]

(1) The triple phase boundary is greatly extended beyond simply the interface between the porous anode and non-porous electrolyte. This has also been described as ‘delocalizing’ the electrochemically active region. Oxygen dianions can diffuse from the non-porous electrolyte layer further into the porous anode layer, which increases the number of triple phase boundary sites.

(2) Nickel, in its pure form, tends to aggregate to form larger particles when exposed to high temperatures, known as sintering. During early SOFC development, this process occurred in the extreme, which greatly reduced the number of active sites. Incorporation of YSZ into the Ni to form a cermet greatly reduces the observed degree of aggregation.

(3) There is a considerable mis-match between the thermal expansion coefficients of Ni and YSZ. Contact between the anode and YSZ upon sintering or heating to operational temperatures can cause the anode to shear and loose physical and electrical contact with the electrolyte layer. This will have detrimental effects on the performance of the cell. Incorporating YSZ into the anode cermet allows for a more favourable match of thermal expansion coefficients, thus reducing the possibility of loss of contact between the anode and electrolyte layers. This also allows the anode material to be more resistant to thermal cycling between operation and room temperatures. This can also reduce microfissuring of the metal component, which, when it occurs, reduces the conductivity of the metal component.

(4) Upon reduction, the metal phase of the anode cermet undergoes a considerable degree of shrinkage (a phase-change effect). Loss of oxygen anions from the metal oxide lattice upon reduction to pure metal is the cause of this observation. This can have detrimental effects for contact of the anode and electrolyte layers as well as contact between anode and current collector. The presence of YSZ in the cermet, a phase that is not reduced upon exposure to a reducing environment, allows for this contact to be maintained to a higher degree than a cell without the incorporation of YSZ would be able to realize. This shrinkage has a positive effect, wherein the porosity of the anode is increased.

The anode metal needs to be chemically resistant to corrosive materials such as oxygen or sulfur. For cases of high polarization, the oxygen concentration on the anode side can increase; therefore, a material resistant to this process is needed. Cycling between the reducing fuel environment and air is also a situation that can happen during normal fuel cell operation, thus a tolerance towards this change in chemical environment is desirable. Sulfur, a known poison at low concentrations, can block active sites. At much higher concentrations, such as those used for this work, sulfur can have different chemical effects on the metal phase of the anode cermet. These effects will be discussed in detail later in this work.

In addition to being electrochemically active towards the desired reduction reactions, the metal phase of the anode cermet needs to be highly electronically conductive. This will reduce resistive and overpotential losses (effects which will be discussed in detail in another section). Nickel fulfils these criteria. Undesired side reactions should also be minimized. Unfortunately, Ni has a tendency to form coke under hydrocarbon pyrolysis conditions. Because of this effect, the tendency towards poisoning of nickel-based anode material in carbon-containing pyrolytic atmosphere, as well as that of sulfur and carbon containing atmospheres will be investigated herein.

2.4.3.1 Triple-phase boundary

The electrochemical reaction itself takes place in a region aptly named the triple-phase boundary or three-phase boundary (TPB). It is here that the three key components meet to effectuate electrochemical oxidation, in the case of the anode. Oxygen dianions, produced at the cathode, migrate through the non-porous electrolyte layer via an ionic conduction mechanism. Gaseous fuel which has diffused through the pores of the anode reaches the solid surface. Electrons produced by the electrochemical oxidation are conducted to the current collector via the reduced metal component. It is where these three phases (namely the reduced metal (alloy), YSZ and the gaseous fuel) contact that the electrochemical reduction at the TPB occurs, figure 2.4.

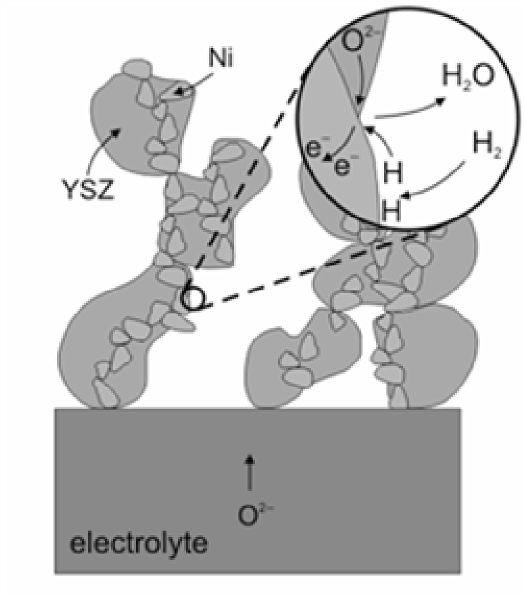

Figure 2.4 Diagram showing a non-porous, oxygen conducting electrolyte in electrical contact with a porous cermet anode of YSZ and Ni, as well as an expansion of the triple phase boundary (TPB) region. [7]

2.4.4 Cathode and Reference Material

Overwhelmingly, strontium doped lanthanum manganite (LSM) is the chosen material for the cathode in SOFC manufacturing. It is both chemically stable and has a high electronic conductivity at high temperatures under an oxidizing atmosphere. However, it has a thermal expansion coefficient which differs from that of YSZ. The solution to this problem has been to mix the two materials together to lessen this difference, thus affording a greater physical and electronic contact between the porous cathode and non-porous electrolyte. The concentrations chosen for mixing of these two materials was 70 % w/w LSM and 30 % w/w YSZ. This ratio ensures that the thermal expansion coefficient of LSM is lowered somewhat to provide a greater match with YSZ without compromising the electronic conductivity of the electrode.

For the reference electrode, LSM is the material chosen, due to both its chemical stability and electronic conductivity. A Pt wire was chosen as the current collector due to its stability, as discussed above. Since both the cathode and reference electrodes are exposed to identical environments (atmospheric chemical composition, pressure and temperature), utilizing the same material for both electrodes is a logical choice.

One important point to consider concerns the reactivity of YSZ with LSM at high temperatures: in the solid phase, at temperatures above 1150^{o}C, La, Mn and Sr react in appreciable amounts with ZrO_2, thus changing the chemistry of both phases. [8] To ensure this effect is minimized, the cathode and reference electrodes are applied, painted, and sintered only after the anode material has been sintered. Thus, this ensures that these electrodes can be sintered at the lower temperature, 1150^{o}C, avoiding both phase mixing and interference in the sintering process of the anode.

2.4.5 Geometric Constraints

The button cell built to run electrochemical tests was designed with a three electrode geometry, which contains working, counter and reference electrodes. Interest for this work is in the processes and performance of the anode (working) electrode, and so it must be possible to measure the overpotential of this electrode independently from the full cell value. By employing a reference electrode in addition to a counter electrode, this is made possible. In this system, the counter (cathode) electrode functions simply as a current carrying electrode. The purpose of the reference electrode, although it is designed to carry minimal current, is to afford operational control on the working electrode as well as to allow measuring of the potential of the working electrode independently of the counter electrode.

An instrument capable of measuring the potential of the working electrode with respect to the reference electrode, shown in figure 2.5. The current of the full cell is monitored across the working and counter electrodes, as shown. For the potential, a difference is applied between the working and reference electrodes and is adjusted via the counter electrode. The purpose of this method is to maintain the potential difference at a steady value.

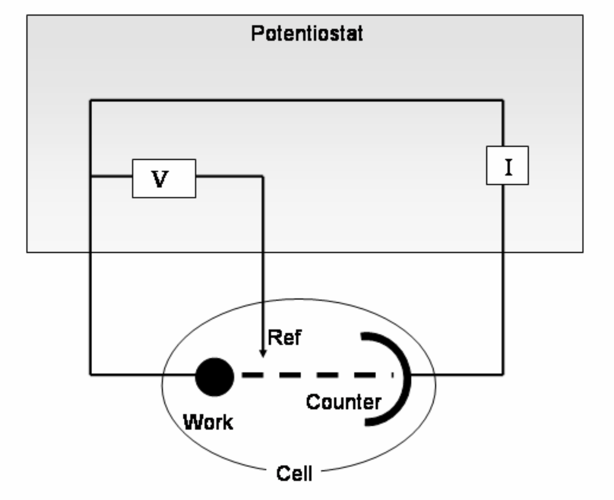

Figure 2.5 Diagram of the working, counter and reference electrodic connections within the potentiostat instrument.

Design of the fuel cell button cell is instrumental to obtaining accurate performance data, as will be elaborated using literature findings. In planning the dimensions of the electrodes, factors such as shrinkage of the electrolyte disk as well as electrode alignment must be considered. Painting and co-sintering of the anode was performed first, where a circular area of diameter 15.6 mm was painted onto the centre of a green YSZ pressed pellet (planar cell) using a mask to ensure size and shape control. Upon co-sintering, the YSZ pellet experiences 23 % size reduction, resulting in an anode diameter of 12.0 mm. A counter electrode was painted on the centre of the opposite side of the pellet with a diameter of 12.0 mm. The alignment of these two electrodes on opposite sides of the YSZ pellet is controlled to the highest degree possible for a hand-painted button cell (with the use of pre-fabricated masks).

The distance measured between the reference and working (as well as reference and counter) is of importance as well. The Pt wire, which functions as the reference electrode, is 5.7 mm away from the edge of both electrodes. With an electrolyte thickness of 1.5 mm, this corresponds to a reference-electrode separation of 3.8 'electrolyte thicknesses' away. This is within agreement of literature conclusions for optimal reference-electrode separation distances. [9-11]

Computational and experimental studies have both shown agreement whereupon the three electrode geometry of a cell needs to meet several requirements to produce accurate results. The first requirement is that the working and counter electrodes must be the same size and shape, and be located opposite each other with high symmetry standards. The second is that the reference electrode must be located a minimum distance away from the edge of the other two electrodes; a distance that is dependent on the thickness of the electrolyte layer. Despite this final statement, a balance between electrolyte thickness and cell performance must be maintained; namely, an electrolyte that is too thin will produce a cell which is subject to high electrode misalignment error (discussed in the following paragraph), but an electrolyte that is too thick will compromise the cell's ability to produce reasonable current density data due to high electrolyte resistance. [12, 13]

Numerical data from the literature supports these parameters for button cell design. For electrolyte layers less than 200 μm in thickness, misalignment of working and counter electrodes can produce large errors in polarization resistances. Thickness of the electrolyte larger than this value can tolerate an experimental misalignment of 0.5 mm with minimal anodic and cathodic overpotential error. A thick electrolyte layer will allow a cell set-up to work in the region of 'predictable errors'. Computational studies have determined a general 'rule' where the electrode alignment requirements for a cell have a tolerance of ± 0.1 'electrolyte thicknesses'. Furthermore, a consensus exists that the reference electrode be located a minimum of three 'electrolyte thicknesses' away from the edge of the working and counter electrodes. Other considerations for the reference electrode include the fact that a central reference electrode has been found to distort polarization measurements, and, for symmetric electrodes, a reference to the side that is in the shape of a strip is preferred over a circular or square shape. [14]

The design of the current button cell geometry has been optimized to fulfill all of the current, known requirements for cell geometry. The misalignment errors for the working and counter electrode have been minimized by the use of masks during painting. The resulting working and counter electrodes have the same size and shape. With an ‘electrolyte thickness’ of 1.5 mm, the electrolyte layer is more than 200 μm thick, and the misalignments are much smaller than the calculated allowable requirements, namely ± 0.15 mm. The reference electrode is on the outside of both the working and counter electrodes and is ‘strip’ shaped. This electrode is also more than three ‘electrolyte thicknesses’ away from the edge of the working and counter electrodes. [15]

Electrode positioning requirements relate to the measurement of specific area resistances. With proper electrode positioning, a uniform current density over the area of the electrode can be achieved, and thus an accurate measurement of the area specific resistances can be obtained.

$$R_p = \frac{\eta}{i} = \frac{\phi_{WE} - \phi_{RE}}{i - R_S} \qquad (2.1)$$

Here, R_p is the polarization resistance, η is the overpotential, i is the current, R_S is the series resistance and φ_{WE} and φ_{RE} are the potential of the working and counter electrodes, respectively. Relating this mathematical relationship back to the placement of the reference electrode, if a uniform current density is not obtained, the measured overpotential will either give a value that is too high or too low. This will be caused by differences in polarization over the area of the electrode.

Measurement of the impedance spectra for the half cells for working and counter electrodes with respect to the reference, and comparison of this data to the full cell can give information about the uniformity of the resistances present. However, it should be emphasized that impedance spectra cannot distinguish between specific causes of error for over- or underestimates of resistance values. The data obtained for each half cell and the full cell is shown in figure 2.6.

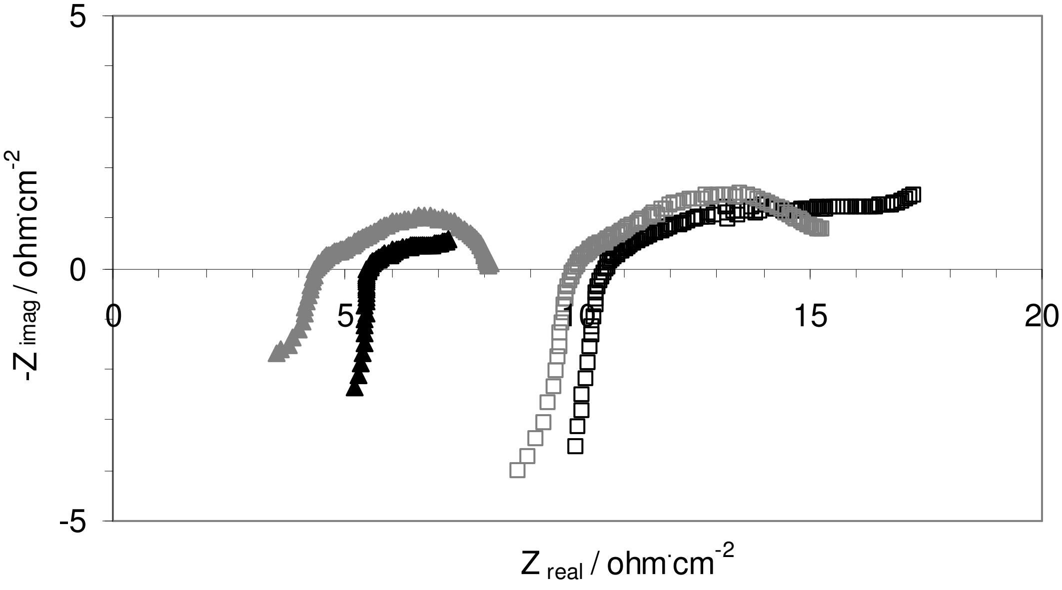

Figure 2.6 Sample of data shown in Nyquist plot form for a $Ni_{0.7}Co_{0.3}O$-YSZ anode at 850°C in hydrogen fuel at 50 sccm flow rate. □ (full cell, measured), □ (full cell, calculated by summation of cathode and anode half cell data), ▲ (half cell, cathode), ▲ (half cell, anode).

Ideally, there is a 50-50 % sharing of the ohmic resistance of each half cell as measured between the working and reference when compared to the counter and reference. Since the area specific resistance of the anode is approximately 3 Ω/cm^2, and that of the cathode is 2.5 Ω/cm^2, the split is 55-45 %, which is slightly off the ideal for the reference-anode and reference-cathode percentage ratio. Since the cathode has the smaller resistance value, it is expected to be the electrode by which small errors due to cross-talk can be attributed. Because it is the anode and its processes which are of interest in this work, the errors associated with cross-talk caused by the cathode are expected to be small.

2.5 Cell Manufacturing

Button cells were manufactured by pressing 3.60 g of 8-YSZ (TZ-8YS, Tosoh Corporation) uniaxially using a circular, 1 inch die under 4 metric tonnes for 1 min. An anode slurry was prepared by grinding by mortar and pestle 0.15 g of the dried, green (as-synthesized, unsintered) anode powder and 0.1 mL of a pre-mixed liquid phase composed of 30 % Triton-X100 (Avocado Research Chemicals, Ltd) functioning as a pore former and 70 % distilled water, by volume. The anode active layer was then painted onto the disk using a mask to produce a circular electrode centered on the YSZ green disk with an effective area of 1.33 cm^2 and with a thickness of 100 μm. The electrolyte and anode were then co-sintered to 1380 ^{o}C (Thermolyne 46100 High Temperature Furnace, B-type thermocouple) for 4 hours with ramp rates of 2 ^{o}C/min. A current collector consisting of Pt gauze cut into squares with 9 mm sides (52 mesh woven from 0.1 mm diameter wire, Alfa Aesar) was embedded in additional anode material by painting and sintering again at 1380 ^{o}C for 4 hours with identical ramp rates.

An identically sized cathode was painted using a mask onto the centre of the opposite side of the YSZ disk with its own current collector. The cathode electrode was prepared using a lanthanum strontium manganate (LSM-15, NexTech Materials) and 8-YSZ mixture in the ratio 70/30 % by mass. The cathode was painted with the same Triton/water mix used for the liquid phase of the anode. The current collector was identical in size, shape, and composition as that used for the anode. The current collector was embedded in the LSM-15 slurry used to construct the cathode upon painting. A reference electrode consisting of a Pt wire with diameter 0.2 mm was wrapped around the edge of the YSZ-electrolyte disk and painted to secure it using the same LSM-15 slurry as the cathode. The cathode and reference electrodes were then sintered simultaneously at 1150 ^{o}C for 4 hours with ramp rates of 2 ^{o}C/min to produce the completed 3-electrode button cell, figure 2.7.

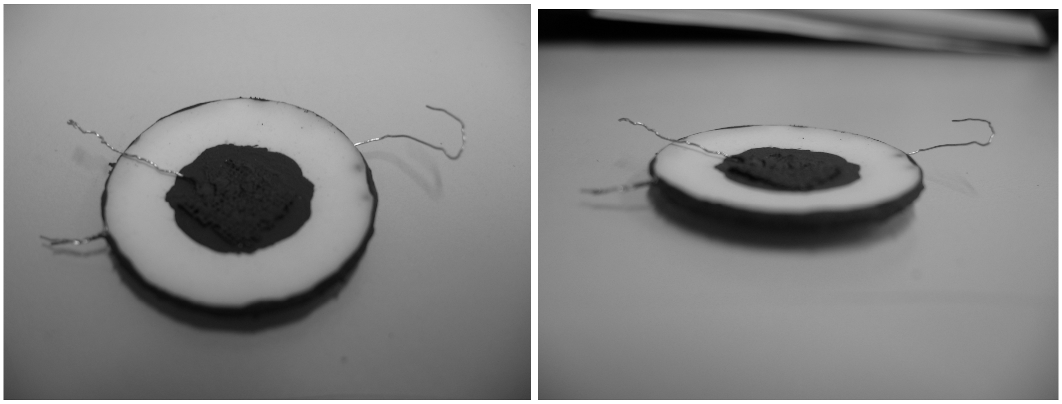

Figure 2.7 Photograph of the button cell before testing, showing top view (left) and angled side view (right) of the cathode. The reference electrode can be seen around the edge of the button cell. The anode is located on the underside of the disk.

2.6 Characterization Techniques - Materials

2.6.1 SEM & EDS Measurements

The SEM model available for imaging is the JEOL JSM-7500F SEM. No coating was applied to the specimens before observation to avoid damaging the microstructure. For fuel cell cross section images, the button cell was cracked mechanically to yield a native cross section and the sample was subsequently mounted vertically to avoid the need for tilting the stage during image collection. Images were obtained by collecting secondary/backscattered electrons (in the LEI mode of the JEOL microscope to collect lower secondary electrons), which maximizes surface topographical information by making this the primary source of contrast (as opposed to compositional information). In order to maximize the quality of photographs taken, the length of scanning exposure time was 11 s per frame. This parameter was chosen to minimize drift, charging and sample damage during image collection. The acceleration voltage was kept low to minimize charging while still retaining good image quality. The probe current and working distance conditions are optimized for collecting backscattered electrons with the JEOL microscope. Typical conditions include: acceleration voltage 1.0 V, probe current 8 mA, working distance 8.0 mm, magnification between 50 and 10 000 x.

The EDS model available for gathering compositional data is the EDS X-Sight. Whenever possible, EDS data was collected while imaging through SEM to gain complementary data. Images taken with conditions maximized for EDS data collection (high acceleration voltage and probe current settings) are highly susceptible to charging. Image quality is not maximized for these “site of interest” images because the settings are optimized for EDS data collection instead. Typical conditions include: acceleration voltage 20.0 V, probe current 10 mA, working distance 8.0 mm, magnification between 50 and 1000 x.

2.6.2 Powder X-Ray Diffraction

2.6.2.1 Bragg’s law

The constructive interference patterns observed when the powder X-ray diffraction method is employed can be derived via a simplified model system. If the repeating units of a crystalline lattice are simplified to periodic points along lattice planes, as shown in figure 2.8, a mathematical model can be found. The simple crystal has definable path length differences from adjacent planes with the definable periodic spacing distance d_{hkl}. Using simple trigonometry, the following relationships are true.

$$(AB + BC) = (d_{hkl}\sin\theta + d_{hkl}\sin\theta) = 2d_{hkl}\sin\theta \qquad (2.2)$$

For cases of constructive interference, which yield peaks in the resulting diffractogram of interest, the path length corresponds to an integer multiple of the wavelength of the source of radiation. This simplifies the relationship to yield the relationship known as Bragg’s law.

$$n\lambda = 2d_{hkl}\sin\theta \qquad (2.3)$$

The integer *n* can be simplified into the lattice plane term,

$$\lambda = 2d_{nh \cdot nk \cdot nl} \sin\theta \qquad (2.4)$$

where *nh nk nl* are called Laue indices, which correspond to the lattice planes with spacing $\frac{d_{hkl}}{n}$. Here *n* is incorporated into the Laue indices for simplicity, since all integer values of *n* will yield one single peak.

Bragg's law also applies for more general situations where the distance AB does not equal BC, as in the case of crystals with repeating planes of atoms which are not arranged in rectangular patterns. It is the sum AB + BC which is important, and this will still be equal to the term $2d_{hkl}\sin\theta$. As long as the material under consideration is crystalline, Bragg's law does not depend on the positions of the atoms, but on the spacing of the planes within the material. This equation, where waves scattered from planes with path length difference of zero will yield constructive interference, is considered in two-dimensions here. This relationship can be represented in three-dimensions by Ewald's synthesis, which involves a reciprocal lattice and a sphere of reflection. This will not be derived herein, since it yields the same results as the Bragg law, but in three-dimensions.

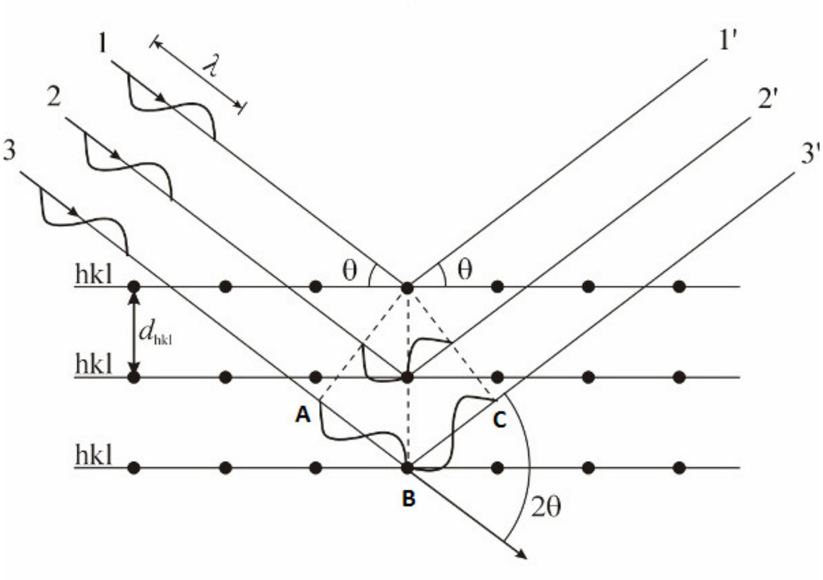

Figure 2.8 Diagram showing a simplified crystal lattice and the mathematical relation of plane spacing, d_{hkl}, angle, θ, and photon path length *ABC* for planes of increasing depth below the crystal surface.

2.6.2.2 X-ray scattering considerations

An important consideration when employing X-ray diffraction is the effect of scattering of the photons with respect to electrons of atoms and the effects this can have on the incident and diffracted beam. Since atoms have finite and varying sizes, they cannot be considered as ideal points where diffraction occurs. Scattering from different points in a large atom can result in a phase shift in the wavelength of the emerging photon. Because the size of atoms is on the same order as the wavelength of X-rays, the path difference between scattered photons will become increasingly destructive as the angle, θ, increases. Thermal motion, which is described as vibration of the atom within its lattice site, can make it appear to have a larger size, which can cause larger amounts of scattering. Furthermore, for crystals with more than one atom scattering photons in a unit cell, a "wide-slit" diffraction model needs to be considered, since the waves are distributed across a theoretical slit of larger width. The incident beam also attenuates as it travels deeper into the crystal since it is scattered by atoms, such that atoms deeper in the crystal interact with less photons. The diffracted beam then needs to travel through the crystal to leave the surface and be detected. These effects will be important in the following sections pertaining to peak broadening and fitting for the purpose of determining crystal lattice parameters.

2.6.2.3 Peak broadening effects and considerations

Peaks which are observed due to photons that have left the surface of the material show broadening effects. This is due to crystallite size and strain in the crystal lattice. Broadening can also be caused by instrumental factors, which are much easier to account for in spectral analysis.

X-ray tubes consist of a heated filament, which acts as a cathode and emits electrons, and a target for the electrons, which is an anode made of copper. Though most of the electron energy is converted to phonons (heat) upon interaction with the anode, some is converted to photons in the X-ray region of the electromagnetic spectrum. The strongest signal, designated $K_{\alpha 1}$ can be separated from other nearby strong signals (such as $K_{\alpha 2}$) using a crystal monocromator, and used as the incident beam. However, for the instrument available for use, the $K_{\alpha 2}$ signal is removed from the spectra mathematically using software during data processing. $K_{\alpha 1}$ corresponds to one of the three transitions from the L- to the K-shell of a copper atom, which gives the strongest signal. The wavelength of this peak is 1.540598 Å, given to 7 significant figures. Thus, the effect of peak broadening due to instrumental factors, β_{inst}, can be subtracted out of each measured peak, β_{meas}, to give the corrected broadening, β_{hkl}, due to Scherrer, [16] equation 2.5.

$$\beta_{hkl} = \beta_{meas} - \beta_{inst} \qquad (2.5)$$

For peak broadening effects caused by crystal size, β_{τ}, the Scherer equation is considered; for those effects caused by lattice strain, β_{ε}, the Wilson [17] equation is presented, equation 2.6. It is assumed that these two effects are independent of each other and that they can be summed to give the corrected peak broadening.

$$\beta_{hkl} = \beta_{\tau} + \beta_{\varepsilon} \qquad (2.6)$$

Each of the broadening effects can be described mathematically. For peak broadening due to crystal size, the Scherrer equation, 2.7, relates the mean crystallite size, τ, to the crystallite broadening at half-intensity maximum, β_{τ}, where K is the 'shape-factor' which is usually given a value of 0.9, and θ_{hkl} is the Bragg angle.

$$\tau = \frac{K\lambda}{\beta_{\tau} \cos\theta_{hkl}} \qquad (2.7)$$

The second of the important broadening effects due to the material is that of microstrain. It is caused by a wide range of imperfections in the material such as dislocations, vacancies, defects and shear planes. The resulting material has a distribution of *d* values around the ideal, unstrained values. This causes a range of 2θ values above and below the average, which broadens the peak in the diffraction pattern. Microstrain also causes tensile and compressive forces within the material. Thus, peak broadening due to microstrain is given by the Wilson formula, where ε is the root mean square value of the microstrain.

$$\beta_{\varepsilon} = 4\varepsilon \tan\theta_{hkl} \qquad (2.8)$$

Since these values can be summed to give the measured peak broadening, it follows that the following Williamson-Hall equation[18] can be derived (second step).

$$\beta_{hkl} = \beta_{\tau} + \beta_{\varepsilon} = \left[\frac{K\lambda}{\tau \cos\theta_{hkl}}\right] + \left[4\varepsilon \tan\theta_{hkl}\right] \qquad (2.9)$$

$$\beta_{hkl} \cos\theta_{hkl} = \left[\frac{K\lambda}{\tau}\right] + \left[4\varepsilon \sin\theta_{hkl}\right] \qquad (2.10)$$

Interestingly, since microstrain follows a *tanθ* function, but crystallite size effects follow a $\frac{1}{\cos\theta}$ function, it allows for simpler deconvolution of the two effects. Also, due to the Williamson-Hall relation, a plot of $\beta_{hkl}\cdot\cos\theta_{hkl}$ as a function of $4\cdot\sin\theta_{hkl}$, the microstrain factor, ε, can be found from the slope and the crystallite size corresponds to the intercept.

2.6.2.4 Diffractogram fitting considerations (Reitveld method)

In order to accurately calculate parameters such as lattice size and broadening effects, the spectrum needs to undergo a mathematical refinement to fit the peaks to a calculated spectrum. The accuracy of this fit is directly proportional to that of the parameters calculated, so a lot of work has been put into the mathematics of determining the most accurate fit possible. A pseudo-Voigt function has been chosen to fit the experimental data. It employs a combination of both Lorentzian and Gaussian functions to determine the best fit for each peak. Mathematically, the purpose behind this decision is because it is used to determine the fraction of Lorentzian and Gaussian components needed to best fit an observed experimental diffractogram. The specific pseudo-Voigt function[19] used for the data colleted is presented below.

$$I_i = I_p \frac{r}{1 + k\Delta 2\theta^2 + (1-r)e^{-0.6931k\Delta 2\theta^2}} \qquad (2.11)$$

Here, I_p is the experimental peak height, r is the Lorentzian component of the function in the pseudo-Voigt, known as the mixing/tailing factor, and I_i is the intensity calculated from the fitting of each data point, shown here.

$$\Delta 2\theta = 2\theta_i - 2\theta_p \qquad (2.12)$$

In this relation, $2\theta_p$ is the experimental peak position, and $2\theta_i$ is the calculated peak position. Finally, in the above pseudo-Voigt function, the last parameter, k, is given by the equation shown below.

$$k = \frac{4(1 \pm S)}{W^2_{1/2}} \qquad (2.13)$$

Here, $W_{1/2}$ is the peak width at half height and S is the 'skewness' parameter.

An iterative mathematical and computational approach is used to determine the convergence of the pseudo-Voigt function. As such, it employs a least-squares refinement method to calculate, and thus ultimately minimize, the residual, denoted S_y.

$$S_y = \sum w_i (y_i - y_{ci})^2 \qquad (2.14)$$

Here, $w_i = \frac{1}{y_i}$, followed by y_i is the experimental peak intensity at the i^{th} step, and y_{ci} is the calculated peak intensity at the i^{th} step. As with all computational models, the starting model must be close to the correct model. The program will calculate the minimum closest to the data set that has been input, which may not correspond to the global minimum, but to a local minimum. As such, chemical intuition and background knowledge are important, and Reitveld [20] himself has warned about being careful to avoid using this method as a black-box approach. In the subsequent chapter, the Reitveld fitting method was used to accurately calculate the peak positions for crystal parameter determination.

2.6.2.5 Experimental and practical powder X-ray diffraction considerations and parameters

All experimental powder X-ray diffractograms were collected on a Philips X'Pert system with PW3020 twin goniometers equipped with a copper filament source. Typical experimental parameters include: scan angle from 15 to 90°, step size is 0.020°, time per step is 2.00 s, scan speed is 0.01000°/s, total scan time is 2:05:00 h:min:s, continuous scan mode was used, the scan axis is goniometer mode, and the sample was set spinning at 1 revolution/s.

The background noise was subtracted out of the spectrum automatically by the Jade 6.1 software. This was followed by a subtraction of the $K_{\alpha 2}$ peak contribution, where the $K_{\alpha 2}$ value was assumed to be one half of $K_{\alpha 1}$. The effect of the $K_{\alpha 2}$ peak is more important at low angles, since this is where the $K_{\alpha 1}$ and $K_{\alpha 2}$ peaks have more overlap. This process increases the accuracy of the diffractogram towards proper peak placement, intensity and broadening. Two important assumptions were made when fitting the data to determine particle size and microstrain: crystallite particles were assumed to be spherical, though they are not close to this shape in reality, and microstrain was assumed to be constant throughout the particles, though this would be an impossible case to obtain. The 'skewness' parameter was set to be zero, and so assumed to be constant at this value. All other parameters were left free during refinement using the presented pseudo-Voigt function in the Jade 6.1 software program.

2.6.3 Gas Adsorption for Determination of Surface Area

Heterogeneous catalysis depends directly on the amount of surface area available for the adsorption of reactant molecules or atoms. Here 'adsorption' denotes the condensation of gases onto a surface. In a closed vessel with a specific mass of solid (adsorbent) cooled to the condensation temperature of a gas (adsorbate), if a known, small amount of the gas is introduced a certain amount will condense onto the surface of the solid. The decrease in pressure is related to the amount of gas that adsorbed onto the solid. By repeating this process, an adsorption isotherm can be built by collecting data points after infusing known amounts of gas into the closed vessel. By systematically removing known amounts of gas, a desorption isotherm can also be built.

The shapes of each of five common isotherm shapes observed have been classified by Brunauer, Deming, Deming and Teller (BDDT), [21] [22] denoted as types I to V. However, some isotherms do not fit into one of the set classifications and can exhibit characteristics of more than one of the accepted classifications. These isotherm shapes relate directly to the attractive (dispersion) forces, which result in physisorptive interactions, described by a Lennard-Jones potential curve, between adsorbate and adsorbent. Identifying the class under which the experimental isotherm belongs relates directly to which type of adsorbate-adsorbent interaction dominates, which in turn allows for the correct choice of mathematical model with which to determine the surface area of the material.

The most common adsorbate, dinitrogen gas, has the ability to interact with both non-polar and polar adsorbents by condensing the gas on the surface of interest. The unsintered materials (as synthesized) resemble type IV isotherms showing both a convex shape at low relative pressures and hysteresis at medium to high relative pressures. In the region $P/P_o = 0 – 0.5$, the rapid rise in the volume of adsorbed material shows unrestricted monolayer and multilayer adsorption. The linear region, at approximately $P/P_o = 0.2 – 0.4$ for both isotherms, shows the region after monolayer coverage has been completed and multilayer coverage dominates. Both $Ni_xCo_{(1-x)}$ compositions of unsintered materials show mesoporosity, as shown by the hysteresis loop, figure 2.9, creating a difference in profile for the forward and reverse isotherms. Although both show porosity associated with agglomeration of particles, panel A shows that of defined size whereas B shows that of undefined size.

Under the old classification put forward by de Boer in 1958, [21] panel A shows type A behaviour, and panel B shows type E; however, under the more modern IUPAC classification, they correspond to types H1 and H2 respectively. Emptying of the pores, as shown by the desorption isotherm, occurs at approximately the same relative pressure, 0.45. For type IV isotherms, the Brunauer, Emmett and Teller (BET) [23] region is not affected by the existence of hysteresis caused by mesopores pores. The data utilized to determine the BET surface area is in the pre-hysteresis region, namely $P/P_o = 0.05 – 0.35$. In this region of monolayer formation, the adsorbate does not distinguish between the external and internal surface of the adsorbate. Emphasis will not be placed on this data, as the material was not used in this form for any electrochemical fuel cell experiments, though the surface area of the two materials presented was calculated and is shown below for comparison purposes with the sintered materials.

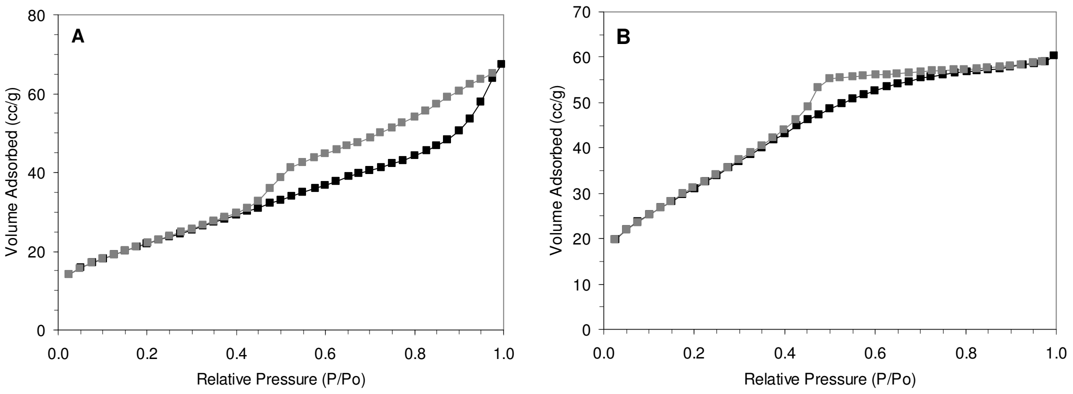

Figure 2.9 Nitrogen adsorption isotherm for unsintered (as synthesized) samples, (A) $Ni_{0.85}Co_{0.15}O$-YSZ, (B) $Ni_{0.70}Co_{0.30}O$-YSZ. ■ Adsorption Isotherm, ■ Desorption Isotherm

The isotherms, shown in figure 2.10, for the sintered samples are presented and show type III behaviour, an isotherm characteristic of a non-porous (or macroporous) solid. There are two notable differences between these isotherms and those of the unsintered materials. The lack of hysteresis of the samples shows a very small pore volume. The 'steps' seen in the data are an artifact of the instrument rather than the material, since these measurements are near the threshold of measurement for the instrument. The sharp increase at high relative pressure corresponds to condensation of the adsorbate on the material. The second difference of note is the concavity of the sample isotherms relative to the pressure axis. This is caused by weak adsorbate-adsorbent interaction forces. Although the curvature (concavity) has changed from the unsintered samples (the 'as synthesized' samples have a downward curvature, whereas the sintered samples have an upward curvature), the extent of the change is small, indicating a change in surface morphology is the likely cause, as would be expected for a sintered sample.

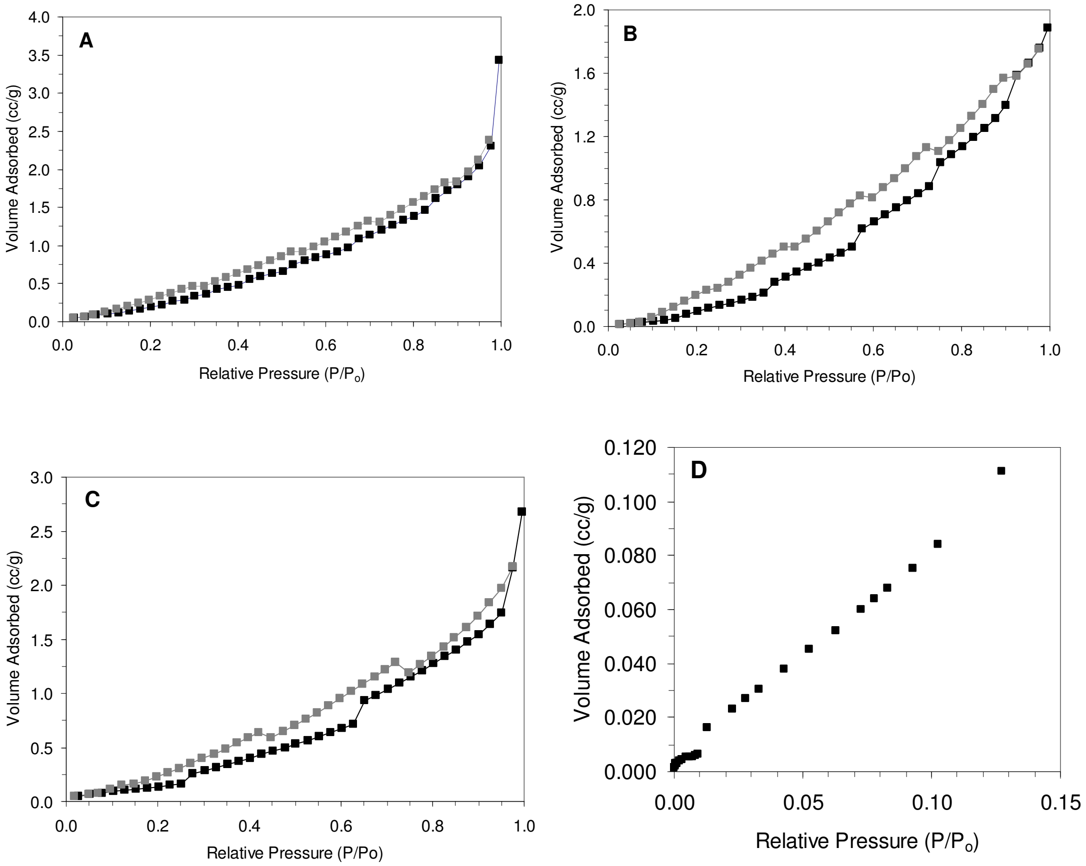

Figure 2.10 Nitrogen adsorption isotherms for anode samples sintered to 1380°C for 4 h (A) NiO-YSZ, (B) $Ni_{0.95}Co_{0.05}O$-YSZ, (C) $Ni_{0.70}Co_{0.30}O$-YSZ. (D) Data at extremely low relative pressure for NiO-YSZ (adsorption only). (■) Adsorption Isotherm, (▨) Desorption Isotherm

In calculating the BET surface area, some considerations need to be taken into account. The most important among which is that, for the case of a type III isotherm, the procedure for calculating the monolayer capacity is not applicable. This is due to the weak adsorbent-adsorbate interactions producing a tendency to accumulate multilayers before a complete monolayer coverage is established. This results in the absence of a defined ‘knee’ shape at low relative pressure, which shows the transition from mono- to multilayer. However, for values of *c* (*vide infra*) between 2 and 3, although the point of inflection is not easily visualized, it exists nonetheless, corresponding to a monolayer formation, thus allowing the use of the BET equation.

Developed in 1938 by Brunauer, Emmet and Teller, [23] the BET equation is defined as follows.

$$\frac{1}{v\left(\frac{P_o}{P}-1\right)}=\frac{c-1}{v_m c}\left(\frac{P}{P_o}\right)+\frac{1}{v_m c} \qquad (2.15)$$

Here, P and P_o are the equilibrium and saturation pressure of the adsorbate, v is the volume of gas adsorbed, v_m is the volume of gas adsorbed to create a monolayer, and c is the BET constant.

$$c=\exp\left(\frac{\Delta H_1-\Delta H_L}{RT}\right) \qquad (2.16)$$

Here, ΔH_1 is the enthalpy of adsorption of the first layer (monolayer), ΔH_L is the enthalpy of adsorption of the following layers, R is the universal gas constant and T is the temperature. In a different form which is applicable to experimental data, the BET equation can be expressed as follows.

$$\frac{\left(\frac{P}{P_o}\right)}{n\left(1-\frac{P}{P_o}\right)}=\frac{1}{n_m c}+\frac{c-1}{n_m c}\left(\frac{P}{P_o}\right) \qquad (2.17)$$

Here n is the molar quantity of adsorbate on 1 g of solid, and n_m is the molar monolayer capacity, which are essentially interchangeable with their corresponding v's (*vide supra*). Though mathematically more awkward, a plot of $\frac{(P/P_o)}{n(1-P/P_o)}$ versus P/P_o will give a straight line in the aforementioned BET region with slope $s=\frac{c-1}{n_m c}$ and intercept $i=1/n_m c$. The value of the BET constant c can then be calculated by $c=\frac{s}{i+1}$. Through the plot below, figure 2.11, and in agreement with discussion above, the value for *c* for a typical isotherm was calculated to be 2.7, which, for a type III isotherm, proves the existence of an inflection point at low relative pressure, and allows the use of the BET model to calculate surface area. The high R^2 value shows good correlation of the experimental data in the BET region with a linear trend. A small amount of scatter is observed for this data set, though no consistent trend in the scatter was observed between the other data sets (not shown).

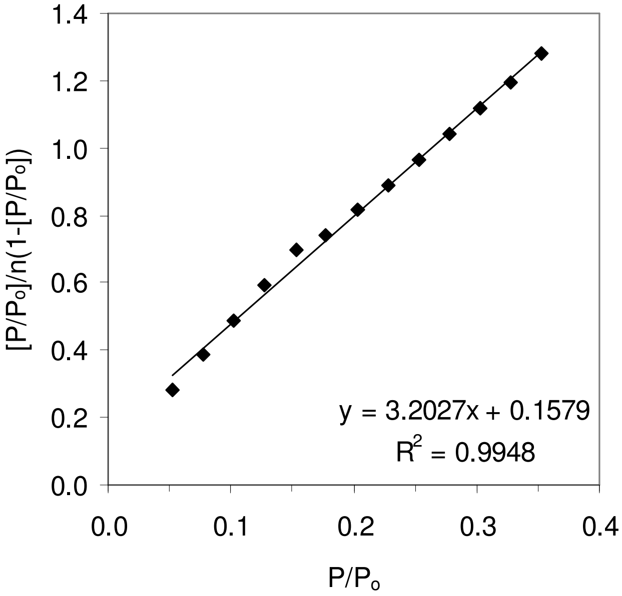

Figure 2.11 Plot of adsorption data for $Ni_{0.7}Co_{0.3}$-YSZ catalyst powder in the low relative pressure region for determination of the BET constant *c* through the slope and intercept of the best fit linear trend. The R^2 value shows good correlation to a linear trend.

This brings the discussion full circle since the type of isotherm is dependent on the value *c*. When *c* is large, the adsorbate-adsorbent interaction is strong, and a type IV isotherm is observed. Conversely, when *c* is small, the adsorbate-adsorbent interaction is weak and a type III isotherm is observed.

The major assumptions associated with this model do produce some inherent error. The major source of which is the assumption that the enthalpy of adsorption does not vary with respect to surface coverage during buildup of the monolayer. This assumption also applies to subsequent layers, though this is less important when considering the BET model, which applies to only the formation of the first monolayer. Another point to consider is the existence of micropores. Due to the relatively small size difference between micropores (<20 Å) and the diameter of an N_2 molecule (4.3 Å), a solid which contains micropores will not give a meaningful BET surface area.

To confirm the absence of micropores, a t-plot was obtained, which relates the statistical thickness of the adsorbed layer and gas phase pressure,

$$\xi = a\left[\frac{1}{\ln\left(\frac{P_o}{P}\right)}\right]^{1/b} \qquad (2.18)$$

where ξ is the statistical thickness, and a and b are constants equal to 6.0533 and 3.00 respectively for nitrogen. [21] A plot of the adsorbed volume of gas (V) versus ξ in the relative pressure region $P/P_o = 0.05 - 0.30$ gives the micropore volume equal to the y-intercept. For all data obtained for the sintered samples plotted in this region, the intercept was equal to zero, thereby indicating that the micropore volume is zero. This exclusion of micropores from the anode material further validates the use of the BET equation in the calculation of total material surface area.

For the case of a mixed solid, such as a Ni-YSZ anode cermet, the area of the active metal surface can be determined using dihydrogen gas. It is especially important to find the surface area of the catalytically active metal. The method for calculating this relates the amount of adsorbate required to form a monolayer of hydrogen chemisorbed onto the metal surface with the number of active catalyst sites.

During this process two adsorption cycles are performed. The isotherm generates a plot corresponding to total physisorption of hydrogen onto the surface of the cermet. The second adsorption cycle achieves physisorption exclusively on the ceramic surface. The key to this process is the difference between interaction methods of the ceramic and metal surfaces with dihydrogen gas at the working temperature. Interaction of the adsorbate (H_2) with the metal catalyst surface results in chemisorption, which includes the dissociation of the dihydrogen to form two chemical bonds with the single hydrogen atoms and the metal surface. This is the reason why desorption curves are not collected. Following this step by an evacuation cycle and a subsequent second adsorption curve generates a measurement of the ceramic surface area. Simply subtracting the two can give a measure of the active metal surface area. The irreversible (at the given working temperature) dissociation of hydrogen from the metal surface has the effect of creating a deviation from the ideal Langmuir isotherm, which can be utilized as described.

The ideal Langmuir isotherm possesses a type I shape, where rapid monolayer formation at low partial pressures creates a steep rise in the isotherm, followed by a plateau when no further formation of monolayers occurs. The observed trend does not match this ideal as shown in figure 2.12; the increasing amount of volume adsorbed strongly suggests multilayer formation continues as pressure is increased. Despite this, the Langmuir equation was utilized based on its widespread popularity and success in the literature. The Langmuir equation is shown below.

$$\frac{1}{V} = \frac{1}{V_M} + \frac{1}{V_M K_C P^{1/2}} \qquad (2.19)$$

Here V is the volume of gas adsorbed during the cycle, V_M is the volume of gas needed to cover a monolayer on the solid surface, $K_C = \frac{k_{ca}}{k_{cd}}$ represents the ratio of the adsorption and desorption rate constants and P is the pressure. A straight line with y-intercept $\frac{1}{V_M}$ can be obtained by plotting $\frac{1}{V}$ versus $\frac{1}{P^{1/2}}$. An assumption in the Langmuir model, which generates inherent errors should be noted. The heats of adsorption are assumed to be constant within the model, namely the heat of adsorption does not vary with surface coverage. Also, although the model assumes not hydrogen spillover and adsorption onto the YSZ surface, a small amount does occur. Thus, the value calculated for the active metal surface area of this type of catalyst will be slightly lower than the isotherm indicates.

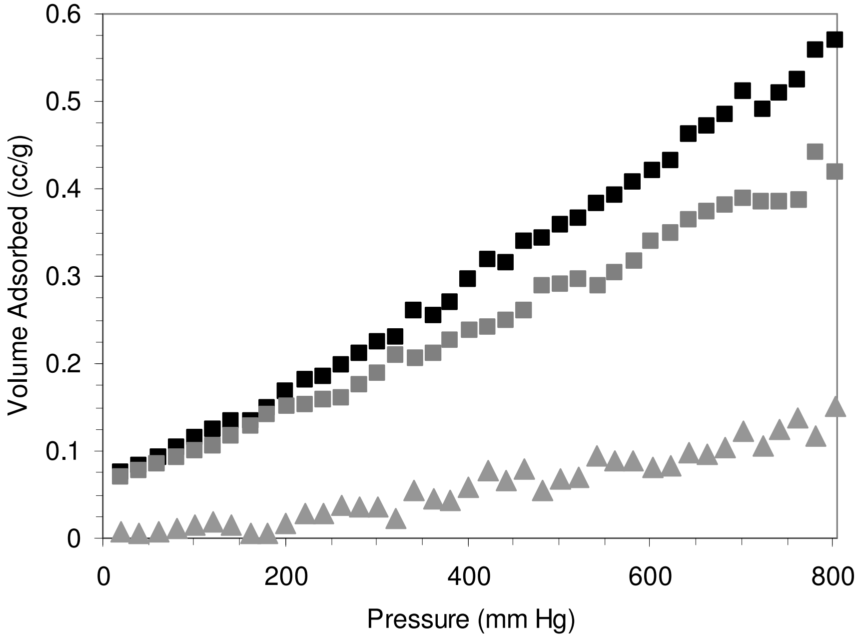

Figure 2.12 Sample chemisorption isotherm for hydrogen on Ni$_{0.7}$Co$_{0.3}$-YSZ. ■ Combined (total) adsorption, collected for a fresh catalyst powder, which shows both physi- and chemisorption. Physisorption data was collected at 600^{o}C. ■ Weak adsorption, collected after the combined adsorption analysis and evacuation which shows physisorption only. ▲ Difference (strong) adsorption, which is the mathematical difference between the combined and the weak adsorption data, showing only the chemisorption of hydrogen.

2.7 Characterization Techniques - Electrochemical

2.7.1 Direct Current (DC) considerations

2.7.1.1 The Butler-Volmer equation – electrochemical reaction rate dependence on overpotential

For a reaction at equilibrium, the interfacial electron transfer reaction can be considered for the anodic current at the electrode/electrolyte interface. The cathodic current can also be considered, but only the anodic case will be described below. The net cathodic and anodic electron flow is equal at equilibrium and represents the forward and reverse reaction, so the currents are equal towards each other, but opposite in direction and sign, equation 2.20.

$$\overset{\leftarrow}{i} = \vec{i} \quad \text{and} \quad i_{cath} = -i_{anod} \qquad (2.20)$$

Consider a general electrochemical reaction as occurring at the anode written as follows, where a reductant (such as a hydrocarbon fuel) loses electrons to produce an oxidant, equation 2.21.

$$\mathrm{Re}\,d + ne^- \rightleftharpoons Ox \qquad (2.21)$$

As written, a negative potential will result in a forward reaction, which will produce a positive net current, which can also be called an anodic current. For this case, the current density can be written as follows, which is called the Butler-Volmer equation. [24-26]

$$i = i_o\left[\exp\left(\frac{-\alpha\eta F}{RT}\right) - \exp\left(\frac{(1-\alpha)\eta F}{RT}\right)\right] \qquad (2.22)$$

Here, i_o is the exchange current density, which will be described more in detail below, where α is the transfer coefficient, which is usually set to a value of 0.5. This coefficient defines the amount of overpotential that pushes each of the anodic and cathodic reactions. The Faraday constant, universal gas constant and temperature are given by the factors F, R and T respectively. Under cell operation, a potential is generated which differs from the equilibrium potential; at these specific conditions, the overpotential, η, is given as

$$\eta = E_{FC} - E^o \qquad (2.23)$$

where E_{FC} is the measured potential, and E^o is the theoretical potential at standard conditions.

The Butler-Volmer equation takes into account both the forward and reverse, namely the cathodic and anodic, currents, which both contribute to the overall current. For the special case at high positive overpotentials, also known as high anodic overpotentials, which is the case for this work, the Butler-Volmer equation can be simplified. Since in this case overpotential, η, is very positive,

$$\exp\left(-\alpha\eta F / RT\right) > \exp\left((1-\alpha)\eta F / RT\right) \quad (2.24)$$

then the cathodic term can be dropped to yield the following equation for the anodic reaction.

$$i = i_o \exp\left(-\alpha\eta F / RT\right) \quad (2.25)$$

Simply taking the natural logarithm of both sides yields the following relation.

$$\ln i = \ln i_o + b^{-1}\eta \quad \text{where} \quad b^{-1} = \frac{\beta F}{RT} \quad (2.26)$$

This can also be written in the following way to yield the Tafel equation.

$$\eta = a - b\log i \quad \text{where} \quad b = \frac{2.303RT}{\alpha F} \quad (2.27)$$

Using these two relationships, the data can be plotted as ln(i) against η to obtain the exchange current density, i_o, for a specific reaction. The inverse Tafel slope can also be found from this plot.

In reference to the plot described above, when analyzing raw experimental data, the region where the slope will be measured must be chosen with great care. It is assumed, for this purpose, that the first reaction step is the rate determining step. This corresponds to the first electron transfer reaction. From the relation, $\frac{RT}{\alpha F}$, and taking into account that the operating temperature for the SOFC described herein is, at its lowest, 800°C, a Tafel value of approximately 190 mV is found. Therefore, the overvoltage corresponding to 190 mV is taken to be the beginning of the linear region used to determine the exchange current density values from DC data. The region above this value, spanning approximately 200 mV, was used to calculate these values. At even higher overpotential values, diffusion limitation occurs (concentration polarization), causing the plot to curve downward, and thus ending the ohmic region.

The symmetry factor, α, in the Butler-Volmer equation is independent of overpotential, η, as will be shown in the following discussion. The effect of current produced overpotential on activation energy must be considered. For a linear curve (simplification) with an energy shift of $X\eta$, as shown in figure 2.13, the change in potential difference effects the electrodic reactions. The slopes and angles, θ and γ, remain constant, thus producing a parallel shift for the curves and a constant symmetry factor, α. Care must be taken in using this relationship, since this is true for reactions with high activation energy, $E^{\neq}_{e}$, and low current density, i_o; therefore, for all but the very fastest electrode reactions, the symmetry factor is independent of overpotential. [27]

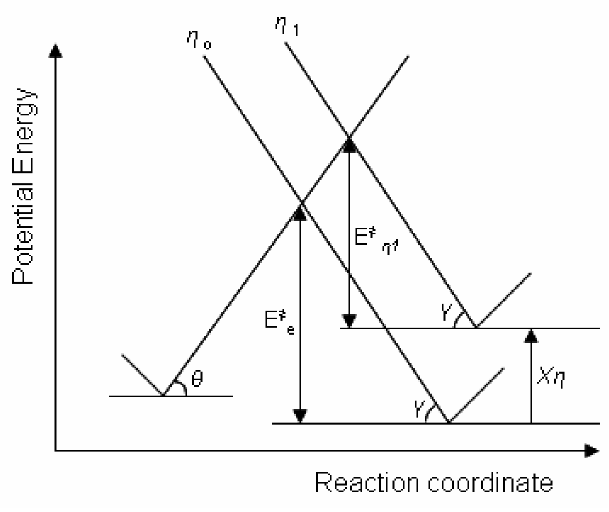

Figure 2.13 Potential energy diagram which demonstrates that for a reaction of low exchange current density, i_o, the symmetry factor, α, is independent of overpotential, η, when the angles, θ and γ, are constant.

2.7.2 Alternating Current (AC) considerations

2.7.2.1 Electrochemical Impedance Spectroscopy (EIS)

The characterization method of EIS is a powerful time-dependent tool used to characterize specific limitations of a cell so that the performance can potentially be improved. By applying a potential of a given value with a small amplitude AC signal ($\overline{E}$) and phase (ω) and measuring the current response ($\bar{i}$, $\omega + \phi$), specific information can be gathered, as can be visualized in the figure. By varying the frequency of the AC signal, and by applying this alternating signal at different potentials, the following information can be gathered. For high, medium and low applied frequencies respectively, information about charge transfer activation (also named kinetic losses), ion and electron transport (also named ohmic losses), and concentration losses (also named mass transfer losses) can be obtained.

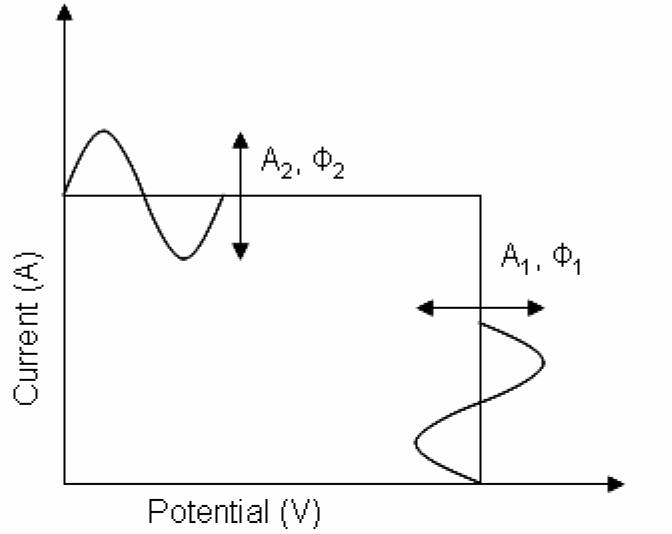

Figure 2.14 Diagram depicting mathematical parameters for alternating potential and current response for electrochemical impedance spectroscopy.

The two specific kinds of information that can be obtained from EIS, namely amplitude and phase angle can be represented by a sinusoidal signal for the voltage applied.

$$\tilde{E} = \bar{E}\sin(\omega t) \qquad (2.28)$$

The current response is also represented by a sinusoidal equation with a different amplitude and phase.

$$\tilde{i} = \bar{i}\sin(\omega t + \phi) \qquad (2.29)$$

Here $\tilde{E}$ and $\tilde{i}$ are the oscillating voltage and current, $\bar{E}$ and $\bar{i}$ are the amplitude of voltage and current, $\omega = 2\pi f$ is the angular frequency, ϕ is the phase shift and t is time. The amplitude and phase angle of the current is measured, which lags behind in response to the amplitude and phase angle of the applied potential.

Applying equivalent circuit models to the data obtained by this method, it is possible to get both qualitative and quantitative information about the sources of impedance in a fuel cell. The circuit models are constructed using three main circuit elements: ideal resistors (R), capacitors (C), and inductors (L). Since real systems rarely behave ideally, specialized circuit elements are often used as well, namely the constant phase element (Q) and Warburg element (W).

For an ideal resistor element (R), it is denoted by the symbol shown in figure 2.15, has a phase angle, $\phi = 0$, and has impedance Z_R, which relates to Ohm's law as shown.

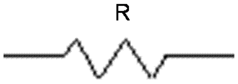

Figure 2.15 Resistance circuit element (R).

$$Z_R = \frac{\bar{E}}{\bar{i}} = R \qquad (2.30)$$

For an ideal capacitor element (C), the charge, q, on the plates of the capacitor relates to the potential across the plates. The capacitor is designated by the symbol shown in figure 2.16.

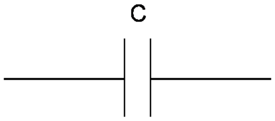

Figure 2.16 Capactiance circuit element (C).

$$q = CE \qquad (2.31)$$

Since the current is measured as a factor of charge and time, substituting in the phase-sensitive wave equation gives the following, equations 2.32 and 2.33.

$$\tilde{i} = {}^{\partial q}\!/_{\partial t} = C\,{}^{\partial \tilde{E}}\!/_{\partial t} \qquad (2.32)$$

$$\tilde{i} = \omega C\bar{E}\cos(\omega t) = \frac{\bar{E}}{\frac{1}{\omega C}}\sin\left(\omega t + \frac{\pi}{2}\right) \qquad (2.33)$$

Converting the phasors $\tilde{E}$ and $\tilde{i}$ to complex notation and simplification gives equation 2.34. This is possible since the phasor $\tilde{E}$ has a phase difference of $\phi = -\frac{\pi}{2}$ in relation to the phase of the current.

$$\tilde{E} = -j\left(\frac{1}{\omega C}\right)\tilde{i} \qquad (2.34)$$

Here the term $-j\frac{1}{\omega C}$ is equivalent to R and is also frequency and capacitance dependent.

When these two phase elements are placed in series, an equivalent circuit model for an ideal polarizable electrode is obtained. Here only capacitive current is able to move as the potential is cycled. The equivalent circuit diagram is shown in figure 2.17.

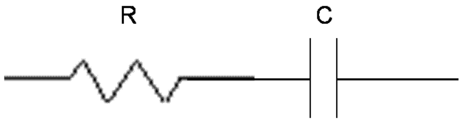

Figure 2.17 Series RC circuit element.

The total potential drop in this equivalent circuit is the sum of the resistive and capacitive elements. This can then be expressed in complex notation form.

$$\tilde{E}_{tot} = \tilde{E}_R + \tilde{E}_C \qquad (2.35)$$

$$\tilde{E}_{tot} = iR - jX_C\tilde{i} \qquad (2.36)$$

$$\tilde{E}_{tot} = \tilde{i}(R - jX_C) \qquad (2.37)$$

$$\tilde{E}_{tot} = \tilde{i}Z_{tot} \qquad (2.38)$$

$$Z_{tot} = R - jX_C \text{ , where } Z_{tot} = Z_r + Z_i \qquad (2.39)$$

Here, applying the relations derived previously for resistive and capacitive elements, a complex notation form has been obtained, which can be expressed as the sum of the real and imaginary impedances, Z_r and Z_i respectively. This relationship can be expressed graphically as a plot of the real component as a function of the imaginary component; this type of plot is a Nyquist plot. In this relation, the real component is independent of frequency, and the imaginary component approaches zero with increasing frequencies. A plot of this specific case is shown below.

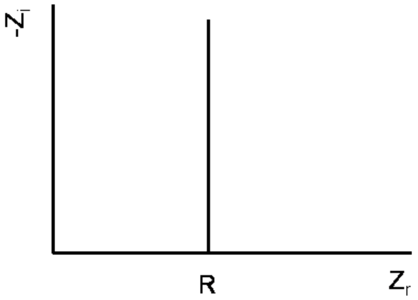

Figure 2.18 Nyquist plot and mathematical parameters for an RC series circuit for an ideal polarizable electrode.

For a real system where oxidation is irreversible and dependent on potential, an equivalent circuit with both capacitive and faradaic currents is necessary. This equivalent circuit is shown in figure 2.19.

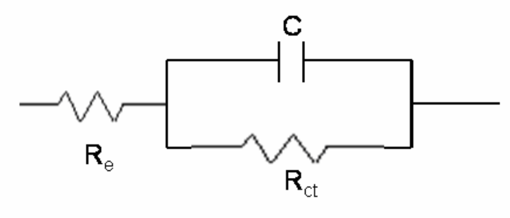

Figure 2.19 Serial equivalent circuit containing an RC element.

Following a derivation which depends on potential, mass transfer and surface coverage, an expression for the total impedance can be obtained. This derivation accounts for the oscillating current density, and also takes into account the uncompensated resistance from the electrolyte, R_e.

$$Z_{tot} = \frac{\widetilde{E}_{tot}}{\widetilde{i}_{tot}} = R_e + \frac{R_{ct}}{1 + j\omega R_{ct} C} \qquad (2.40)$$

This expression, when represented graphically, shows a semicircle with defined intercepts, as shown.

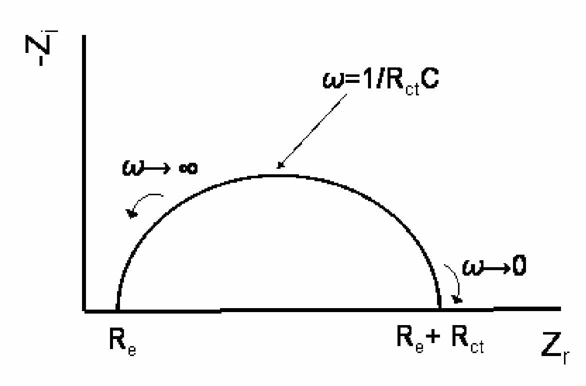

Figure 2.20 Nyquist plot and mathematical parameters for a reaction with double layer capacitance in parallel with a Faradaic charge transfer.

For a real system, which follows an irreversible oxidation and is dependent on both potential and mass transfer, an impedance which is slightly more complex is observed. Although a very similar derivation can be followed when compared to the case of an irreversible reaction dependent on potential only, the total impedance which results is shown in figure 2.21. The equivalent circuit for this case is also shown. Here, Z_d is a circuit element which cannot be expressed with the conventional circuit elements.

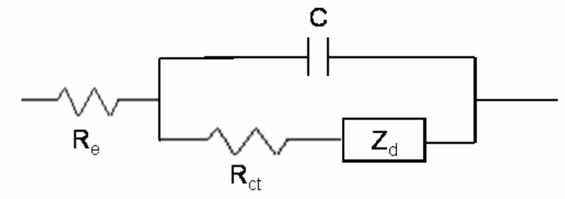

Figure 2.21 Serial equivalent circuit depicting an RC element containing Z_d, and unconventional circuit element.

$$Z_{tot} = \frac{\widetilde{E}_{tot}}{\widetilde{i}_{tot}} = R_e + \frac{R_{ct} + Z_d}{1 + j\omega C\left(R_{ct} + Z_d\right)} \qquad (2.41)$$

In the Nyquist plot shown in figure 2.22, the straight portion of the plot at low frequencies is frequently referred to as the Warburg segment.

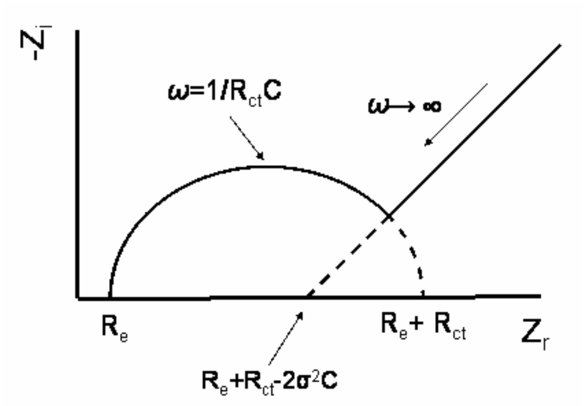

Figure 2.22 Nyquist plot and mathematical parameters for an irreversible oxidation-dependent reaction with double layer capacitance in parallel with Faradaic charge transfer resistance and a diffusion impedance element, Z_d.

Here, diffusion dominates, where the expression for Z_d is the diffusion impedance. This relationship is derived using Fick's first law of diffusion, where D is the diffusion coefficient, $\hat{\theta}'(0)$ is the surface coverage and δ is the diffusion layer thickness.

$$Z_d = \frac{R_{ct} k \delta}{D \hat{\theta}'(0)} \exp\left(\frac{\alpha F \bar{E}}{RT} \right) \qquad (2.42)$$

An additional circuit element which will be applied in describing the real system of the fuel cell electrode is the inductor (L).

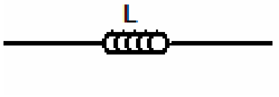

Figure 2.23 Inductor element (L).

Although inductors are normally formed by a coiled wire, straight wires do have an associated inductance, though this effect is expected to be small. The impedance of an inductor can be calculated given the equation below.

$$Z_L = j\omega L \qquad (2.43)$$

The impedance of an inductor increases as frequency increases, which is the opposite trend to that of a capacitor, where the impedance decreases with increasing frequency. Because the wire lead connecting the electrodes of the fuel cell with the potentiostat instrument are quite long (on the order of 2 m), inductance was included in the equivalent circuit modeling. Without magnetic shielding, at high frequencies, wire leads in close proximity generate magnetic fields, which can interfere with one another. Another cause for the observed inductance is through instrumental artifacts. This can be caused by the current measuring resistor at high frequencies. In the Nyquist plot, the inductance is normally observed at high frequency below the horizontal (real impedance) axis.

A final equivalent circuit element necessary to describe real systems is the constant phase element (Q).

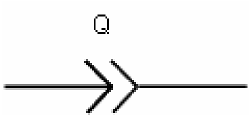

Figure 2.24 Constant phase element (Q).

This element was arbitrarily developed to fit data observed in the Nyquist plot, which show a depressed semi-circle shape. The characteristic of a depressed semi-circle is a half-circle with the centre a specified distance below the horizontal axis. Below is a plot which shows the relation of this depression below the x-axis, where the centre of the circle is shown located an angle $(1-n)*90^o$ as measured from the origin.

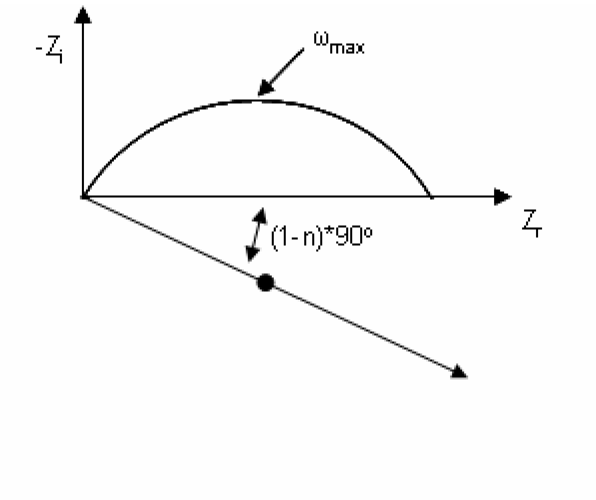

Figure 2.25 Nyquist plot and mathematical parameters for a depressed semi-circle.

Mathematically, there are two parameters for fitting experimental data to a constant phase element, namely the admittance, $\frac{1}{|Z|}$, and the depression parameter *n*.

$$\frac{1}{Z} = Y = Q^o\left(j\omega\right)^n \qquad (2.44)$$

For the special case where n=1, the admittance is equal to the capacitance, the semi-circle is ideal and equivalent to an ideal capacitor.

$$\frac{1}{Z} = Y = j\omega Q^o = j\omega C \qquad (2.45)$$

The true capacitance can be calculated knowing ω_{max}, where this parameter represents the frequency where the imaginary component is at its maximum value, the frequency at the top of the depressed semi-circle.

$$C = Q^o\left(\omega_{\max}\right)^{n-1} \qquad (2.46)$$

The causes of a depressed semi-circle are usually derived from multiple overlapping processess. Typically, a surface with high roughness will show CPE behavior due to a distribution of reaction rates, varying thickness or composition of the electrode, and non-uniform current distribution. For the anode as synthesized, it is designed to be porous, and thus has a high surface roughness. A distribution of reaction rates is frequently caused at polycrystalline metal surfaces; the cermet anode is expected to contain many energetically different crystalline surfaces. Anode thickness was controlled as stringently as possible, as described previously, although it was expected to have some variation due to the fact that they were manufactured by hand. The composition of the cermet anode is intentionally variant with two predominant phases, namely ceramic oxide and metal alloy. Finally, with a varying microstructure and mesh current collector, the current is expected to have a small distribution. 'Edge effects' are also proposed to cause a variation in the current, where the current distribution at the centre of the electrode may vary from that at the edge of the current collector.

2.7.2.2 Impedance of SOFC anodes

Presented below, figure 2.26, is a typical impedance spectrum measured for the most common anode material in this work: $Ni_{0.7}Co_{0.3}$-YSZ. Important features include an inductance 'tail' observed at high frequencies below the horizontal axis, as well as two depressed semi-circles. The first semi-circle is small and observed at high frequencies, the second is much larger at lower frequencies. At the lowest observed frequencies, an up-turning corresponding to the onset of the diffusion dependent Warburg is present. This impedance spectrum shows behaviour corresponding to an irreversible oxidation reaction with potential and mass transfer dependence, as discussed above. One difference to the model discussed, however, is the presence of an additional impedance arc.

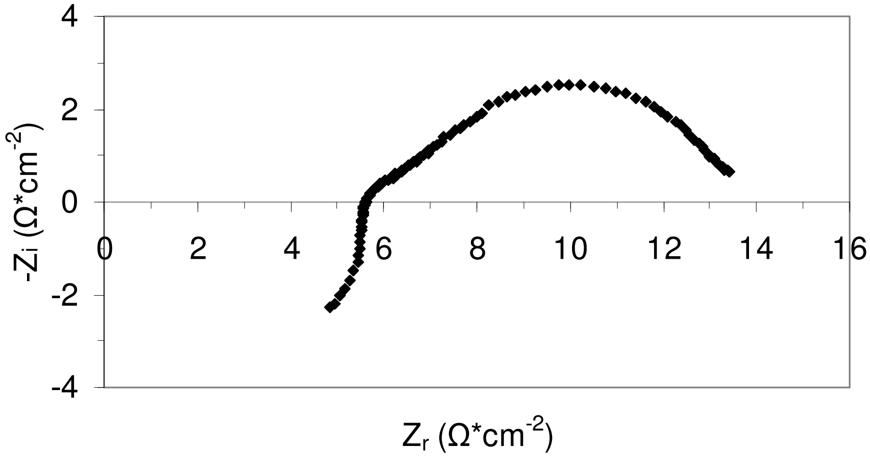

Figure 2.26 Example of a typical impedance spectrum collected for a button cell with $Ni_{0.7}Co_{0.3}$-YSZ anode at 850°C and 50 sccm flow of H_2 at OCV.

An equivalent circuit model is chosen to represent the impedance data, which optimizes two factors: the fit of the experimental data and the best sensible fit of logical combinations of circuit elements. The circuit elements for an inductor (L), resistor (R), capacitor (C), and constant phase element (Q) are ordered in logical combination. One of the most common elements is the RC (or similar RQ) combination in parallel, shown below. A constant phase element is included when the semi-circle it directly models is depressed by a factor $0 < n < 1$ (derived above). Note that these elements are shown in parallel, by far the most common combination in impedance circuit modeling.

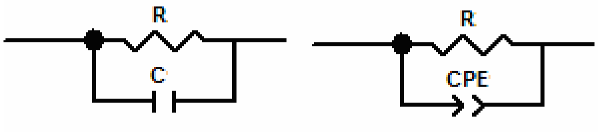

Figure 2.27 Circuit elements RC and RQ.

Circuit models proposed by predominant researchers in the field of equivalent circuit modeling will be presented in figure 2.28, followed by the circuit model chosen to represent the working electrode for this research. Mogensen [28, 29] presents circuit (2.28a) which consists of a series combination $L_1R_1(R_2Q_1)(R_3C_1)$. The inclusion of the inductor is uncommon, but highly logical given the presence of lead wires with a length which is much larger than the thickness of the working electrode. Here the resistor R_1 represents the 'serial resistance', which corresponds to the resistance of the lead wires, electrical connections and electrolyte. Finally, a series combination of the two circuit elements R_2Q_1 and R_3C_1 are included to model the high frequency, depressed semi-circle and the low frequency ideal semi-circle, respectively.

Equivalent circuit model (2.28b), proposed by Fleig, [30-33] is mathematically equivalent to circuit (2.28a) with the exception of the inductor. Circuit model (2.28c), also proposed by the same research group, provides two RQ circuit elements for the case where both semi-circles show depressed characteristics. Although both circuits (2.28b) and (2.28c) are mathematically similar to circuit (2.28a), during experimental data fitting they provide similar fitting agreement, circuits (2.28b) and (2.28c) provide distinction between the two R elements of the RC and/or RQ elements. This becomes especially important when modeling electrochemical impedance spectra for mixed fuel systems, as will be discussed in subsequent chapters.

The circuit model chosen to model the experimental data presented herein is shown below as circuit (2.28d). This includes an inductor to model high frequency data, a resistor to determine the serial resistance, and two RQ circuit elements to model the high and low frequency, depressed semi-circles observed. This is expected for a working electrode with surface irregularities and high porosity. It is assumed that each of the observed semi-circles in the impedance spectrum is related to a reaction or transport process. The simplicity of this assumption indicates that the current flows through identical sample structures for all frequencies, which may not be the case in the real system. Furthermore, some models presented in the literature include three or even four RC or RQ circuit elements in series. This emphasizes the ongoing debate pertaining to the number of processes occurring on the working electrode. The possibility that a larger number of processes are occurring on the electrode than there are definable, observable semi-circles in the experimental spectrum exists. In this work, since two definable semi-circles are observed in the experimental data, the equivalent circuit (2.28d) was used. Other circuits with three or four serial RQ elements were investigated, but did not provide a fit as optimal as circuit (2.28d), nor would they provide any further chemical insight.

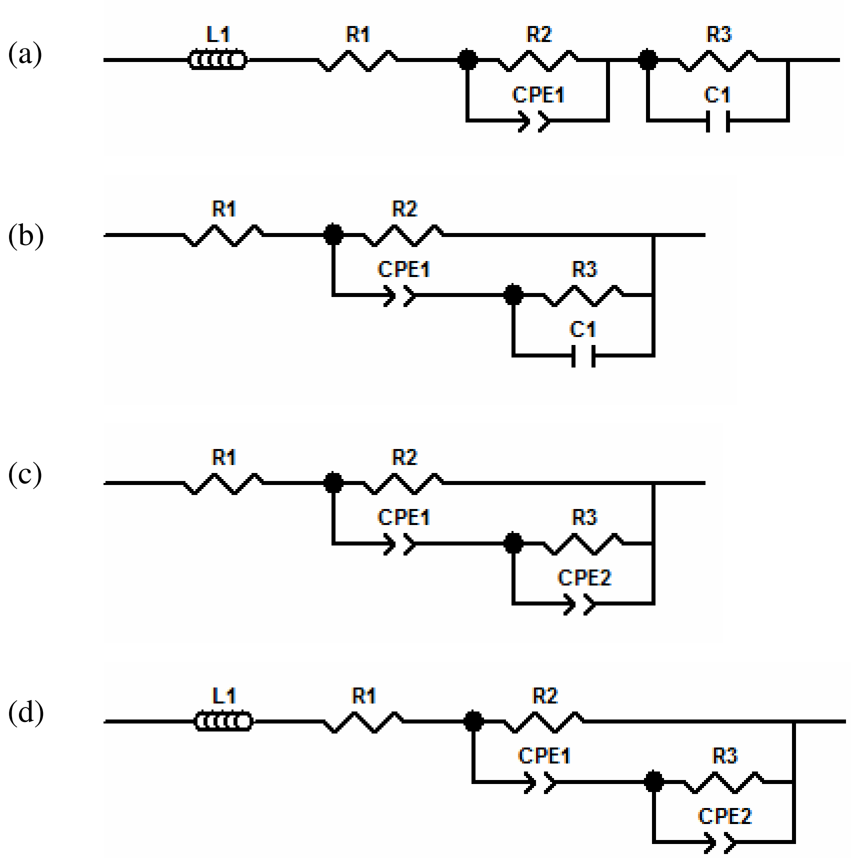

Figure 2.28 Serial equivalent circuit models proposed by Mogensen (a), and Fleig (b), (c). Equivalent circuit model proposed for fitting to experimental data for this research work (d).

2.8 Electrochemical Measurements - General

All electrochemical measurements were performed using a VoltaLab ® PGZ 301 Dynamic EIS Voltammetry instrument. The button cell, supported by an alumina tube, was positioned in a Faraday cage made from a grounded alumel wire wrapped around a quartz tube. The shielded cell was then placed into a tube furnace. The liquid fuel flow rate was controlled using a Shimadzu liquid chromatograph pump (LC-9A) and the gaseous fuel flow rates were regulated with Mass Flow Controllers purchased from MKS.

The temperature of the furnace was controlled using a Barber Colman temperature controller. An overview of the fuel cell set-up is shown in figure 2.29.

Succeeding softening the pyrex ring and ramping to the operating temperature, the following electrochemical measurement program was collected. OCV was measured for 1 hour during the reduction to the anode alloy metal: $Ni_xCo_{(1-x)}$. A minimum of 1.0 V value for the OCV was required to proceed with electrochemical testing. If a lower, non-zero value was achieved, the temperature was ramped back to 900^oC for 15-20 additional minutes before returning to the operation temperature to further soften the Pyrex ring in order to seal any small gaps between the Pyrex ring and button cell. The cell was then polarized with an anodic overpotential of 400 mV for 15 hours during which time the metal reduction was completed and the anode was allowed to stabilize. A 2 hour cycle of open circuit voltage measurement (OCV), electrochemical impedance spectroscopy (EIS), voltammetry (CV), and chronoamperometry (CA) was repeated 7 times (over a total of 14 hours) to ensure the measurements used for reporting were stable and to observe any changes which occurred within the initial introduction of a new fuel.

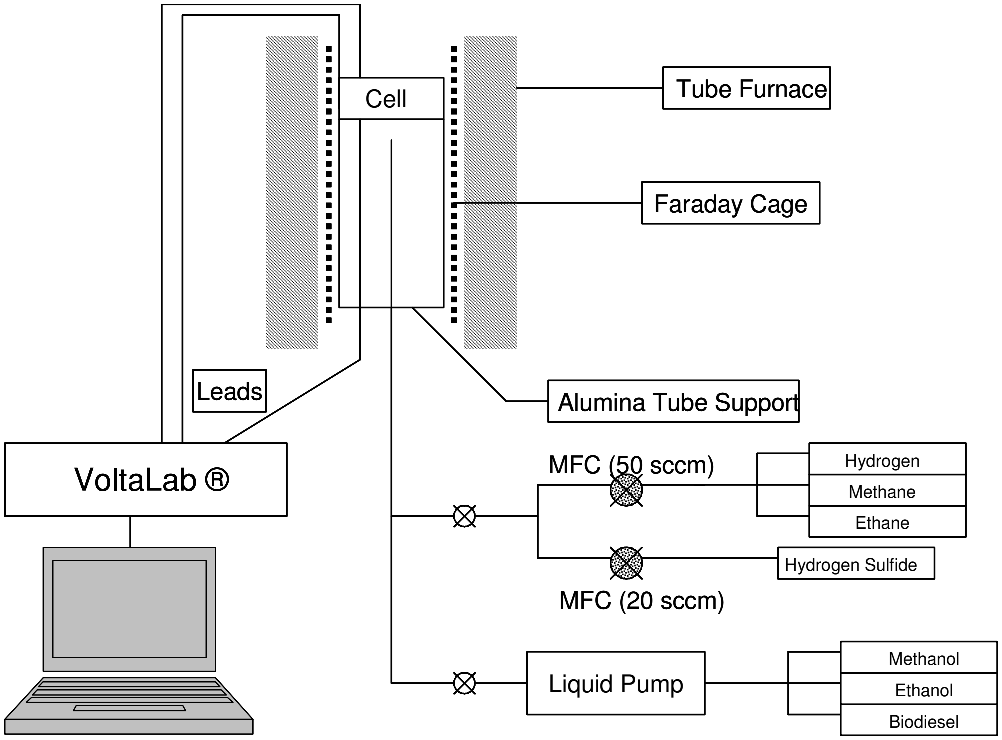

Figure 2.29 Schematic overview of the entire fuel cell set-up.

For OCV measurements, with the exception of the initial measurement for 1 hour during anode reduction, all following measurements were observed for 10 min, during which time the measurement reached a stabilized value. These values are plotted in simple time-voltage graphs herein.

For EIS measurements, 6 spectra were taken at different overpotentials from OCV in 50 mV steps over the frequency range 100 kHz to 250 mHz with an AC amplitude of 10 mV. The equivalent circuit used to fit impedance data was: $L_1R_1[R_2CPE_1[R_3CPE_2]]$ as discussed above. The equation used to obtain the exchange current density (i_o) values from the charge transfer resistance (R_{CT}, also represented as R_3 in the proposed equivalent circuit) values is the following as derived from the low-field approximation of the Butler-Volmer equation: $I_O = RT/nFR_{CT}$. This raw impedance data is most often represented as a Nyquist or Cole-Cole plot where the real and imaginary components are plotted against each other. The less common representation, in contemporary literature, of this data is a plot of the real component (■) or the phase angle (■) in degrees against the logarithm of the frequency, known as a Bode plot.

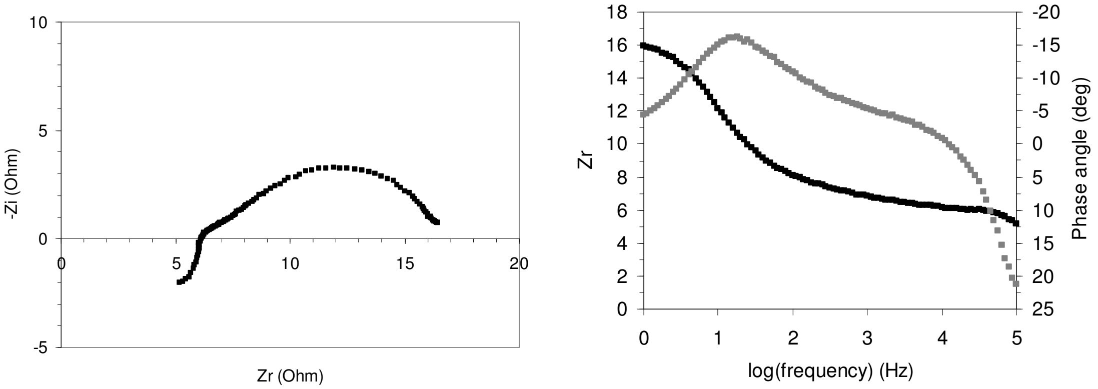

Figure 2.30 Sample Nyquist (left) and Bode (right) plots for Ni$_{0.7}$Co$_{0.3}$-YSZ anode. For the case of the Bode plot, the real component data (■) and the phase angle data (■) are shown on the same graph.

Voltammetry measurements were obtained from 200 mV to 1100 mV of anodic overpotential at a scan rate of 2 mV/s. This range is large in order to ensure that the region of interest was collected. This is because the OCV value can fluctuate by as much as 250 mV between button cells, which is used to correct the raw output voltages to overpotential values. Exchange current density values from this DC data were then obtained from the Tafel plot. This was accomplished by plotting the natural logarithm of the current versus overpotential and extracting the data to obtain the y-axis intercept.

Chronoamperometry measurements were taken from -60 mV to 940 mV of anodic overpotential in 50 mV increments (for a total of 21 measurements) while measuring the current for 140 sec at each potential to allow a stable value to be reached for reporting and calculations. This data was used to obtain power (performance) data where the relation P=IV was used to calculate the power in Watts. This data is represented in plots with horizontal axis for current density, primary vertical axis as voltage, and secondary vertical axis as power. If the stability of the power output of the cell was of concern over a certain period of time, the maximum value of the downward parabolic plot was extracted from each graph and plotted as a function of time.

2.9 References

[1] C.M. Grgicak, R.G. Green, J.B. Giorgi, J. Mater. Chem. 16 (2006) 885.
[2] M. Guillodo, P. Vernoux, J. Fouleier, Solid State Ionics 127 (2000) 99.
[3] M. Brown, S. Primdahl, M. Mogensen, J. Electrochem. Soc. 147 (2000) 475.
[4] S.C. Singhal, K. Kendall, High temperature solid oxide fuel cells, Elsevier Ltd., New York, 2003.
[5] N.Q. Minh, T. Takahashi, Science and Technology of Ceramic Fuel Cells, Elsevier, New York, 1995.
[6] E. Baur, H. Preis, Elektrochem. 43 (1937) 727.
[7] C.M. Grgicak, Anodes for solid oxide fuel cell (SOFC) systems operating in multiple fuel environments: Effects of microstructure and composition, University of Ottawa, Ottawa, 2007.
[8] N.Q. Mihn, J. Am. Ceram. Soc. 76 (1993) 563.
[9] M. Nagata, Y. Itoh, H. Iwahara, Solid State Ionics 67 (1994) 215.
[10] S. McIntosh, J. Vohs, R. Gorte, J. Electrochem. Soc. 150 (2003) A1305.
[11] V.V. Krishnan, S. McIntosh, R.J. Gorte, J.M. Vohn, Solid State Ionics 166 (2004) 191.
[12] S. Chan, X. Chen, K. Kohr, J. App. Electrochem. 31 (2001) 1163.
[13] H.-T. Chen, Y.-M. Choi, M. Liu, M.C. Lin, J. Phys. Chem. C 111 (2007) 11117.
[14] J. Winkler, P. Hendriksen, N. Bonanos, M. Mogensen, J. Electrochem. Soc. 145 (1998) 1184.
[15] S. Jiang, J. App. Electrochem. 31 (2004) 1163.
[16] R. Jenkins, R.L. Snyder, Introduction to X-ray Powder Diffractometry, John Wiley & Sons, Inc., New York, 1996.
[17] C. Hammond, The Basics of Crystallography and Diffraction, Third Edition, Oxford University Press, New York, 2009.
[18] G. Williamson, W. Hall, Acta Metall. 1 (1953) 22.
[19] M.D. Inc, MDI Jade 6.1, Material Data Inc., 2002.
[20] R.A. Young, The Reitveld Method, Oxford University Press, New York, 1993.
[21] S.J. Gregg, K.S.W. Sing, Adsorption, Surface Area and Porosity, Academic Press, New York, 1982.
[22] S. Brunawer, L.S. Deming, W.S. Deming, E. Teller, J. Am. Chem. Soc. 62 (1940) 1723.
[23] S. Brunawer, P. Emmett, E. Teller, J. Am. Chem. Soc. 60 (1938) 309.
[24] T. Erdey-Gruz, M.Z. Volmer, J. Phys. Chem. A 150 (1930) 203.
[25] J. Butler, Trans. Faraday Soc. 19 (1923) 729.
[26] J. Butler, Trans. Faraday Soc. 28 (1932) 379.
[27] J.O.M. Bockris, A.K.N. Reddy, M. Gamboa-Aldeco, Volume 2A Modern Electrochemistry, Second Edition, Fundamentals of Electrodics., Kluwer Academic/Plenum Publishers, New York, 2000.
[28] R. Barfod, M. Mogensen, T. Klemenso, A. Hagen, Y.-L. Liu, P.V. Hendriksen, J. Electrochem. Soc. 154 (2007) B371.

[29] S.H. Jensen, A. Hauch, P.V. Hendriksen, M. Mogensen, N. Bonanos, T. Jacobsen, J. Electrochem. Soc. 154 (2007) B1325.

[30] F.S. Baumann, J. Fleig, G. Cristiani, B. Stuhlhofer, H.-U. Habermeier, J. Maier, J. Electrochem. Soc. 154 (2007) B931.

[31] J. Fleig, P. Pham, P. Sztulzaft, J. Maier, Solid State Ionics 113-115 (1998) 739.

[32] J. Fleig, J. Maier, J. Electrochem. Soc. 144 (1997) L302.

[33] J. Fleig, J. Electroceram. 16 (2004) 637.

3

$Ni_xCo_{(1-x)}O$-YSZ Cermet Anodes Prepared Chemically – Synthesis and Materials Characterization

3.1 Introduction

The materials properties of the anode of solid oxide fuel cells[1] are of particular interest since it is this electrode, which is exposed to the various fuels, which will be presented herein, that produce usable current. Of these, it is the microstructure of the anode material which affects the triple phase boundary (TPB), as introduced in the previous chapter. The size of the triple phase boundary (measured as a length or area, a point which is under debate in the literature – the reason for this will be discussed in detail during mechanistic descriptions in subsequent chapters), has a direct effect on the activation polarization of the anode. Activation polarization can be minimized by concomitant minimization of the cermet anode particle size, thus increasing the TPB. Gas diffusion through the pore channels as well as surface transport of physisorbed ions can be affected by poor microstructure.

The need to optimize anode microstructure is not restricted to minimizing activation polarization, but also maximizing electrochemical reaction rates. The length of the TPB has been shown to be directly related to the reaction rate for hydrogen oxidation. [2-4] The optimization of the TPB can be achieved by tailoring the YSZ, pore and metal ratios. Thus this puzzle can be approached mathematically by employing the Bruggeman equation, shown below. [5]

$$\kappa = \kappa_C (1 - f)^{3/2} \qquad (3.1)$$

Here, κ is the conductivity of the cermet material, κ_C is the bulk conductivity of the metallic phase, and f is the fraction of pore space in the material. The power output of the fuel cell will increase as the pore space in the material is decreased; however, an adequate amount of gaseous fuel must reach the TPB, thus the compromise in this relation describes an optimum ratio.

By design, the cermet anode has two materials designed with electronic and ionic conduction pathways for the Ni component and YSZ component, respectively. Ni provides the primary pathway for conduction through the anode material, with a considerably higher conductivity than YSZ at typical operating temperatures (600-1000^{o}C). For this reason, a continuous pathway for electronic conduction is required through the anode cermet. The ratio of metallic and oxide components must be designed with care to produce a cermet material with the desired electronic conductivity. By experiment, the transition between a cermet material which is ionically conductive and one which is electronically conductive occurs between a Ni content of 30 – 40 v/v %.[6-8]

It should be noted, however, that the ratio of the metallic component in the cermet is not the only factor to be considered; the microstructure, as discussed above, can affect the overall conductivity of the material, thus justifying the range of optimal Ni content given. The size ratio, given by $\frac{d_{YSZ}}{d_{MO}}$, where d is the particle diameter for YSZ and metal oxide (MO) particles, can affect the electrical conductivity. As can be deduced, the electrical conductivity increases as the surface area of the YSZ component decreases. The smaller the Ni particle size, the larger the conductivity derived from the ability of the Ni particles to contact with one another.

Experimental findings to support the importance of the function of porosity during fuel transport in Ni-YSZ anodes have been published, which relates back to the Bruggeman equation. [9, 10] In addition to these studies, a microstructure composed of small particles has been shown to produce a small charge transfer resistance. [3, 4] This is further corroborated by research that shows that a cermet electrode with a small $\frac{d_{YSZ}}{d_{MO}}$ ratio will show a small resistance due to a large TPB. [11]

To synthesize the precursor to the metal cermet anode material, a co-precipitation method was employed, which was developed previously. [12] A common method of obtaining mixed metal oxides is by mixing the precursor components mechanically, or employing a porous oxide matrix where the metal salts can be impregnated. [10] [13] Although these two methods can generate an electrode with a very precisely known chemical composition, separation of metal oxide and YSZ phases, or inhomogeneous mixing can cause large phase separations in the resulting cermet material.

The co-precipitation method allows for mixing of the two phases on a very small scale, allowing for great phase mixing; however, depending on the precipitating agent employed, the composition of the final material can differ from that which was desired. By producing a precursor with the highest possible phase mixing of the metal and oxide components, a uniform particle size distribution is expected along with a uniform metal distribution throughout the material.

Of the three precipitation agent compositions investigated, namely NH_3, NH_3 + NaOH, and NaOH, the latter was found to produce the most reliable material compositions, with all of the desired metal ions precipitating out of solution as $Ni(OH)_2$. [14] [12] However, the particle size distribution of the resulting material was large, with particles observed to range from the nanometer to the micrometer scale. Precipitation with NH_3 was found to be unreliable material compositions due to the incomplete precipitation of Ni upon nickel-ammonia complex formation, hence the aforementioned choice of NaOH as the precipitation agent.

During fabrication of the button cell from the synthesized anode material, a very high temperature (1380^{o}C) is used to co-sinter the anode and electrolyte components. This is done to ensure good physical and electrical contact between these two layers. The metallic and oxide components have thermal expansion coefficients which differ enough to cause cracking and warping of the electrolyte layer of the button cell upon co-sintering. Mixing of the metal and electrolyte oxide phases, in addition to greatly increasing the TPB, lowers the thermal expansion coefficient of the anode phase, allowing for greater physical contact of the resulting sintered cell. This effect then produces a button cell with greater electrical conductivity, which lowers the polarization losses at the anode. [15]

Upon co-precipitation, the anode cermet precursors are in the form of the metal oxide mixed with the YSZ phase, for example NiO-YSZ. The active anode cermet used in electrochemical measurements is in the form of the reduced metal oxide, which has the form Ni-YSZ, where this reduction occurs near or at the operating temperature under a reducing atmosphere, usually hydrogen, a short time before electrochemical measurements. The development of a reliable, optimized, reproducible method for the synthesis of the anode material is essential, due to the strong relationship between cermet microstructure and electrochemical performance. This relationship will be examined throughout this thesis.

Traditionally, anode cermets composed of a metallic phase of Ni particles is used, since this metal has been found to have high electrochemical activity with traditional SOFC gaseous fuels. However, Ni is prone to coke formation and sulfur poisoning when exposed to carbon-containing fuels or fuels with small amounts of sulfur, as can be observed by the formation of carbon particles and rods on the surface of Ni particles during fuel cell operation for the case of carbon poisoning, or lowered electrochemical activity for the case of sulfur poisoning. [16]

A secondary metal, which has higher resistance to coke and sulfur poisoning, can provide a synergistic effect. Upon formation of an alloy, the resulting metallic phase can act as part of an anode cermet, which shows greater poison resistance and maintains a strong electrochemical activity. Cobalt is an optimal choice to accomplish this goal. [17] With an identical crystal phase as Ni and very similar melting point, it is an ideal candidate to form an alloy with Ni upon co-sintering. Cobalt possesses a greater resistance to sulfur and carbon poisoning, with a lower tendency towards bond formation with sulfur and carbon compared to pure Ni metal.

Employing NaOH as precipitation agent, a series of $Ni_xCo_{(1-x)}O$-YSZ is synthesized for use as anode cermet electrodes. This material is characterized by several methods, namely surface area determination, X-ray diffraction and scanning electron microscopy, for the purpose of comparing microstructure with electrochemical activity.

3.2 Experimental

3.2.1 Anode Cermet Material Synthesis

The synthesis of the anode cermet materials is outlined in the previous chapter in detail. Appropriate amounts of the metal chlorides, $NiCl_2*6H_2O$, $CoCl_2*6H_2O$, Y_2O_3 and of $ZrCl_4$, were co-precipitated using NaOH to form cermet materials of the form $Ni_xCo_{(1-x)}O$-YSZ, where x ranges from 1 to 0.7 in increments of 0.05 units. Upon completion of the synthesis of each material in the series, a portion of each sample was sintered at 1380°C for 4 hours with ramp rates of 10°C/min for materials analysis, as will be described below.

3.2.2 Materials Characterization

The total surface area of some green cermet powders and of all sintered powders was collected and found by employing the BET method with N_2 as the vector gas. Chemisorption experiments to determine the active metal surface area were conducted with H_2 as the vector gas. Both surface area experimental methods were performed on an

Autosorb-1C (Quantachrome Corporation), employing the equations, instrument parameters and assumptions outlined in the previous chapter.

The particle size, shape and morphology was determined using the Scanning Electron Microscope (SEM) from JEOL Model JSM-7500F SEM. Particle composition was determined by X-ray dispersive spectroscopy (EDS) using the detector EDS X-Sight. All powder samples were held to an aluminium sample stage with carbon tape. All equations, instrument parameters and assumptions used for this set of analyses are outlined in the previous chapter.

Crystallite size and powder composition were determined by X-ray diffraction (XRD) with the Phillips PW1830 model with a CuKα radiation source with a wavelength of 1.54 Å. All equations, instrument parameters and assumptions used for this set of analyses are outlined in the previous chapter. A variable temperature XRD attachment (Anton Parr) was used to investigate the crystallization of the powders.

3.3 Results and Discussion – Materials Characterization

3.3.1 Determination of Surface Area for the $Ni_xCo_{(1-x)}O$-YSZ Cermet Series

Surface area measurements of samples as synthesized and after sintering are determined using N_2 as the adsorbent gas. The un-calcined (green) samples possess surface areas of 196.9 and 156.5 m^2/g obtained for NiO-YSZ and $Ni_{(0.70)}Co_{(0.30)}O$-YSZ, respectively. The justification for choosing these two samples, as well as only determining the surface area for two of the seven powders synthesized, is that the powders will not be used in this form in the fuel cell. However a range of surface areas for the "as synthesized" powders provides a complete characterization as well as a good comparison point for the more relevant sintered materials. An interesting point of research for a future project could be to maintain a higher surface area and thus potentially further improve the performance of the fuel cell.

Upon sintering of the series of NiCoO-YSZ powders described in section 3.2.1, their surface areas decreased roughly by two orders of magnitude and are presented in

Table 3.1. These surface areas are lower than expected for a highly active heterogeneous catalyst. This is likely due to the high amount of coarsening expected and observed for Ni particles upon heating to the indicated sintering temperature. An increase in the metal loading from traditional heterogeneous catalysts causes an increase in the particle size. The shrinkage upon sintering of the NiO-YSZ cermet has also been previously characterized, and this material was found to lose approximately 20 % of its original size. [18] The mixing of YSZ with NiO has also been shown to reduce the amount of coarsening experienced by the metallic phase, which will allow for a higher resulting surface area. [19] The values given in table 3.1 for the surface area of the sintered anode powders are considered to be very similar to each other. Since each measurement was only recorded once, a systematic calculation of the error for these values was not possible.

Table 3.1 External surface area (SA) of sintered $Ni_xCo_{(1-x)}O$-YSZ cermet powder series. The correlation (R^2) for each data point is shown. The second half of the sample name (O-YSZ) has been omitted for clarity.

Sample	**External SA (m^2/g)**	**Correlation (R^2)**
Ni(1.0)Co(0)	0.58	0.994
Ni(0.95)Co(0.05)	0.85	0.989
Ni(0.90)Co(0.10)	0.59	0.997
Ni(0.85)Co(0.15)	0.53	0.997
Ni(0.80)Co(0.20)	0.58	0.980
Ni(0.75)Co(0.25)	0.55	0.983
Ni(0.70)Co(0.30)	0.64	0.988

The values presented in table 3.1 show significant coarsening of the anode cermet powder upon sintering compared to the green, “as-synthesized” powder, by approximately two orders of magnitude. As mentioned above, since nickel is prone to significant coarsening upon heating to the sintering temperature, 1380°C, and the material is composed of a significant portion of nickel, this is an expected result. However, it is desirable to obtain a high surface area catalyst since the expected catalysis, the oxidation of the gaseous fuel at the TPB, would expect to produce a cell with higher performance with a higher surface area. These values are highly comparable to those obtained previously in this laboratory. [18, 20] Since the NiCo alloyed anodes are unique to this research, there are no other references with which to compare it directly. Similar cermet powder for testing with respect to the catalytic steam reforming of ethanol, with a $Ni_{(1-x)}Co_x$-YSZ composition (x = 0, 0.32 and 0.5), were synthesized by Resini *et al.* [21] with a metallic component of 50 % w/w, however a surface area was not reported. Despite this fact, the surface area of the sintered material is within the expected range.

A common method to increase the surface area, among others, is to decrease the sintering temperature. In the first case, a decrease in the sintering temperature would reduce the amount of coarsening experienced by the metallic phase, thus resulting in a material with a surface area closer to that of the green anode powder. However, the reasoning for employing a high sintering temperature is to ensure good grain-grain and grain-electrolyte contact. A reduction in these contacts would result in a less robust anode with higher grain boundary resistances due to current constriction at these locations.

3.3.2 Characterization of the Cermet Material by Powder X-Ray Diffraction

Cermet powders of the composition $Ni_xCo_{(1-x)}O$-YSZ (x = 1.0 to 0.7) were tested directly after synthesis, having never been exposed to temperatures above 120^oC for drying, figure 3.1. The lack of crystallinity is evident for the two NiCoO-YSZ cermet powders shown, with short, broad peaks and a low signal-to-noise ratio. The NiO-YSZ cermet powder shows slightly more crystallinity, with marginally sharper peaks, but it still possesses a low signal-to-noise ratio. These materials, as can be seen, do not have large crystals; however, crystal formation is expected upon sintering.

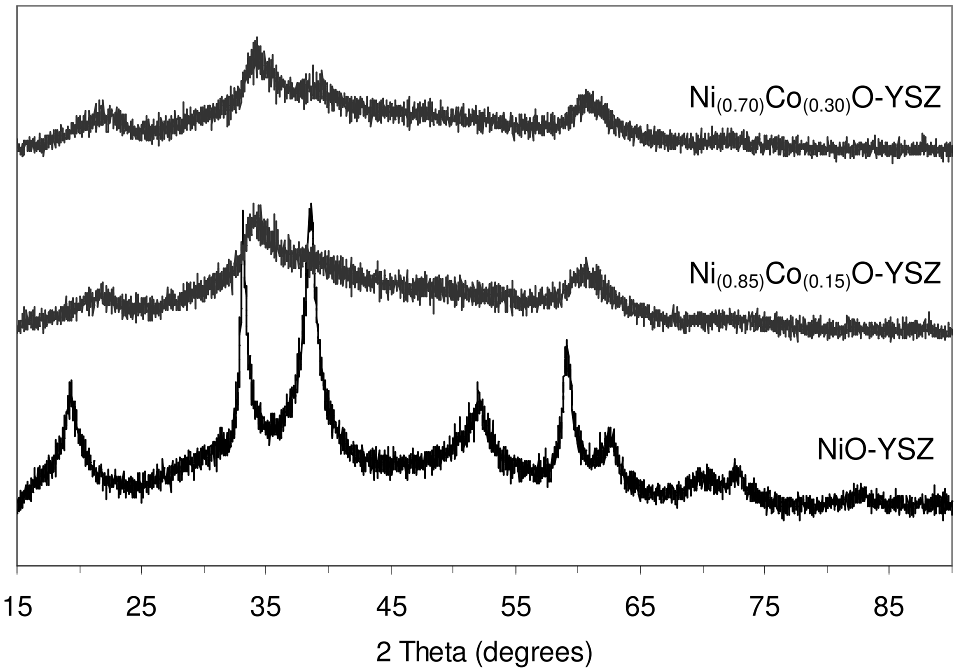

Figure 3.1 Powder X-ray diffraction data for powders “as synthesized” before sintering.

During fuel cell operation, the cermet powders utilized have been sintered at 1380°C for 4 hours with ramp rates of 2°C/min from and back to room temperature. Powder X-ray diffraction patterns of aliquots of the series of $Ni_xCo_{(1-x)}O$-YSZ synthesized and sintered are shown below, Figure 3.2. The crystallinity of the material has increased dramatically from its “as synthesized” counterpart, with markedly sharper peaks and a much larger signal-to-noise ratio. The PDF identification numbers for the three phases found in the cermet powder are the following: for $Y_{0.08}Zr_{0.92}O_{1.93}$ is #48.0224, for NiO is #47.1049, and for Ni is #04.0850, given by the *Jade 6.1* program. Both the NiO and YSZ crystalline phases are major components of the cermet powder. A very minor Ni component can be observed, which decreases in intensity as the Co concentration increases. A small shift of the peaks belonging to the NiO crystalline phase with increasing concentration of Co is observed; though is not clearly visible in the figure, as it is too small a change in the value of 2 theta.

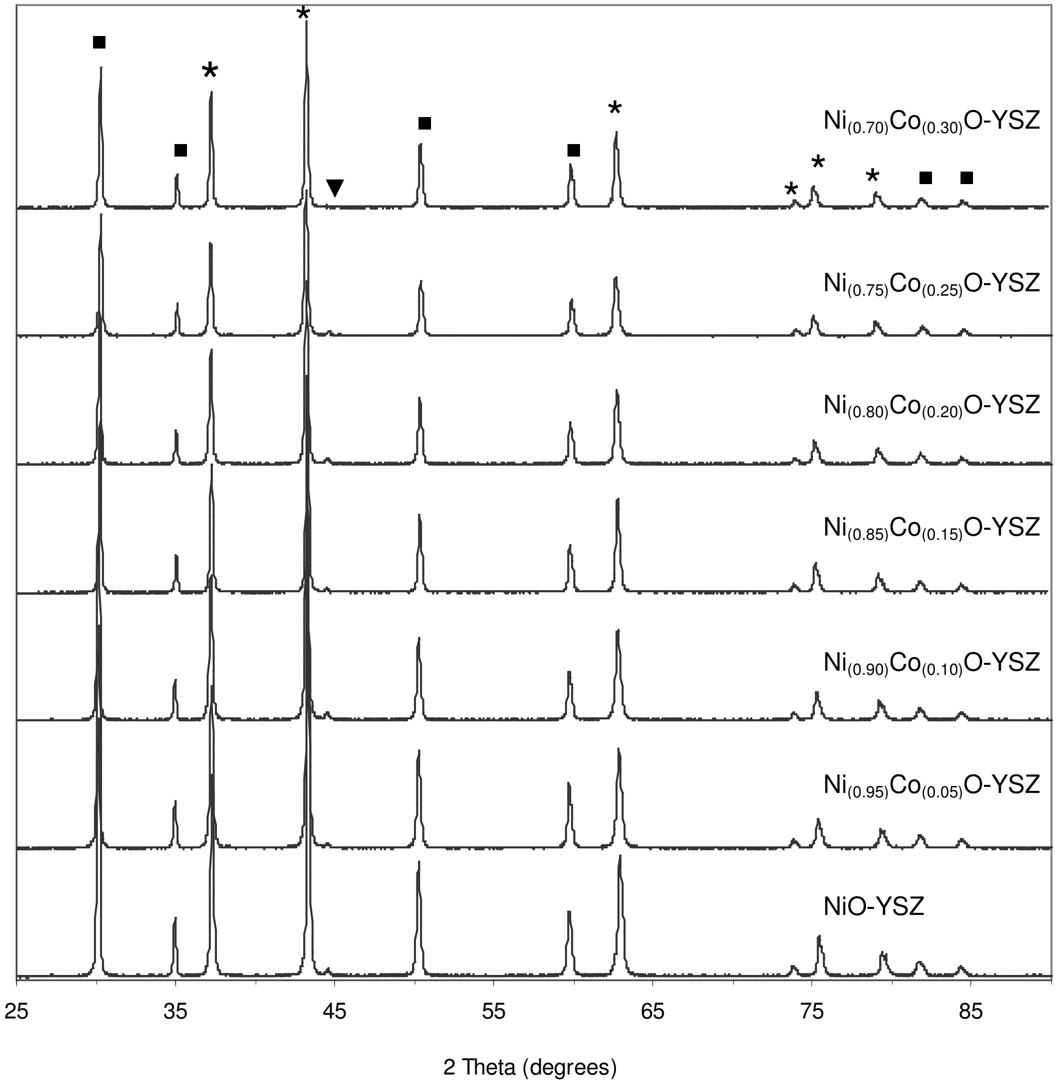

Figure 3.2 Powder X-ray diffraction data for the series of $Ni_xCo_{(1-x)}O$-YSZ cermet powders after sintering to 1380°C for 4 h; (■) YSZ (a major phase), (*) NiO (a major phase), (▼) Ni (a minor phase).

Numerical data found from *Jade 6.1* fitting program fit using the psudo-Voight function presented in the previous chapter is given in table 3.2. Employing a cubic lattice, fitting parameters produced an average lattice value of 5.119 Å for the YSZ phase over the group of samples synthesized by the co-precipitation method. As the amount of Co alloyed into the Ni phase was increased, the lattice parameter increased with a visible trend, as is expected, presented in figure 3.3. Initially, a linear trend of increasing unit cell parameter, *a*, with increasing Co concentration is observed up to a Co concentration of 20 w/w %. Beyond this concentration, a deviation from ideal linearity is observed. No separate cobalt oxide phase was observed, since saturation of the Co within the Ni phase was not surpassed; however, the deviation from ideal linearity suggests a plateau would be observed at higher concentrations, as was previously reported. [20] The ease of solubility of the Co within the Ni lattice is attributed to their similar ionic radii, with values of 0.69 and 0.74 Å for Ni and Co, respectively. [22] The observed trend of increasing unit cell parameter with increasing concentration of Co is that which is expected with this substitution of an atom with a slightly larger ionic radius. No discernable trend in particle size was observed, nor was one expected. The average particle size for the NiO and YSZ phases is 1070 and 1420 Å, respectively. This is in agreement with SEM results, which will be presented below. The large particle size, though undesirable from a catalytic perspective, as the catalytic activity is known to decrease with increasing particle size, is expected for a cermet powder with a relatively large nickel concentration (55 % w/w for the metalic oxide phase).

Table 3.2 Numerical data derived from powder X-ray diffraction analysis for the series of Ni$_x$Co$_{(1-x)}$O-YSZ cermet powders. The second half of the sample name (O-YSZ) has been omitted for clarity. Errors for specific measurements are given in brackets.

Sample	Phase	Particle Size, Å	Strain, %	ESD of fit, deg	R^2	*a*=*b*=*c*,	Density, g/cc	ESD of fit, deg
Ni	YSZ	848(63)	0.085(0.08)	0.00062	0.815	5.1257(0.003)	6.812	0.044
	NiO	1221(174)	0.080(0.01)	0.00038	0.688	4.1761(0.0005)	6.004	0.139
Ni(0.95)Co(0.05)	YSZ	1240(283)	0.092(0.01)	0.00063	0.717	5.1286(0.001)	5.999	0.089
	NiO	798(66)	0.060(0.01)	0.00049	0.508	4.1803(0.0003)	6.791	0.032
Ni(0.90)Co(0.10)	YSZ	3111(2124)	0.136(0.02)	0.0004	0.943	5.1286(0.001)	5.995	0.056
	NiO	1111(118)	0.080(0.007)	0.00032	0.776	4.1852(0.0004)	6.767	0.021
Ni(0.85)Co(0.15)	YSZ	2031(928)	0.098(0.01)	0.00058	0.784	5.1030(0.002)	6.085	0.18
	NiO	990(127)	0.050(0.01)	0.00049	0.834	4.1896(0.0004)	6.857	0.166
Ni(0.80)Co(0.20)	YSZ	975(81)	0.085(0.007)	0.00035	0.908	5.1272(0.001)	5.999	0.041
	NiO	737(245)	0.057(0.03)	0.00031	0.751	4.1935(0.0004)	6.751	0.057
Ni(0.75)Co(0.25)	YSZ	1041(135)	0.079(0.01)	0.00041	0.835	5.1085(0.006)	6.065	0.161
	NiO	1425(211)	0.080(0.009)	0.00016	0.875	4.1967(0.0005)	6.858	0.108
Ni(0.70)Co(0.30)	YSZ	688(48)	0.028(0.01)	0.00034	0.508	5.1087(0.005)	6.064	0.171
	NiO	1235(145)	0.064(0.009)	0.00016	0.815	4.1984(0.0005)	6.852	0.144

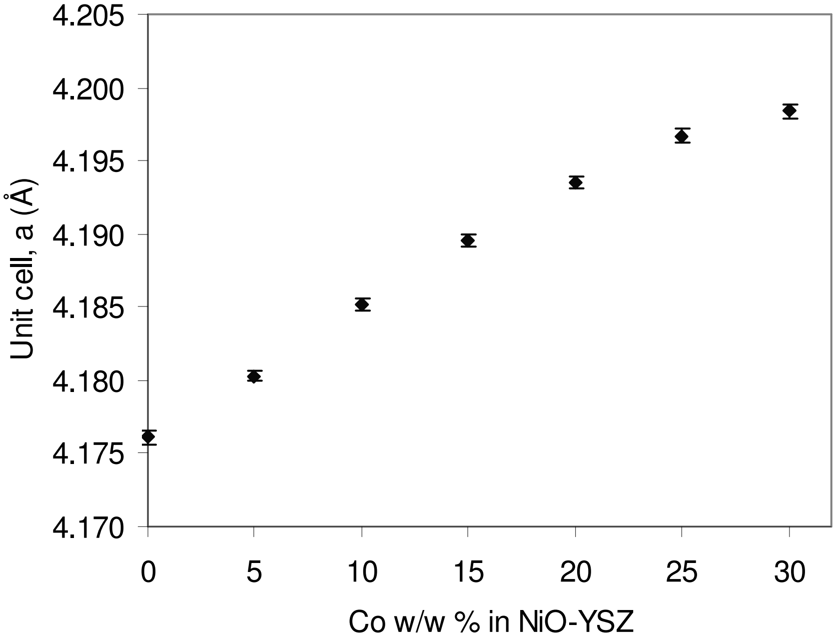

Figure 3.3 Unit cell parameters of the NiO phase in the $Ni_xCo_{(1-x)}O$-YSZ samples synthesized over the Co concentration shown.

3.3.3 Characterization of Cermet Material by Scanning Electron Microscopy and Energy Dispersive X-Ray Spectroscopy

Following sintering of an aliquot of the synthesized powders, as described in the experimental section above, SEM micrographs were collected. All the co-precipitated cermet powders in the series $Ni_xCo_{(1-x)}O$-YSZ showed the same physical characteristics, therefore, the $Ni_{0.85}Co_{0.15}O$-YSZ cermet, the intermediate Co concentration, will be presented. At low magnification, shown in figure 3.4a, there are two particle size ranges, one of very small size (too small to accurately determine at this magnification) and one of larger size, of the range of approximately 20 to 100 micrometres. At higher magnification, figures 3.4 c and d, the large particle shown has a size of several tens of micrometres, whereas the small particles have sizes of less than to a few micrometres. In comparison with the average particle size found by pXRD, these particles are much larger than expected. The most likely reason for this is that the large particles visualized here, are composed of an agglomeration of smaller crystallites. At still higher magnification, figure 3.4b, the high degree of crystallinity of the particles can be observed, which agrees well with the crystallinity found by pXRD. There also appears to be two types of particles in this picture: crystalline and amorphous. An investigation using EDS can show the difference in chemical composition of these two particle types.

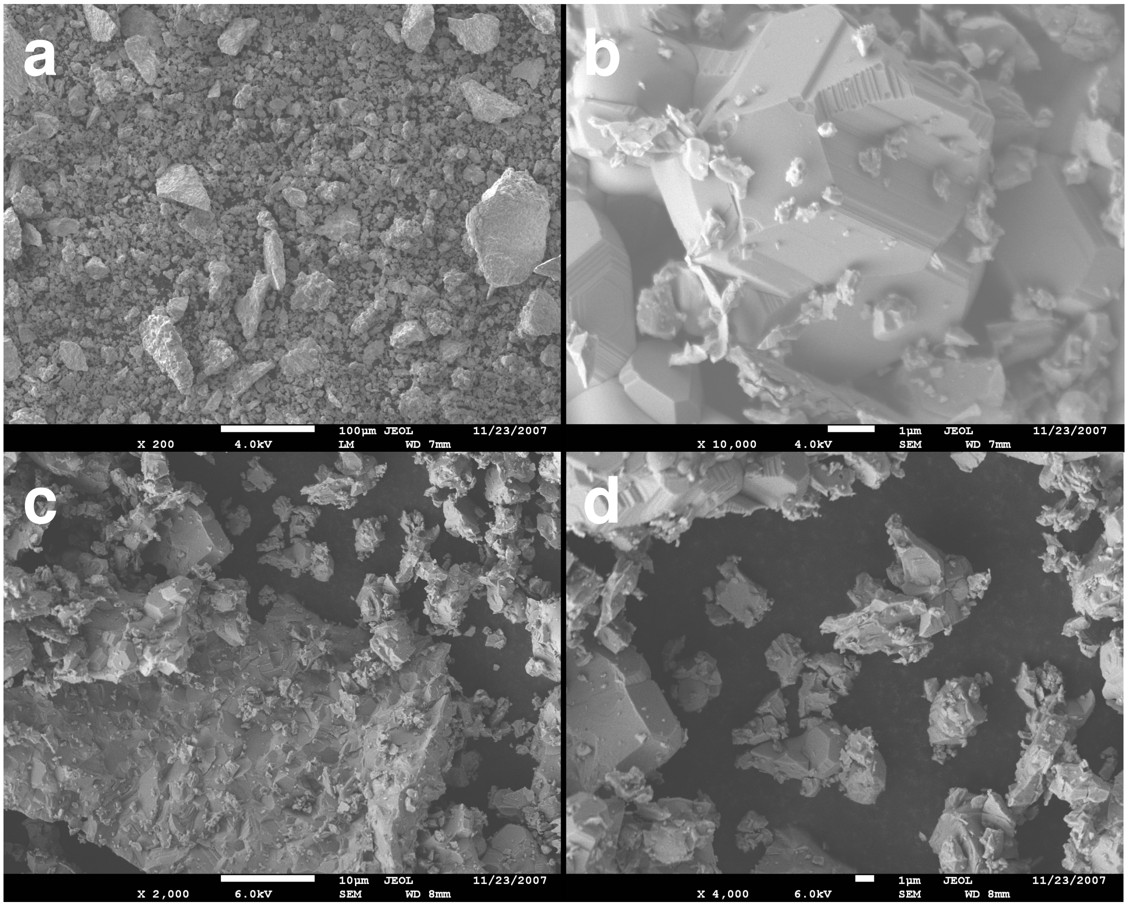

Figure 3.4 SEM micrographs of the $Ni_{0.85}Co_{0.15}O$-YSZ cermet powder after sintering. (a) shows two particle size ranges, mag 200 x, bar 100 µm; (b) shows high crystallinity, mag 10 000 x, bar 1 µm; (c) shows a large particle, mag 2000 x, bar 10 µm; (d) shows small particles, mag 4000 x, bar 1 µm.

EDS spectra of the two particle types are presented in figure 3.5. The SEM pictures corresponding to ‘point of interest’ sites show a large amount of charging and are much less sharp than those presented in figure 3.4. This is due to the settings required for EDS, as described in the previous chapter. It should also be noted that a quantitative analysis for a rough surface such as a powder is not possible using this technique. A qualitative and comparative approach is taken when comparing peak heights and percentage analyses performed by the EDS software program, *Inca*. Particles for analysis were chosen with care, where the largest particle showing the desired characteristics was chosen, as well as a particle with a flat surface perpendicular to the beam direction to approximate a smooth, flat surface as closely as possible.

The spectrum of an amorphous particle, shown in figure 3.5a, is for the type of particle that also tends to be much smaller on average. The EDS shows a composition of approximately 2:1 for Ni:Zr, as shown in table 3.3. The Zr peak at 2 keV is also large relative the the Ni peak at 7.5 keV, shown in figure 3.5a. For the case of the spectrum of a highly crystalline particle, shown in figure 3.5b, which is also usually the much larger particle, an enrichment in Ni is observed. The EDS composition is many times higher for Ni compared to Zr, and the corresponding Zr peak has diminished compared to the Ni peak. The high crystallinity and presence of crystal facets of the particle chosen to collect the spectrum shown in figure 3.5b, as is also shown in figure 3.4b suggesting a particle composed of pure nickel. Reasons for the observation of a signal for zirconium are that there may have been some zirconium present on the surface of the nickel particle, or perhaps the dispersion of the point beam collected signal for zirconium from a nearby source. This observation is in agreement both with previous findings, [12] and with the known propensity for Ni to coarsen and form large, crystalline agglomerate particles upon sintering to high temperatures. Although the overall composition of the anode cermet is known, the microscopic composition of individual particles varies; however, the composition is expected to fall near one of two types, as discussed.

Table 3.3 EDS ‘quantitative’ composition of the two types of particles corresponding to the spectra presented in figure 3.5.

Sample	Ni:Zr wt %	Ni:Zr atom %
small, amorphous	23:15	9:4
large, crystalline	53:9	34:4

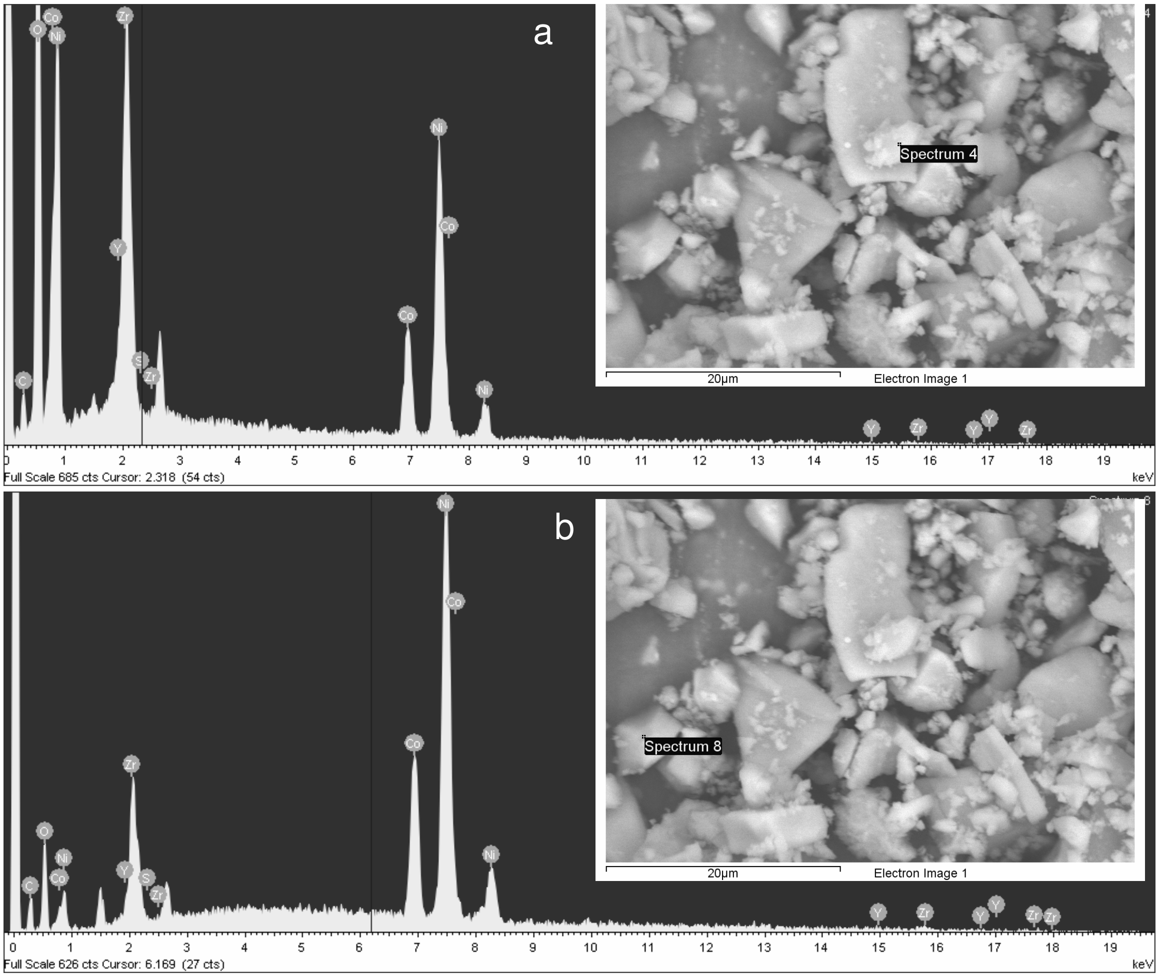

Figrue 3.5 EDS of the two particle types observed in the $Ni_{0.85}Co_{0.15}O$-YSZ sample. (a) shows an amorphous particle, (b) shows a crystalline particle. The measurement bar on both SEM images shows 20 µm.

3.4 Conclusions

A series of cermet powders of composition $Ni_xCo_{(1-x)}O$-YSZ were synthesized for use as anode materials for SOFCs in varying fuel environments, as will be explored in subsequent chapters. The surface area values of the sintered powders, although approximately two orders of magnitude lower than that of the green powders, are within the expected range for a NiO-YSZ cermet. The pXRD spectra of the sintered powders showed increased crystallinity compared to their green counterparts, with predominant phases of NiO and YSZ, as expected. A small nickel phase is observed at low Co concentration. The Co is incorporated into the crystal lattice of the NiO, thus forming a true alloyed material with unit cell parameters, which increase with increasing Co concentration. SEM and EDS spectra indicate two types of particles: small amorphous particles composed predominantly of YSZ, and large crystalline particles composed of nickel. The large nickel particles observed are caused by the known propensity for nickel to coarsen upon heating to the temperature used for sintering the anode material herein.

3.5 References

[1] W. Zhu, S. Deevi, Mater. Sci. Eng. A362 (2003) 228.

[2] J. Mizusaki, H. Tagawa, T. Saito, S. Ehara, T. Takagi, T. Hikita, M. Ippommatsu, S. Nakagawa, K. Hashimoto, J. Electrochem. Soc. 141 (1994) 2129.

[3] C.W. Tanner, K.-Z. Fung, A.V. Virkar, J. Electrochem. Soc. 144 (1997) 21.

[4] M. Brown, S. Primdahl, M. Mogensen, J. Electrochem. Soc. 147 (2000) 475.

[5] D. Bruggeman, Ann. Phys. 24 (1935) 636.

[6] D.W. Dees, T.D. Clark, T.E. Easler, D.C. Fee, F.C. Mrazek, J. Electrochem. Soc. 134 (1987) 2141.

[7] T. Matsushima, H. Ohrui, T. Hirai, Solid State Ionics 111 (1998) 315.

[8] J. Lee, H. Moon, H. Lee, J. Kim, K., K. Yoon, Solid State Ionics 148 (2002) 15.

[9] R. Wilkenhoener, R. Vaben, H. Buchkremer, D. Stover, J. Mater. Sci. 34 (1999) 25.

[10] F. Tiez, F.J. Dias, D. Simwonis, D. Stover, J. Eur. Ceram. Soc. 20 (2000) 1023.

[11] T. Fuki, K. Murata, S. Ohara, H. Abe, M. Haito, K. Nogi, J. Power Sources 125 (2004) 17.

[12] C.M. Grgicak, R.G. Green, W.-F. Du, J.B. Giorgi, J. Am. Ceram. Soc. 88 (2005) 3081.

[13] S. Park, R.J. Gorte, J.M. Vohs, App. Catal. A. 200 (2000) 55.

[14] Y. Li, Y. Zie, J. Gong, Y. Chen, Z. Zhang, Mater. Sci. Eng. B86 (2001) 119.

[15] Y.J. Leng, S.H. Chan, K.A. Kohr, S.P. Jiang, P. Cheang, J. Power Sources 117 (2003) 26.

[16] J. Liu, V. Birss, J. Hill, AIChE J. 56 (2009) 1651.

[17] S.W. Jung, J.M. Vohs, R.J. Gorte, J. Electrochem. Soc. 154 (2007) B1270.

[18] C.M. Grgicak, R.G. Green, J.B. Giorgi, J. Mater. Chem. 16 (2006) 885.

[19] R. Swilkenhoener, R. VaBen, H.P. Buchkremer, D. Stover, J. Mater. Sci. 34 (1999) 257.

[20] C.M. Grgicak, Anodes for solid oxide fuel cell (SOFC) systems operating in multiple fuel environments: Effects of microstructure and composition, University of Ottawa, Ottawa, 2007.

[21] C. Resini, M.C.H. Delgado, S. Presto, L.J. Alemany, P. Riani, R. Marazza, G. Ramis, G. Busca, Int. J. Hydrogen Energy 33 (2008) 3728.

[22] R. Shannon, Acta Crystallogr. 1976 (1976) 751.

4

Electrochemical Characterization of $Ni_xCo_{(1-x)}$-YSZ Cermet Anodes in H_2 fuel

4.1 Introduction

Charge transfer reactions, which are the key fundamental reaction of the electrochemical reaction of fuels at the anode, occur at the triple phase boundary (TPB). The active sites along this TPB are where the oxide electrolyte, reduced metal and fuel-filled pore abut each other; here is where the electrochemical reaction of hydrogen, supplied through the open pore, meets the oxygen dianions, conducted through the oxide phase (equation 4.1).

$$H_{2(gas)} + O^{2-}{}_{(electrolyte)} \rightleftharpoons H_2O_{(gas)} + 2e^{-}{}_{(electrode)} \quad (4.1)$$

This reaction is not concerted; therefore, an understanding of the multi-step mechanism by which it occurs, and by extension, the rate determining step of this mechanism, which occurs on the cermet anode, will lead to a fundamental understanding of its kinetics. This understanding can thus lead to opportunities to optimize the performance of the fuel cell.

The exact multi-step mechanism of electrochemical hydrogen oxidation on the Ni-YSZ cermet anode has not yet been determined with confidence, several reaction mechanisms have been presented, but two mechanisms are popularly presented and corroborated among research groups. Common steps to all mechanisms involve the dissociative adsorption of hydrogen on the surface, diffusion of H_{ad} or H^{+}_{ad} to the TPB, one or more charge transfer reactions, followed by desorption of the water product. Which step constitutes the rate determining step continues to be debated.

One popular mechanism is presented by Mogensen *et al.*[1] derived from mathematical fitting of an equivalent circuit to Electrochemical Impedance Spectra (EIS) data. Three arcs are described and mathematically fitted for the anode, and physical processes were assigned to each of these arcs. The first arc, at high frequency, referred to as process I, is not dependent on the partial pressure of reactant gases, electrode potential or polarization. This resistive arc depends strongly on variations in particle size distribution, and is assigned to the transport of charged species such as H^{+}, O^{2-} and OH^{-} across the Ni-YSZ interface. The second resistive arc, referred to as process II remains unclear, but has been found to be dependent on the partial pressure of reactant gases, which suggests an electron transfer process. The final resistive process III, depends strongly on diffusion, and is a function of the test geometry. It has also been attributed to gas conversion impedance, which requires a stable electrode in an atmosphere separate from the working electrode. The proposed mechanism is shown below, which models the three impedance processes outlined and respects the changes observed in each of these impedance arcs towards reactant partial pressure, temperature, and overpotential. The third step of the mechanism, the formation of an OH^{-} species at the TPB from an adsorbed proton, reaction 4.4, is proposed to be the rate determining step.

$$H_{2(gas)} \rightleftharpoons 2H_{ad,M} \quad (4.2)$$

$$2\times\left(H_{ad,M}\right) \rightleftharpoons 2\times\left(H^{+}_{ad,M} + e^{-}{}_{M}\right) \quad (4.3)$$

$$2\times\left(H^{+}_{ad,M} + O^{2-}_{YSZ}\right) \rightleftharpoons 2\times\left(OH^{-}_{YSZ}\right) \quad (4.4)$$

$$2OH^{-}_{YSZ} \rightleftharpoons H_2O_{(gas)} + O^{2-}_{YSZ} \quad (4.5)$$

Holtappels *et al.*[2] propose a different mechanism found from EIS where the second step, the formation of an OH$^-$ species at the TPB from an adsorbed hydrogen radical, reaction 4.7, is the rate determining step. This mechanism occurs via a series of charge transfer reactions, and water formation occurs through hydroxide intermediates. It has also been suggested by experimental EIS at open circuit voltage that more than one reaction mechanism may be occurring in parallel at different rates. [3]

$$H_{2(gas)} \rightleftharpoons 2H_{ad,M} \quad (4.6)$$

$$H_{ad,M} + O^{2-}_{YSZ} \rightleftharpoons OH^{-}{}_{YSZ} + e^{-}{}_{M} \quad (4.7)$$

$$H_{ad,M} + OH^{-}{}_{YSZ} \rightleftharpoons H_2O_{(gas)} + e^{-}{}_{M} \quad (4.8)$$

In order to probe these, or other, possible mechanisms, the main technique of choice is EIS. Through a study of the electrode processes, it is possible to segregate individual processes, thus pointing to the rate determining steps in the electrochemical mechanism. In a typical Nyquist plot (*vide infra*), a number of arcs, which ideally corresponds to the number of electrode processes occurring on the cermet anode, may be deconvoluted via an appropriate curve-fitting computer program. However, since fundamental science does not always conform to the ideal, there is much debate in the literature about the physical interpretation and number of arcs, and thus electrochemical processes, which occur on a given cermet anode, for example Ni-YSZ, with a given fuel, such as hydrogen. [1, 4-7] In addition, if two physical processes have similar rates, they would not necessarily be distinguishable via this technique. It has been suggested that a possible explanation for these deviations could be due to small amounts of impurities within the starting material, which tend to collect and form a rim ridge between the electrolyte and electrode as well as between some grain boundaries, coupled with unique fabrication procedures, thus producing results described as “laboratory specific”. [8]

Fairly recently, computational techniques and interests have advanced towards surface reactions on bulk solids, a very useful and complementary tool for experimental fuel cell chemists. Hypothesized by Mogensen *et al.*,[9] the TPB is extended by spillover reactions of charged electrochemical intermediates. With polarization of the cermet anode, it was hypothesized that hydroxide anions and oxygen dianions could migrate over the metal surface, becoming available for reaction with dissociated, chemisorbed fuel intermediates. This would extend the TPB from a one dimensional line to a two dimensional area, vastly increasing the surface area available for reaction sites. The reactions responsible for this increase, known as spillover reactions, will be outlined herein.

Recently, Shishkin and Ziegler [10] published a computational paper outlining all possible spillover reactions on a bulk YSZ+O surface with a Ni cluster, which simulates the Ni-YSZ cermet, and distinguishes those which are thermodynamically and kinetically favourable. Here, YSZ+O designates a vacancy free YSZ surface site. The presence of a Ni cluster on a YSZ+O produces a charge transfer from Ni to the YSZ+O, which partially fills the valence shell of the extra oxygen atom.

Surprisingly, dissociative adsorption of hydrogen on the YSZ+O surface is a favourable, exothermic reaction, but it possesses a prohibitively high kinetic barrier, equation 4.10. Water formation and desorption on the YSZ+O surface is also thermodynamically favourable, but not kinetically feasible, equations 4.16 and 4.17. Therefore the direct oxidation of hydrogen on the YSZ+O (as well as the free YSZ surface) does not occur due to high kinetic barriers.

As expected, the dissociative adsorption of hydrogen on the Ni surface is both exothermic and has a very low kinetic barrier, equation 4.9. Oxygen spillover from the YSZ+O to the Ni across the TPB, equation 4.11, is a thermodynamically plausible reaction with a low kinetic barrier. This is in agreement with Mogensen *et al.*’s hypothesis (*vide supra*). Subsequent two-step oxidation and desorption of water, equations 4.14 and 4.15, is also thermodynamically and kinetically favourable.

Therefore, adsorption and direct oxidation of a molecule of hydrogen on the surface of a Ni cermet, involving oxygen spillover from YSZ, is possible.

A second mechanism for the oxidation of hydrogen on a Ni cermet can be proposed. Two spillover reactions of hydrogen atoms from Ni to the YSZ+O surface, equation 4.12, followed by the two-step oxidation of hydrogen on the YSZ+O surface, equations 4.16 and 4.17, is an exergonic process. However, the corresponding reaction involving the free YSZ surface is not possible due to high kinetic barriers. Therefore, an alternative mechanism involving the spillover of hydrogen from Ni to YSZ+O, which can occur simultaneously with the direct oxidation of hydrogen on the Ni surface, is plausible. This is in agreement with the hypothesis of Brown *et al.* [3] (*vide supra*).

$$H_{2(gas)} \rightleftharpoons 2H_M \quad (4.9)$$

$$H_{2(gas)} \rightleftharpoons 2H_{YSZ} \quad (4.10)$$

$$O_{YSZ} \rightleftharpoons O_M \quad (4.11)$$

$$H_M \rightleftharpoons H_{YSZ} \quad (4.12)$$

$$OH_{YSZ} \rightleftharpoons OH_M \quad (4.13)$$

$$H_M + O_M \rightleftharpoons OH_M \quad (4.14)$$

$$OH_M + H_M \rightleftharpoons H_2O_M \rightleftharpoons H_2O_{(gas)} \quad (4.15)$$

$$H_{YSZ} + O_{YSZ} \rightleftharpoons OH_{YSZ} \quad (4.16)$$

$$OH_{YSZ} + H_{YSZ} \rightleftharpoons H_2O_{YSZ} \rightleftharpoons H_2O_{(gas)} \quad (4.17)$$

The mechanisms outlined here provide evidence that the TPB can be extended to encompass, not only a two dimensional area rather than a one dimensional line, but can be extended to an area on both the Ni and YSZ surfaces adjacent to each other on the cermet anode.

4.2 Experimental

Fuel cell button cells were prepared for experimentation through methods outlined in chapter 2. The specific precursor compositions used were the following: NiO-YSZ, $Ni_{0.9}Co_{0.1}O$-YSZ, $Ni_{0.8}Co_{0.2}O$-YSZ, and $Ni_{0.7}Co_{0.3}O$-YSZ. The area of the working electrode used to calculate the current and power densities is 1.333 cm^2.

All electrochemical measurements were performed in pure hydrogen with a flow rate of 50 sccm at either 750°C, 800°C, or 850°C, as indicated. A minimum of 1.0 V for the value of OCV was required to continue with electrochemical measurements, after reduction of the metal phase of the cermet anode was complete. All of the electrochemical parameters used for measurements are summarized in chapter 2. Equivalent circuit modeling of AC data was done using the software from *ZView*.

4.3 Results and Discussion

4.3.1 Exchange current density from impedance voltammetry

Among many methods of probing the mechanism and performance experimentally of SOFCs, EIS yields the greatest amount of information. For all cermet anode compositions exposed to pure hydrogen fuel, a common shape was observed. The spectra show two arcs at high- and mid-frequency, figure 4.1. The high-frequency arc, which is independent of overpotential, shows a peak frequency of 4000 Hz. The mid-frequency arc is dependent on overpotential, and its radius decreases with increasing overpotential, as is expected. The peak frequency of the arc decreases with increasing overpotential as the radius of the arc decreases. The beginning of a Warburg element can be observed at low-frequency at OCV and low overpotentials. A full Warburg element would be expected to be observed at all overpotentials with data collected at very low frequencies. This circuit element corresponds to the diffusion limitation impedance, [11, 12] and is observed in an experimental cell where a stable reference electrode is present in a different atmosphere from the working electrode (typically on the opposite side of the cell from this electrode). Due to the nature of the complexity of the Warburg element with regard to fitting parameters, further analysis of this low-frequency data range was not performed.

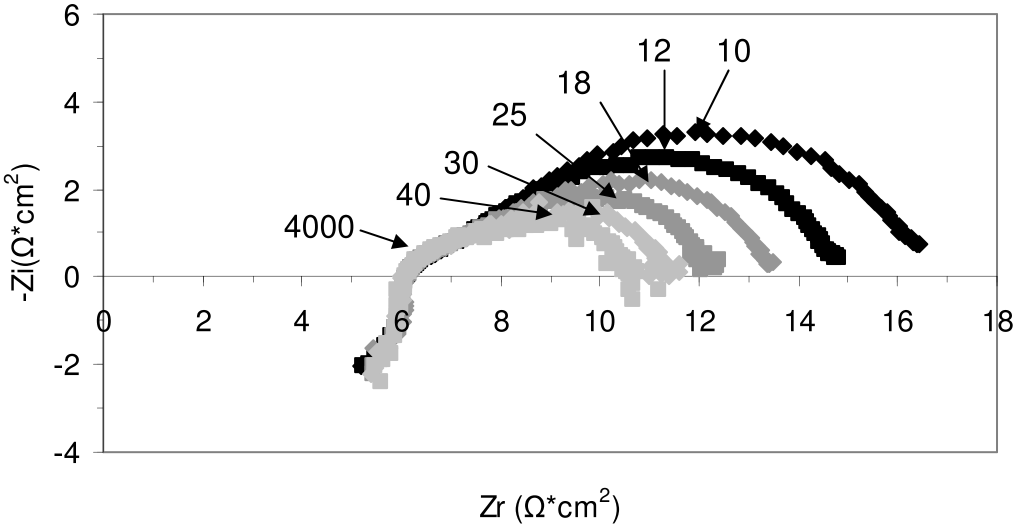

Figure 4.1 Impedance spectra of a $Ni_{0.7}Co_{0.3}O$-YSZ cermet anode in pure hydrogen at 850°C, plotted as a Nyquist plot, at the following overpotentials: (◆) η=0 mV at OCV, (■) η= 50 mV, (◆) η=100 mV, (■) η=150 mV, (◆) η=200 mV, and (■) η=250 mV. The frequency, in Hertz, of each of the low frequency arcs is indicated; the frequency of the high frequency arc is also indicated.

Typical mathematical fits using a complex non-linear least squares (CNLS) fit provided by the program ZView for the $Ni_{0.7}Co_{0.3}O$-YSZ cermet anode in pure hydrogen is shown below, figure 4.2. The equivalent circuit used to fit this data is presented in chapter 2; it contains inductor, resistor, and constant phase elements, and can be summarized by the form $[L_1R_1(R_2CPE_1(R_3CPE_2))]$. As can be seen, the fit of the mathematical curve (solid line) with the experimental data points is very good across the full range of negative imaginary impedance values (as shown on the Nyquist plot) and negative theta values (as shown in the Bode plot). The experimental data contains minimal noise; therefore, errors associated with the mathematical fit for data obtained in hydrogen are expected to be very small. Other equivalent circuits with three and four QR elements were applied to the experimental data; however, the errors associated with the

CNLS fit were lowest for the equivalent circuit with 2 QR elements, thus this one was chosen for all data fitting in this research thesis. Furthermore, assigning additional circuit elements implies that more processes could be assigned, which is perhaps not physically meaningful. Equivalent circuits with two or three elements are most common in the literature for the half cell corresponding to the anode side of planar cermet Ni-YSZ based anodes. [5]

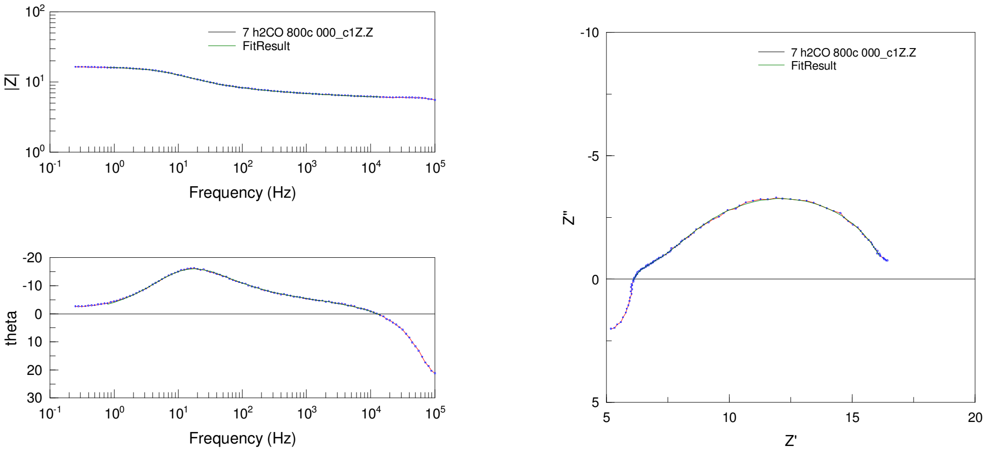

Figure 4.2 Examples of typical mathematical (complex non-linear least squares, CNLS) fits for a button cell with Ni$_{0.7}$Co$_{0.3}$-YSZ anode material for both Bode plot (left) and Nyquist plot (right). The fit is ideal over the indicated frequency (left) and real impedance (right) values. [The author apologizes for the unavoidably small font within the figure.]

The physical origin of each of the circuit elements, which correspond to the high- and mid-frequency arcs in the Nyquist plot, was evaluated by performing experiment for a given button cell of known bulk anode composition at various overpotentials. The variation of the resistive circuit elements, within the indicated equivalent circuit, with overpotential is presented below, figure 4.3. As can be seen, the processes associated with resistive elements R_1 and R_2 are not dependent on overpotential, and are constant over the observed range. Here, R_1 is equivalent to the series resistance, which represents the contact resistances of the electrodes, electrolyte layer, and wires within the cell components, and thus is independent of the overpotential value. The physical process(es) associated with the high-frequency arc, resistive element *R_2*, remains under debate in the literature, and thus is not well understood; however, its lack of a bias towards overpotential suggests it is associated with a bulk transport process rather than a charge transfer process. Finally, the mid-frequency arc, resistive element *R_3*, shows a clear trend with overpotential, thus the associated physical process will possess a bias towards overpotential. The electrode processes associated with transport of charged species, such as those involved in the electrochemical oxidation of hydrogen will be indicated by this element. As previously indicated, the small amount of information available in the literature concerning each individual process is conflicting, thus it is not possible to determine a rate determining step from this data set at this time. However, based on the variational trend of *R_3* and the independence of *R_1* and *R_2* with overpotential, the mechanism presented in the introduction section by Mogensen et al. is the most likely one followed on the NiCo-YSZ catalysts synthesized and tested herein.

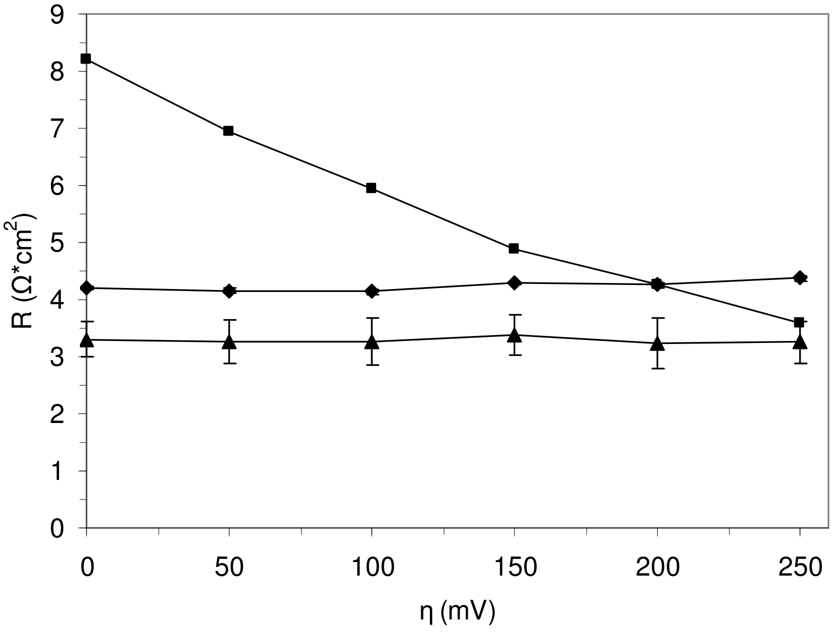

Figure 4.3 Resistor element fitting parameters for the indicated equivalent circuit over the overpotential range shown for the $Ni_{0.7}Co_{0.3}O$-YSZ cermet anode at 850°C. Resistors (♦) *R_1*, (▲) *R_2*, and (■) *R_3* as indicated. Error bars are included for all three data series, although only those for *R_2* are large enough to be visible.

Exchange current density measurements are indicative of the performance and kinetics of an individual anode when the half cell is measured with a three electrode set up. For the case of EIS, the low field approximation of the Butler-Volmer equation [13] [14] relates the inverse of the charge transfer resistance to an exchange current density value, as shown in the equation below.

$$i_o = \frac{RT}{nFR_{CT}} \qquad (4.18)$$

Here, R is the universal gas constant, T is the temperature of the electrochemical process, n is the number of electrons transferred during the process, F is Faraday's constant, and R_{CT} is the charge transfer resistance, which corresponds to resistive element R_3 in the nomenclature of this document.

4.3.2 Exchange current density data from cyclic voltammatry

The exchange current density values can also be obtained from direct current (DC) methods such as cyclic voltammetry (CV) using the Tafel expression as described in chapter 2. By collecting current-voltage data at a slow enough scan rate to simulate steady state conditions, exchange current density values can be extracted, as shown in figure 4.4.

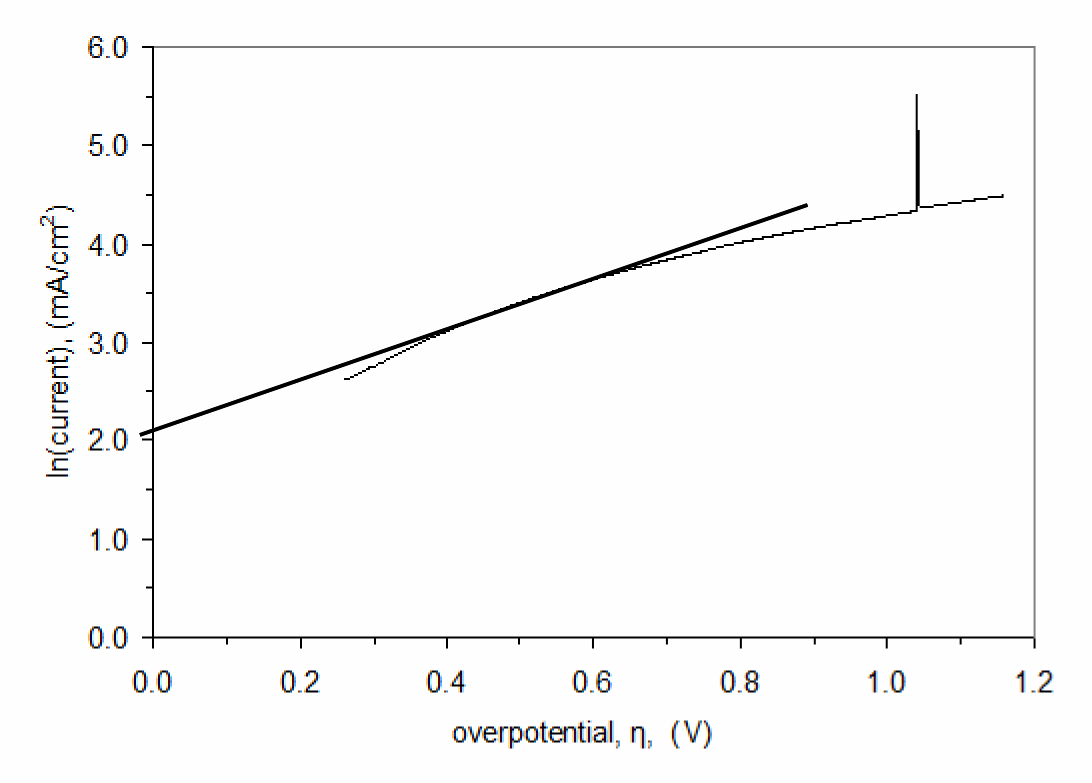

Figure 4.4 Direct current data plotted as overpotential and ln(current) for a $Ni_{0.7}Co_{0.3}O$-YSZ cermet anode in pure hydrogen fuel at 850°C for the purpose of extracting exchange current density values. The peak at high overpotential is due to an instrument crossover, and thus is unrelated to any electrochemical process on the anode. The broad line shows the region of fit and extrapolation to the vertical axis.

Here, the exchange current density can be extracted from the intercept of the vertical axis. The method for choosing the region from which to extract data was derived and outlined in chapter 2. Due to the lack of passivation expected and observed, the range of the overpotential during data collection was not restricted. The expected, continued linearity at high overpotentials was not observed, therefore, the Tafel region was chosen with great care according to three criteria: firstly, the correlation coefficient for the chosen Tafel region must have a value of 0.99 or higher, and, secondly, the Tafel region must commence at high overpotentials, in this case with a value greater than 180 mV. The exchange current density values derived from these two very different techniques are expected to show good agreement with each other.

4.3.3 Data analysis and comparison – exchange current density in pure hydrogen fuel

Comparison of the exchange current density values at two different temperatures is presented in the table below. Each row in the two columns presenting i_o values in table 4.1 represents a different button cell. Though they were manufactured by hand, via the outlined procedure in chapter 2, the smallest possible tolerance for error, given the manufacturing process, was maintained. Two tolerance criteria were followed. Firstly, the cell had to show an OCV value of 1.0 V or higher, which shows that the button cell is free of leaks due to electrolyte cracks or improper pyrex seals. Secondly, the cell dimensions need to meet measurement criteria such that the anode and cathode are both the same size, shape, and located directly adjacent to each other on the electrolyte disk. As can be observed by the high standard deviation values shown, there is a wide range of values corresponding to cells manufactured and tested under each set of conditions. However, the average values produced from each group of cells tested at the same temperature shows good agreement of the average values calculated from both AC (EIS) and DC measurement techniques.

Table 4.1 Exchange current densities found for the $Ni_{0.7}Co_{0.3}O$-YSZ cermet anode in pure hydrogen fuel by EIS and DC (cyclic voltammetry) methods for comparison of absolute, average and standard deviation (SD) values at the two different temperatures indicated. Each row indicates a separate button cell measurement.

Temperature (^oC)	i_o (EIS) (mA/cm^2)	Average, SD (EIS) (mA/cm^2)	i_o (DC) (mA/cm^2)	Average, SD (DC) (mA/cm^2)
850	5.5	11.3, 6.5	6.8	10.0, 2.9
	12.5		7.9	
	13.5		10.1	
	24.3		14.4	
	10.1		13.7	
	10.1		7.1	
	2.3		11.2	
	12.3		8.7	
800	0.3	1.1, 0.78	0.3	1.3, 1.0
	1.2		2.3	
	1.7		1.3	

The large variation of exchange current density values calculated for button cells manufactured and tested under as closely related conditions as possible points to a challenge in data processing as well as to variations in microstructure. In subsequent chapters, the values which are obtained must be interpreted with regard to an increase or decrease in cell performance upon changing various factors such as cobalt concentration, temperature, or fuel composition. For this reason, each cell will be treated separately from its neighbours, namely those which are manufactured and tested under the same conditions. Ratios of values corresponding to the change in performance upon altering the inlet gas in comparison to the performance of the cell in pure hydrogen fuel will be utilized to determine the amount by which the performance rose or fell with a change in this condition.

4.3.4 Performance from potentiostatic measurements in pure hydrogen fuel

When extracting current from a fuel cell, it is essential to know where the optimal current density lies to produce the optimal performance of the cell. In order to accomplish this, current data is collected using potentiostatic measurements at a range of overpotentials, as shown in figure 4.5A. Here the data from many fuel cells at 850°C with an anode cermet composition of $Ni_{0.7}Co_{0.3}O$-YSZ was collected in pure hydrogen fuel. As can be observed there exists a clear distinction between the activation polarization range at low current density, below 10 mA/cm^2, and the ohmic polarization range at medium to high current density, above 10 mA/cm^2. A region containing concentration polarization is not observed.

The ohmic polarization range is of most importance; this is the linear region, which includes the resistances of the electrolyte, cell components and electrodes, and thus is linear and changes proportionally with the current density. It is in this current density region where the maximum power output of the fuel cell is found. The simple relation between current, *i*, potential, *V*, and performance as expressed by electrical power, *P*, can be used to determine this value, using the equation below.

$$P = iV \qquad (4.19)$$

By plotting the performance over the range of current density values, the maximum can be determined. As can be observed, figure 4.5B, similarly to the current exchange data presented above, there is a range of maximum performance values found for a cell with the same anode composition, temperature and fuel. Though all of the button cells have the same composition, for clarity, the points belonging to individual cells have been connected. As can be observed, three cells showed a large activation polarization drop. It is suspected that these three cells had physical defects which caused this measurement. Separate OCV measurements of these cells showed satisfactory values, above 1.0 V. The suspected cause of these low overpotential measurements at zero current density are likely the combination of a physical defect, as discussed above, and the order of chronoamperometry measurement, progressing from cathodic to anodic currents over time. The average and standard deviations for performance values for the data presented for the $Ni_{0.7}Co_{0.3}O$-YSZ cermet anodes in pure hydrogen fuel at 850°C are 15.2 and 4.7 mW/cm^2, respectively. Because of this large variation, a method of comparison applying ratios, as discussed in the previous section, will be applied to determine changes in performance with fuel composition and/or temperature.

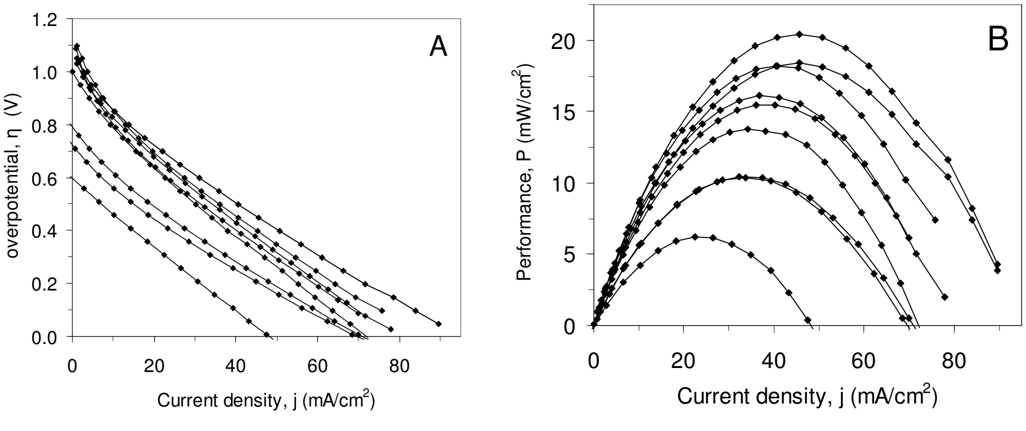

Figure 4.5 Data from many $Ni_{0.7}Co_{0.3}O$-YSZ cermet anodes in pure hydrogen fuel at 850°C. (A) Data derived from potentiostatic measurements at various overpotentials for the purpose of constructing (B) performance plots.

The performance of the cermet anode in pure hydrogen fuel was characterized over the first 14 hours of operational testing to determine both its stability and performance value before introducing an alternate fuel source. The peak value of the performance of an individual button cell, as observed in figure 4.5B, calculated over time can be plotted to determine its stability. As can be observed in figure 4.6, the power of each individual cell tested, connected with indicator lines for clarity, showed great stability for a minimum of 10 hours prior to changing the fuel type. One cell did not show stabilization until the fourth hour of measurement. This type of plot will be presented in subsequent chapters to demonstrate the change in performance with different fuel sources over the time of electrochemical testing.

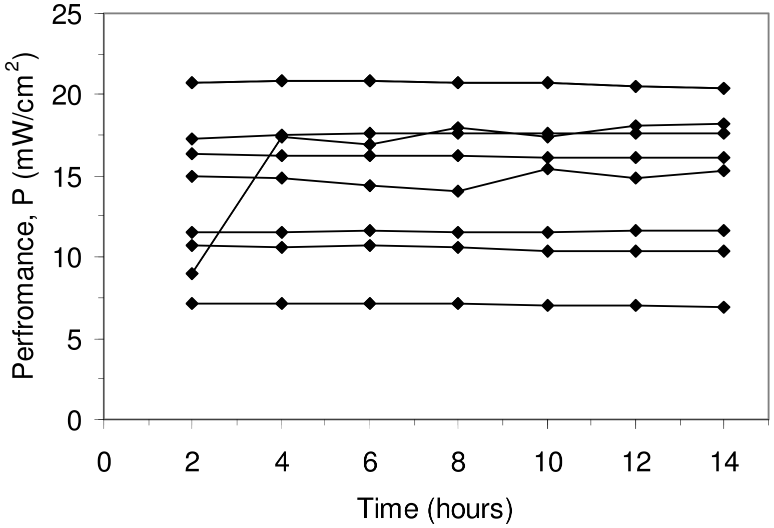

Figure 4.6 Performance data for the $Ni_{0.7}Co_{0.3}O$-YSZ cermet anodes in pure hydrogen fuel at 850°C over the first 14 hours of data collection, demonstrating the stability of the anode for many button cells in hydrogen gas.

4.3.5 Open circuit voltage (OCV) measurements in pure hydrogen fuel

Open circuit voltage is the potential difference between two electrical terminals under zero load, when the circuit is open. There is no current traveling externally through the circuit, although a voltmeter instrument will apply a very small current one in order to measure the potential difference. Following reduction of the metal oxide phase to its corresponding metal under high temperature and reducing conditions, a minimum of 1 V for OCV was required. The reasoning for this is twofold: an OCV value of less than 1V can indicate a poor pyrex seal between the alumina cell support and the button cell itself, and it can also indicate poor connection between the anode and current-collector following reduction. With respect to the first possibility, cycling the cell to a higher temperature to further soften the pyrex seal is the most common solution. For the second possibility, due to the expected shrinkage of the porous anode cermet material upon removal of the oxygen from the oxide lattice, on occasion, this causes delamination of the current collector from the anode material. In this case, thermal cycling will not rectify the problem, in fact, it will likely cause further delamination. Due to the high operating temperature of the fuel cell, there is no practical way to re-attach the current collector, thus a new cell must be installed.

The value of OCV is useful in determining the overall reactions, which are taking place on the anode half-cell, however it cannot be used to determine the mechanism of the reaction or reactions taking place, nor their rate determining step. With respect to the common $Ni_{0.7}Co_{0.3}O$-YSZ cermet anode, average OCV values of 1.32 V and 1.23 V were obtained for many cells run at 800°C and 850°C, respectively. This agrees well with the expected electrochemical potential of 1.2 V calculated by the Nernst equation for the electrochemical oxidation of hydrogen. Furthermore, the slightly larger value obtained at the lower temperature of 800°C is in agreement with the expected relation between OCV and fuel utilization: namely, OCV will increase as fuel utilization decreases. The lower temperature is expected to produce a series of cells with slightly lower electrochemical rates, thus utilizing less fuel, and resulting in the higher OCV value observed. This is justified by examining the Nernst equation, presented in Chapter 1, at low concentration of products. Although this is a simple case with pure hydrogen fuel showing the expected value for hydrogen oxidation, it provides a baseline value for subsequent chapters where the fuel will be a mixture of two pure inlet gases. An observed change in the OCV value will provide valuable insight into the reaction or combination of reactions occurring on the anode surface.

4.4 Conclusions

Although still unknown in the literature via experimental techniques, fuel cell modeling through computational chemistry in the literature is able to provide evidence for possible mechanisms for the electrochemical oxidation of hydrogen on a cermet anode composed of Ni-YSZ. Through fitting an equivalent circuit model, for EIS data, and extrapolating the Tafel region, for cyclic voltammetry data, the exchange current density values for many button cells of composition $Ni_{0.7}Co_{0.3}O$-YSZ are calculated. Although there is large variation from one button cell to the next, the average values for exchange current density extracted from the two different methods are in good agreement. From the data presented, the average exchange current density for a $Ni_{0.7}Co_{0.3}O$-YSZ cell at 850^{o}C is 11.3 and 10.0 mA/cm^2 for EIS and cyclic voltammetry data respectively, and at 800^{o}C is 1.1 and 1.3 mA/cm^2, approximately one order of magnitude lower, for EIS and cyclic voltammetry data respectively. Although performance values for the corresponding button cells shows similar variation from one cell to the next, all cells show good stability with time in pure hydrogen fuel, a characteristic necessary to assess the performance value of each cell before changing the inlet fuel to study the effects of sulfur and carbon poisoning in the subsequent chapters.

4.5 References

[1] S. Primdahl, M. Mogensen, J. Electrochem. Soc. 144 (1997) 3409.

[2] P. Holtappels, J. Bradley, J. Irvine, A. Kaiser, M. Mogensen, J. Electrochem. Soc. 146 (1999) 1620.

[3] M. Brown, S. Primdahl, M. Mogensen, J. Electrochem. Soc. 147 (2000) 475.

[4] P. Holtappels, J. Bradley, J. Irvine, A. Kaiser, M. Mogensen, J. Electrochem. Soc. 148 (2001) A923.

[5] J. Fleig, J. Maier, J. Electrochem. Soc. 144 (1997) L302.

[6] P. Holtappels, I. Vinke, L.D. Haart, U. Stimming, J. Electrochem. Soc. 146 (1999) 2976.

[7] R. Barfod, M. Mogensen, T. Klemenso, A. Hagen, Y.-L. Liu, P.V. Hendriksen, J. Electrochem. Soc. 154 (2007) B371.

[8] M. Mogensen, K.V. Jensen, M.J. Jorgensen, S. Primdahl, Solid State Ionics 150 (2002) 123.

[9] D. Kek, M. Mogensen, S. Pejovnik, J. Electrochem. Soc. 148 (2001) A878.

[10] M. Shishkin, T. Ziegler, J. Phys. Chem. C 113 (2009) 21667.

[11] S. Primdahl, M. Mogensen, J. Electrochem. Soc. 145 (1998) 2431.

[12] S. Primdahl, M. Mogensen, J. Electrochem. Soc. 146 (1999) 2827.

[13] J. Butler, Trans. Faraday Soc. 19 (1923) 729.

[14] J. Butler, Trans. Faraday Soc. 28 (1932) 379.

5

Electrochemical Characterization of $Ni_xCo_{(1-x)}$-YSZ Cermet Anodes in H_2S/H_2 fuel

5.1 Introduction

Due to their high operating temperature, SOFCs have a wide range of fuels upon which they can be operated, such as hydrogen, syngas, small hydrocarbons and biogas. [1, 2] Hydrocarbon fuels are one choice, which has generated attention due to their availability, ease of transport and existing infrastructure. However, hydrocarbon fuels frequently have high concentrations of sulfur compounds, where natural gas provided to residential and industrial buildings contains a minimum concentration of H_2S for safety reasons. This common sulfur compound causes the cermet anodes to lose performance with exposure due to material degradation upon reaction with the sulfur. Because of this difficulty, research into the mechanism of performance loss and material degradation can provide vital information towards the development of an anode material for SOFCs, which is tolerant to sulfur poisoning. Although natural gas can provide a bridging technology until a hydrogen infrastructure becomes common, an understanding of the poisoning mechanism for common cermet anode material can lead to an understanding of the sulfur poisoning mechanism.

Currently, the most common anode material is Ni-YSZ, which is very active in the electro-oxidation of hydrogen; however, this material shows high sulfur poisoning at low SOFC operating temperatures and conventionally high sulfur concentrations. The amount of recovery of performance experienced by the anode upon removal of the sulfur from the fuel stream has wide disagreement.[3] [4-6] The predominant reasoning for the irreversible performance loss, regardless of its amount, is due to irreversible surface Ni-S bond formation.[7]

Phase diagrams also indicate that at high enough sulfur concentrations, under the typical SOFC temperature and pressure operation conditions, bulk nickel sulfide phases dominate. [8-10] This is not the case at low (100 ppm H_2S) concentrations, as determined through *in situ* Raman spectroscopy experiments, which show a nickel phase present with a lack of the expected associated morphology changes of the material due to the expansion of the lattice parameters upon the incorporation of sulfur into the metal lattice if metal sulfides had been formed.[11] Here, Cheng and Liu caution other authors about using *ex situ* results in the determining of the correct nickel sulfide phase present at operational temperatures, since more than one phase change occurs to the bulk nickel sulfide upon cooling under the operational sulfur-containing atmosphere, resulting in identification of the final phase upon cooling of bulk nickel sulfide rather than the phase present at high temperatures. The authors confirm the formation of bulk Ni_3S_2 upon slow cooling followed by *ex situ* measurements, as reported by other research groups. The disagreement in the literature as to whether bulk nickel sulfide formation is present or not appears to rely heavily on the operational conditions, namely temperature and H_2S concentration, present. The concentration employed in the present work is extremely high compared to other research groups, which appear in the literature using a H_2/H_2S mixture as the fuel, therefore a bulk nickel sulfide phase is expected, as will be discussed later in this chapter.

Research into alternate materials from the common Ni-YSZ anode under H_2S/H_2 atmosphere, where the concentration of H_2S is low (1 % or less), show promising results. Anodes with nickel-based metallic phase with alternate oxide phase such as scandia stabilized zirconia (SSZ),[12] and alternatively Cu/CeO_2 anodes have shown tolerance to sulfur poisoning at 450 ppm H_2S at 800°C.[13] Interest in the effect of high concentration, 10 % H_2S in H_2, sulfur in the fuel feed of a relatively simple system arises from the high sulfur content in some fuel sources such as the tar sands in western Canada. The research presented in the present chapter is one of the few examples in the literature of such high concentration. [14-16]

In a recent research paper by Dong *et al.*, [16, 17] *in situ* Raman spectroscopy was performed under conditions very similar to those used in the present research thesis, namely they were 10 % H_2S in H_2 at 950°C. This surface-sensitive technique identified the predominant surface phase as NiS. Powder XRD experiments identified the bulk phase to be Ni_7S_6 with a small amount of Ni_3S_2. It was noted by the authors that, due to the similarity of the stoichiometry between Ni_7S_6 and NiS, it was concluded that both phases could be present on the surface of the nickel sulfide particles. A large amount of agglomeration was observed upon formation of the bulk sulfides and is likely due to the fact that many nickel sulfide phases have melting points lower than the operational temperature for this study, resulting in a mobile liquid phase.

SOFCs which can function to oxidize pure H_2S as fuel are known, although this system would not be practical due to the high toxicity of this gaseous compound; however, it can provide answers to many questions regarding the fundamental chemical mechanism as well as material or surface poisoning. The first reported cell to use pure H_2S as fuel had a $CuFe_2S_4$ anode material. [18] Other metal sulfide based anodes have been developed based on molybdenum sulfide mixed with sulfides of other transition metals, such as Ni, Co, or Fe. Among these, the anode alloying cobalt and molybdenum sulfides showed the best long term performance in H_2S containing fuels. [19, 20] Despite the fact that experimental evidence shows that these molybdenum sulfide based anode materials show good long term performance in H_2S containing fuels, an understanding of the details of the H_2S oxidation reaction mechanism is lacking, as indicated in these studies by OCV values which are larger than expected from simple H_2S oxidation (*vide infra*).

A solid oxide fuel cell has the same cathodic reaction where molecular oxygen is reduced to produce two dianionic oxygen species, regardless of the reaction occurring at the anode, as shown below.

$$O_2 + 4e^- \rightarrow 2O^{2-} \qquad (5.1)$$

For a fuel cell with H_2S available to the anode, following migration through the electrolyte, the oxygen dianion can then react with H_2S by two reactions.

$$H_2S + O^{2-} \rightarrow H_2O + \frac{1}{2}S_2 + 2e^- \qquad (5.2)$$

$$H_2S + 3O^{2-} \rightarrow H_2O + SO_2 + 6e^- \qquad (5.3)$$

Here, the standard state potentials at 727°C are 0.786 V and 0.761 V for equations 5.2 and 5.3, respectively. Above 700°C, H_2S can undergo thermal decomposition, also known as H_2S pyrolysis, which can greatly complicate the system.

$$H_2S \rightarrow H_2 + \frac{1}{2}S_2 \qquad (5.4)$$

Here, hydrogen is produced, which can then be oxidized as a second fuel in addition to the H_2S through equations presented in chapter 4. Since the OCV value of hydrogen is much higher than that known for H_2S, an elevated OCV obtained from an H_2S fueled cell would indicate the oxidation of hydrogen produced via the presented thermal decomposition reaction in addition to the intended fuel. The sulfur produced in reactions 5.2 and 5.4 can be oxidized given sufficient oxygen available at the TPB, as shown below.

$$\frac{1}{2}S_2 + O^{2-} \rightarrow SO_2 + 4e^- \qquad (5.5)$$

The SO_2 produced by reactions 5.3 and 5.5 can react with excess H_2S by the second step of the Claus process to produce water.

$$2H_2S + SO_2 \rightleftharpoons 2H_2O + \frac{3}{n}S_n, \quad \text{where } n = 2\text{-}8 \qquad (5.6)$$

However, at low temperatures, the equilibrium reaction 5.6 favours the products. Thus, at high SO_2 partial pressures, formation of the products shown is not expected to occur in appreciable amounts through this particular reaction.

The high operating temperatures of SOFCs, as well as the enclosed and sealed environment of the anode make it difficult to study the details of the surface reactions occurring on the cermet anode. Thankfully, recent advances in DFT calculations of gases interacting with solid surfaces have allowed for speculation of likely surface mechanisms with observation of thermodynamic and kinetic parameters of reaction intermediates.

A very detailed, recent first-principles study by Alfonso[21] of the dissociation of H_2S adsorbed on a Ni(111) surface provides detailed parameters for this surface reaction. The overall decomposition of H_2S on the Ni(111) surface was found to be exothermic, where the first of the two adsorbed steps outlined below, reaction 5.8, is expected to be the rate determining step since it possesses the larger of the two energy barriers.

$$H_2S_{(g)} \rightarrow H_2S_{(M)} \qquad (5.7)$$

$$H_2S_{(M)} \rightarrow SH_{(M)} + H_{(M)} \qquad (5.8)$$

$$SH_{(M)} \rightarrow S_{(M)} + H_{(M)} \qquad (5.9)$$

Here, where *(M)* indicates species adsorbed on the nickel metal surface, the overall change in energy, ΔE_{rxn}, is -2.15 eV, which corresponds to the net reaction of 5.8 and 5.9, the largest of all of the corresponding late transition metal surfaces investigated in this particular paper. Coupled with the favourable adsorption energy of H_2S from the gas phase of -0.56 eV to a ‘top’ site of the Ni(111) surface, reaction 5.7, the overall decomposition of H_2S gaseous fuel is expected to be highly favourable on low energy nickel surface.

With the ease of formation of adsorbed sulfur, an interest in the favoured sulfur surface coverage and its effect on the surface dissociation of hydrogen was recently studied by Galea *et al.*. [3] Based on thermodynamic considerations, the optimal surface coverage is 50 %, which corresponds to a sulfur surface coverage, θ_S, of 0.50 monolayers (ML). Where $\theta_S = 0.25$ ML, adsorbed hydrogen on the Ni(111) surface is favoured, but when $\theta_S = 0.50$ ML, the removal of adsorbed hydrogen becomes less favourable. As will be explored more in depth in a subsequent chapter, adsorbed sulfur has the effect of increasing the kinetic barriers of surface reactions, and forces surface reactions to travel through a less stable reaction pathway. It was found that a large number of surface sulfur atoms surrounding another adsorbed surface species, causes this second species to be more weakly adsorbed. Also, the simple idea is presented of the sterics of large sulfur atoms occupying the thermodynamically favourable three-fold hollow sites and blocking the surface where otherwise surface reactions such as the dissociation of molecular hydrogen could take place. This occupying of potentially active surface sites causes a decrease in the overall performance of a cell where the anode is exposed to sulfur.

A follow up study was published detailing the complete desulfurization of a Ni(111) surface poisoned with adsorbed sulfur by employing molecular oxygen. Through formation and desorption of surface SO_2, it was found that the thermodynamics of complete surface cleaning are favourable. [22] However, under pyrolytic conditions, the desorption of S_2 is highly unlikely, indicating that a drastic fuel environment change is required to remove adsorbed sulfur from a Ni surface. Finally, a recent *ab initio* study by Monder and Karan[23] shows that, given a system with parallel surface decomposition of H_2S and H_2, the expected surface sulfur coverage is higher than previously predicted by computational studies. [3, 10] By neglecting the effects of parallel competitive H_2 surface adsorption and assuming that all translational and rotational entropy is lost upon adsorption, these previous studies were shown to fall short of reality. Thus, it was concluded that the amount of surface poisoning experienced is dependent on both P_{H_2}

and P_{H_2S} rather than simply the ratio, $\frac{P_{H_2S}}{P_{H_2}}$, namely for lower P_{H_2}, the surface coverage is higher, independent of the ratio. This study by Monder and Karan neglects the known formation of bulk nickel sulfide species; therefore, this area of research is in an exciting stage of development and new findings in the near future are anticipated.

Reactions of Ni with H_2S from the gas phase, as outlined in equations 5.10 and 5.11, yield possible bulk nickel sulfide phases. [24]

$$Ni + H_2S \rightleftharpoons NiS + H_2 \qquad (5.10)$$

$$3Ni + xH_2S \rightleftharpoons Ni_3S_x + xH_2 \qquad (5.11)$$

In determining whether these reactions occur to produce bulk nickel sulfide or pure nickel with surface adsorbed sulfur, phase diagrams are useful, figure 5.1A and B. Here, a theoretical phase diagram of nickel with a varying range of hydrogen and H_2S partial pressures is presented, figure 5.1A. [10] For the most common concentration and temperature of these two gases used in this work, 10% v/v H_2S/H_2, a value of 0.95 for the bottom horizontal axis and 1123 K (850^{o}C) for the vertical axes is obtained. Although this value is not represented on the plot below, it is expected to lie very close to the experimental border (black line) between the adsorbed sulfur on pure nickel (dark grey region) and the bulk Ni_3S_2 (light grey region). It is hypothesized that a bulk Ni_3S_2 phase will be obtained under the given experimental conditions. An experimental phase diagram produced in 1954 for various H_2S/H_2 partial pressures for nickel is shown in figure 5.1B. At a pressure ratio of 0.1 H_2S/H_2 and 800 to 850^{o}C, a liquid phase for nickel sulfide is expected. Cooling, as was done after every button cell experiment, passes through several phase transitions in the nickel phase diagram, resulting in a final phase of Ni_3S_2. This is in agreement with experimental data which will be presented in this chapter. It should be noted, however, that there are phase areas which have yet to be identified in this diagram. More evidence in this high concentration region by either experiment or calculation is required to draw definitive conclusions regarding the predominant phase present under these experimental conditions. Fundamental research to produce a phase diagram with confidence in this high concentration region would be a great asset.

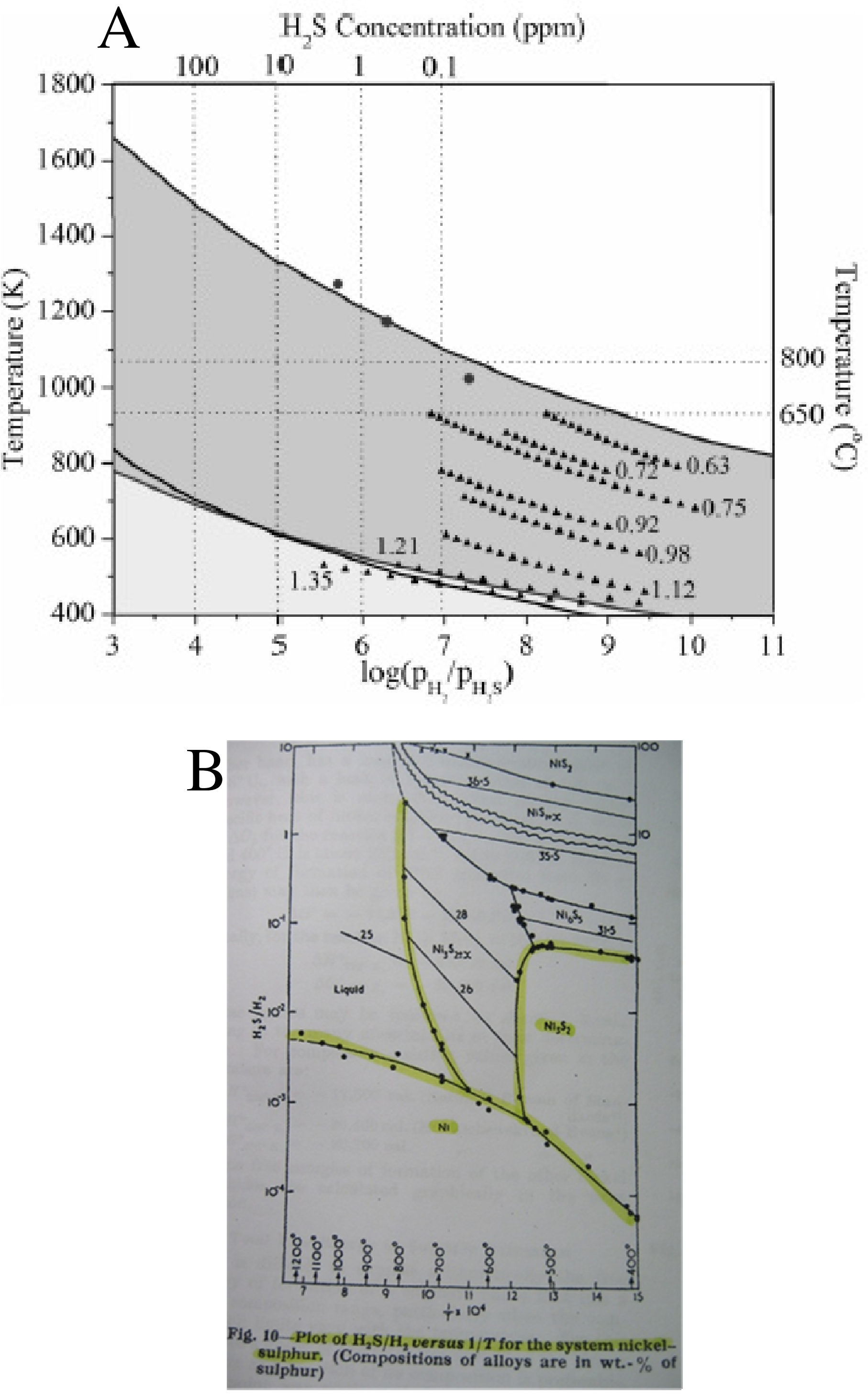

Fig. 10—Plot of H_2S/H_2 versus $1/T$ for the system nickel-sulphur. (Compositions of alloys are in wt.-% of sulphur)

Figure 5.1 (A) Calculated phase diagram using DFT for nickel in the partial pressure gas mixture range shown. The regions are as follows: pure nickel (white), increasing surface coverage in the downward vertical direction (dark grey), and Ni_3S_2 (light grey). The black points indicate experimental results for low relative partial pressures of H_2S. The boundary lines are as follows: the phase boundary between nickel and nickel with adsorbed sulfur (black line bounding white and dark grey regions), calculated phase boundary of adsorbed sulfur and bulk (grey line bounding two grey regions), and experimental bulk Ni_3S_2 phase diagram boundary (black line bounding two grey regions). (B) Experimental phase diagram for nickel at various partial pressure gas mixtures shown. [10] [9]

A detailed gas phase radical mechanism of the pyrolysis of H_2S was developed by Binoist *et al.* [25] between 800°C and 1100°C in a tubular quartz flow reactor. As can be seen in figure 5.2 below, the radical mechanism is quite complex and agrees well with the experimental data collected by the authors. As emphasized, a radical mechanism is necessary to explain coupled reactions such as this system, which undergo cross reactions and contain common radical intermediates. This details the reaction pathways towards various gas phase species, which can then adsorb and react on the surface of the cermet anode catalyst.

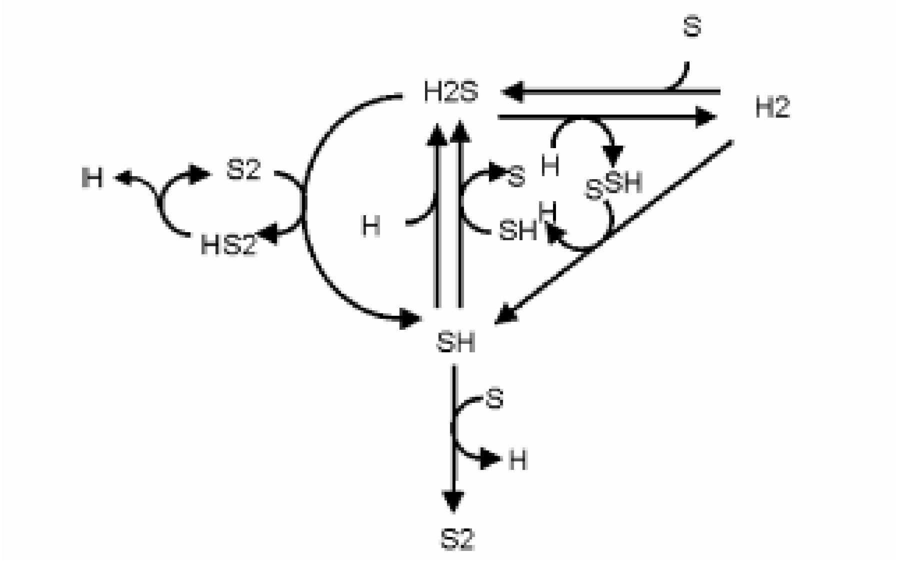

Figure 5.2 Primary reaction pathways followed during the pyrolysis of hydrogen sulfide between 800°C and 1100°C. [25]

When considering the possible types of electrochemical measurements used to determine the degree of sulfur poisoning experienced by the anode under a set of operating conditions, seemingly contradictory numerical results can be misleading. In a recent paper by Cheng *et al.*, [26] it was found that, due to sulfur poisoning effects, the drop in power output of the cell decreases when drawing more current from the cell potentiostatically, but the power increases when more current is drawn galvanostatically. Equivalent circuit analysis indicate the importance of comparing the anode polarization resistance rather than the drop in power output of the cell, when determining the amount of sulfur poisoning that the anode is experiencing. Although this research was carried out under low ppm concentrations of H_2S, the importance of correct data analysis is emphasized.

Considering systems with fuel input that contains both H_2 and H_2S, few research groups have performed work in determining the mechanism under different possible conditions. Marquez *et al.* [27] performed theoretical work to obtain information on hydrogen electro-oxidation in the presence of H_2S. Although the oxidation of H_2 is thermodynamically favoured on the surface of the cermet anode, the oxidation of H_2S is also thermodynamically possible. With both fuel molecules present in the gas phase, it was also found that the diffusion coefficient of hydrogen decrease in the presence of H_2S compared to the value for pure hydrogen. Finally it was also found that on the surface, hydrogen moves slower in the presence of H_2S. Therefore, due to thermodynamics, the oxidation of H_2 is favoured over that of H_2S, but transport limitations slow down the oxidation of H_2 when H_2S is present.

5.2 Experimental

Fuel cell button cells were prepared for experimentation through methods outlined in chapter 2. The specific cermet bulk compositions used were the following: NiO-YSZ, $Ni_{0.9}Co_{0.1}O$-YSZ, $Ni_{0.8}Co_{0.2}O$-YSZ, and $Ni_{0.7}Co_{0.3}O$-YSZ. The area of the working electrode used to calculate the current and power densities is 1.333 cm^2.

All electrochemical measurements were performed in pure hydrogen with a flow rate of 50 sccm at either 750°C, 800°C, or 850°C, as indicated. A minimum of 1.0 V for the value of OCV was required to continue with electrochemical measurements, after reduction of the metal phase of the cermet anode was complete. Sulfur poisoning experiments were performed using a mixture of H_2S and H_2 with a total flow of 50 sccm, where the concentration of sulfur poison will be indicated, but will range from 0.75 % to 100 % v/v in a balance of H_2.

All of the electrochemical parameters used for measurements are summarized in chapter 2. Equivalent circuit modeling of AC data was done using the software from *ZView*.

5.3 Results and Discussion

5.3.1 Exchange current density from electrochemical impedance spectroscopy (EIS) and direct current voltammetry

In order to assess the catalytic activity of a specific series of anode materials, both EIS and direct current voltammetry data was collected. This series of anode materials, as will be outlined in the tables below, contains increasing concentrations of cobalt alloyed with a balance of nickel, while maintaining a constant overall metal concentration by mass of 70 % as calculated for the anode cermet material after reduction in hydrogen. The synergistic effect of these two alloyed metals is investigated here with differing parameters, as discussed below.

The sulfur resistance of the $Ni_xCo_{(1-x)}$-YSZ cermet anode series in a sulfur-poisoned hydrogen environment is explored in this section. The relationship between three parameters will be discussed, namely the composition of the metal phase of the anode (the $Ni_xCo_{(1-x)}$ ratio), the temperature of the button cell and its surrounding fuel environment, and the amount of H_2S poison present in a balance of hydrogen as fuel. The method of assessing the amount of sulfur poisoning, which occurs when varying these three parameters, will be through the measurement of the calculated exchange current density via EIS and direct current voltammetry measurements.

5.3.1.1 Exchange current density data at high H2S concentration

A series of four cermet anode compositions with increasing concentrations of cobalt in nickel as the metallic phase were synthesized with the post-reduction composition as shown in table 5.1. Following sufficient time to stabilize, namely 14 hours, data presented below shows the amount of sulfur poisoning which occurred upon addition of 10 % v/v H_2S to a fuel stream of H_2. A baseline was assessed for each button cell individually, since not only is variation in catalytic activity expected from one cermet anode composition to another, but from one button cell of the same composition to another; the reason for this is due to unavoidable variations in microstructure from one button cell to another despite the efforts to manufacture each cell with as small a tolerance for variation as possible, even though they are all manufactured by hand.

As measured by both EIS, table 5.1, and direct current voltammetry, table 5.2, the exchange current densities are presented to determine the amount of sulfur poisoning experienced by each cell composition. Separate button cell runs are shown as individual rows in each table. The exchange current density for the cell in pure hydrogen presents the baseline for the individual button cell; this shows good agreement at high cobalt concentrations of the form $Ni_xCo_{(1-x)}$-YSZ, where x=0.80, 0.70. For the larger variation observed at low cobalt concentrations, where x=1.0, 0.90, the exchange current density values derived from EIS data are expected to have a higher degree of accuracy than those corresponding to direct current measurements. The reasoning behind this argument is twofold. Firstly, the EIS measurements take place over a much shorter time span, thus changes in microstructure and anode composition are minimized. Secondly, the region of the direct current density data known as the Tafel region is difficult to visualize and pinpoint, as was discussed in detail in chapter 2. The fitting of the EIS data by the ZView program is much less subject to errors of fit, and so the data gained by this method is expected to be more reliable.

Upon addition of 10 % v/v H_2S to the hydrogen fuel stream, the catalytic activity dropped significantly, in most cases by 2 to 5 orders of magnitude. Since these data points presented represent the catalytic activity after a time period long enough to undergo conversion to bulk hydrogen sulfide species at this H_2S concentration and environmental temperature, 14 hours at 850°C, it can be hypothesized that the loss in activity observed is due to delamination of the anode and current collector from the YSZ electrolyte disk. Upon addition of sulfur to the nickel lattice, an expansion which is significant due to the large size of the sulfur atom is expected. Due to the fact that the anode material is brittle, fragile, and porous, a change in the size of the particles or particle migration/coarsification, which is common for nickel at high temperatures, this hypothesis is valid. In addition to this, many nickel sulfide species are liquid at 850°C, thus a loss of structural integrity of the pore system can be theorized upon the liquification of the metallic phase.

In order to determine if the amount of poisoning could be reduced upon reduction of the sulfur poison in the fuel feed, the concentration was reduced by an order of magnitude, to 1 % v/v H_2S in hydrogen. No recovery, in fact a loss of catalytic activity for those cermet anode compositions which had retained some activity, was observed. All of the anode compositions experienced a reduction in activity by 5 orders of magnitude compared to the values collected in pure hydrogen fuel. The lack of any recovery supports the argument of delamination and destruction of the anode and current collector microstructure, which supported the observed catalytic activities in pure hydrogen.

Table 5.1 Exchange current density (i_o) values for various anode and fuel compositions as indicated, expressed in units of mA/cm^2 at 850°C. These values were derived from EIS measurements using the low field approximation of the Butler-Volmer equation, as described in chapter 2, and the charge transfer resistance, as obtained from fitting the raw EIS data with the ZView program. The data derived from direct current voltammetry for the same four button cells is presented in table 5.2. Individual button cell tests are shown as rows.

Anode Material	H_2	10 % H_2S/H_2	1 % H_2S/H_2
Ni-YSZ	31.7	8.02E-05	7.65E-05
$Ni_{(0.90)}Co_{(0.10)}$-YSZ	41.5	7.50E-05	6.80E-05
$Ni_{(0.80)}Co_{(0.20)}$-YSZ	12.6	2.21E-01	9.36E-05
$Ni_{(0.70)}Co_{(0.30)}$-YSZ	5.50	5.96E-02	6.33E-05

Table 5.2 Exchange current density (i_o) values for various anode and fuel compositions as indicated, expressed in units of mA/cm^2 at 850°C. These values were derived from direct current voltammetry measurements, as described in chapter 2, through the vertical intercept of an overpotential vs. ln(current) plot. The data derived from EIS measurements for the same four button cells is presented in table 5.1. Individual button cell tests are shown as rows.

Anode Material	H_2	10 % H_2S/H_2	1 % H_2S/H_2
Ni-YSZ	11.8	8.33E-05	5.92E-05
$Ni_{(0.90)}Co_{(0.10)}$-YSZ	14.4	6.30E-05	6.87E-05
$Ni_{(0.80)}Co_{(0.20)}$-YSZ	12.4	2.27E-02	7.99E-05
$Ni_{(0.70)}Co_{(0.30)}$-YSZ	6.79	1.68E-02	1.03E-05

The data collected for the four cells of varying NiCo concentrations, as indicated in tables 5.1 and 5.2, present the effects of anode microstructure destruction upon addition of a high concentration of H_2S poison to the H_2 fuel feed. As seen by the smaller loss of exchange current density by the cells with high Co concentration ((1-x) = 0.20 and 0.30), the addition of Co to the anode produces a cermet with higher tolerance to the sudden addition of H_2S. Although all cells eventually succumb to microstructure destruction, the Co appears to provide chemical and mechanical tolerance to this change in chemical fuel environment.

5.3.1.2 Exchange current density data at intermediate H_2S concentration at various temperatures

Due to the apparent stress imposed on the lattice of the metallic phase of the cermet anode material upon addition of a high concentration of H_2S, it was postulated that a lower concentration of the sulfur poison at the onset of H_2S introduction to the fuel feed would allow for the expected conversion to the metal sulfide phase more gradually, and thus reduce the amount of physical destruction and delamination experienced by the porous cermet anode material and current collector. Since the $Ni_{(0.70)}Co_{(0.30)}$-YSZ cermet anode material was one of the compositions which was able to tolerate the addition of a high concentration of sulfur poisoning, it was chosen to investigate the synergistic behaviour of nickel and cobalt towards tolerating sulfur poisoning at several temperatures.

Presented in tables 5.3 and 5.4 are the EIS and direct current voltammetry data for the $Ni_{(0.70)}Co_{(0.30)}$-YSZ cermet anode material at 750°C, 800°C and 850°C. Firstly, an intermediate concentration of 7 % v/v H_2S in hydrogen allowed the anode to experience a reduction of approximately 50 % of its original activity with pure hydrogen for the temperatures of 750°C and 850°C, a much better tolerance to the initial introduction of the sulfur poison when compared to the introduction of 10 % v/v H_2S. Additionally, two separate trials at 800°C produced a 7.7-fold and 3.6-fold increase in the observed exchange current density respectively upon addition of 7 % v/v H_2S. It is clear from these observations that, for the $Ni_{(0.70)}Co_{(0.30)}$-YSZ anode composition, lowering the initial H_2S concentration allows the cell to either retain a large portion or increase its catalytic activity, despite the fact that H_2S is a well established poison for high temperature Ni-YSZ based fuel cells. A likely explanation is the slower conversion of the metallic phase to its corresponding metal sulfide is slower upon reduction of the initial H_2S concentration as well as the temperature of the fuel cell environment.

As the concentration was slowly raised through 10 %, 15 %, and 20% v/v H_2S, the exchange current density values were either maintained or continued to increase. With each successive poison concentration increase, once the bulk metallic phase has been converted to its thermodynamically stable metal sulfide phase, further large stresses on the metallic lattice are not expected. The apparent propensity for the metal sulfide to operate on a high concentration of H_2S in hydrogen (10 % - 20 %) is clear from the data presented below.

For the highest and lowest temperatures tested, 750°C and 850°C, as the concentration of H_2S approached 100 %, the exchange current density was either maintained, as in the lower temperature case, or experienced a sharp increase. Surprisingly, for the $Ni_{(0.70)}Co_{(0.30)}$-YSZ anode composition at 850°C, after gradual increase of the poison concentration until pure H_2S is reached, an 8.6-fold increase in the exchange current density compared to that of pure hydrogen is observed. It should be noted that this cell had been run on various poisoned fuel compositions for 60 hours (5 x 12 hours) prior to the commencement of the pure H_2S 12 hour measurements. This provides promising evidence for long term stability of $Ni_{(0.70)}Co_{(0.30)}$-YSZ cermet anodes exposed to high concentrations of H_2S.

The cell initially run at 800°C experienced complete loss of activity upon exposure to 50 % v/v H_2S, while those at 750°C and 850°C were able to withstand these concentrations. A separate button cell of the same anode composition was used to repeat the measurement at this puzzling temperature, however, a severe reduction of 4 orders of magnitude was observed at the same fuel composition. An explanation for this observation is that the two button cells, as observed by the lowered exchange current densities in pure hydrogen, were not as robust when compared to those at the higher and lower temperatures. This initial fragility was likely magnified upon the microstructural stresses imposed by the phase changes with the addition of H_2S to the fuel inlet.

Table 5.3 Exchange current density (i_o) values for the $Ni_{(0.70)}Co_{(0.30)}$-YSZ cermet anode composition at various temperatures and fuel compositions as indicated, expressed in units of mA/cm^2. These values were derived from EIS measurements. Here, the columns represent four separate cell test runs. The data derived from direct current voltammetry for the same four button cells is presented in table 5.4.

Fuel	750°C	800°C	800°C	850°C
H_2	10.11	0.270	0.685	2.30
7 % H_2S/H_2	4.61	2.08	2.48	1.68
10 % H_2S/H_2	6.94	1.41	3.79	1.41
15 % H_2S/H_2	3.25	3.07	4.44	1.42
20 % H_2S/H_2	4.81	2.53E-04	3.98	1.20
50 % H_2S/H_2	3.67	-	1.90E-04	1.53
100 % H_2S	2.73	-	2.00E-04	19.8
H_2	4.14E-03	-	1.50E-04	1.01

Table 5.4 Exchange current density (*i_o*) values for the $Ni_{(0.70)}Co_{(0.30)}$-YSZ cermet anode composition at various temperatures and fuel compositions as indicated, expressed in units of mA/cm^2. These values were derived from direct current voltammetry measurements. Here, the columns represent four separate cell test runs. The data derived from EIS measurements for the same four button cells is presented in table 5.3.

Fuel	750°C	800°C	800°C	850°C
H_2	8.29	0.338	0.835	2.76
7 % H_2S/H_2	4.57	1.44	0.226	1.07
10 % H_2S/H_2	2.50	6.82E-02	0.373	0.965
15 % H_2S/H_2	1.24	0.112	0.504	1.24
20 % H_2S/H_2	1.12	0.168	0.616	1.07
50 % H_2S/H_2	4.13	-	3.40E-04	1.59
100 % H_2S	2.26	-	3.08E-04	6.14
H_2	5.60E-03	-	1.53E-04	1.37

Lowering the initial poison concentration to 7 % v/v H_2S allowed the $Ni_{(0.70)}Co_{(0.30)}$-YSZ cermet anode composition to retain catalytic activity as the sulfur poison concentration was then raised slowly to 100 % H_2S at 750°C and 850°C. However, damage to the cell structure could not always be avoided, and at the median temperature of 800°C, two independent button cells experienced a drastic drop in exchange current density or a complete loss of current upon reaching 50 % v/v H_2S. As was discussed in the introduction, the effect of sulfur poisoning is reduced with an increase in operation temperature. As is observed for the cell at 850°C, 50 % of the exchange current density is recovered upon re-introduction of pure hydrogen following the outlined series of H_2S/H_2 concentrations; therefore, for the $Ni_{(0.70)}Co_{(0.30)}$-YSZ anode composition, a higher temperature produces a cell with the best concentration of the most robust microstructure and lowest effect of sulfur poisoning.

5.3.1.3 Exchange current density data at low H_2S concentration

As discussed above, upon the sudden addition of 10 % v/v H_2S to the H2 fuel, all of the cermet anode compositions suffered performance deterioration mostly due to the physical damage of the cell (delamination). It was postulated that further lowering the initial sulfur concentration could result in a cell that would successfully retain its exchange current density at a level comparable to that in pure hydrogen fuel as the concentration is raised past the level, which previously created problems at this temperature.

As can be observed in table 5.5, following measurement in pure hydrogen, a small amount of H_2S was introduced, 0.75 % v/v. Following stabilization after 12 hours of measurement, the exchange current density produced a larger value, by 1.8 times in the case of the EIS measurements. With the exception of a decrease upon addition of 1.1 % v/v H_2S, the cell produced comparable or higher exchange current density values for all sulfur poison concentrations, including pure H_2S.

It would appear that as long as the sulfur poison is introduced gradually enough for the cell to avoid experiencing a large change in the lattice parameters upon the conversion of the metallic phase of the cermet to bulk metal sulfide, the cell is able to tolerate a wide range of H_2S concentrations from low (0.75 % v/v) up to pure H_2S as fuel.

Table 5.5 Exchange current density (i_o) values for the $Ni_{(0.70)}Co_{(0.30)}$-YSZ cermet anode for various fuel compositions at 800°C. These values were derived from EIS measurements (EIS), or derived from direct current voltammetry measurements (DCV), as indicated.

Fuel	i_o (mA/cm^2) EIS	i_o (mA/cm^2) DCV
H_2	1.65	1.30
0.75 % H_2S/H_2	3.01	1.44
1.1 % H_2S/H_2	0.128	0.558
1.73 % H_2S/H_2	1.54	1.67
2.44 % H_2S/H_2	2.72	2.26
10 % H_2S/H_2	2.00	1.68
100 % H_2S	2.37	1.67

It is believed that the combination of the synergistic relationship of the nickel and cobalt alloyed in the metallic phase of the cermet anode coupled with a sulfur poison concentration high enough to easily generate a bulk metal sulfide phase at the operational temperatures outlined above are responsible for the ability of this material to retain and in some cases surpass the exchange current density observed in the pure hydrogen fuel. The overall electro-oxidation reactions occurring on the surface of the anode are important to understanding why the anode can retain or surpass its catalytic activity with a large concentration of sulfur poison present. In order to accomplish this, the value for the open circuit voltage (OCV) can be compared to the known values for specific reactions.

5.3.2 Open circuit voltage (OCV) data to shed light on the electrochemical mechanism

All OCV values for the three concentrations designated as high, medium and low as presented in section 5.3.1 are shown below in tables 5.6 to 5.8. The value of the OCV for a cell with a given fuel environment can indicate which reaction is occurring; alternatively, given a fuel mixture, an intermediate value between two known values will indicate a mixed mechanism. This method can be used to determine which fuel(s) is/are being electrochemically oxidized on the anode surface.

As can be seen for the three tables presented in this section, the value for the OCV in pure hydrogen ranges between 1.02 V and 1.36 V. Since the expected value is near 1.2 V for the electro-oxidation of pure hydrogen, these values are within the expected measurement variation. The variation above the expected value is attributed to the low fuel consumption, where OCV is expected to rise as the percentage of fuel consumption lowers, as is predicted by the Nernst equation, equation 1.23; conversely, the variation below the expected value is likely due to imperfections in the softened pyrex seal, where a small oxygen leak is expected to lower the OCV value.

Upon addition of 10 % H_2S/H_2 as the fuel, there was no change observed in the OCV value for the two highest cobalt concentrations in the cermet anode material, as indicated in table 5.6. This is diagnostic evidence that the predominant electrochemical mechanism on the cermet anode surface did not change from hydrogen electro-oxidation. Values which are not shown correspond to a significant loss in exchange current density. These values were determined to be unreliable due to unfavourable changes in microstructure and/or delamination of the anode material or the current collector. Both of these changes would likely result in significant current constriction.

Table 5.6 OCV values for various $Ni_xCo_{(1-x)}$-YSZ cermet anode compositions at 850°C for the fuel compositions shown. These values were collected for the same button cells as those presented in tables 5.1 and 5.2.

Anode Material	H_2 OCV (V)	10 % H_2S/H_2 OCV (V)	1 % H_2S/H_2 OCV (V)
Ni-YSZ	1.06	-[a]	-[a]
$Ni_{(0.90)}Co_{(0.10)}$-YSZ	1.05	-[a]	-[a]
$Ni_{(0.80)}Co_{(0.20)}$-YSZ	1.06	1.09	-[a]
$Ni_{(0.70)}Co_{(0.30)}$-YSZ	1.26	1.24	-[a]

[a] OCV values were unreliable due to a severe decrease in the measured exchange current density values for these button cells (see tables 5.1 and 5.2).

Shown in table 5.7, two complete sets of data ranging between 7 and 100 % H_2S/H_2 were collected at 750 and 850°C. As the H_2S concentration is increased to 20 % H_2S/H_2 at 750°C, the predominant reaction is hydrogen electro-oxidation. However, upon addition of 50 % H_2S/H_2 and subsequently pure H_2S, the notable drop in OCV indicates a rise in the amount of H_2S undergoing electro-oxidation. As stated for equations 5.2 and 5.3, the OCV for H_2S is lowered compared to hydrogen, which serves to reinforce this conclusion. Complete recovery is shown upon returning the fuel composition to pure hydrogen at 850°C. Experimental evidence by Yates and Winnick [28] indicate 8.6 % hydrogen will be produced by gas phase decomposition of H_2S at 700°C. This is corroborated by calculations done by Monder [29] for this gas phase decomposition in the temperature range of 750°C to 850°C, giving percentage decomposition amounts of 5.5 % and 10.1 %, respectively. This low amount of thermal decomposition is in agreement with the observed OCV values, which do not differ to a large extent from the value measured for pure hydrogen. Given the lowered values for the oxidation of H_2S, equations 5.2 and 5.3, it is not expected that an appreciable amount of electro-oxidation of this species is occurring on the anode surface.

Table 5.7 OCV values for the $Ni_{(0.70)}Co_{(0.30)}$-YSZ cermet anode composition for various fuel compositions and temperatures as indicated. These values were collected for the same button cells as those presented in tables 5.3 and 5.4.

Fuel	750°C OCV (V)	800°C OCV (V)	850°C OCV (V)
H_2	1.02	1.36	1.33
7 % H_2S/H_2	1.06	1.32	1.32
10 % H_2S/H_2	1.05	1.31	1.3
15 % H_2S/H_2	1.03	1.3	1.3
20 % H_2S/H_2	1.01	1.3	1.29
50 % H_2S/H_2	0.912	-[a]	1.24
100 % H_2S	0.546	-[a]	1.13
H_2	-[a]	-[a]	1.33

[a] OCV values were unreliable due to a severe decrease in the measured exchange current density values for these button cells (see tables 5.3 and 5.4).

As is indicated in table 5.8, an intermediate drop in OCV value is observed upon addition of H_2S. The value for 10 % H_2S/H_2 agrees well with that in table 5.7. Upon addition of pure H_2S, a value intermediate to those found for 750 and 850°C in table 5.7 is indicated, showing that an increase in temperature increases the amount of hydrogen undergoing electro-oxidation. This is in agreement with the expected pyrolysis of H_2S, which increases with temperature.

Table 5.8 OCV values for the $Ni_{(0.70)}Co_{(0.30)}$-YSZ cermet anode composition for the various fuel compositions indicated at 800°C. These values were collected for the same button cell as those presented in table 5.5.

Fuel	OCV (V)
H_2	1.35
0.75 % H_2S/H_2	1.34
1.1 % H_2S/H_2	1.34
1.73 % H_2S/H_2	1.33
2.44 % H_2S/H_2	1.33
10 % H_2S/H_2	1.29
100 % H_2S	0.988

5.3.2.1 Trends in resistances with intermediate H_2S concentration

Values for the serial resistance (R_S) at the high frequency intercept, and the charge transfer resistance (R_{CT}) the low frequency depressed semi-circle arc, are obtained from the EIS data with different fuel environments as indicated in figure 5.3. At the 850°C temperature and $Ni_{(0.70)}Co_{(0.30)}$-YSZ cermet anode composition, increasing the H_2S concentration with intermediate steps shows a gradual increase in the series resistance, approaching a plateau at 50 % H_2S/H_2. A likely hypothesis for this observation is the conversion of the bulk nickel sulfide phase through various compositions with increasing sulfur concentration in the fuel stream, passing through compositions, which may be NiS_2, Ni_7S_6, NiS, Ni_3S_4 or Ni_3S_2, or a mixture of two or more of these compositions. Since nickel sulfide is known to be conductive and metallic, [30] the resistance will not increase drastically; however, the electrical conductivity of nickel sulfide is lower than that of pure nickel, [31] thus it will increase the series resistance of the anode half cell. Upon returning to pure hydrogen, a comparable value for R_S was observed, though it is slightly higher than the original one, likely due to irreversible microstructural transformations.

In the case of the charge transfer resistance, an initial large increase followed by a plateau is observed upon addition of 7 to 15 % H_2S/H_2. This large increase is likely due to the rapid adsorption of sulfur onto the anode surface followed by conversion of the metallic phase to its corresponding metal sulfide. Once this change in bulk and surface composition has occurred, at these concentrations, the amount by which the surface oxidation reaction is inhibited remains constant.

An interesting and unexpected change in R_{CT} is observed as the concentration of H_2S is further increased until pure H_2S is applied as the fuel. The R_{CT} value begins to decrease, and eventually falls well below that of pure hydrogen. The cermet anode with its metallic phase is expected to be a metal sulfide, which gives a very low R_{CT} value for the electro-oxidation of pure H_2S. Although at this temperature, a small amount of hydrogen is expected to be present due to pyrolysis, the predominant fuel is still expected to be H_2, as shown by the OCV value in table 5.8 (at 1100°C, only 8.6 % hydrogen will result from the pyrolysis reaction). [28] As indicated by the OCV value, if hydrogen is present, the anode will use it preferentially as fuel over H_2S.

Recovery of the anode upon returning to pure hydrogen fuel is not observed. The value for R_{CT} is comparable to those obtained for 7 to 15 % H_2S/H_2. This indicates irreversible adsorption of sulfur on the surface of the metallic phase of the cermet anode. Sulfur is known to occupy up to 0.50 ML at high sulfur concentration (vide supra). Upon removal of the sulfur, desorption of sulfur lower than 0.25 ML is highly unfavourable, and is not expected to occur in a pyrolytic atmosphere. [3] This can have a significant effect on surface reactions, as is observed by the large value for R_{CT} for hydrogen following a pure H_2S atmosphere. In conjunction, changes in microstructure upon exposure to sulfur and prolonged exposure to high temperature can be responsible for the irreversibility observed in the R_{CT} value for pure hydrogen.

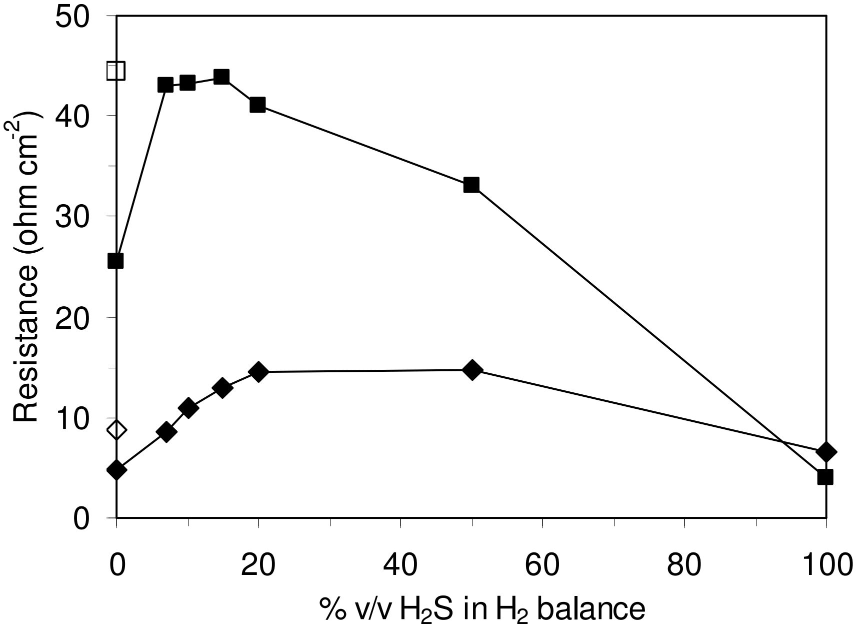

Figure 5.3 Resistance values at 850°C for the $Ni_{(0.70)}Co_{(0.30)}$-YSZ cermet anode composition. The serial resistance (R_S) (♦) and the charge transfer resistance (R_{CT}) (■) for increasing H_2S concentration are shown. Open shapes indicate R_S (◊) and R_{CT} (□) upon returning to pure hydrogen fuel following pure H_2S fuel.

5.3.3 Data for post mortem anode material

Following cooling the anode material slowly in either pure hydrogen or a H_2S/H_2 fuel mixture, as indicated, materials data was collected to gain insight into the electrochemistry of the anode. Due to logistical difficulties, it was not possible to cool down the anode material quickly, namely to 'quench' the anode material, in order to capture the material in a state that would more closely resemble an *in situ* composition. Because of this, as will be discussed, chemical changes occurred upon slow cooling.

5.3.3.1 Scanning electron microscopy (SEM) and energy dispersive X-ray spectroscopy (EDS)

Upon inspection of the post-mortem cermet anode material following fuel testing in a H_2S/H_2 environment, interesting characteristics could be distinguished. Powder recovered from an anode which became delaminated with increasing H_2S concentration at 800^oC and subsequently cooled slowly in 10 % H_2S/H_2 can be seen in figure 5.4. The largest noteworthy characteristic is the formation of spheres which appear to be solid, non-porous and on occasion possess crystal facets. Spheres of different size, approximately 15 μm in panel A, and 40 μm in panel B are visible. These spheres are always attached to a large porous particle. Ridges which appear to be consistent with crystallinity are visible in the sphere in panel A. This indicates a significant change in microstructure from the starting, as-synthesized, material. In order to further characterize changes in the physical features of the microstructure of the cermet anode material, comparisons with precursor material are invaluable.

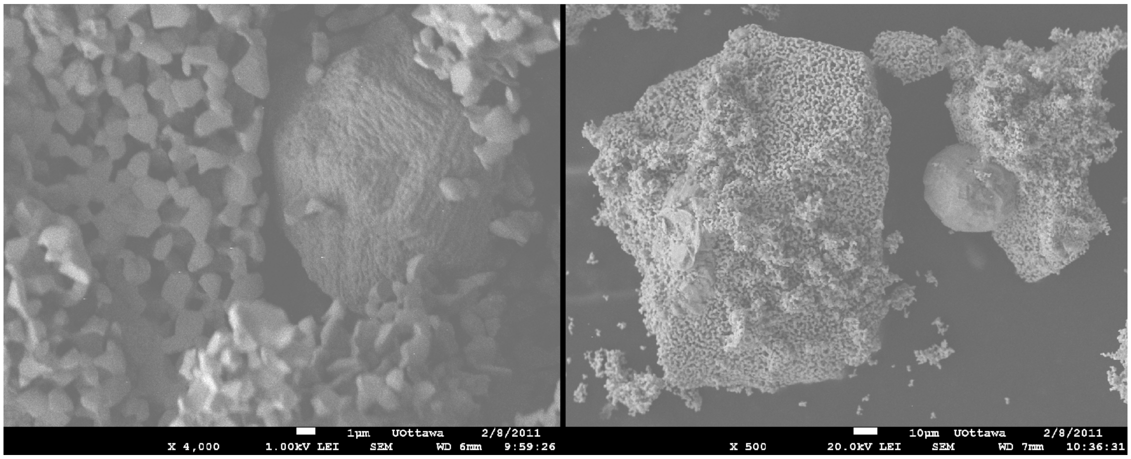

Figure 5.4 Post-mortem SEM images of $Ni_{(0.70)}Co_{(0.30)}$-YSZ cermet anode following exposure of increasing concentrations of H_2S/H_2 mixtures up to pure H_2S at 800°C. (A) shows a magnification of 4000x with a measurement bar of 1 μm, (B) shows a magnification of 500x with a magnification bar of 10 μm.

The cross-section of the cermet anode prior to exposure to high temperature and a reducing environment is shown in figure 5.5A. Here the porous material of the anode can be seen with large pores on the order of several micrometres visible between large agglomerates of particles on the order of several tens of micrometres. The dense, non-porous material of the YSZ electrolyte layer is visible at the bottom of the image. The success of the co-sintering process to form a porous anode layer which has good physical, and thus electrical, connection to the electrolyte layer is visible. In addition to these features, a cross section of an agglomerate particle can be seen just to the left of the centre of the image; here the protrusions of the individual particles are clear. These particles appear to be on the order of approximately one to three micrometres. Upon reduction of the material in hydrogen at 850°C for a minimum of 1 hour, the metallic phase of the anode is reduced. The lattice of this phase, upon loss of oxygen, experiences a contraction, producing a secondary pore structure, figure 5.5B. Here the pores and particles are less than 1 μm, greatly increasing both the surface area and total pore volume.

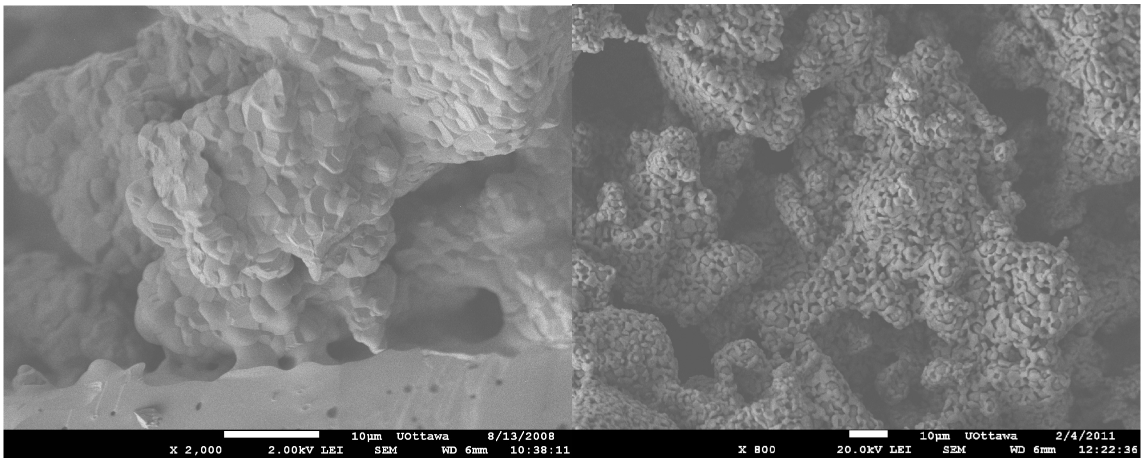

Figure 5.5 (A) Precursor cross-section of the $Ni_{(0.70)}Co_{(0.30)}$-YSZ cermet anode before exposure to fuel cell operating conditions (high temperature and reducing environment). This image shows a magnification of 2000x and a measurement bar of 10 µm. (B) Identical anode material following exposure to a clean reducing atmosphere (no sulfur or carbon compounds) at 850°C for a minimum time of 1 hour. This image shows a magnification of 800x and a measurement bar of 10 µm.

Upon reduction at high temperature and exposure to H_2S, followed by slow cooling in 10 % H_2S/H_2, the microstructure of the cross-section of the anode is visibly altered, as can be seen in figure 5.6. The large agglomerations of particles which were visible before the reduction are now porous. This creates two size ranges of pores: one of small size, on the order of one micrometre generated upon the reduction of the anode material, and another of larger size, on the order of ten micrometres, which existed upon co-sintering of the anode precursor powder. This newly porous material still possesses good physical contact with the non-porous YSZ electrolyte, as can be seen at the bottom of the image.

A second feature is comprised of large spheres, as introduced above, where six are visible in the image below ranging from approximately 5 to 15 micrometres in diameter. These spheres form both at the interface of the working electrode and electrolyte layer as well as beyond the expected active region of 10 µm, as discussed in chapter 2. In order to determine the possible mechanism of formation of these spheres, information about their elemental composition, as collected by EDS, can shed light on this curiosity.

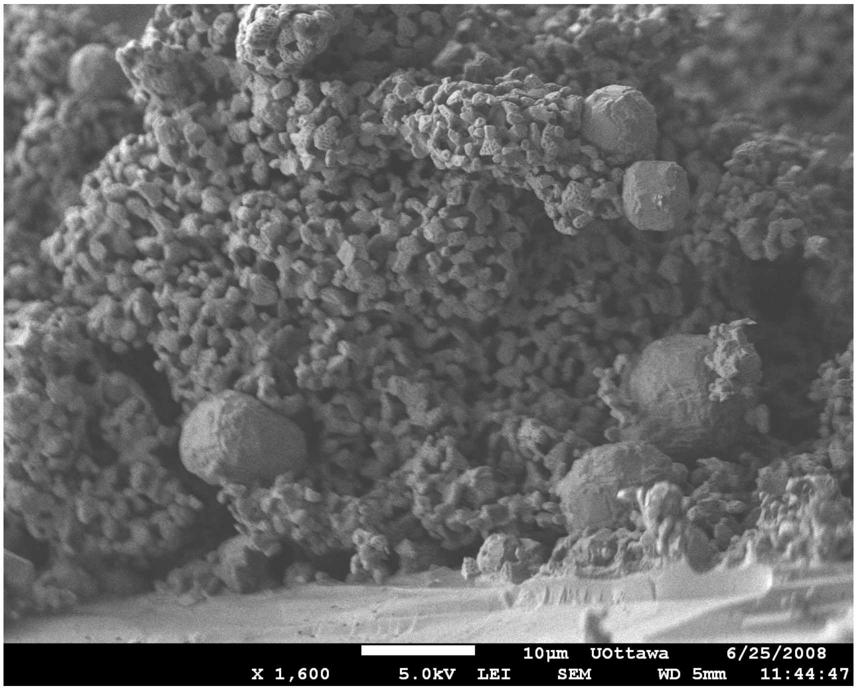

Figure 5.6 Cermet cross-section of the $Ni_{(0.70)}Co_{(0.30)}$-YSZ cermet anode post-mortem, following exposure to varying H_2S/H_2 concentrations at 850^{o}C. This image shows a magnification of 1600x and a measurement bar of 10 µm.

The EDS spectrum, as shown in figure 5.7, shows the spectra for the two microstructural features. In panel A, the spectrum for the solid spheres shows a strong enrichment in sulfur (~2.4 keV), as well as nickel and cobalt (~0.9 and ~7.6 keV), which indicates that this particle is likely a NiCo (alloyed) sulfide. A minor peak is visible for yttrium and zirconium (~2.1 keV), which is likely due to a contribution of the surrounding environment of the spectral region. This provides definitive evidence that this particle is composed of a nickel-cobalt sulfide. The exact formulation cannot be determined by this method, since a flat surface is required for quantitative EDS, which is not present on this round particle. Also of note, since the powder was cooled slowly in a hydrogen atmosphere, the presence of nickel-cobalt sulfide spheres in the post mortem cermet material indicates the irreversibility of the formation of this metallic sulfide phase under the pyrolytic conditions during cooling.

The amorphous, porous particle shown in panel B possesses the opposite characteristics, namely strong zirconium and yttrium peaks, and weak sulfur, nickel, and cobalt peaks when compared to the previous spectrum. This indicates a particle composed predominantly of YSZ. The apparent separation of these two phases upon exposure to H_2S at high temperature has been previously reported by Lussier *et al.* [32] [33] They observed that the nickel in their Ni-YSZ anode experienced a “depletion in the anode, thereby compromising the percolating and electronically conductive Ni phase in the anode”. This is a similar effect as can be seen in this post-mortem EDS spectrum. The porous YSZ particle contains very low levels of the metal, which would have the effect of reducing the ability of the metal phase to act as a current collector throughout the anode. Given the dispersion of the EDS beam, this minor nickel phase could be either in or around the YSZ phase. However, it should be emphasized that it is possible that this post mortem observation does not reflect the morphology of the anode microstructure *in situ* under the operational conditions at high temperature and under a reducing, H_2S containing atmosphere. Composition changes are possible for the nickel sulfide as the anode material cools down from the high operational temperature, as well as large microstructural changes as the nickel sulfide, likely in a liquid or near-liquid state, cools and solidifies upon slow cooling in a hydrogen environment. *In situ* observations are made difficult due to the physical fuel cell set up, the anode is isolated in a sealed compartment to avoid contact with air, and the fuel cell is operated at high temperature, making any manipulations with the set up impossible once the fuel cell is operational.

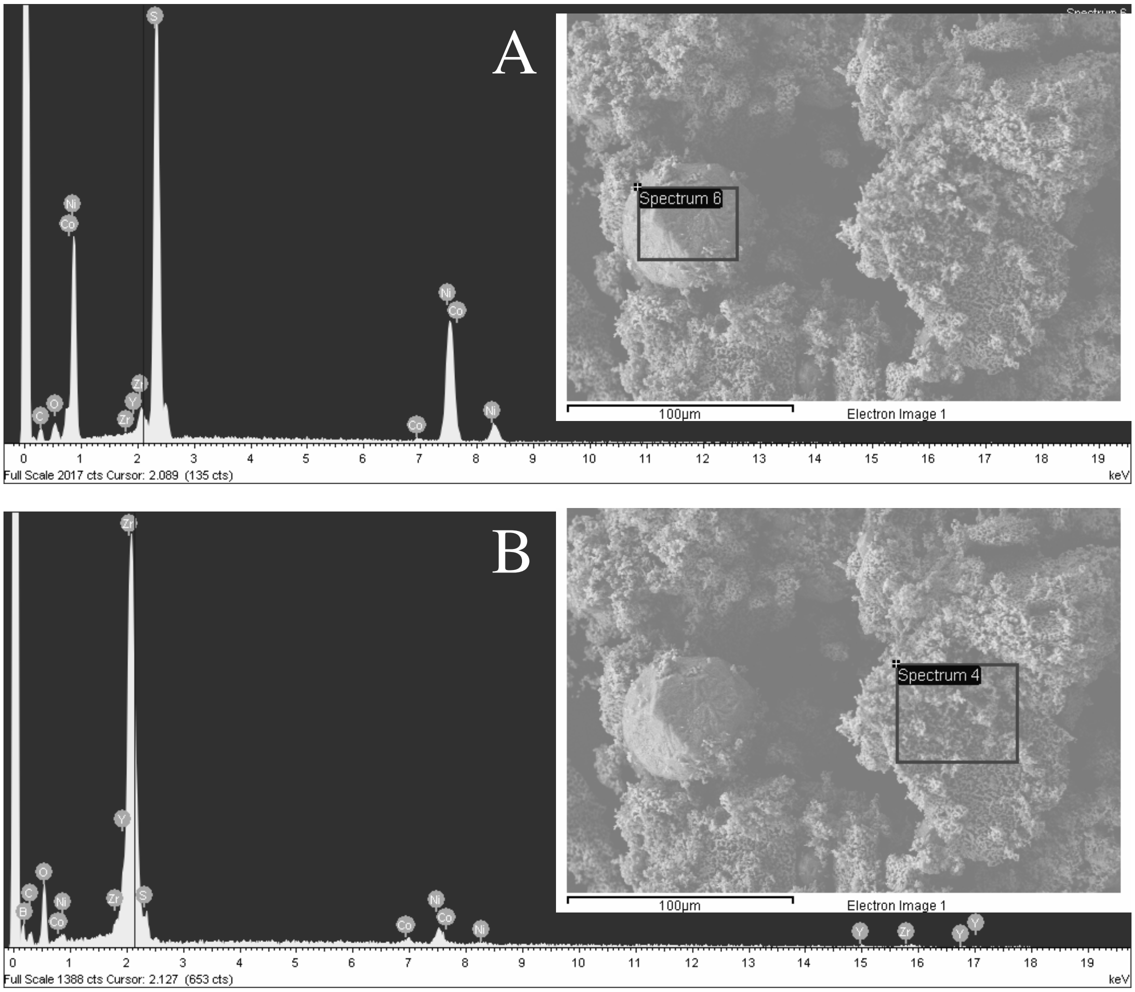

Figure 5.7 EDS spectra of the two morphological features of the $Ni_{(0.70)}Co_{(0.30)}$-YSZ cermet anode post-run with various H_2S/H_2 concentrations at 800°C. (A) shows the EDS of the solid sphere, and (B) shows the EDS of a porous particle. The predominant peaks are as follows: Zr at 2.0 keV, S at 2.31 keV, Co at 0.77 & 6.9 keV, Ni at 0.85 & 7.4 keV.

5.3.3.2 Powder X-ray diffraction (pXRD)

The pXRD spectrum of a $Ni_{(0.70)}Co_{(0.30)}$-YSZ cermet anode following slow cooling in 10 % H_2S/H_2 after exposure to pure H_2S at 850°C is shown in figure 5.8. Three major bulk phases are identified, namely Ni_3S_2 (PDF# 27-0341), YSZ (PDF# 48-0224) and Ni (PDF# 04-0850). The presence of only one sulfide phase, Ni_3S_2, is an artifact of the slow cooling process. Due to logistic difficulties, the high operating temperature, and safety concerns, a fast 'quench' of the anode was not possible, therefore the nickel sulfide phase observed is that which is most thermodynamically stable at low sulfur partial pressure. The observation of a nickel phase, also observed by Lussier *et al.*, upon cooling a nickel anode following treatment with an H_2S atmosphere, is likely due to partial recovery of the metallic phase upon cooling in the hydrogen atmosphere. A shift towards higher 2Theta values indicates a significant concentration of metallic cobalt present. Finally, the expected YSZ phase is also observed. This result is in agreement with the microstructural features observed in the SEM images shown above.

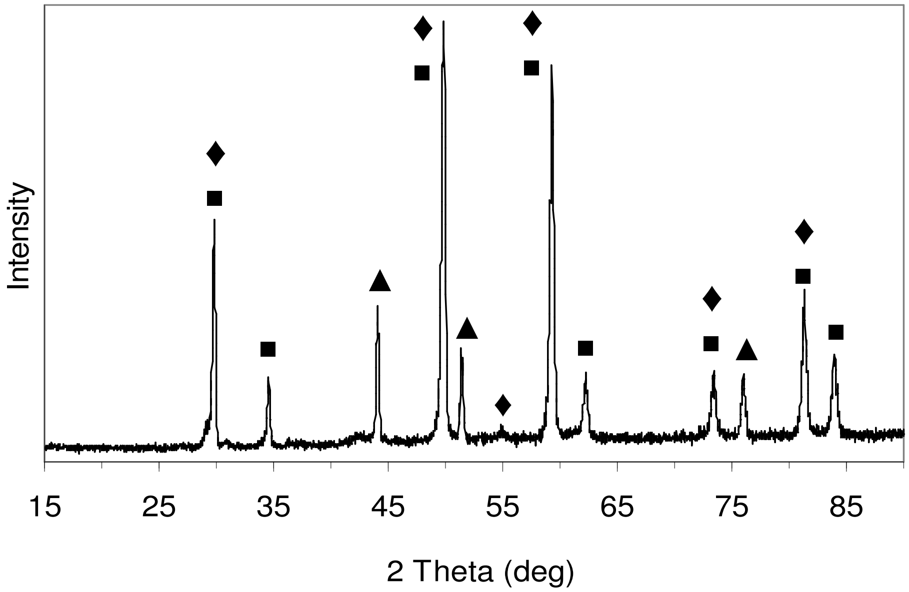

Figure 5.8 Powder XRD spectrum of post-mortem $Ni_{(0.70)}Co_{(0.30)}$-YSZ cermet anode material following slow cooling in H_2 after exposure to pure H_2S at 850°C. Major bulk phases present include Ni_3S_2 (♦), YSZ (■), and Ni (▲).

5.3.4 Cross-section of H_2S treated nickel foil

To back up arguments in section 5.3.1.1 concerning the formation of a bulk metal sulfide phase under operating conditions which include an H_2S containing atmosphere, a pure nickel foil of 0.20 mm thickness was exposed to an H_2S environment to investigate and back up observations of bulk nickel sulfide phase formation. This study was instigated to investigate the depth to which sulfur can percolate in nickel under the given experimental conditions (following paragraph) and the reversibility of this sulfur percolation. Due to practical set-up prohibitions, *in situ* experiments were not possible;

therefore this *ex situ* experiment was undertaken in an attempt to assess the depth of sulfur percolation in the metallic phase in the cermet material.

In order to mimic conditions experienced by the cermet material during fuel cell operation, the nickel foil was placed into a quartz tube and heated to 850°C in a flowing atmosphere of 10 % H_2S/H_2 for 6 hours. It was then allowed to cool slowly in the same atmosphere. The cross-section of the resultant foil is shown in figure 5.9. Whereas the initial pure nickel foil was solid with a uniform thickness and a relatively smooth surface, the resultant foil has very different characteristics. The thickness is no longer uniform and varies between approximately 250 and 300 μm as shown. Large pores on the order of hundreds of micrometres have formed. The surface which was facing upwards in the quartz tube, which is also the upper surface shown in the micrograph, has formed a separate layer, which has lifted off from the bulk foil. Here, spheres of the same shape and size as those observed in the post-mortem cermet anode material, figures 5.4 and 5.6, are seen. Stoklosa and Stringer also reported the formation of "scales" on the surface and inner pores within the material upon the treatment of bulk nickel which undergoes sulfidation in a sulfur vapour atmosphere. [34]

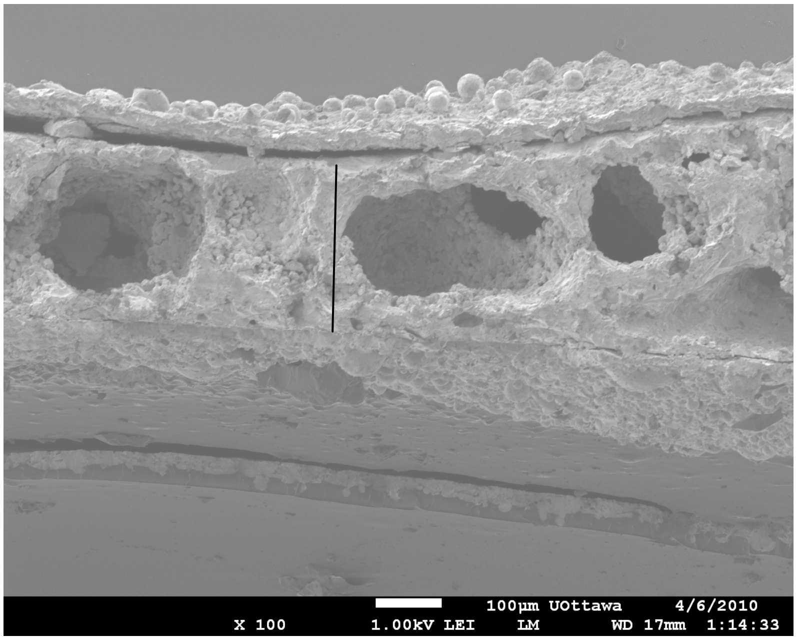

Figure 5.9 SEM image of the cross-section of a piece of Ni foil exposed to an H_2S atmosphere. Magnification is 100x and the measurement bar represents 100 μm. A line was drawn to indicate the location of the 10 point cross-section collection location.

Cross-sectional EDS data at two different locations on the foil were collected with an interest towards the depth of percolation of sulfur into the nickel at conditions identical to those of the cermet anode material for a time of comparable length to that needed for electrochemical measurements to stabilize. It should be noted that, due to the roughness of the foil, quantitative analysis is not possible. As is outlined in table 5.9, EDS line analyses were collected at two different locations on the treated foil. The ten-point analysis corresponds to the cross-section seen to the left of the centre of the image in figure 5.8; the four-point analysis corresponds to a cross-section outside this image. Due to the large pores formed upon treatment, a cross-section which was free of defects was unfortunately not found along the length of the cross-section.

At a depth corresponding to more than 100 μm, the centre points of both analyses contain appreciable amounts of sulfur. Other points nearer to the surface, at both ends of the line analysis, contain high levels of sulfur. Although an ideal quantitative analysis was not possible due to the roughness of the surface, it can be concluded that sulfur was able to percolate the full thickness of the foil and that this process is irreversible under these experimental conditions. With the expected particle size near 1 μm, figure 5.6, the particles in the metallic phase of the cermet material are expected to be composed of bulk nickel sulfide.

Table 5.9 EDS data for the cross section of nickel sulfide foil shown in figure 5.7. Percentages shown correspond to atomic percent of each atom. Points correspond to the number of EDS point spectra collected equidistant along a cross sectional line of the nickel sulfide foil.

Point	% S	% Ni
1	51	49
2	45	55
3	53	47
4	59	41
5	68	32
6	7	93
7	38	62
8	26	74
9	57	43
10	8	92

Point	% S	% Ni
1	39.02	60.98
2	6.04	93.96
3	9.97	90.03
4	50.71	49.29

5.4 Conclusions

Although conversion of the fuel feed following reduction in pure hydrogen to a mixture with high concentration of H_2S, namely 10 % H_2S/H_2, produced a sudden change in anode microstructure and resulted in loss of exchange current density, lowering the amount of H_2S in the initial fuel feed, which allowed for a more gradual microstructural change, allowed the cell to eventually function at concentrations in excess of 10 % H_2S/H_2. The OCV of the cells with various concentrations of H_2S/H_2 did not change significantly from that of hydrogen, indicating that hydrogen is the predominant fuel of choice, even if H_2S is available. Under pure H_2S fuel, the OCV was lowered, as is expected for the electro-oxidation of this species.

Upon reduction of the metallic phase, pores on the order of 1 μm formed, as observed by SEM. With the addition of H_2S/H_2 mixtures at operational temperature followed by slow cooling in a 10 % H_2S/H_2 mixture, metal sulfide spheres formed indicating the irreversibility of the formation of a metal sulfide phase under pyrolytic conditions, as determined by SEM and EDS. To assess the depth of percolation of sulfur in nickel, a nickel foil was treated with 10 % H_2S/H_2 followed by slow cooling; conversion of the full cross-section of the foil indicates that it is likely the (much smaller) metal phase particles in the cermet anode material undergo complete conversion to metal sulfide under operating conditions in a H_2S/H_2 fuel inlet mixture.

5.5 References

[1] R.J. Gorte, S. Park, J.M. Vohs, C. Wang, Adv. Mater. 12 (2000) 1465.

[2] A.M. Sukeshini, B. Habibzadeh, B.P. Becker, C.A. Stoltz, B.W. Eichhorn, G.S. Jackson, J. Electrochem. Soc. 153 (2006) A705.

[3] N.M. Galea, F.S. Kadantsev, T. Ziegler, J. Phys Chem. C 111 (2007) 14457.

[4] K. Sasaki, K. Susuki, A. Iyoshi, M. Uchimura, N. Imamura, H. Kushaba, Y. Teraoka, H. Fuchino, K. Tsujimoto, Y. Uchida, J. N., J. Electrochem. Soc. 153 (2006) A2023.

[5] Y.M. Choi, C. Compson, M.C. Lin, M. Liu, Chem. Phys. Lett. 427 (2006) 25.

[6] E.J. Albenze, A. Shamsi, Surf. Sci. 600 (2006) 3202.

[7] H. Kishimoto, T. Horita, K. Yamaji, M.E. Brito, Y.-P. Ziong, H. Yokokawa, J. Electrochem. Soc. 157 (2010) B802.

[8] P. Lohsoontorn, D.D.L. Brett, N.P. Brandon, J. Power Sources 183 (2008) 232.

[9] T. Rosenqvist, J. Iron Steel Inst. (1954) 37.

[10] J.-H. Wang, M. Liu, Electrochem. Commun. 9 (2007) 2212.

[11] Z. Cheng, M. Liu, Solid State Ionics 178 (2007) 925.

[12] H.-T. Chen, Y.-M. Choi, M. Liu, M.C. Lin, J. Phys. Chem. C 111 (2007) 11117.

[13] H.P. He, R.J. Gorte, J.M. Vohs, Electrochem. Solid-State Lett. 8 (2005) A279.

[14] C.M. Grgicak, R.G. Green, W.-F. Du, J.B. Giorgi, J. Am. Ceram. Soc. 88 (2005) 3081.

[15] C.M. Grgicak, R.G. Green, J.B. Giorgi, J. Mater. Chem. 16 (2006) 885.

[16] J. Dong, D. Cheng, S. Sha, M. Liu, J. Power Sources 156 (2006) 461.

[17] J. Dong, S. Sha, M. Liu, Electrochemical Society Proceedings 2005-07 (2005-07) 1284.

[18] N.U. Pujare, K.W. Semkow, A.F. Sammells, J. Electrochem. Soc. 134 (1987) 2639.

[19] G. Wei, J. Luo, A. Sanger, K. Chuang, J. New Mater. Electrochem. Soc. 8 (2005) 59.

[20] M. Liu, G. Wei, J. Luo, A.R. Sanger, K.T. Chuang, J. Electrochem. Soc. 150 (2003) A1025.

[21] D.R. Alfonso, Surf. Sci. 602 (2008) 2758.

[22] N.M. Galea, J.M.H. Lo, T. Ziegler, J. Catal. 263 (2009) 380.

[23] D.S. Monder, K. Karan, J. Phys. Chem. C 114 (2010) 22597.

[24] M. Gong, X. Liu, J. Trembly, C. Johnson, J. Power Sources 168 (2007) 289.

[25] M. Binoist, B. Labegorre, F. Monnet, P.D. Clark, N.I. Dowling, M. Huang, D. Archambault, E. Plasari, P.-M. Marquaire, Ind. Eng. Chem. Res. 42 (2003) 3943.

[26] Z. Cheng, S. Zha, M. Liu, J. Power Sources 172 (2007) 688.

[27] A.I. Marquez, Y. De Abreu, G.G. Botte, Electrochem. Solid-State Lett. 9 (2006) A163.

[28] C. Yates, J. Winnick, J. Electrochem. Soc. 146 (1999) 2841.

[29] D. Monder, Modelling Studies for Hydrogen Sulphide Fuelled SOFCs., University of Alberta, Edmonton, AB, 2008, p. 204.

[30] V.B. Tare, J.B. Wagner Jr., J. Appl. Phys. 54 (1983) 252.

[31] H. Yagi, J.B. Wagner Jr., Oxid. Met. 18 (1982) 41.

[32] A. Lussier, S. Sofie, J. Dvorka, Y.U. Idzerda, Int. J. Hydrogen Energy 33 (2008) 3945.
[33] C.M. Grgicak, Anodes for solid oxide fuel cell (SOFC) systems operating in multiple fuel environments: Effects of microstructure and composition, University of Ottawa, Ottawa, 2007.
[34] A. Stoklosa, J. Stringer, Oxid. Met. 11 (1977) 263.

6

Electrochemical Characterization of Ni$_x$Co$_{(1-x)}$-YSZ Cermet Anodes in Various Hydrocarbon Fuels

6.1 Introduction

Due to the high operational temperature of SOFCs, they can operate with a diverse range of fuels. For the case of nickel-based cermet anodes, their ability to utilize carbon-containing fuels, such as hydrocarbons, alcohols, and biodiesel, make them an attractive technology for bridging the gap between the existing infrastructure and the predicted future hydrogen infrastructure. [1] This chapter will explore the ability of the developed Ni$_{0.7}$Co$_{0.3}$-YSZ cermet catalyst to utilize pure (dry) hydrocarbon fuel as well as hydrocarbon fuel containing a considerable level of sulfur poisoning in the form of H_2S. As such, the effect of carbon poisoning with an emphasis in fundamental mechanistic research will be explored, as well as the effect of sulfur and carbon poisons in conjunction with each other.

A common method to reduce carbon poisoning is to introduce oxygen into the fuel stream in the form of steam. [2] This stimulates reforming reactions to occur on the catalyst surface. However, this lowers the performance of the fuel cell. It is the desire of this research work to push forward in the development of a catalyst, which does not require the addition of oxygen to the fuel stream by studying the fundamental electrochemistry which occurs on the surface in the presence of pure (dry) hydrocarbon fuels.

6.1.1 Traditional Hydrocarbons as Fuel

At typical SOFC operation temperature, methane, the simplest hydrocarbon, is very unreactive – it does not undergo decomposition reactions at high temperature without a catalyst. However, in the presence of nickel, it is known to decompose readily. Typically, it generates various forms of carbon deposits on the surface of the metal catalyst, such as graphite, carbon rods, tubes, or particles, in either ordered or disordered structures. [3] In the minimal case, carbon can simply coat the metallic surface and block active sites from encountering fresh fuel molecules. This can increase ohmic resistances and reduce the performance of the cell. If left to continue, it can block the pores and severely reduce gas phase diffusion. In the extreme case, carbon formation can be severe enough to destroy the structure of a catalyst. For the case of a porous cermet anode, the formation of carbon can exceed the volume of the natural pore and rupture the anode microstructure. If further coking occurs, it can delaminate the anode from the electrolyte surface. It should, however, be emphasized that it is the problem of uncontrolled coke formation which causes poisoning of the cell, if efficient oxidation can be promoted, carbon poisoning can be readily avoided.

As discussed in previous chapters, the *in situ* measurements of the mechanism of hydrocarbon electro-oxidation on the surface of a cermet anode catalyst is difficult. In recent years, DFT calculations have shed light on the likely mechanisms which can occur on the catalyst surface. For the oxidation of methane in a fuel cell, the overall reaction can be expressed as follows.

$$CH_{4(g)} + 2O_{2(g)} \rightarrow CO_{2(g)} + 2H_2O_{(g)} \qquad (6.1)$$

When considering the detailed mechanism which is followed for a nickel-based cermet anode catalyst, it has been found to differ depending on the surface topology. Whereas, the mechanistic beginning and ending steps are identical for all topologies, for a stepped and terraced catalyst surface, it was found to differ. For a stepped surface, namely for a Ni(211) surface studied, it was found to follow the pathway through equations 6.6A and 6.7A, and for a terraced surface, namely Ni(111), the pathway through equations 6.6B and 6.7B is followed. [4] This study was done at 627°C and under OCV. Here, *M* as a subscript designates a surface chemisorption interaction and a stand-alone *M* indicator designates an empty catalyst surface site.

$$O^{2-}{}_{electrolyte} \rightarrow O_M + 2e^- \qquad (6.2)$$

$$CH_{4(g)} + 2M \rightarrow CH_{3(M)} + H_{(M)} \qquad (6.3)$$

$$CH_{3(M)} + M \rightarrow CH_{2(M)} + H_{(M)} \qquad (6.4)$$

$$CH_{2(M)} + M \rightarrow CH_{(M)} + H_{(M)} \qquad (6.5)$$

$$CH_{(M)} + M \rightarrow C_{(M)} + H_{(M)} \qquad CH_{(M)} + O_{(M)} \rightarrow HCO_{(M)} + M \qquad (6.6A,B)$$

$$C_{(M)} + O_{(M)} \rightarrow CO_{(M)} + M \qquad HCO_{(M)} + M \rightarrow H_{(M)} + CO_{(M)} \qquad (6.7A,B)$$

$$CO_{(M)} + O_{(M)} \rightarrow CO_{2(g)} + 2M \qquad (6.8)$$

$$O_{(M)} + H_{(M)} \rightarrow OH_{(M)} + M \qquad (6.9)$$

$$OH_{(M)} + H_{(M)} \rightarrow H_2O_{(g)} + 2M \qquad (6.10)$$

Upon distinguishing between the two mechanisms, although both are thermodynamically favourable, it was found to be kinetically more likely that the reaction will follow the mechanism which occurs on the stepped surface compared to the corresponding terraced surface. This has strong implications for the mechanism under sulfur poisoning, as will be discussed in the following section.

The most common strategy for the mitigation of carbon poisoning is to inject steam into the fuel stream. Although this reduces coke formation, it also reduces the performance of the cell. Another strategy is to increase the current density. The amount of carbon deposition is related to the availability of oxygen ions conducted through the electrolyte. Electro-oxidation can be completed, as shown in equations 6.11 and 6.12 for methane and higher hydrocarbons, respectively, with the correct number of oxygen dianions available. Other avenues of research include the addition of dopants to the anode cermet, such as ceria, or the development of an effective anode pretreatment program to give optimal microstructure and reduce coarsening effects.

$$CH_4 + 2O^{2-} \rightarrow 2H_2O + CO_2 + 8e^- \qquad (6.11)$$

$$C_xH_y + yO^{2-} \rightarrow \frac{y}{2}H_2O + xCO_2 + 2ye^- \qquad (6.12)$$

This above outlined mechanism, equations 6.2 to 6.10, has implications for catalyst metal selection. It is desirable to select a metal which falls in the “Goldilocks” zone. For the noble metals Au, Ag, Cu, Pt, Pd, and Ir, they bond the reaction intermediates too weakly, whereas reactive metals such as W, Mo, and Fe bind oxygen too strongly, causing alternatively high energy costs upon adsorption, and problems with desorption respectively. Thus, prime metals include Ni, Rh, Ru, Ir and Co with intermediate energy barriers for adsorption. As SOFCs are intended for common and industrial usage, Rh, Ir, and Ru present high costs. [5] Ni and Co fall within the “Goldilocks” zone for both chemical reactivity and cost. Cu presents an activity between that of the noble metals and the prime metals; however, due to problems with coarsening at high temperature derived from its low melting point, it requires alternate anode preparation methods. Bimetallic catalysts have shown higher tolerance for carbon in favouring the formation of C-O bonds rather than C-C bonds. [5] It will then be the intention of this research to continue to investigate the alloyed $Ni_xCo_{(1-x)}O$-YSZ cermet anodes as catalysts.

Although only performed on a Ni(111) surface, the existence of sub-surface carbon has been investigated and its implications towards the surface reaction of hydrocarbons extrapolated. [6] Sub-surface carbon implies the migration of carbon to the sites between the first and second layers of Ni atoms, as well as between the second and third layers. It was found that carbon binds stronger in the octahedral sites of the first layer of subsurface sites than on the surface of a Ni(111) slab. Carbon atoms were found to be able to occupy up to 75 % of the first sub-surface layer sites. It was also concluded that on a Ni(111) surface, subsurface sites are preferred even if surface coverage of carbon is low. Carbon also binds in the second subsurface layer stronger than surface, but not as strongly as the first subsurface layer. These results imply a strong propensity for carbon formed on the surface of a nickel catalyst to migrate to the subsurface sites. This migration has been found to cause a lattice expansion, which, in large enough quantities, could lead to cermet microstructure degradation. Although it was only touched upon in this study, it was suggested that applying hydrocarbon fuel over a Ni(111) surface would likely encounter a surface with a high degree of octahedral sub-surface sites occupied, which could affect the activity of the catalyst.

6.1.1.1 Hydrocarbon Fuels in the Presence of Sulfur Poison

Recent DFT calculations of step-blocking on edge sites on the Ni(211) surface showed that it greatly increases the tolerance of the metallic phase towards coke formation on its surface. [7] Referred to as S-promoter atoms, the sulfur atoms, which adsorb on the surface and have been found to migrate preferentially to the edge sites on a Ni(211) surface, are able to alter the mechanism of methane electro-oxidation. The dissociation of methane to form a carbon and four hydrogen atoms is exothermic on the Ni(211) surface, but endothermic on the Ni(111) surface. Coke formation on the step sites then produces nucleation and growth of carbon over the terrace sites adjacent to the step. By blocking these step sites, which are more active in this undesired dissociation mechanism, carbon formation on the surface of nickel can be discouraged. The surface reaction which then predominates on the terrace site is the dissociation of methane to produce CH_x and H. The activity of the 100 % step-blocked Ni(211) catalyst then corresponds to the terrace reaction mechanism, rather than the edge mechanism, and was found to mimic that of the Ni(111) surface. This presents a possible method of reducing or blocking coke formation on a nickel surface. Other atoms which have been investigated for the purpose of step-blocking are Cu and Au. [7] With the knowledge that sulfur poisoned the anode as well as the fact that sulfur has a blocking effect in the reaction of hydrocarbons on the surface of nickel, the research in this chapter was performed to study how this mechanism worked experimentally.

Experimental evidence for the reduction of coke formation on nickel surfaces in the presence of H_2S has been known experimentally for many years and was operated at the low ppm range and in conjunction with steam reforming. [8] [9] [10] [11] However, the reason behind this observed positive effect remained unknown until recent computational research projects, as outlined above. The prevailing reasoning for this observed effect on sulfur on the reduction of coking had been theorized to be surface reconstruction effects and/or migration of the surface sulfur to the more active surface sites. Research by the same groups into the complete recovery following removal of the sulfur was in agreement: the effect of sulfur poisoning at low concentrations in the presence of carbon is irreversible. [12] The prevailing idea regarding the mitigation of carbon poisoning utilizing sulfur is that it is a promising area of research, which is worth continuing.

Since naturally derived carbon-containing fuels contain various forms of sulfur, it is ideal to perform research in this area. Common sulfur-containing impurities are mercaptains, tetrahydrothiophene, disulfides and carbonyl sulfide. At SOFC operating temperatures, these sulfur compounds are quickly converted to H_2S; therefore, for fundamental research, introducing H_2S as a sulfur-containing poison is appropriate. Furthermore, since removing the sulfur is costly, in fact many research projects have been devoted to the desulfurization process of hydrocarbon fuels. Instead, in this work a high level of sulfur will be introduced into the fuel, as seen in the previous chapter.

This approach will have many advantages, the first of which is to simulate highly sulfurized, naturally derived hydrocarbon fuel, such as that obtained from the Alberta oil sands. At high sulfur concentration, the maximum surface coverage is expected to be achieved, namely a 50 % or 0.50 monolayer coverage. This corresponds to a Ni:S ratio of 2:1 which is limited due to the size and steric repulsions of the sulfur atoms. This coverage will ensure the complete coverage of the step sites on the nickel surface, thus reducing the amount of carbon nucleation at those sites, and minimizing the amount of coking on the metal catalyst surface. [7] As will be demonstrated in the results section, this can be highly advantageous for a carbon-containing fuel; however, due to the nature of sulfur as a poison even at low ppm concentrations, the sulfur eventually poisoned the anode.

At operational temperature, whether a bulk nickel sulfide phase is formed, subsurface layers of nickel sulfide are formed, or only surface adsorption of sulfur occurs is under debate in the literature, and was also investigated in the previous chapter. The higher strength of the bulk nickel-sulfur bond compared to the corresponding surface bond provides strong evidence for the bulk and/or subsurface nickel sulfide formation. [13] However, other researchers believe that bulk nickel sulfide is only formed upon cooling of the anode, thus a nickel cermet with adsorbed sulfur would exist at operational temperatures above 900°C. [14] There is likely a continuous phase transition dependent on many parameters such as temperature, sulfur concentration, pressure, and flow rate, which occurs in the temperature range commonly used for high temperature SOFCs, namely 700-1000°C. A definitive phase diagram, which takes into account these parameters important to SOFC researchers, would be a great asset to the fundamental understanding of the catalytic surface interactions, and would aid greatly in the push forward for the development of cermet anode materials optimized for tolerance to sulfur and coke formation.

6.1.2 Oxygen-Containing Fuels

Due to the strongly pyrolytic nature of hydrocarbon fuels and their propensity to form carbon on nickel-based catalyst surfaces, the addition of steam is common since water acts as a readily available oxidant. However, because some of the fuel is oxidized by water, the performance of the fuel is reduced. Fuels which are hydrocarbon-based, but which also contain oxygen, such as alcohols, are an interesting alternative. Oxygen is introduced naturally into the fuel stream as part of the fuel, and the performance is not expected to drop as a result; on the contrary, in some cases, such as with methanol, it has been observed to increase relative to hydrogen. [15, 16] The reasons for this will be discussed.

The simplest alcohol fuel, methanol, a C_1 alcohol, shows predictable gas phase chemistry at high temperature. Characterized by Cimenti and Hill, [17] at temperatures above 500°C, methanol shows significant decomposition to form H_2 and CO in a ratio of 2:1, equation 6.13, figure 6.1. This effect increases with temperature; at the temperatures of interest in this work, 800°C and 850°C, there is very little methanol expected to exist in the fuel stream, instead H_2 and CO gases will dominate. This increases the partial pressure of available fuel molecules by a factor of 3, and also reduces the number of decomposition steps required to occur on the catalyst surface.

$$CH_3OH \rightarrow 2H_2 + CO \qquad (6.13)$$

Interestingly, although carbon is expected to form at all temperatures shown in figure 6.1, the equilibrium concentration of carbon formation is expected to decrease with temperature increase. At 800°C, the equilibrium concentration of carbon will be only 1.9 mol %. Furthermore, at all temperatures shown, CH_3OH will decompose, namely the equilibrium conversion of CH_3OH is 100 %. However, in practice, the actual gas composition will depend on kinetics and fuel flow rate.

Although not observed at appreciable concentrations when pyrolysis is complete, formaldehyde (HCHO) is an important intermediate in the decomposition of CH_3OH, equations 6.14 and 6.15. However, formaldehyde will be observed if pyrolysis is not complete. Ethylene is unstable relative to CH_4, CO and CO_2, and so is not observed.

$$CH_3OH \rightarrow HCHO + H_2 \qquad (6.14)$$

$$HCHO \rightarrow H_2 + CO \qquad (6.15)$$

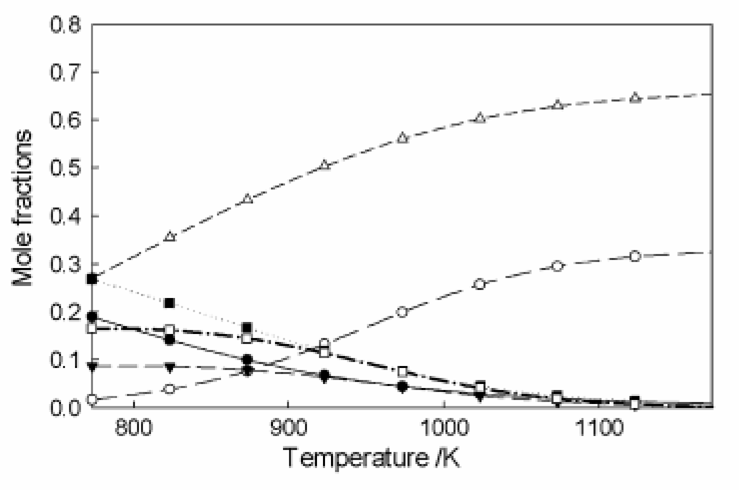

Figure 6.1 Expected equilibrium composition with temperature dependence for the reaction of pyrolysis of pure CH_3OH at OCV. The different chemical species are labeled as follows: (●) CH_4, (○) CO, (▼) CO_2, (▲, open shape) H_2, (■) H_2O, and (□) C (graphite). [17]

The carbon deposition boundary (CDB) has been determined for pure CH_3OH fuel and is shown in figure 6.2. The CDB in the temperature range relevant to this work, namely from 800°C to 850°C shows a very low CDB, thus for most fuel utilizations, no carbon deposition is expected to be observed. This is in agreement with the low mole fractions of carbon expected by the pyrolysis of CH_3OH, as expected in figure 6.1.

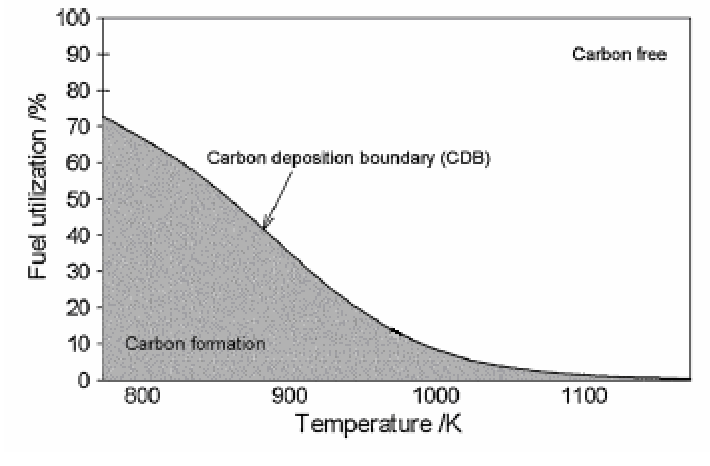

Figure 6.2 Carbon formation region, shown in grey below the carbon deposition boundary, for pure CH_3OH fuel at various typical SOFC operating temperatures as a function of fuel utilization. [17]

In a very recent study, Walker *et al.* performed in situ optical research of a Ni-YSZ anode exposed to CH_3OH fuel. [18] This study was performed at 715°C, at a significantly higher carbon deposition region than the study reported herein. However, their focus was upon the carbon deposition mechanism, which was found for CH_3CH_2OH to follow multiple pathways and occur rapidly (after approximately 5 to 7 min) due to its growth kinetics. Ethanol provides more complex chemistry with very different carbon deposition characteristics. The pyrolysis of CH_3CH_2OH shows the equilibrium compositions presented in figure 6.3 for various SOFC operating temperatures. Similar to CH_3OH, 100 % conversion is expected in this temperature range to the simple species H_2, CO, CH_4, CO_2, H_2O and C (graphite). The primary decomposition reaction is shown as equation 6.16, where, unlike the C_1 alcohol presented above, this C_2 alcohol undergoes decomposition to form carbon, thus carbon formation is expected to occur at higher levels at all temperatures under consideration. Intermediate species expected in the formation of the species seen in figure 6.3 are acetaldehyde (CH_3CHO), acetic acid (CH_3COOH), ethylene (C_2H_4), and formaldehyde (HCHO) following a more complex mechanism. Therefore, although CH_3CH_2OH is expected to produce 4 moles of fuel per mole of alcohol, the significant amount of carbon formation is expected to be detrimental to the porosity of the anode.

$$CH_3CH_2OH \rightarrow 3H_2 + CO + C \qquad (6.16)$$

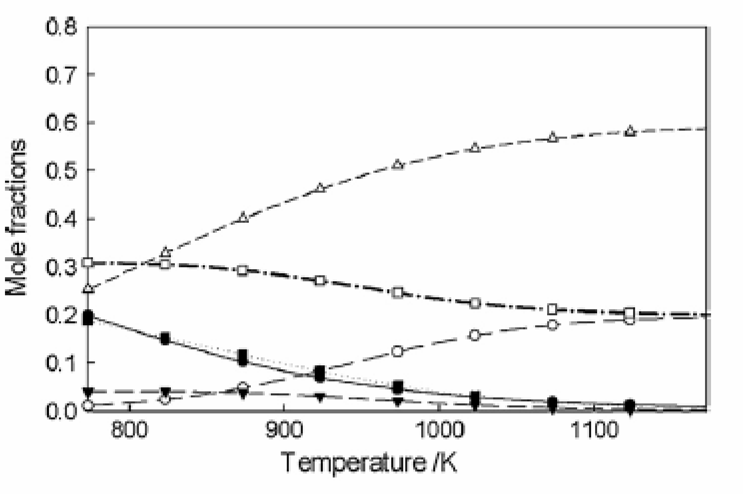

Figure 6.3 Expected equilibrium composition with temperature dependence for the reaction of pyrolysis of pure CH_3CH_2OH at OCV. The different chemical species are labeled as follows: (●) CH_4, (○) CO, (▼) CO_2, (▲, open shape) H_2, (■) H_2O, and (□) C (graphite). [17]

The CDB boundary for CH_3CH_2OH was mapped and is shown in figure 6.4. In agreement with CH_3OH, the CDB decreases with increasing temperature, however, it does not approach zero within this temperature range as shown previously. At 800°C, a minimum of 19.5 % fuel utilization is allowed for CH_3CH_2OH, a significantly higher figure.

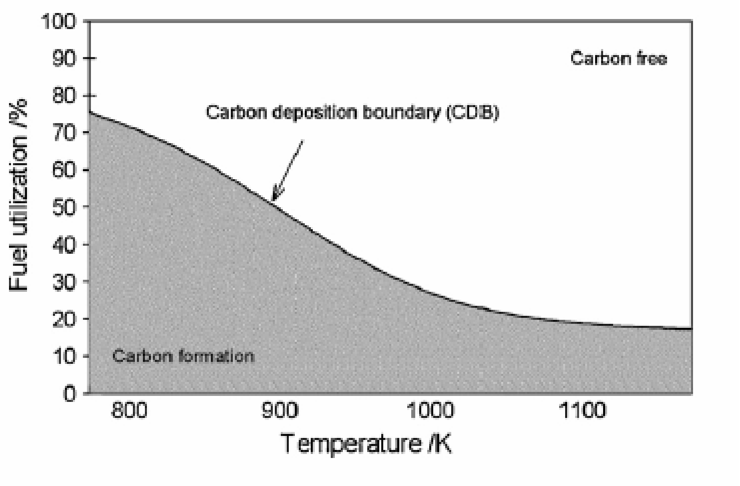

Figure 6.4 Carbon formation region, shown in grey below the carbon deposition boundary, for pure CH_3CH_2OH fuel at various typical SOFC operating temperatures as a function of fuel utilization. [17]

In order to circumvent this drawback, Ye *et al.* have developed a multi-layer anode capable of utilizing ethanol/steam. A tri-layer anode consisting of Cu-CeO_2/Ni-CeO_2/Ni-YSZ. Here, Ni-YSZ acted as a support layer, NiCeO_2 functioned as an interlayer to 'improve the interface combination', and Cu-CeO_2 acted as the catalyst layer adjacent to the YSZ electrolyte. Although performance decrease due to the presence of steam was observed, over the 250 hours of operation, they reported no carbon formation observed in any of these three layers. [19]

Biodiesel, a bridging fuel between that of hydrocarbons and oxygen-containing fuel, can present an alternative fuel for SOFCs. Despite the extensively complex thermal decomposition reactions expected, [20] it can provide a high density fuel. Although it is expected to generate significant carbon formation and poison the anode under its pure form, introduction of sulfur to the fuel stream is expected to mitigate this problem, as discussed above for hydrocarbon fuels. This oxygen-containing fuel is also expected to lower the pyrolytic character of the environment experienced by the anode without significant reduction in its performance.

6.2 Experimental

Fuel cell button cells were prepared for experimentation through methods outlined in chapter 2. The specific cermet bulk compositions used was the following: $Ni_{0.7}Co_{0.3}O$-YSZ. The area of the working electrode used to calculate the current and power densities is 1.333 cm^2.

All electrochemical measurements were performed in pure hydrogen with a flow rate of 50 sccm at either 800^{o}C, or 850^{o}C, as indicated. A minimum of 1.0 V for the value of OCV was required to continue with electrochemical measurements, after reduction of the metal phase of the cermet anode was complete. Experiments with hydrocarbon fuels directly following hydrogen were performed with the dry fuels and a total flow rate of 50 sccm. Sulfur experiments were performed using a mixture of H_2S and H_2 with a total flow of 50 sccm, where the concentration of sulfur poison will be indicated, but will range from 1 % to 10 % v/v in a balance of H_2. This was done to determine a baseline in the sulfur-containing hydrogen fuel as well as to generate the sulfidated anode. The high level of sulfur added to the fuel stream functions to increase the rate of sulfur poisoning for research purposes; also, due to experimental limitations, only high levels of sulfur could be measured accurately for introduction into the fuel stream. Hydrocarbon experiments which follow exposure to sulfur fuel utilize dry fuels with the indicated amount of H_2S and a total flow of 50 sccm. Exchange current density and open circuit voltage measurements represent the values obtained after 12 hours of measurement, to allow for stabilization, unless otherwise indicated.

All of the electrochemical parameters used for measurements are summarized in chapter 2. Equivalent circuit modeling of AC data was done using the software from *ZView*.

Elemental analysis and ion chromatography scanning was performed by Robertson Microlit Laboratories, Madison, NJ, USA. Elemental analysis has a detection limit of 0.02 %, and ion chromatography scanning has a detection limit of 1 ppm sulfur.

An NMR experiment was performed to characterize the biodiesel fuel on a 500 MHz Bruker instrument.

6.3 Results and Discussion

To assess the catalytic activity of the developed $Ni_{0.7}Co_{0.3}$-YSZ cermet catalyst with a wide range of fuels, the measurement of exchange current density was once again employed. These hydrocarbon fuels range from small traditional hydrocarbons, methane and ethane, through small alcohols, methanol and ethanol, as well as a large oxygen-containing fuel, biodiesel. Since it is very common for hydrocarbons to naturally contain varying amounts of sulfur, the catalytic activity of the fuels with a known amount of sulfur, in the form of hydrogen sulfide, was employed. This also represents fundamental research into the reactions of the dry fuel occurring on the surface of the anode; no steam was added to the fuel stream to effectuate *in situ* reforming.

6.3.1 Exchange current density measurements for hydrocarbon based fuels

6.3.1.1 Single metal Ni-YSZ cermet anode material

The most common cermet anode material for SOFCs is Ni-YSZ. In order to formulate a basis for comparison within the hydrocarbon investigations, a pure Ni-YSZ cermet anode was fabricated through the precipitation method used to fabricate the alloyed cermet anodes (*vide infra*). In keeping with the results outlined in the previous chapter, addition of 10 % followed by 1 % v/v H_2S in hydrogen fuel produced a drop in activity by many orders of magnitude when compared to pure hydrogen on a clean anode catalyst material, table 6.1. While continuing to flow the H_2S, the primary fuel was quickly switched to methane; the exchange current density value was observed to recover many orders of magnitude to approach the level previously observed for pure hydrogen on the clean surface. This is a twofold marked result: upon changing the primary fuel from hydrogen to methane, a many fold increase was observed; and this represents an exchange current density value of a fuel with 10 % v/v H_2S, a commonly known SOFC anode poison. The possible existence of a synergistic effect between the sulfur and carbon present in the fuel stream as well as on the catalyst surface was an interesting prospect. The sulfur tolerance exhibited by the developed alloy catalyst, $Ni_{0.7}Co_{0.3}$-YSZ, would also be an interesting area of investigation, as shown in chapter 5. [21]

Table 6.1 Exchange current density (i_o) values, with units of mA/cm^2, derived from EIS measurements (EIS) and direct cyclic voltammetry measurements (DCV) for the Ni-YSZ cermet anode at 850°C.

Fuel	i_o (EIS)	i_o (DCV)
H_2	31.7	11.8
H_2/H_2S 10 %	8.02E-05	8.33E-05
H_2/H_2S 1 %	7.65E-05	5.92E-05
CH_4/H_2S 10 %	23.0	4.78

6.3.1.2 Alloyed metal $Ni_{0.7}Co_{0.3}$-YSZ cermet anode material

6.3.1.2.1 Hydrocarbon fuels containing sulfur poisoning

With the anode catalyst which previously showed good tolerance to sulfur, the anode was tested with a higher hydrocarbon, as outlined in table 6.2A, as well as with the same hydrocarbon in conjunction with H_2S. A drastic drop in exchange current density upon addition of ethane was observed, followed by severe anodic delamination upon addition of sulfur. Addition of the two poisons simultaneously, as outlined in table 6.2B, resulted in a much smaller decrease in the exchange current density, indicating there is an importance to the order of exposure of the anode surface to the two poisons under investigation in this chapter. Although the addition of H_2S is not capable of reversing the formation of surface carbon, which will be discussed in subsequent sections of this chapter, it can be observed that the carbon poisoning is not as severe with H_2S present. Ethane is also known to be more difficult to control the occurrence of surface coking when compared to the simplest hydrocarbon fuel, one with no carbon-carbon bonds: methane. Also, as shown in table 6.2, the variation in microstructure between the two cells tested can cause a difference in the exchange current densities, as discussed in detail in chapter 4.

Table 6.2 Exchange current density (i_o) values, with units of mA/cm^2, derived from EIS measurements (EIS) and direct cyclic voltammetry measurements (DCV) for the $Ni_{0.7}Co_{0.3}$-YSZ cermet anode at 850°C. Sections A and B represent different button cell tests respectively, for a total of two cells for this table.

(A)

Fuel	i_o (EIS)	i_o (DCV)
H_2	8.79	8.71
CH_3CH_3	0.0188	-[a]
CH_3CH_3/H_2S 10 %	-[b]	-[b]

(B)

Fuel	i_o (EIS)	i_o (DCV)
H_2	9.36	10.6
CH_3CH_3/H_2S 10 %	0.496	0.366

[a] Calculation of the exchange current density value from the voltammetry measurements involves taking the Ln of the current values. Here, the current never became positive (anodic), thus the mathematical Ln does not exist, and no anodic value could be reported.

[b] Due to severe anode delamination, data could not be collected for this fuel mixture.

Investigation in the values of the catalytic activity of the alloyed cermet anode in poisoned methane fuel was investigated. Given that exposure to the sulfur poison prior to the carbon poison reduces the effect of coking on the surface of the anode, following measurement of a hydrogen baseline, the anode was first exposed to sulfur poisoning. As is outlined in table 6.3, following initial loss of activity, the exchange current density rose to a value slightly higher than that for the clean catalyst under hydrogen upon switching the primary fuel from hydrogen to methane. As discussed in the introduction to this chapter, the blocking effects of the sulfur on the surface of the anode play a key role in not only reducing the loss of catalytic activity due to coking, but the physical destruction of the porous microstructure caused by the coking. As a fundamental investigation, the exchange current density of pure hydrogen was measured following this series of fuels, as shown. The original activity of the clean catalyst was not recovered, which is likely due to the irreversible presence of sulfur on the anode surface, which, as discussed in the previous chapter, inhibits the catalytic electro-oxidation of hydrogen on the surface of the anode.

Table 6.3 Exchange current density (i_o) values, with units of mA/cm^2, derived from EIS measurements (EIS) and direct cyclic voltammetry measurements (DCV) for the $Ni_{0.7}Co_{0.3}$-YSZ cermet anode at 850°C.

Fuel	i_o (EIS)	i_o (DCV)
H_2	7.74	5.84
H_2/H_2S 10 %	0.462	0.504
CH_4/H_2S 10 %	8.12	7.50
H_2	1.88	3.54

It is known that as the temperature of the fuel cell is lowered, the effect of the sulfur poisoning increases; however, an associated cost is inherent with operating a fuel cell at high temperatures, thus an investigation at a lower temperature was undertaken. For a cell operated at 800°C, as presented in table 6.4, an identical fuel program was followed prior to introduction of the sulfur poisoned methane. Initially, a slight drop in catalytic activity observed for pure hydrogen, compared to the cell operated at 850°C as presented in table 6.3, as well as the sulfur poisoned hydrogen was observed, as is to be expected for a lower temperature. In contrast to the cell presented above, upon introduction of methane/H_2S an activity higher than that for hydrogen on a clean anode was not obtained, and more than a 50 % drop in exchange current density was observed. Thus, although the cost of heating a cell to a lower temperature is reduced, the amount of current available from a poisoned cell would be considerably lowered.

Table 6.4 Exchange current density (i_o) values, with units of mA/cm^2, derived from EIS measurements (EIS) and direct cyclic voltammetry measurements (DCV) for the $Ni_{0.7}Co_{0.3}$-YSZ cermet anode at 800°C.

Fuel	i_o (EIS)	i_o (DCV)
H_2	5.48	6.14
H_2/H_2S 10 %	0.373	0.412
CH_4/H_2S 10 %	2.19	1.51

6.3.1.2.2 Alcohols and other oxygen-containing fuels

In order to produce internal reforming, many researchers add steam to the fuel feed. This reduces the degree of the pyrolytic atmosphere, however, there is an inherent uncertainty associated with the amount of steam which is introduced. This also has the effect of lowering the performance of the cell. As will be observed, with the correct choice of oxygen containing fuel, the performance can be enhanced by an oxygen-containing fuel in comparison to pure hydrogen.

In the case of short-chain alcohols as fuel, as is outlined in table 6.5 A and B, the presence of oxygen can have a positive effect on the activity of the catalyst. As is the case of methanol (A), the presence of an effective oxygen atom insertion into one of the C-H bonds of methane, produces a cell which exhibits exchange current density values higher than that in pure hydrogen. As discussed in the introduction, methanol undergoes decomposition at typical SOFC operating temperatures to produce hydrogen and carbon monoxide to various extents. These two gases can then be directly electro-oxidized on the anode surface. Given the operating temperature measured, and the elevated exchange current density, this is believed to occur (the direct use of $CO + H_2$ as fuel will be discussed in Chapter 7).

Upon the effective insertion of a methylene group into methanol to generate ethanol, the electrochemical effects observed are clear. The creation of a carbon-carbon bond, similar to the case of ethylene reported above, has detrimental effects on the exchange current density of the cell run on ethanol as fuel compared to hydrogen, table 6.5B. A large loss in activity is observed upon addition of ethanol for a cell run for the same number of hours compared to methanol. Biodiesel is an interesting fuel, since it carries an oxygen atom in the molecule, yet has an extended hydrocarbon chain. Although it was expected to cause coking and anode delamination, an experiment with pure biodiesel as fuel was carried out for comparison purposes; a subsequent experiment with sulfur in the fuel stream, as observed previously with hydrocarbon fuels, was expected to extend the life of the anode and reduce the amount of coking experienced on the anode surface.

Table 6.5 Exchange current density (i_o) values, with units of mA/cm^2, derived from EIS measurements (EIS) and direct cyclic voltammetry measurements (DCV) for the $Ni_{0.7}Co_{0.3}$-YSZ cermet anode at 850°C. Sections A and B represent different button cell tests respectively, for a total of two cells for this table.

(A)

Fuel	i_o (EIS)	i_o (DCV)
H_2	11.8	10.1
CH_3OH	18.3	13.7

(B)

Fuel	i_o (AC)	i_o (DC)
H_2	24.5	14.3
CH_3CH_2OH	0.939	1.85

Following measurements in pure hydrogen fuel, biodiesel produced drastically different results, namely the current collector was completely electrically separated from the anode active region due to severe coking after only 6 hours of operation with this fuel. Upon post-mortem examination of the cell, the tube inlet was filled with carbon, as can be observed in Figure 6.5. A loss of approximately one order of magnitude was observed after 6 hours of operation, before the cell lost electrode contact, table 6.6A.

Figure 6.5 Picture of the excessive coking observed during operation of a button cell with the composition of $Ni_{0.7}Co_{0.3}$-YSZ at 850oC in pure biodiesel fuel.

Encouragingly, following measurement in hydrogen gas, and introduction of H_2S poison, the cell was able to produce exchange current densities for the full time of measurement with 10% H_2S in the fuel feed, table 6.6B. Upon reducing the H_2S content by half, the exchange current density rose approximately 4-fold. Post-mortem observations showed anode delamination due to coke formation, however, the extent was drastically reduced from the pure biodiesel experiment. Further experiments to tune the ratio of biodiesel/H_2S could yield promising results for long term, reduced coke formation operation of a SOFC with biodiesel as primary fuel.

Table 6.6 Exchange current density (i_o) values, with units of mA/cm^2, derived from EIS measurements (EIS) and direct cyclic voltammetry measurements (DCV) for the $Ni_{0.7}Co_{0.3}$-YSZ cermet anode at 850°C. BD designates biodiesel fuel for clarity. Sections A and B represent different button cell tests respectively, for a total of two cells for this table.

(A) Fuel	i_o (EIS)	i_o (DCV)
H_2	6.80	6.80
Biodiesel	0.711[a]	0.918[a]

(B) Fuel	i_o (EIS)	i_o (DCV)
H_2	10.2	7.13
H_2/H_2S 10 %	3.11	2.76
BD/H_2S 10 %	0.499	0.586
BD/H_2S 5 %	2.13	2.26

[a] measurements indicate i_o values after 6 hours of measurement, since the cell 'died' between the 6 and 8 hour measurements. Refer to the text and experimental section for details.

6.3.1.2.2.1 Materials Characterization for Biodiesel

Due to the fact that the biodiesel utilized in this work was purchased from a private company, materials characterization was performed: elemental analysis (EA) with corresponding ion chromatography scan (ICS), and nuclear magnetic resonance (NMR) spectroscopy.

Results of the EA of the biodiesel are indicated as table 6.7. The amount of nitrogen present is below the detection limit of the method. The ratio of hydrogen to carbon corresponds to 1.959, which approaches that of a saturated CH_2 chain. This result is as expected, since biodiesel is predominantly an unsaturated chain with a small number of saturation sites along the hydrocarbon backbone. ICS was used to determine the amount of sulfur present in the pure fuel. At 66 ppm, for experiments where no sulfur was added, this corresponds to the concentration of sulfur present in the fuel stream. Therefore, for the results of the pure biodiesel experiment presented in table 6.6A, it remains unknown how many or which surface sites would be blocked by this concentration of sulfur. Although incomplete reforming is expected to occur, it is known that there is not enough sulfur to produce a bulk metal sulfide phase.

Table 6.7 Elemental analysis, unless otherwise indicated, as mass percentage of the indicated elements.

C	H	N	S[a]
77.07 %	12.67 %	< 0.02 %	66 ppm

[a] Ion chromatography scan

A $^{13}C\{^{1}H\}$ NMR experiment (^{13}C with proton decoupling), was performed for the biodiesel fuel, figure 6.6. As can be observed, many peaks between 22 and 32 ppm indicate saturated, CH_2 alkanes. The peak at 14 ppm shows the small number of expected terminal CH_3 groups adjacent to a hydrocarbon chain. In the region of 126 to 132 ppm, a small amount of unsaturated, aliphatic groups are present. Although the EA analysis is incapable of indicating the presence or amount of oxygen, there is evidence of oxygen present in this NMR spectrum. The peak at 51 indicates a carbon adjacent to a carbonyl, namely -*C*-(C=O)-, whereas the peak at 174 ppm shows that of the carbonyl itself, namely -C-(*C*=O)-. The triplet centered around 77 ppm is the solvent, $CHCl_3$.

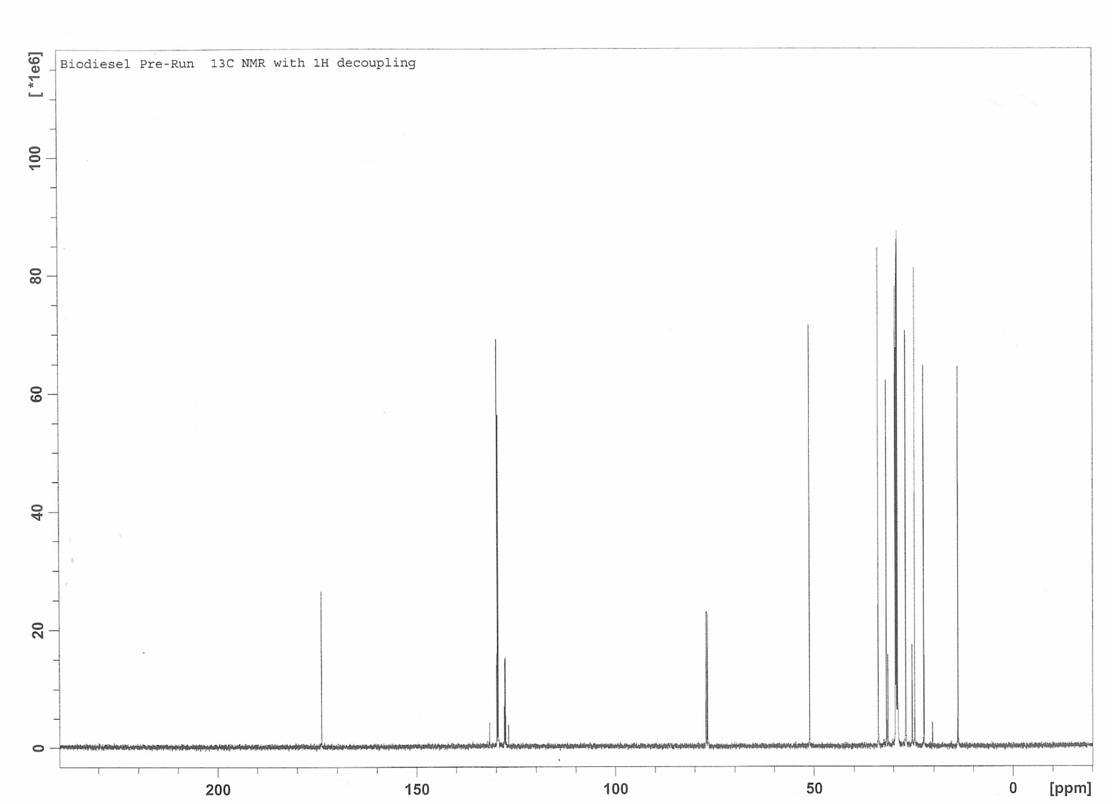

Figure 6.6 NMR spectrum in $CHCl_3$, $^{13}C\{^1H\}$, of biodiesel.

After exposing the biodiesel to fuel cell operating conditions, a thick carbon 'sludge' was collected from the anode cavity. The $^{13}C\{^1H\}$ NMR spectrum of this product is shown, figure 6.7. As can be observed there are no longer signals for aliphatic chain groups below 60 ppm. A large group of peaks corresponding to aromatic, cyclic carbon species is observed between 119 and 131 ppm. This provides strong evidence that aromatization and cyclization reactions were occurring within the strongly pyrolytic atmosphere of the anode cavity with pure biodiesel. Also, in order to produce a spectrum with comparable signal strengths as that collected for biodiesel, a much longer acquisition time was required; despite this, the noise observed in the baseline is still larger. This is due to the low solubility of the carbon product, which provides further evidence that likely cyclic aromatic species were produced. A similar thick 'sludge' was observed for the experiment with biodiesel with 10 % v/v H_2S, however, the amount produced was much lower.

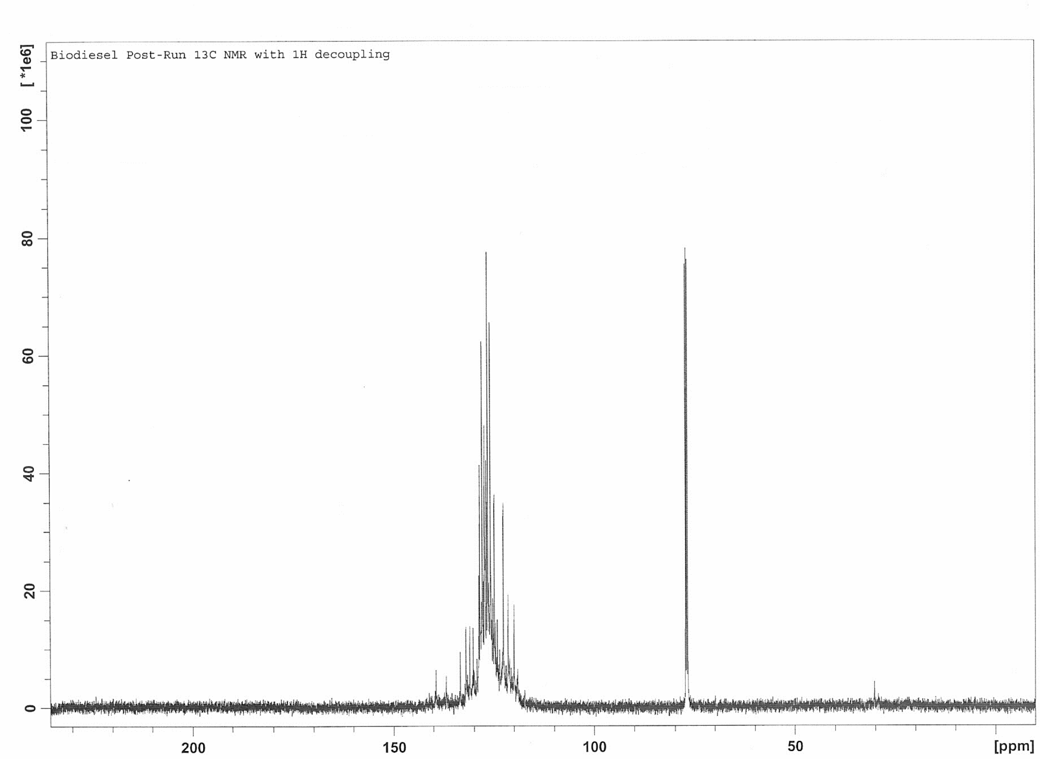

Figure 6.7 NMR spectrum in $CHCl_3$, $^{13}C\{^1H\}$, of carbon 'sludge' collected after exposing biodiesel to fuel cell conditions.

6.3.1.2.3 Open circuit voltage (OCV) values and mechanistic insights

As discussed in the previous chapter, the OCV value for the H_2/H_2S mixture shown in tables 6.8A and B show values which indicate that hydrogen is the fuel undergoing electro-oxidation. Methane with H_2S does not produce an appreciable change in the OCV values, which again indicates that hydrogen electro-oxidation dominates as the mechanism on the catalyst surface. As discussed in the introduction, sequential removal of hydrogen atoms from the methane molecule towards an aldehydic intermediate support this observation. Oxidation of H_2S would produce a lowering in the OCV value, thus this is not expected to be occurring in a large amount since the OCV value is not lowered with respect to pure hydrogen. However, the small amount of hydrogen produced in the pyrolytic decomposition of this species is likely oxidized.

Table 6.8 Open circuit voltage (OCV) values, with units of volts, measured for the $Ni_{0.7}Co_{0.3}$-YSZ cermet anode at 800°C (A), and 850°C (B).

(A)

Fuel	OCV
H_2	1.17
H_2/H_2S 10 %	1.21
CH_4/H_2S 10 %	1.22

(B)

Fuel	OCV
H_2	1.15
H_2/H_2S 10 %	1.16
CH_4/H_2S 10 %	1.24
H_2	1.10

Under the pyrolytic fuel cell operating conditions, methanol and ethanol are known to undergo thermal decomposition, as discussed in the introduction. As shown by the results of the OCV of both fuels when compared to pure hydrogen, table 6.9A and B, no significant change is observed, indicating that hydrogen is likely the predominant fuel of choice for the anode under these operating conditions. Since the OCV value of carbon monoxide is known to be very close to that of hydrogen, the electro-oxidation of carbon monoxide cannot be distinguished from that of hydrogen by this data, although it is expected to occur.

Table 6.9 Open circuit voltage (OCV) values, with units of volts, measured for the $Ni_{0.7}Co_{0.3}$-YSZ cermet anode at 850°C.

(A)

Fuel	OCV
H_2	1.19
CH_3OH	1.12

(B)

Fuel	OCV
H_2	0.983
CH_3CH_2OH	1.07

In agreement with data in the previous chapter as well as that presented for methane (table 6.8) and alcohols (table 6.9), no appreciable change in the value of OCV is observed for biodiesel fuel in pure form or with H_2S poison, table 6.10A and B. As expected, hydrogen is the predominant species undergoing electro-oxidation. The removal of hydrogen species from the biodiesel fuel molecule is in agreement with the cyclization and aromatization reactions observed by NMR (figure 6.7). Due to the strength and kinetic stability of the carbon-carbon bond, the evidence by NMR shows that few carbon-carbon bonds were broken, rather they were formed following dehydrogenation.

Table 6.10 Open circuit voltage (OCV) values, with units of volts, measured for the $Ni_{0.7}Co_{0.3}$-YSZ cermet anode at 850^{o}C. BD designates biodiesel fuel for clarity. Sections A and B represent different button cell tests respectively, for a total of two cells for this table.

(A)

Fuel	OCV
H_2	1.32
BD	1.11

(B)

Fuel	OCV
H_2	1.32
H_2/H_2S 10 %	1.25
BD/H_2S 10 %	1.19
BD/H_2S 5 %	0.967

6.3.1.3 Data for post mortem anode material

As discussed in the previous chapter, the inability to examine the anode in situ, at typical operating temperature and under reducing atmosphere, dictates that the only option available for anode microstructure characterization following electrochemical tests is to perform post-mortem observations following cooling and exposure to room temperature and atmosphere. The following section outlines these post-mortem observations following the electrochemical tests described in previous sections in this chapter; however, as discussed in previous chapters, changes in chemistry, morphology, and microstructure are possible during the cooling process. Furthermore, the data presented represent anode material which survived the cooling process intact and remained connected to the non-porous YSZ electrolyte; frequently, due to the extremely fragile nature of the porous cermet material, the anode did not survive the cooling process, thus it was not possible to collect post-mortem images and data.

6.3.1.3.1 Scanning electron microscopy (SEM) and energy dispersive X-ray spectroscopy (EDS)

As discussed above, exposure of the $Ni_{0.7}Co_{0.3}$-YSZ cermet anode to pure CH_3CH_3 at 850°C produced severe losses of exchange current density and OCV values. Post mortem images, figure 6.8, show the formation of extremely large carbon rods, more than 1 mm in length, and on the order of 100 μm thick. Since the pores of the cermet anode range from less than 1 μm to several μm, the growth of carbon rods on this order of magnitude are catastrophic to the microstructure. Upon close examination, it is observed that the thick rods are composed of groups of many rods, which are tangled together, thus forming the larger structures. This carbon rod growth is common for Ni-YSZ based cermet anodes upon exposure to carbon-containing fuel; however the scale upon which the rods formed was surprising.

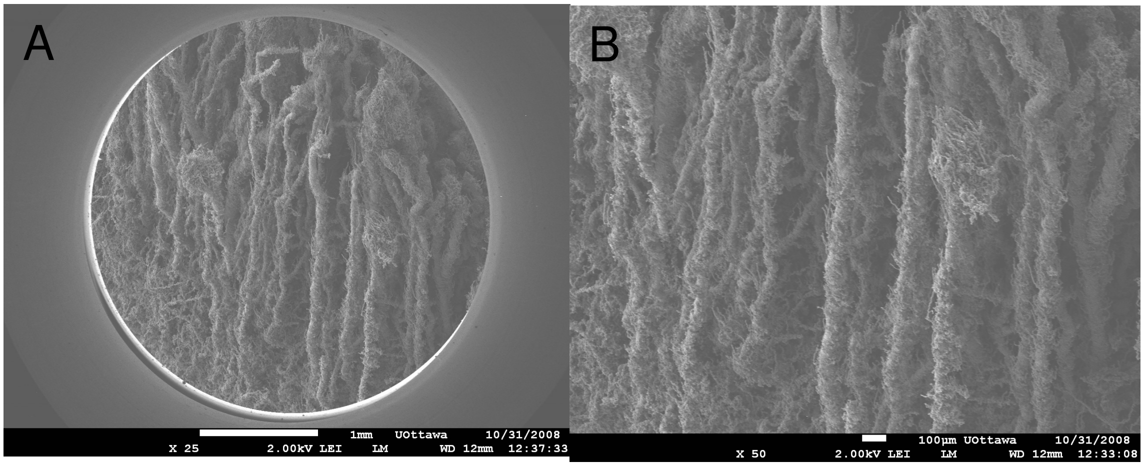

Figure 6.8 SEM image of carbon rod formation observed upon exposure of the $Ni_{0.7}Co_{0.3}$-YSZ cermet anode to CH_3CH_3 at 850^{o}C. (A) The rods are extending from the anode surface, bottom left, and are more than 1 mm long. This image shows a magnification of 25x and a measurement bar of 1 mm. (B) The rods are composed of many smaller rods. This image shows a magnification of 50x and a measurement bar of 100 µm.

Interesting structures were observed upon cooling the anode slowly in a CH_4/H_2S 10 % atmosphere from 850^{o}C, as shown in figure 6.9. Rod-like structures collected in the image of the post-mortem anode, figure 6.9A, had not been previously observed under H_2/H_2S atmosphere, as outlined in the previous chapter. Upon closer inspection, figure 6.9B, there appears to be two types of these rods. The first rod shaped structure, as observed emerging from a spherical particle, found previously to be composed of the metal phase and sulfur, likely in the form of an alloyed metal sulfide, appeared to be between 10 and 20 µm in length and approximately 0.5 - 2 µm in diameter. As also observed in figure 6.8D, they can increase in diameter along their length and appear to be amorphous. This type of rod is only seen emerging from the spherical metal sulfide particles.

The second type of rod observed is composed of two parts, figures 6.9B and C. Growing only from the porous, YSZ enriched material, this type of rod is on average slightly longer, between 20 and 25 µm, and much thicker, from 1 to 10 µm. Although the 'body' of this type of rod appears to be amorphous, the sphere on the end of the rod shows a crystalline, stepped morphology.

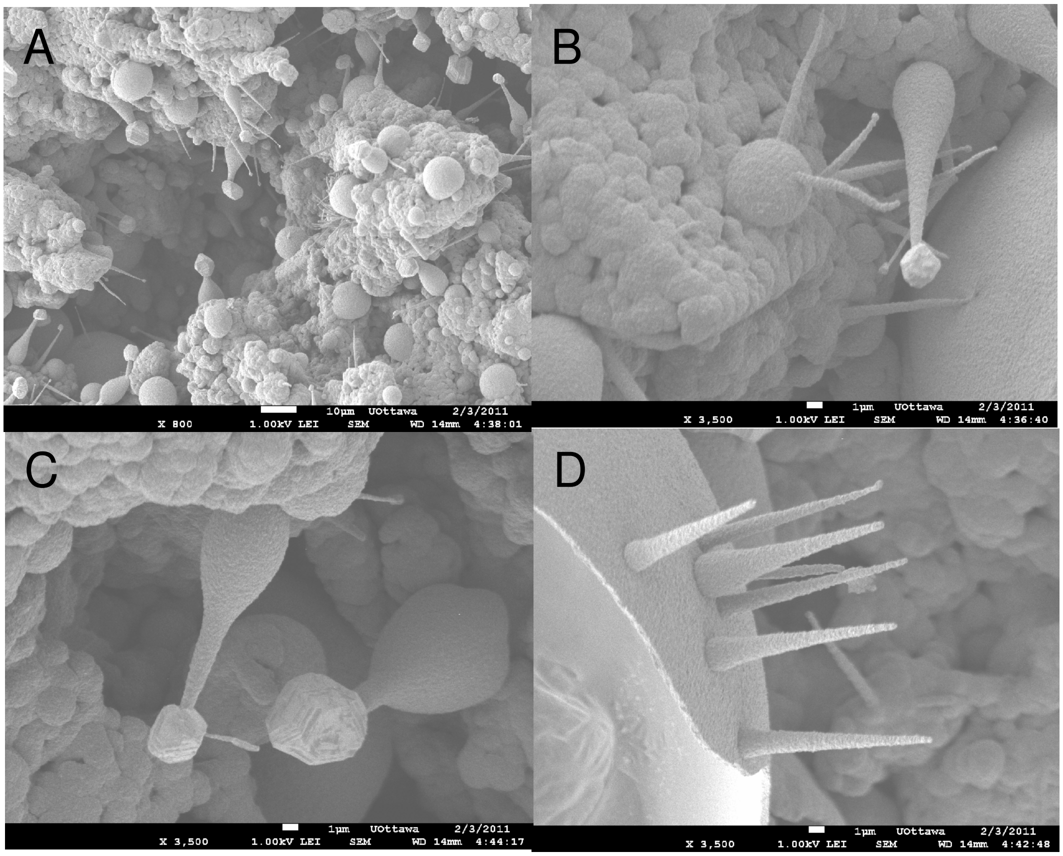

Figure 6.9 SEM image of structural formations observed upon cooling a $Ni_{0.7}Co_{0.3}$-YSZ cermet anode following exposure to a CH_4/H_2S 10 % atmosphere at 850°C. (A) This image shows a magnification of 800x and a measurement bar of 10 µm. (B) to (D) These images show a magnification of 3500x and a measurement bar of 1 µm.

EDS data for one of the rod shaped structures shows that it is composed primarily of sulfur (2.4 keV), nickel and cobalt (0.8 to 0.9 keV and 7.0 to 8.3 keV), as observed in figure 6.10. The importance of this composition will be discussed.

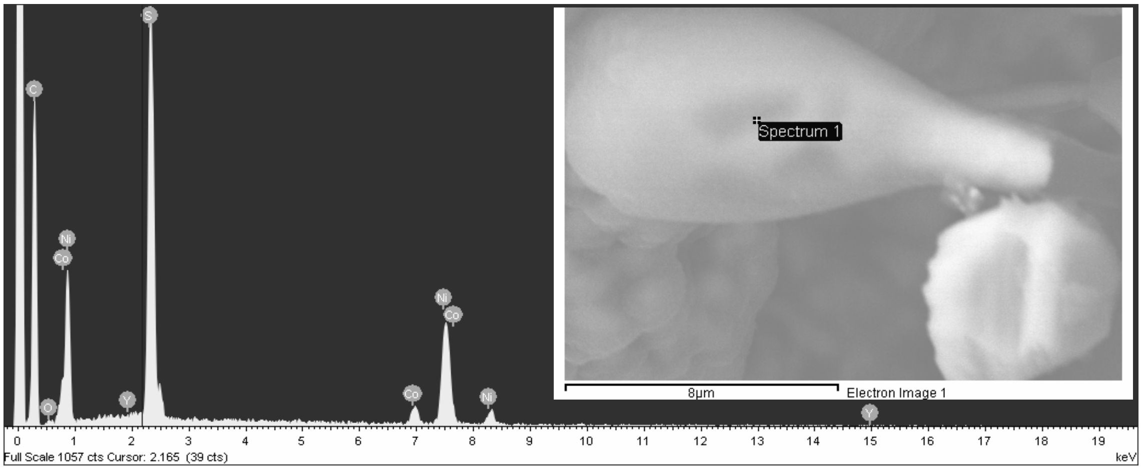

Figure 6.10 EDS of the 'body' of one of the structural formations observed upon cooling a $Ni_{0.7}Co_{0.3}$-YSZ cermet anode following exposure to a CH_4/H_2S 10 % atmosphere at 850°C.

The magnitude of the formation of metal sulfide spheres on the surface as well as their migration and segregation from the YSZ porous structure is shown in figure 6.11. Although the rod shaped structures are observed throughout the cross-section, figure 6.11B (at the presented magnification, these features are not shown), the vast majority of the metal sulfide is seen to have migrated to the surface of the porous structure to form spheres, figure 6.11A. The size of these metal sulfide spheres is on the order of 100 μm, two orders of magnitude larger than the original particle size following reduction in hydrogen. This represents an immense capacity for the metal sulfide to undergo agglomeration upon solidification and cooling. It remains unknown how these features are formed; however, the known high mobility of metal sulfides, coupled with their low melting point, suggest that this observed structure formation is likely possible due to these effects.

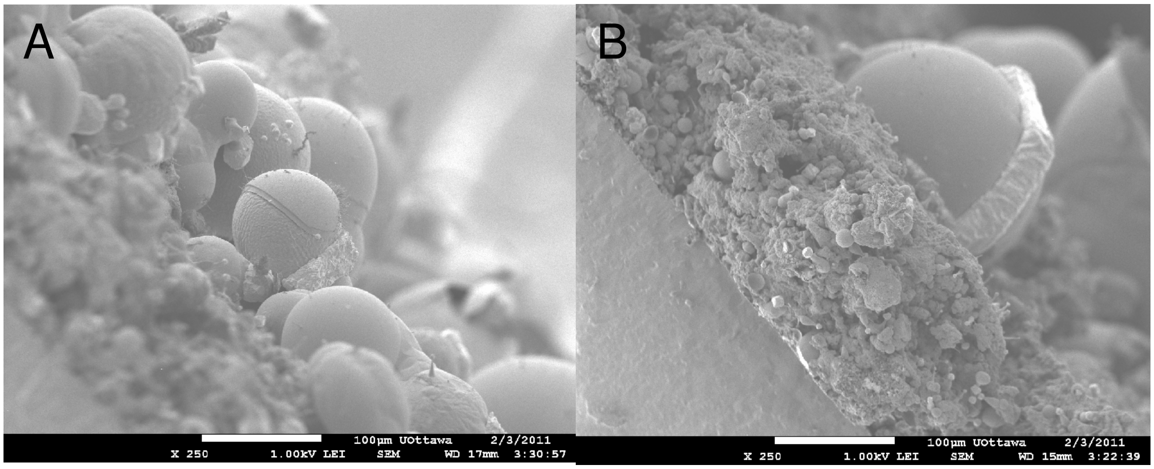

Figure 6.11 SEM cross-section images are presented of the same $Ni_{0.7}Co_{0.3}$-YSZ cermet anode shown above. The non-porous YSZ electrolyte is visible in the bottom left corner of both images, (A) and (B) These images show a magnification of 250x and a measurement bar of 100 µm. (A) This image has been tilted beyond 90^{o} for broad surface visualization.

Methanol possesses many chemical qualities which make it an ideal SOFC primary fuel. It carries an oxygen atom for each equivalent of carbon atoms, lowering the extreme pyrolytic atmosphere experienced with such fuels as methane and hydrogen. It does not require any carbon-carbon bonds to be broken during its electrochemical oxidation. Furthermore, under typical SOFC operating temperatures, methanol is expected to undergo an increasing amount of gas phase decomposition with increasing temperature into the products H_2 and CO in a 2:1 ratio, as discussed in the introduction section. These chemicals easily undergo clean oxidation, as is shown in figure 6.12. At both magnifications shown, the post-mortem anode does not show any evidence of surface coke formation in the form of particles, rods or tubes. The anode shows that its porosity has been preserved, there is no coke formation within the pores; its microstructure has been preserved and no evidence of delamination or loss of material structure is seen due to coke formation within the pores.

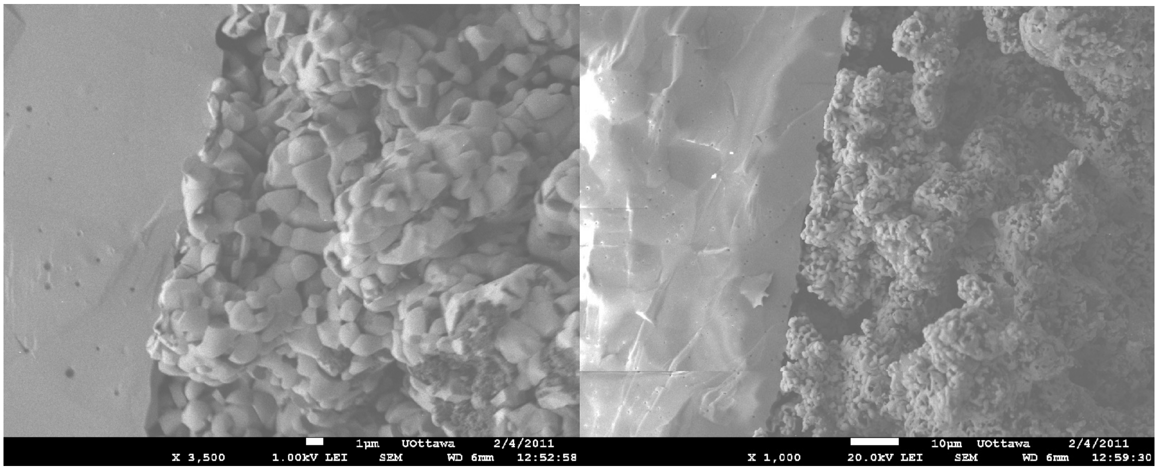

Figure 6.12 SEM cross-section images are presented of the $Ni_{0.7}Co_{0.3}$-YSZ cermet anode following exposure to CH_3OH fuel. The porosity has been preserved and there are no observable carbon particles, rods, or tubes. (A) This image shows a magnification of 1500x and a measurement bar of 1 µm. (B) This image shows a magnification of 1000x and a measurement bar of 10 µm.

Finally, as an interest into the possibility of leaching of the Pt from the current collector into the metallic phase of the cermet anode during the sintering process or extended high temperature exposure upon electrochemical testing, EDS experiments were attempted. One button cell was able to survive electrochemical testing and cooling with the current collector intact. However, due to the overlap of the Pt and Zr primary peaks, resolution of these two peaks was impossible, and the existence of leaching could not be proven or disproved. Further complications arise with the nature of the EDS technique itself and the nature of the sample. Data collection time to obtain peak resolution, if at all possible, would be prohibitively high. Also, the nature of the sample is not ideal, it is neither flat nor polished; instead it is both porous and irregularly shaped.

6.4 Conclusions

In agreement with computational results, which indicate that the mechanism is changed following blocking of active step sites, the exchange current density of methane was found to increase in the presence of H_2S relative to poisoned hydrogen. Interesting changes to the anode structure were observed in the post-mortem SEM images, indicating a large amount of migration of the metallic phase. In the case of ethane, though no increase in exchange current density was observed, a lengthening of the functional lifetime of the cell was observed by several days, indicating reduced carbon poisoning. Operation of the SOFC with pure ethane produced large carbon rods, as observed by SEM. A similar effect in the exchange current density was observed for biodiesel fuel in the presence of sulfur poison, namely the lifetime of the button cell was lengthened. An NMR study of the fuel pre- and post-operation, indicate that the saturated aliphatic chain underwent a significant amount of cyclization and aromatization upon operation. Methanol is a promising SOFC fuel since it produced exchange current density values larger than hydrogen, and showed no evidence of coke formation by post-mortem SEM. OCV results indicated that the electro-oxidation of hydrogen was the predominant mechanism in all cases, and that the electro-oxidation of H_2S was not observed in appreciable amounts to affect the OCV value.

6.5 References

[1] S. McIntosh, R. Gorte, Chem. Rev. 104 (2004) 4845.

[2] J.-M. Klein, Y. Bultel, M. Pons, P. Ozil, J. Fuel Cell Sci. Technol. 4 (2007) 425.

[3] M.B. Pomfret, J. Marda, G.S. Jackson, B.W. Eichhorn, A.M. Dean, R.A. Walker, J. Phys. Chem. C 112 (2008) 5232.

[4] J. Kleis, G. Jones, F. Abild-Pedersen, V. Tripkovic, T. Bligaard, J. Rossmeisl, J. Electrochem. Soc. 156 (2009) B1447.

[5] D.B. Lingram, S. Linic, J. Electrochem. Soc. 156 (2009) B1457.

[6] J. Xu, M. Saeys, J. Phys. Chem. C 112 (2008) 9679.

[7] N.M. Galea, D. Knapp, T. Ziegler, J. Catal. 247 (2007) 20.

[8] R. Kikowatz, K. Flad, G. Horz, J. Vac. Sci. Technol. A 5 (1986) 1009.

[9] J.R. Rostrup-Nielsen, J. Catal. 85 (1983) 31.

[10] T.R. Smith, A. Qood, V.I. Birss, Appl. Catal., A 354 (2009) 1.

[11] J.N. Kuhn, N. Lakshminarayanan, U.S. Ozkan, J. Mol. Catal. A: Chem. 282 (2008) 9.

[12] F.P. Nagel, T.J. Schildhauer, J. Sfeir, A. Schuler, S.M.A. Biollaz, J. Power Sources 189 (2009) 1127.

[13] G.J. Offer, J. Mermelstein, E. Brightman, N.P. Brandon, J. Am. Ceram. Soc. 92 (2009) 763.

[14] J. Dong, D. Cheng, S. Sha, M. Liu, J. Power Sources 156 (2006) 461.

[15] K. Sasaki, K. Watanabe, K. Shiosaki, K. Susuki, Y. Teraoka, Electrochem. Soc. Proceed. 07 (2007) 1295.

[16] K. Sasaki, H. Kojo, Y. Hori, R. Kikuchi, K. Eguchi, Electrochem. 70 (2002) 18.

[17] M. Cimenti, J.M. Hill, J. Power Sources 186 (2009) 377.

[18] B.C. Eigenbrodt, M.B. Pomfret, D.A. Steinhurst, J.C. Owrutsky, R.A. Walker, J. Phys. Chem. C 115 (2011) 2895.

[19] X.-F. Ye, S.R. Wang, Q. Hu, Z.R. Want, T.L. Wen, Z.Y. Wen, Electrochem. Commun. 11 (2009) 823.

[20] A. Osmont, L. Catoire, P. Dagaut, J. Phys. Chem. A 114 (2010) 3788.

[21] C.M. Grgicak, Anodes for solid oxide fuel cell (SOFC) systems operating in multiple fuel environments: Effects of microstructure and composition, University of Ottawa, Ottawa, 2007.

7

Ni$_{0.7}$Co$_{0.3}$-YSZ Cermet Anode for Oxidation of CO/H_2 Fuel Mixtures

7.1 Introduction

Solid oxide fuel cells (SOFCs) are gaining a lot of interest due to their fuel flexibility, high fuel-electricity conversion efficiency, and long-term stability for practical applications [1, 2]. Among many common fuels such as hydrogen, heavier liquid fuels such as alcohols (methanol, ethanol, etc), hydrocarbons (methane, ethane, etc) and biodiesel are being considered. At common operating temperatures for SOFCs (800-1000 ^{o}C), heavier liquid fuels undergo thermal decomposition to form predominantly hydrogen and carbon monoxide [3, 4]. Because of this, a greater understanding of how SOFCs utilize and tolerate different ratios of H_2 and CO is essential. Additionally, independently produced syngas can be used directly as a fuel.

With a mixture of H_2 and CO as fuel, each has a corresponding electrochemical oxidation reaction at the anode:

$$H_2 + O^{2-} \rightarrow H_2O + 2e^- \quad (7.1)$$

$$CO + O^{2-} \rightarrow CO_2 + 2e^- \quad (7.2)$$

In a recent computational paper, Andreassi *et al.* [5] found the contribution made by CO direct oxidation to be 12.5 % for a cell running on a fuel ratio of 80/20 CO/H_2 at 800 ^{o}C with a Ni-8YSZ cermet anode. This effect becomes increasingly important at high current densities, where the model must consider both H_2 and CO direct oxidation in order to best simulate what is observed by experiment. Therefore, CO direct oxidation is present under SOFC operation conditions and is non-negligible.

With a mix of H_2 and CO in the fuel feed, the water-gas shift reaction (WGSR) must also be considered:

$$CO + H_2O \rightarrow CO_2 + H_2 \quad (7.3)$$

This equation shows that when appreciable concentrations of water vapour are present in the fuel feed or anode compartment, particularly at high fuel utilization, the CO concentration will be lowered and H_2 produced. The kinetics of this reaction are fast and favourable, much more so when compared to the direct oxidation of CO, so the presence of water vapour will cause the reaction to proceed, generating H_2. However, according to Andreassi *et al.* [5], considering only the WGSR (and not CO oxidation) underestimates the voltage given experimentally.

Traditionally, the most common anode material for SOFCs with a YSZ electrolyte layer is a Ni-YSZ cermet. Although Ni has a high activity for H_2 electrochemical oxidation, it is not an effective catalyst for CO oxidation. Additionally, because H_2 has a lower surface diffusion resistance on Ni when compared to CO, the amount of H_2 which can be oxidized is expected to be higher. This contributes to a rate constant which is 2 to 3 times higher at temperatures between 750 and 1000 ^{o}C for H_2 compared to CO on Ni-YSZ cermet anodes [6].

Carbon poisoning is a major concern when operating a cell with a Ni anode and a carbon-containing fuel due to the propensity for Ni to cause coke formation. With a CO fuel, two carbon deposition mechanisms must be considered:

$$2\,CO \rightarrow C + CO_2 \qquad (7.4)$$

$$CO + H_2 \rightarrow C + H_2O \qquad (7.5)$$

The first mechanism is the Boudouard disproportionation reaction [7, 8] (equation 7.4) in which CO is converted into carbon at the anode surface, thus both lowering the amount of CO available for electrochemical oxidation and causing carbon deposition on the anode surface. The second mechanism, equation 7.5, reduces CO using H_2 to produce carbon and water vapour. This carbon deposition also contributes to carbon poisoning of the anode, and the water vapour is likely to participate in the WGSR, thus consuming more CO fuel to produce H_2.

Some reported performances with Ni-YSZ based cermet anodes have shown a global trend: performance with a CO/H_2 mixed fuel, as measured by exchange current densities or power densities, produces intermediate values when compared to pure H_2 or CO fuel. [5, 6, 9-11] However, the trend between the higher pure H_2 value and the lower CO values is monotonic but not linear. The region with H_2 rich CO/H_2 fuel ratios can produce performance values much closer to the higher H_2 fuel, and CO rich CO/H_2 fuel ratios produce values closer to the lower CO fuel [6]. This observation (the “S” shaped curve) has been linked to the amount of carbon deposition which occurs at varying CO/H_2 fuel ratios. The largest cell deactivations reported in the literature [6, 9, 11, 12] correspond to the 75/25 CO/H_2 fuel ratio range, where carbon deposition has been observed to occur in the largest quantities. Conversely, much lower carbon deposition occurs near 25/75 CO/H_2 fuel ratios. The lowest carbon deposition is observed for pure CO fuel [12]. This indicates that CO reduction by H_2 (equation 7.5) is a possible mechanism for the carbon deposition.

Costa-Nunes *et al.* [10] observed a larger power density for a cell running on H_2 fuel at 700 ^{o}C with Cu-Co-CeO_2-YSZ anode when compared to its cobalt free analogue, Cu-CeO_2-YSZ. When the cell with Cu-Co-CeO_2-YSZ anode was run with 3 consecutive fuels, H_2, syngas, and CO, an increase in power densities was observed across this fuel series, in contrast with the nickel anodes. It was concluded that it was the addition of Co that produced an increasingly higher power density along this fuel gas series, in addition to the increased power density when running on pure H_2, relative to its Co free counterpart.

Since Ni-YSZ anodes are not effective in the direct oxidation of CO, and coking leads to poor performance with this fuel, in the present work we explore the addition of Co to a Ni catalyst to produce a NiCo-YSZ cermet anode which has recently shown promise in operation with other carbon containing fuels [13]. The synergistic effect of the two metals in the bimetallic NiCo alloy is expected to directly oxidize H_2 and CO respectively, producing a catalyst uniquely suited for this fuel mixture. The chosen Ni/Co ratio for this work was 70/30 due to success with this concentration of Co with previous systems containing sulfur [13, 14]. Further tuning of the Ni/Co ratio in the anode cermet could result in even higher performances.

7.2 Experimental

Anode materials were synthesized containing a metal component comprising 55 % by mass NiCoO of the total cermet material, with the mass balance of 8YSZ. The metallic component was synthesized to contain 70 % Ni and 30 % Co by mass, by a precipitation method described previously [15, 16]. Button cells were then manufactured for testing with cathode and reference electrodes of LSM, and pure Pt current collectors and leads. The total fuel flow used for all experiments was 50 sccm.

The fuel cell set-up has been described previously [13, 14]. Briefly, the cell configuration used was a button cell with Pyrex® ring seals at the top of an alumina tube support. A potentiostat (VoltaLab®) was used to collect all electrochemical measurements at 800 ^oC, as measured by a K-Type thermocouple placed just above the counter electrode. In the construction of the setup, open circuit voltage (OCV) values greater than 1.1 V (for pure H_2 fuel) were considered as an indication of a properly working cell, sufficient to proceed with minimal current or molecular leakage.

The OCV was measured for 1 hour during the reduction of the anode with hydrogen to produce the anode alloy metal: $Ni_{0.7}Co_{0.3}$-YSZ. The cell was then polarized with an anodic overpotential of 400 mV for 15 hours during which time the metal reduction was completed and the anode was allowed to stabilize. A 2 hour cycle of electrochemical impedance spectroscopy (EIS), voltammetry, and chronoamperometry (CA) was repeated 7 times to ensure the measurements used for literature reporting were stable and to observe any changes which occurred within the initial introduction of a new fuel. All values reported are taken from the final 2 hours of measurement, which were found to be stable after the first ~6 hours of measurement.

For EIS measurements, each spectrum was taken at OCV over the frequency range of 100 kHz to 250 mHz with an AC amplitude of 10 mV. The equivalent circuit used to fit impedance data was: $L_1R_1[R_2CPE_1[R_3CPE_2]]$. The equation used to obtain the exchange current density (i_0) values from the charge transfer resistance (R_{CT}, here set to be equal to R_3) values is the following, as derived from the low-field approximation of the Butler-Volmer equation: $i_0 = RT/nFR_{CT}$ [17]. Voltammetry measurements were obtained from 200 mV to 1100 mV of anodic overpotential at a scan rate of 2 mV/sec. These values were set to ensure the region containing exchange current density information was collected. Exchange current density values from DC measurements were obtained from the Tafel plot and match qualitatively the values obtained from EIS measurements, as in previous work [14, 18].

7.3 Results

7.3.1 OCV data at varying CO concentrations in H_2

Experiments were performed with varying CO/H_2 ratios following increasing and decreasing trends. The behavior is exemplified in Figure 1 for two cells which show qualitatively the trends observed. For the cell designated as “cell 1”, data for pure H_2 was collected followed by increasing amounts of CO until pure CO was reached, at which point a measurement at 50/50 CO/H_2 was collected, followed by a return to pure H_2. For “cell 2”, data for pure H_2 was initially collected for comparison purposes with “cell 1”, then the fuel was switched rapidly to pure CO and the concentration of CO was systematically lowered until pure H_2 was collected. A further checkpoint at 50/50 CO/H_2 was then collected followed by a return to pure H_2.

The OCV values of the button cells are shown in Figure 7.1. The initial OCV value for Cell 1 (open symbols) with hydrogen is quite high at 1.36 V, as is expected with a low fuel utilization. The measurements made with varying mixtures of CO and H_2 appear to have a relatively constant value near 1.12 V. Exposure to pure CO gave a lower than expected value of 0.50 V, whereas returning to H_2 showed a small amount of recovery, but did not return to the original value for pure hydrogen, indicating possible carbon poisoning. The second button cell Cell 2 (full symbols) was also initially exposed to pure hydrogen and had an OCV value of 1.26 V, similar to the first cell. In order to assess the reversibility of the data collection, the input fuel was immediately switched to pure CO followed by increasing amounts of H_2. Initially, with pure CO, an OCV value much closer to that according to the Nernst equation was obtained, 1.04 V. Excellent agreement was observed between cells 1 and 2 when exposed to varying CO/H_2 mixtures. The same plateau was observed with a similar constant value, indicating the independence of the order of data collection in relation to the chemical mechanism occurring. However, upon returning to a 50:50 mixture, a large drop in the OCV value was observed, (~0.8 V) indicating an inability of both cells to tolerate fuel mixture cycling and the accumulation of carbon over time. This is also confirmed by the lowered final OCV point at 0.68 V in pure H_2.

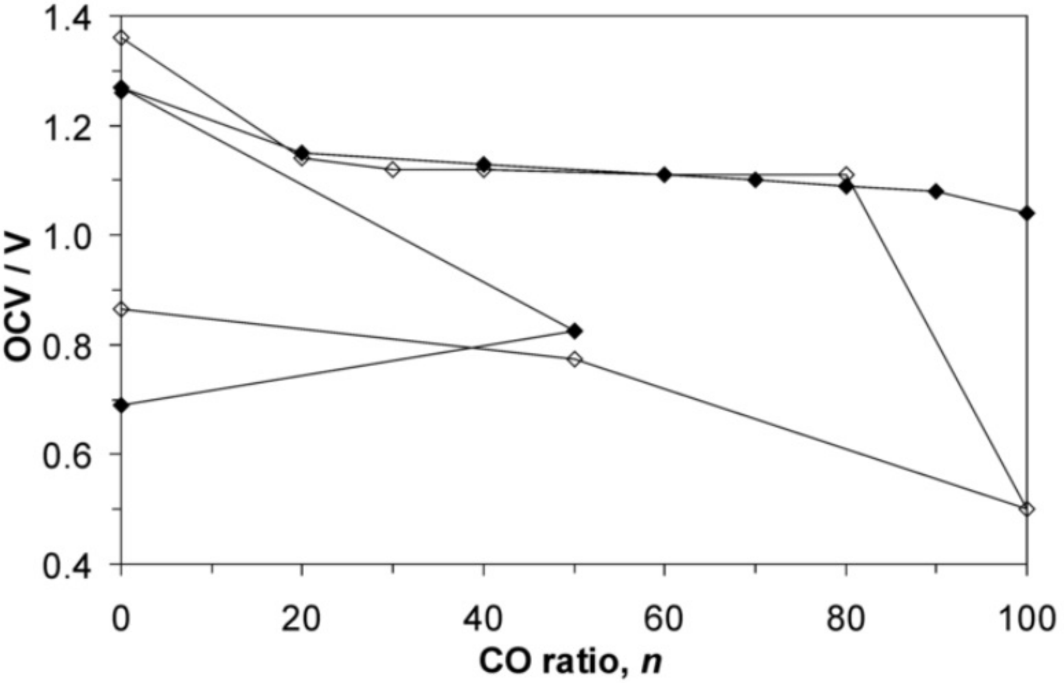

Figure 7.1 OCV values for cell 1 (open symbols) and cell 2 (filled symbols) collected at various CO/H_2 fuel ratios. The value of n, corresponds to the ratio of CO in the fuel inlet with a balance of H_2, where *n* is given by the formula: $n_{CO}/(100-n)_{H2}$.

7.3.2.1 Exchange current density at varying CO concentrations in H_2

Impedance data was collected for the same two cells as previously described, in the same order of H_2 and CO ratios. Figure 7.2 show the exchange current densities obtained. The first cell initially showed an exchange current density value of 1.2 mA/cm^2 in pure hydrogen. For fuel feed ratios of 20/80 and 30/70 CO/H_2, the exchange current density values increased by a factor of 5.7 and 7.3 times respectively. This is a highly encouraging result, since these ratios of hydrogen and CO represent those of the thermal decomposition products expected at the operation temperatures of SOFCs for some common small molecules, such as CH_3OH, as well as possible fuel mixtures, such as CH_3OH and H_2 [19, 20]. These findings are also important since this is the first example of a Ni-based cermet anode producing exchange current densities which are larger for CO/H_2 fuel mixtures when compared to pure H_2. Cell 2 values for exchange current density in the 20/80 and 30/70 CO/H_2 region (after exposure to pure CO and increasing H_2 content) are comparable to those of the pure hydrogen collected initially. These values were not higher than that for initial pure hydrogen, likely due to cumulative carbon poisoning during measurements at higher CO concentration. The reasoning for this observation will be further discussed below.

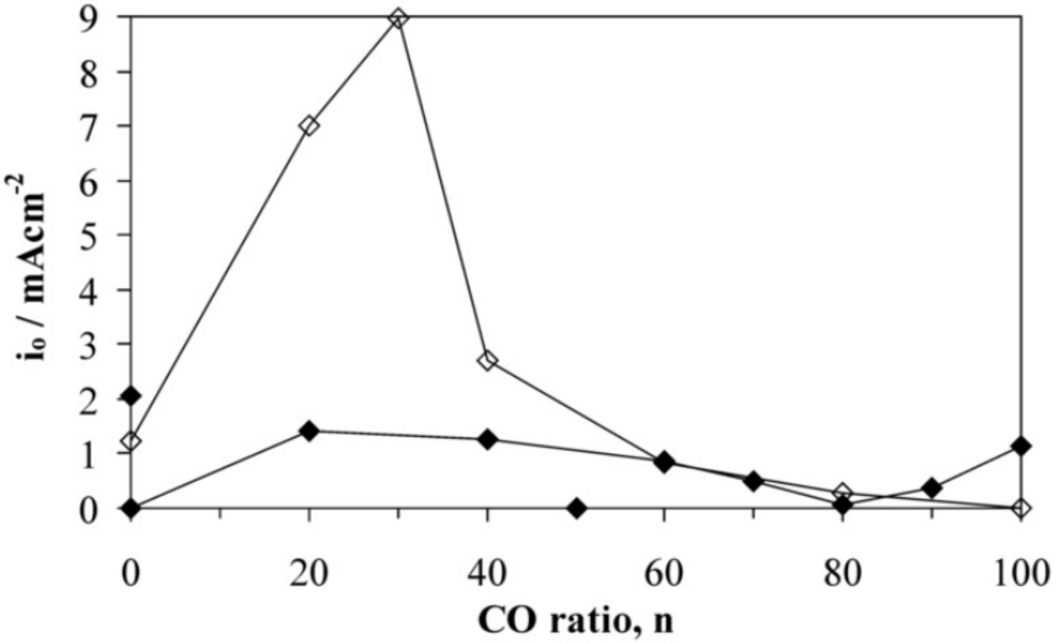

Figure 7.2 Exchange current densities (i_o) values for cells 1 and 2 (open and filled shapes, respectively) collected at various CO/H_2 fuel ratios. The data is calculated from impedance spectra measurements (AC). For cell 2, the initial H_2 value is indicated at 2.1 mA/cm^2, followed by the next point with pure CO at 1.1 mA/cm^2. Decreasing amounts of CO in the fuel ratio then follow towards pure H_2. The value of n, corresponds to the ratio of CO in the fuel inlet with a balance of H_2, where *n* is given by the formula: $n_{CO}/(100-n)_{H2}$.

The fuel ratio between 60/40 and 80/20 CO/H_2 is clearly a composition which results in poisoning, likely carbon poisoning. For Cell 1, the exchange current density dropped below that of pure hydrogen for the first time. Continuing to a fuel composed of pure CO, and later 50/50 CO/H_2, and subsequently returning to pure hydrogen showed a complete loss of current output from all of these fuel compositions. It is proposed that poisoning by carbon in the 60/40 and 80/20 CO/H_2 fuel region is irreversible following the outlined fuel concentration program. Post-mortem examination of this cell showed a complete delamination of the porous anode cermet material from the non-porous YSZ electrolyte support disk, indicative of carbon poisoning.

The second cell showed an exchange current density in CO of 1.1 mA/cm^2, which is comparable to that of the initial hydrogen fuel. Following a decrease in the CO concentration in the fuel, the cell experienced a drop in exchange current density, producing values in excellent agreement with those of the first cell. This confirms that the low exchange current density values shown in the region of 60/40 and 80/20 CO/H_2 fuel are due to this fuel composition producing a carbon poisoning effect, not because of cumulative carbon deposition, as might be proposed for the first cell before collecting the "reverse" data for the second cell. Although a modest improvement was observed in the region of 20/80 and 30/70 CO/H_2, the exchange current density of this cell never exceeded that of the original pure hydrogen. The carbon poisoning in the higher CO concentration region is the likely reason for this observation. Similar to the first cell, returning to a composition of 50/50 CO/H_2 and pure hydrogen showed no current coming from the cell. Post-mortem examination of this cell was also impossible due to complete delamination of the porous anode cermet material.

As can be observed in the raw impedance spectra, figure 7.3, the initial data for both cells in hydrogen is highly comparable (all panels). However, the low CO concentration data for cell 1 (A) shows low charge transfer resistances compared to hydrogen. The serial resistance for the 20/80 and 30/70 CO/H_2 fuel is increasing compared to hydrogen. The reason for this initial increase is likely due to a small amount of surface carbon formation. For the low CO concentrations of cell 2 (B), the cell has already been exposed to the carbon poisoning region at high CO concentrations, so the series resistance is observed to be higher than that for the pure hydrogen, as previously observed for cell 1. However, the charge transfer resistance is also higher for this cell in the same fuel composition region. It is postulated that there is a larger amount of intercalated carbon in the lattice of the metallic phase, which would have the effect of increasing the charge transfer resistance (*vide infra*). For cells 1 and 2 at high CO concentration (C and D, respectively) an increase in both the charge transfer resistances and serial resistances can be observed when compared to hydrogen. This region is expected to have the highest capacity for carbon poisoning for reasons that will be discussed in section 7.3.2.2. One important point to note is that cell 2, exposed to the high CO concentration and high carbon poisoning region (D) first experienced recovery when the CO concentration was lowered (B) to give impedance arcs much closer to that of the pure H_2 before the cell was exposed to any carbon sources.

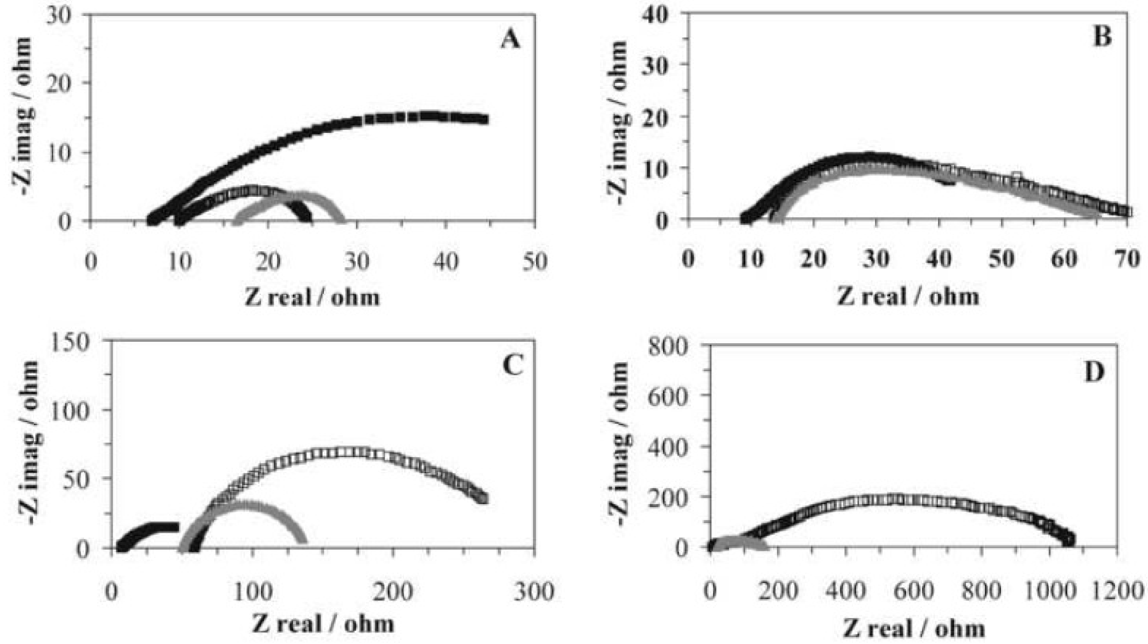

Figure 7.3 Raw impedance data for Cell 1 (panels A, C) and Cell 2 (panels B, D). Data from pure H_2 (black squares), and low CO concentration, in the range 20/80 (grey triangles) to 30/70 (open squares) CO/H_2 is shown (panels A, B). Data from pure H_2 (closed squares) and high CO concentration, in the range 60/40 (closed triangles) to 80/20 (open squares) CO/H_2 is shown (panels C, D). Note the different vertical and horizontal axes between panels.

Interspersed between electrochemical impedance spectral measurements, direct current cyclic voltammetry data was collected. The exchange current density values calculated from this data show identical trends as that of the EIS, however the values were more noisy than their EIS derived counterparts due the length of time needed to collect the cyclic voltammetry data as compared to the impedance data. Namely more microstructural changes can occur over the longer data collection period. The values obtained do, however, underscore the large increase in the exchange current density value with low CO/H_2 ratios, as seen with the EIS derived data.

7.3.2.2 Exchange current density data obtained from voltammograms at varying CO concentrations in H_2

Both cells show similar qualitative trends in the data collected by DC, figure 7.4, as by the AC measurements presented above. One noteworthy difference for the first cell is that in the low CO concentration region, the exchange current density values are not as high as those obtained by the AC measurements. An improvement of approximately 2.5 times from the pure hydrogen value to the low CO concentration values is likely due to a combination of a larger hydrogen value and slightly lower values obtained in the low CO concentration region. The reasoning for these differences is proposed to be a larger error associated with DC measurements as compared to AC, making the latter a more reliable method for measurement. The DC measurements take considerably longer to collect with the given parameters when compared to AC measurements. During this extended time, the physical changes which occur during measurement are expected to be larger for the DC measurements. The actual values for the AC measurements are expected to be more reliable, and the DC measurements provide a qualitative confirmation.

The second cell shows an identical value of 1.1 mA/cm^2 for pure CO when compared to the value obtained from AC measurements. The pure hydrogen value, as is the case for both cells in the DC series, is larger compared to its AC counterpart. Identical regions of exchange current density enhancement at low CO concentrations and consistent poisoning at high CO concentrations, supports both sets of data. The exchange current densities also fail to surpass the pure hydrogen value, indicating carbon poisoning at high CO concentrations. The inability of both cells to tolerate fuel composition cycling is also indicated here with a complete loss of current output for the 50/50 CO/H_2 data point collected after scanning once through the fuel compositions, regardless of direction.

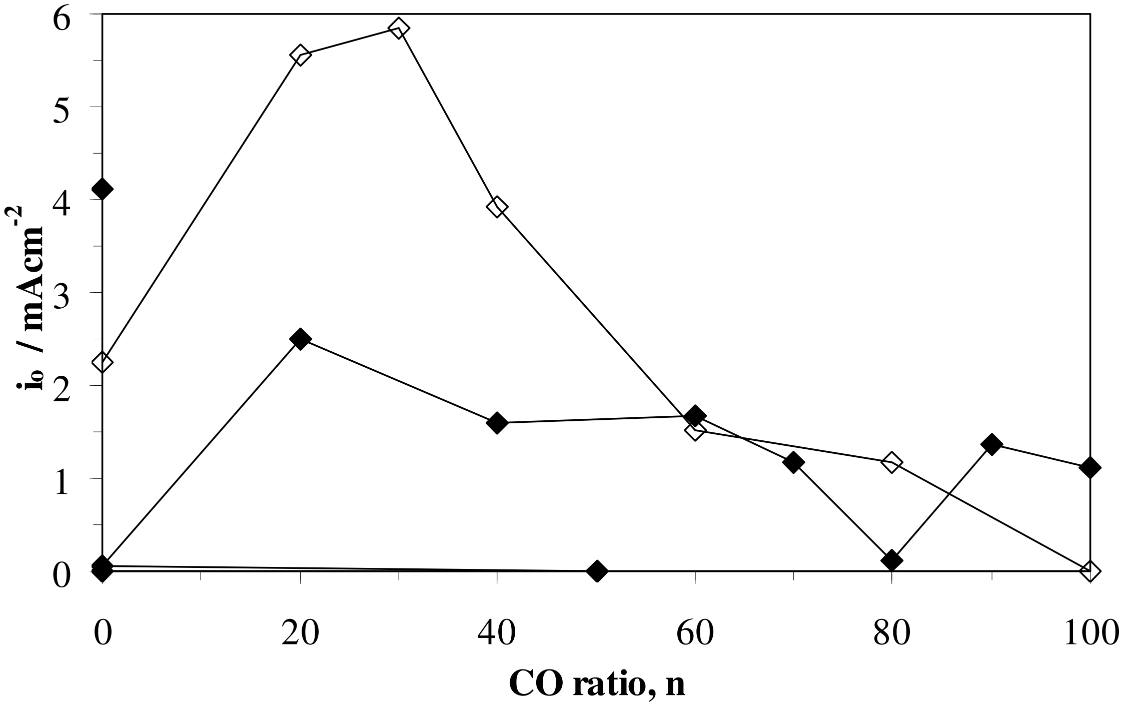

Figrure 7.4 Exchange current density (i_o) values for cells 1 and 2 (open and closed shapes, respectively) collected at various CO/H_2 fuel ratios. For cell 2, the initial H_2 value at 4.1 mA/cm^2 is followed by the point at 1.1 mA/cm^2 for pure CO. Decreasing amounts of CO in the fuel ratio then follow towards pure H_2. The value of n, corresponds to the ratio of CO in the fuel inlet with a balance of H_2, where *n* is given by the formula: $n_{CO}/(100-n)_{H2}$.

7.3.3 Long term performance with fuel ratio 25/75 CO/H_2

As discussed above, a fuel ratio of 25/75 provided enhanced performance. However, the presence of CO seemed to indicate a progressive carbon poisoning of the cell upon introduction of CO to the fuel mixture, particularly for high CO content. To test long term performance, a button cell was run for 7 days with the promising fuel mixture of 25/75 CO/H_2 following initial measurements with pure H_2. Figure 7.5 shows the OCV and i_o values observed.

A large value, 1.25 V, was obtained for pure H_2, as expected (day 0), Figure 7.5A. Following the addition of the 25/75 CO/H_2 fuel mixture, the OCV value dropped to a stable value of approximately 1.11 V (1.12 V for days 5-7). This small drop is not consistent with a simple reduction in the H_2 partial pressure, indicating that both H_2 and CO direct oxidation reactions are occurring simultaneously on the catalyst surface.

The corresponding exchange current density data is shown in Figure 7.5B. The value shown here for H_2 (4.7 mA/cm^2) is slightly higher than that presented in Figure 7.2 indicating a more robust button cell for this experiment. Nevertheless, the value is within the expected error range for the EIS derived i_o comparing multiple cells. In agreement with trends observed for cells 1 and 2, *vide supra*, switching the fuel to a mixture of 25/75 CO/H_2 produced a rise in the i_o value to 24.7 mA/cm^2 in day 1. This represents a 5.3 fold increase in i_o, again within error of other cells. However, despite this initial increase, the i_o values observed fell below the value found for pure hydrogen at days 5 and 6, and finally approached zero after 7 days of testing at the 25/75 CO/H_2 fuel ratio. Despite this eventual fall in performance, the initial 25/75 CO/H_2 fuel ratio data showed a significant increase in performance when compared to pure H_2; therefore, further research to prolong this higher performance area would yield important SOFC progress.

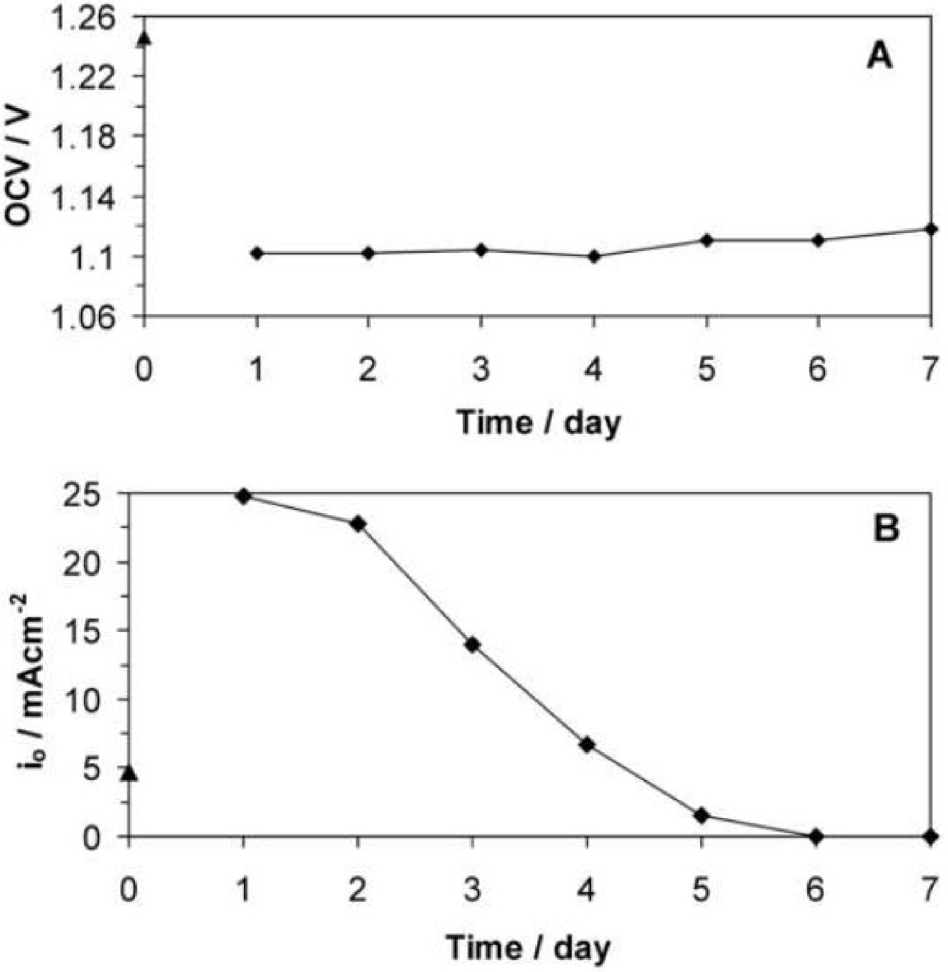

Figure 7.5 Fuel cell run continuously for 9 days. Following H_2 measurements for 2 days (Day 0, triangle), a fuel ratio of 25/75 CO/H_2 was run for 7 days (Days 1-7, diamonds). (A) OCV values (B) i_o values derived from electrochemical impedance data.

7.3.4 Scanning electron microscopy of post-run anode material

Post-run micrographs of the anode following 7 days running with a fuel mixture of 25/75 CO/H_2 are shown in Figure 7.6. Due to complete delamination of the current collector from the YSZ electrolyte disk following the 7 day run, a post-run cross sectional image was impossible to collect. However, it was possible to collect anode material which remained attached to the current collector, mount the powder sample onto carbon tape, and image it by SEM.

In figure 7.6, Panel A shows the agglomerate configuration with a size range from tens to hundreds of microns. Panel B outlines the particle sizes which range from approximately 0.1 to 2 microns. A small amount of charging is seen (bright particles) likely due to the low electron conductivity of YSZ-rich particles furthest from the carbon tape mount. Pores ranging in sizes similar to the particle size stated above can be seen with no visible carbon obstructions. Both at low magnification, panel A, and higher magnification, panel B, there is no evidence for visible, organized carbon structures such as microtubes or microrods, which might have grown under the outlined fuel cell conditions during this extended run. Such structures are usually observed with Ni and Co anodes under methane fuel. General carbon buildup was not observed either. Therefore, no direct SEM evidence to support the uncontrolled formation of coke on the anode could be found; however, due to the loss of exchange current density with time, and the complete delamination of the anode and current collector from the YSZ electrolyte disk, it can be hypothesized that preferential reactivity of different sites may lead to anode delamination. Due to the apparent physical breakdown of the anode in this region, no material was able to be recovered for direct imaging.

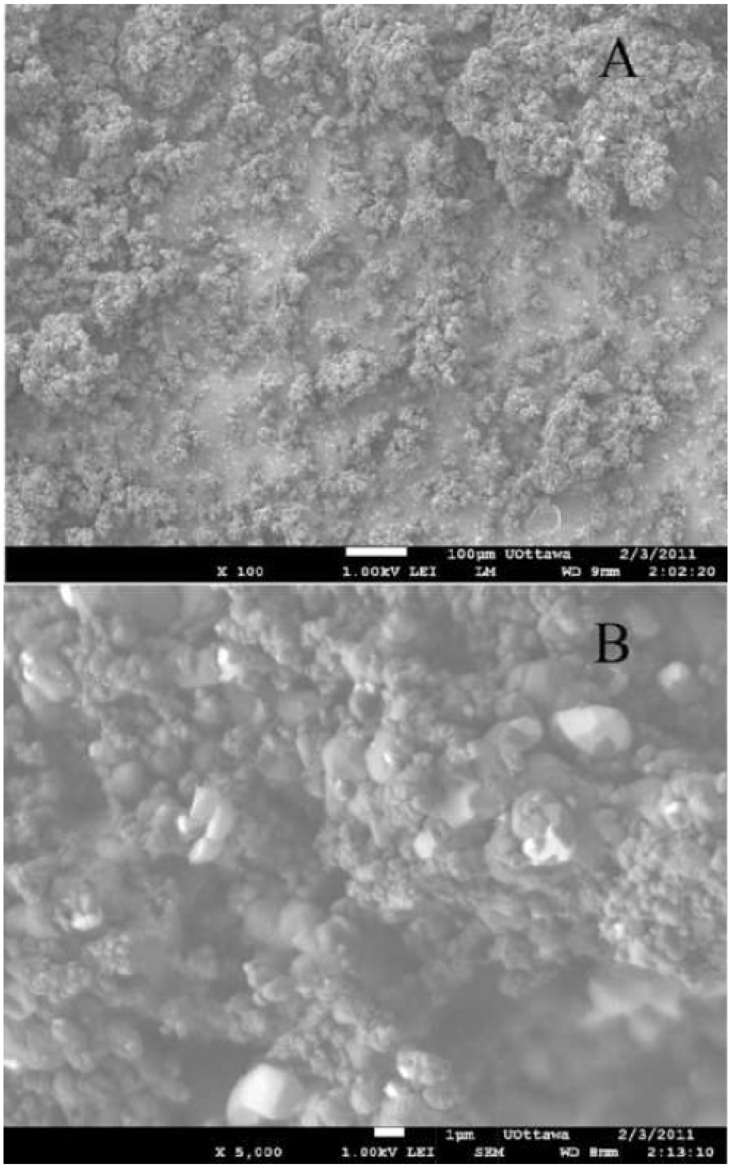

Figure 7.6 Scanning electron micrograph of the $Ni_{0.7}Co_{0.3}$-YSZ anode material post-run following the 7 day run with a fuel mixture of 25/75 CO/H_2. Panel A shows a magnification of 100x with a measurement bar of 100 µm, and panel B shows 5000x with a measurement bar of 1 µm. The powder sample was mounted on carbon tape.

7.4 Discussion

Drawing from the OCV data, the value for pure H_2 is slightly higher than expected. This is likely due to the trend in increasing OCV with decreasing fuel consumption, and the expected low fuel consumption with the high fuel flow rate utilized. Also at low fuel consumption, the concentration of products is expected to be extremely low, leading to a very small term in the Nernst equation. The plateau at a slightly lower value than pure H_2 for all CO/H_2 fuel mixtures is indicative of a constant ratio of reactions occurring over this entire range. With a rate approximately 3 times slower than that of H_2, the oxidation of CO is expected, especially at higher potentials, to produce CO_2. As shown by Andreassi *et al.* [5] the oxidation of CO is a factor which cannot be neglected when considering the global mechanism with a CO/H_2 fuel mixture. Carbon monoxide adsorbed on nickel does not have favourable desorption thermodynamics at 850°C [21]. It is likely either to undergo an electrochemical oxidation to form surface CO_2 followed by desorption to the gas phase, or disproportionation via the Boudouard reaction to contribute to carbon poisoning (equation 7.4). Carbon formation on the surface can also occur via CO reduction (equation 7.5). The direct oxidation of CO is expected to give an OCV of 0.98 V [5]. The value obtained of 1.04 V is within expected error and follows the rule of highest expected OCV with low fuel consumption. The values for the 50/50 CO/H_2 data point show reasonable agreement.

Impedance spectra indicated important trends for the exchange current density at each fuel composition. The most noteworthy observation is that the data produced larger exchange current densities in the 20/80 and 30/70 CO/H_2 fuel composition range. This cell had not yet experienced the carbon poisoning range between 60/40 and 80/20 CO/H_2 fuel. Although the direct electrochemical oxidation of H_2 on Ni is approximately 2-3 times faster than on Co [6], it is proposed that Co sites in the alloy are responsible for CO oxidation. This observation has been recorded previously for a Cu-Co-CeO_2-YSZ anode when compared to the Co-free Cu-CeO_2-YSZ equivalent cell [10]. In this work, the cell containing Co also gave activities 5 to 8 times higher for CO when compared to H_2.

For the carbon poisoning range between 60/40 and 80/20 CO/H_2, two carbon poisoning mechanisms can be proposed. It is difficult to assess to what extent these two mechanisms occur in the present system, since post-mortem examination of the button cell by SEM was not possible due to anode delamination. The first mechanism states that carbon deposited on the surface can block active catalyst sites. Since catalysis occurs preferentially on more energetic edge, step and kink sites, it is reasonable to assume that these could be poisoned more quickly, resulting in a large decrease in overall catalyst activity [22]. The second carbon poisoning mechanism is the intercalation of carbon into the bulk of the metal. This can have a large effect in decreasing the overall conductivity of the metallic phase of the anode cermet, which would greatly lessen the amount of current output observed. In addition to this, intercalation of carbon causes an expansion of the metal lattice, resulting in an increase in particle size. This can cause a sintering-like effect to reduce anode surface area and pore volume, thus reducing anode activity.

The amount of surface carbon poisoning can be reduced by the addition of water into the fuel stream, but this has only shown a small ability to remove a significant amount of carbon [23]. The reaction with the fastest expected rate is the electrochemical oxidation of H_2 on Ni surface. Since this reaction produces a small amount of water, it is expected to result in a small amount of the water gas shift reaction to occur, which has very fast kinetics on the Ni surface producing additional usable hydrogen. However, it is known that the presence of water vapour can lead to a decrease in OCV. Since the OCV was observed to be very high, this reaction is expected to occur in negligible amounts. The presence of both CO and H_2 in the fuel stream allow for CO reduction to occur producing carbon, equation 7.5. At the high operation temperatures used, a small amount of CO disproportionation via the Boudouard reaction, Equation 7.4, to produce elemental carbon is also expected.

The long term effects of running a button cell at the CO/H_2 concentration, which produced the highest i_o values (25/75) was investigated. Days 1-3 produced i_o values significantly higher than pure H_2 fuel. It is proposed that a synergistic effect of the NiCo alloy in the anode produces optimal conditions for the oxidation of both fuels in this particular ratio. It is possible that the similarity in the two ratios, 25/75 CO/H_2 fuel, and 30/70 Co/Ni alloy is a key to this observed initial increase in i_o values. That is, that CO is preferentially oxidized on Co sites of the alloy and hydrogen is oxidized on Ni sites and the concentration relates to the relative rates of oxidation and surface mobility of the two gases. Nevertheless, by day 4, the observed i_o values were comparable to that of pure H_2, and finally by day 7, it had fallen to approximately zero.

No visible, organized carbon structures were observed following the post-run microscopy of the anode exposed for 7 days under 25/75 CO/H_2 fuel conditions. Since this fuel ratio has been previously reported to produce low coking, our observations further confirm this statement. However, if carbon poisoning is not prevalent in this regime, a different mechanism must cause the eventual degradation of the fuel cell. It is hypothesized that preferential reactivity of different sites may give rise to a change in the anode microstructure over time under operating conditions. This change eventually prevents the proper electrical contact between the anode cermet and the current collector mesh.

7.5 Conclusions

A cermet anode of alloyed NiCo-YSZ has been discovered to give higher exchange current density values for low ratio of CO/H_2 fuels in the range 20/80 and 30/70 compared to pure H_2. This is the first example of a Ni-based anode providing higher performance with a CO/H_2 mixed fuel than for a pure H_2 fuel. It is postulated that the reason for this is the synergetic behaviour between the Co and Ni in the CoNi alloy of the cermet via preferential reactivity. This system would have industrial applications since it combines both two available fuels, H_2 and CO, and two relatively inexpensive metals, Ni and Co. Lower performances when compared to pure H_2 fuel were observed for high ratios of CO/H_2 in the range 60/40 to 80/20. It is expected that carbon poisoning in this range contributed to the lowered values. Finally, continuous running of a cell with fuel ratio 25/75 CO/H_2 for 7 days produced i_o values, which were observed to increase significantly above the values for pure H_2 during days 1-4, but fell below this value during subsequent days. No visible coking was observed leading to the hypothesis that changes in microstructure of the anode cermet are the cause for the loss of exchange current density.

7.6 References

[1] S. McIntosh, R. Gorte, Chem. Rev. 104 (2004) 4845.

[2] A.B. Stambouli, E. Traversa, 6 (2002) 433-455.

[3] J.H. Koh, B.S. Kang, H.C. Lim, Y.S. Yoo, 4 (2001) 812-815.

[4] M.F. Liu, P. R.R, D.H. Dong, J.F. Gao, X.Q. Liu, G.Y. Meng, 185 (2008) 188-192.

[5] L. Andreassi, C. Toro, S. Ubertini, 6 (2009) 021307 (021301-021315).

[6] Y. Matsuzaki, I. Yasuda, 147 (2000) 1630-1635.

[7] O. Boudouard, 148 (1909) 348-351.

[8] Y. Tang, J. Liu, 35 (2010) 11188-11193.

[9] K. Sasaki, H. Kojo, Y. Hori, R. Kikuchi, K. Eguchi, Electrochem. 70 (2002) 18.

[10] O. Costa-Nunes, R.J. Gorte, J.M. Vohn, 141 (2005) 241-249.

[11] X.-F. Ye, S.R. Wang, J. Zhou, F.R. Zeng, H.W. Nie, T.L. Wen, 195 (2010) 7264-7267.

[12] V. Alzate-Restrepo, J.M. Hill, 195 (2010) 1344-1351.

[13] J.S. O'Brien, J.B. Giorgi, 28 (2010) 221-231.

[14] C.M. Grgicak, M.M. Pakulska, J.S. O'Brien, J.B. Giorgi, 183 (2008) 26-33.

[15] C.M. Grgicak, R.G. Green, W.-F. Du, J.B. Giorgi, J. Am. Ceram. Soc. 88 (2005) 3081.

[16] C.M. Grgicak, R.G. Green, J.B. Giorgi, J. Mater. Chem. 16 (2006) 885.

[17] B. Kenney, K. Karan, 153 (2006) A1172-A1180.

[18] C.M. Grgicak, Anodes for solid oxide fuel cell (SOFC) systems operating in multiple fuel environments: Effects of microstructure and composition, University of Ottawa, Ottawa, 2007.

[19] M. Cimenti, J.M. Hill, J. Power Sources 186 (2009) 377.

[20] K. Sasaki, K. Watanabe, K. Shiosaki, K. Susuki, Y. Teraoka, 2003 (2003) 1295-1304.

[21] M. Shishkin, T. Ziegler, J. Phys. Chem. C 113 (2009) 21667.

[22] C.M. Chun, J.D. Munford, T.A. Ramanarayanan, 147 (2000) 3680-3686.

[23] A. Weber, B. Sauer, A.C. Muller, B. Herbstritt, I. Yvers-Tiffee, 152 (2002) 543-550.

8

General Conclusions

8.1 Conclusions

A series of cermet powders of composition $Ni_xCo_{(1-x)}O$-YSZ were synthesized for testing as cermet anode materials for SOFCs. The surface area values of the sintered powders, which showed increased crystallinity compared to the 'as-synthesized' powders, were approximately two orders of magnitude lower than that of the green powders; this is within the expected range for a NiO-YSZ cermet. The Co is incorporated into the crystal lattice of the NiO, thus forming a true alloyed material with unit cell parameters, which increase with increasing Co concentration. Two types of particles were found by SEM and EDS: small, amorphous particles of YSZ and large, crystalline particles of nickel. The known propensity for nickel to coarsen with elevated temperature supports this observation.

The electrochemical oxidation of hydrogen on a cermet anode composed of $Ni_{0.7}Co_{0.3}O$-YSZ was investigated using a series of many button cells manufactured by hand to tolerances as high as possible. Through fitting an equivalent circuit model, for EIS data, and extrapolating the Tafel region, for cyclic voltammetry data, the exchange current density values for these button cells was determined. Although there is large variation from one button cell to the next, the average values for exchange current density extracted from the two different methods was found to be in good agreement. From the data presented, the average exchange current density for a $Ni_{0.7}Co_{0.3}O$-YSZ cell at 850^{o}C is 11.3 and 10.0 mA/cm^2 for EIS and cyclic voltammetry data respectively, which indicates that, although a relatively large variation was found (expected to be due to microstructural variation) the average values for both methods of measurement is in good agreement in hydrogen.

Following reduction in pure hydrogen, the fuel was changed to a mixture with high concentration of H_2S, namely 10 % H_2S/H_2. It was found that this produced a sudden change in anode microstructure and resulted in loss of exchange current density. Lowering the amount of H_2S in the initial fuel feed, which allowed for a more gradual microstructural change, allowed the cell to eventually function at concentrations in excess of 10 % H_2S/H_2. Determined by the OCV values in various concentrations of H_2S/H_2, hydrogen is the predominant fuel of choice, even if H_2S is available. Only under pure H_2S fuel was the OCV was lowered, as is expected for the electro-oxidation of this species. Slow cooling in a 10 % H_2S/H_2 mixture following electrochemical testing produced metal sulfide spheres, as determined by SEM and EDS. A nickel foil was treated with 10 % H_2S/H_2 followed by slow cooling in order to assess the depth of percolation of the sulfur in the nickel phase. Complete conversion to metal sulfide under operating conditions in a H_2S/H_2 fuel inlet mixture to a depth far in excess of the diameter of particles observed in the button cell microstructure indicate that the metal sulfide can form in bulk under the given fuel cell operating conditions.

Investigation in hydrocarbon, alcohol and biodiesel fuels was then undertaken to test the fuel variability of the given cermet anode material. The exchange current density of methane was found to increase in the presence of H_2S relative to poisoned hydrogen, which supports the theory that blocking of active step sites by sulfur can alter and enhance the performance under otherwise strongly coking conditions. In the case of ethane, though no increase in exchange current density was observed, a lengthening of the functional lifetime of the cell was observed, indicating reduced carbon poisoning. A similar effect in the exchange current density was observed for biodiesel fuel in the presence of sulfur poison, namely the lifetime of the button cell was lengthened. This is a promising result for hydrocarbon-based fuels which naturally contain high levels of sulfur, such as those extracted from the Alberta sands. Methanol is a promising oxygen-containing SOFC fuel since it produced exchange current density values larger than hydrogen, and showed no evidence of coke formation by post-mortem SEM.

Since oxygen-containing fuels are known to decompose in the gas phase at typical SOFC operating temperatures, the performance in a mixture of various CO/H_2 fuels was then investigated. It was found that cermet anodes of composition $Ni_{0.7}Co_{0.3}O$-YSZ gave higher exchange current density values for low ratio of CO/H_2 fuels in the range 20/80 and 30/70 compared to pure H_2. This is the first example of a Ni-based anode providing higher performance with a CO/H_2 mixed fuel than for a pure H_2 fuel. It is postulated that the reason for this is the synergetic behaviour between the Co and Ni in the NiCo alloy of the cermet via preferential reactivity. The range 60/40 to 80/20 gave lower performances when compared to pure H_2 fuel for high ratios of CO/H_2 where it is expected that carbon poisoning contributes to the lowered values. Finally, continuous running of a cell with fuel ratio 25/75 CO/H_2 for 7 days produced exchange current density values, which were observed to increase significantly above the values for pure H_2 during days 1-4. Despite the fact that the exchange current density value fell below that of pure hydrogen during the subsequent days of testing, no visible coking was observed leading to the hypothesis that changes in microstructure of the anode cermet are the cause for the loss of exchange current density.

Appendix

<u>Presented here is a set of sample calculations for the determination of exchange current density values from raw electrochemical impedance spectroscopy data.</u>

Presented in figure A1 is a sample of raw impedance data from a $Ni_{0.7}Co_{0.3}$-YSZ anode button cell at 800°C in H_2 at 50 sccm in Nyquist plot form.

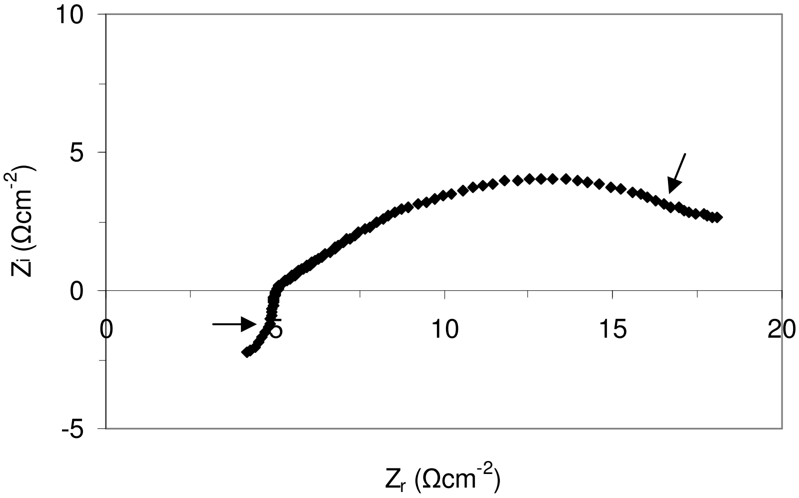

<u>Figure A1</u>. A Nyquist plot of a button cell with a $Ni_{0.7}Co_{0.3}$-YSZ anode at 800°C in H_2 at 50 sccm. The data between the arrows will be used for the fitting shown in figure A2.

Presented in figure A2 is the CNLS fit of the raw data. The lowest and highest frequency data have been removed to avoid Warburg and problems fitting the induction parameter respectively. This fit was obtained through the *ZView* software. The numerical results of fitting the shown equivalent circuit are presented in figure A3.

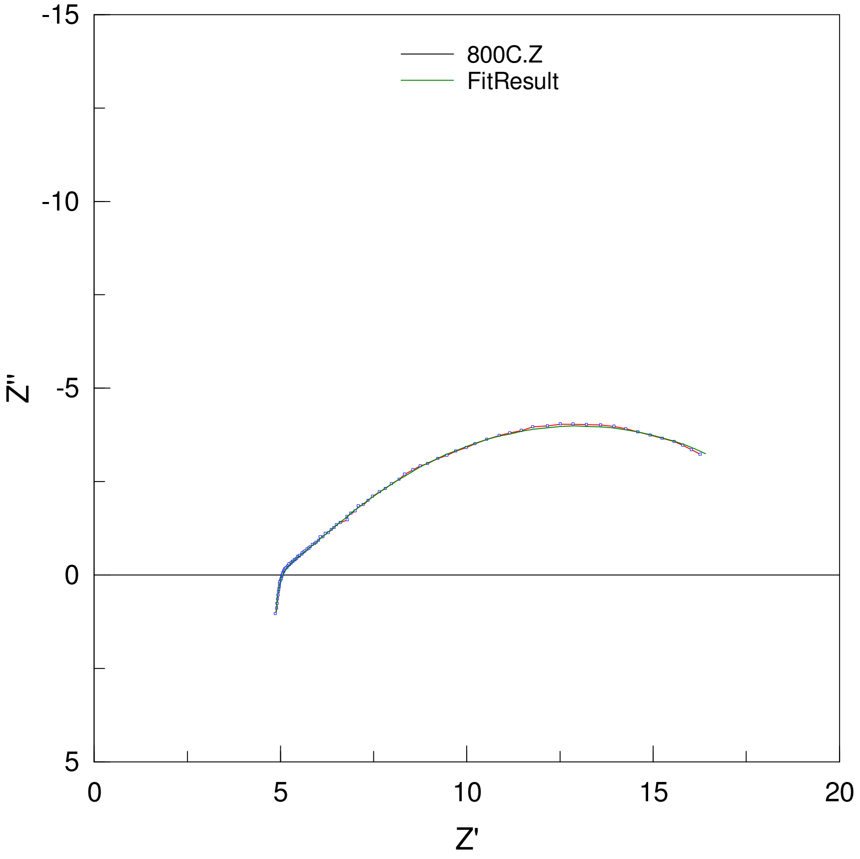

Figure A2. CNLS fit of the raw data using the *ZView* software.

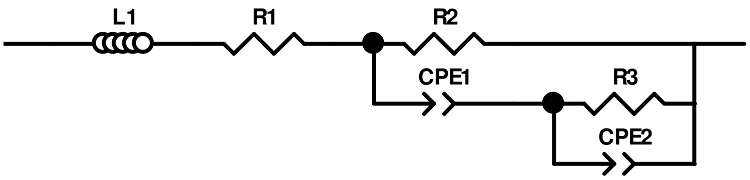

Element	Freedom	Value	Error
L1	Free(+)	4.0431E-6	6.9644E-8
R1	Free(+)	5.45	0.027774
R2	Free(+)	15.25	0.12141
CPE1-T	Free(+)	0.0093648	0.00030708
CPE1-P	Free(+)	0.66585	0.012289
R3	Free(+)	1.964	0.41663
CPE2-T	Free(+)	0.025345	0.0062364
CPE2-P	Free(+)	0.45104	0.033183

Figure A3. Numerical values obtained from fitting the equivalent circuit shown to the data in figure A2 using the *ZView* software.

Here, as shown in figure A3, the value for R_2 is equivalent to R_{CT} (normally designated as R_3, however, here the values for R_2 and R_3 have been mathematically reversed in the data fitting). Using the low field approximation of the Butler-Volmer equation for the anodic current, the exchange current density can thus be easily calculated to have a value of 6.06 mA.

$$i_o = \frac{RT}{nFR_{CT}}$$

$$i_o = \frac{(8.314 J/molK)(1073K)}{(1)(96485C/mol)(15.25\Omega)}$$

$$i \ = 0.00606A = 6.06mA$$

To assess the error associated with the fit of the equivalent circuit with different endpoints in the low frequency data range, a series of fits was obtained. As shown in figure A4, the range of fit was varied from that of the entire low frequency data set (P_0 to P_{15}) to that past the maximum imaginary data value on the charge transfer semicircle (P_0 to P_1). The corresponding charge transfer resistance (R_{CT}) values were plotted, as is shown in figure A5, where the points on the horizontal axis correspond to those designated in figure A4. As can be observed, in the lowest frequency, Warburg region, (P_{13} to P_{15}) the values are unstable. The values stabilize towards the value used for the calculation of R_{CT} at P_{10}. At increasing frequency values (P_1 to P_9, P_1 to P_8, etc), the values diverge from the most accurate value for R_{CT} because less data corresponding to that process is included. Thus, the error associated with the choice of data range for fitting is minimized in the stable region of figure A5, namely between points P_8 and P_{10} in the figure.

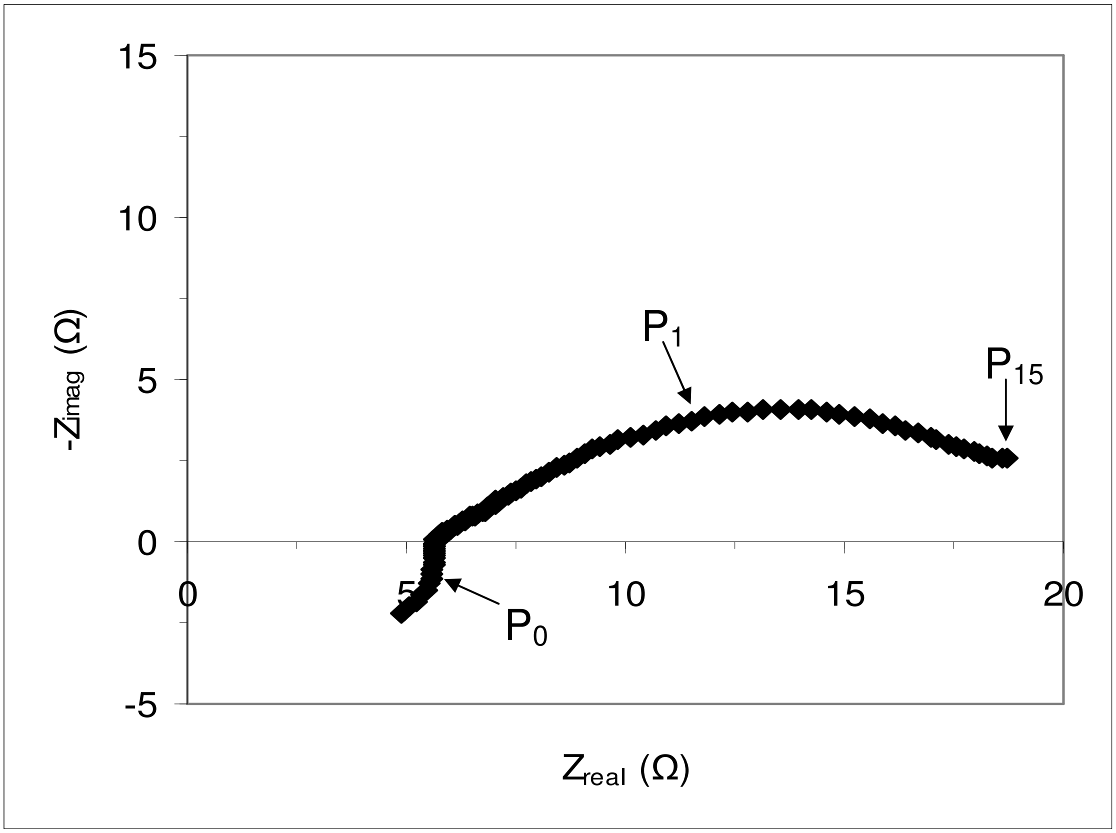

Figure A4. Nyquist plot indicating the data ranges utilized for data fitting of R_{CT} for Figure A5. The increasing data range used corresponded to P_0 to P_1, increasing to P_0 to P_{15}.

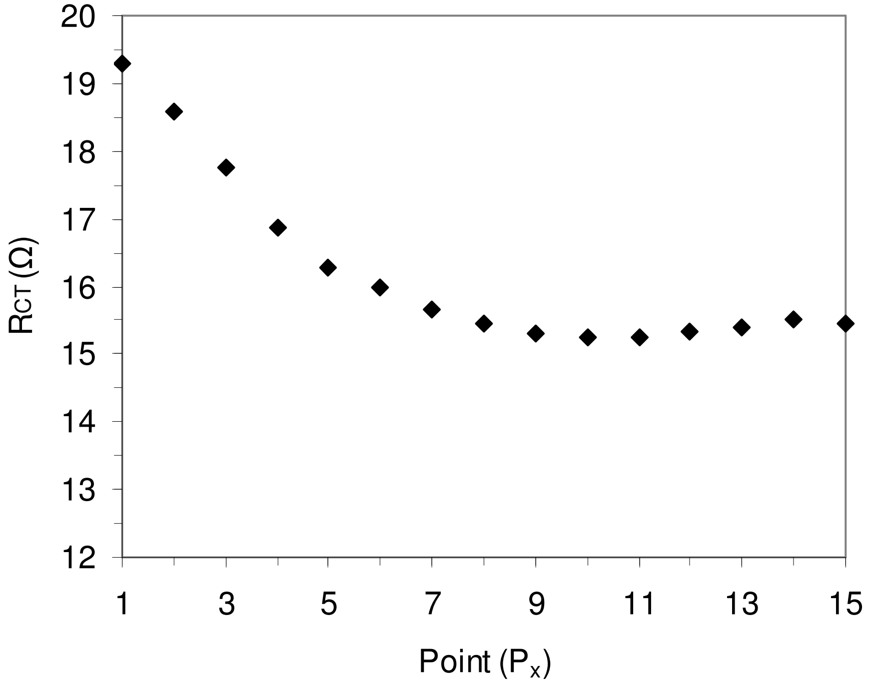

Figure A5. R_{CT} values obtained from fitting the data in the ranges shown in figure A4.